Exotic phases in strongly correlated parafermion chains

PhD thesis, Utrecht University, December 2021

Printed by: ProefschriftMaken.nl

ISBN: 978-94-6423-598-2

DOI: 10.33540/828

About the cover: The objects studied in this thesis possess a three-, four- or six-fold rotational symmetry, just like the tiles in the tessellation. The one-dimensional character of the models in the thesis is reflected by the red diagonal and javelins flying through the background.

Exotic phases in strongly correlated parafermion chains

Exotische fases in sterk gecorreleerde parafermionketens

(met een samenvatting in het Nederlands)

Proefschrift

ter verkrijging van de graad van doctor aan de Universiteit Utrecht op gezag van de rector magnificus, prof. dr. H.R.B.M. Kummeling, ingevolge het besluit van het college voor promoties in het openbaar te verdedigen op woensdag 12 januari 2022 des middags te 4.15 uur

door

Jurriaan Johannes Wouters

geboren op 18 april 1993 te Amersfoort

Promotor: Prof. dr. R.A. Duine
Copromotor: Dr. D. Schuricht

Contents

Contents

Preface

This thesis is the result of four years of research, done at the Institute for Theoretical Physics of Utrecht University under the supervision of Dr. D. Schuricht. The research focusses at zero temperature behaviour of strongly correlated 1D systems, in particular Majorana and parafermion chains.

Chapter 1 gives an introduction to the thesis, with some motivation and background for studying parafermion systems. Thereafter Chapters 2 and 3 focus on exact ground states in (among others) parafermion systems, while Chapters 4, 5 and 6 discuss a combination of numerics and analytics to understand the phase diagram of extended parafermion models.

The summer of 2020 I spent investigating the origins of the Institute for Theoretical Physics in Utrecht. This resulted in both a Dutch and English article, presented side by side at the end of this thesis.

I hope the reader finds the thesis inspiring and learns a thing or two.

Jurriaan Wouters
August 2021, Utrecht

List of publications

This thesis is based on the following publications:

- J. Wouters, H. Katsura and D. Schuricht, *Exact ground states for interacting Kitaev chains*, Physical Review B 98(11), 155119 (2018).
- J. Wouters, H. Katsura and D. Schuricht, *Interrelations among frustration-free models via Witten's conjugation*, SciPost Physics Core 4(4), 027 (2021).
- I. Mahyaeh, J. Wouters and D. Schuricht, *Phase diagram of the $\mathbb{Z}_3$-Fock parafermion chain with pair hopping*, SciPost Physics Core 3(2), 011 (2020).
- J. Wouters, F. Hassler, H. Katsura and D. Schuricht, *Phase diagram of an extended parafermion chain*, arXiv:2106.15823 (2021) currently under review at SciPost Physics Core.

Other publications to which the author has contributed:

- D.M.F Hartmann, J.J. Wouters, D. Schuricht, R.A. Duine and A. Kamra, *Intersublattice entanglement entropy as an extensive property in antiferromagnets*, Physical Review B 104(6), 064436 (2021).
- J. Wouters, A. Gotis, R. Kang, D. Schuricht and L. Fritz *in preparation.*

Historical publications in non-scientific journals by the author:

- J.J. Wouters, *Celebrating 105 Years Institute for Theoretical Physics*, Fylakra, 65(3), 30 (2021).
- J.J. Wouters, *Ornstein en de ontwikkeling van het Utrechtse Instituut voor Theoretische Fysica*, Nederlands Tijdschrift voor Natuurkunde 87(9), 42-46 (2021).

1 Introduction

Computers have an important position in modern day life. With the sustained improvement of computational speed, applications that seemed out of reach a decade ago are implemented in the cheapest smartphones nowadays. The possibilities seem endless, however, there are many challenges still insurmountable. Some problems involve calculations that will never be feasible on an ordinary computer for the shear vastness of possible outcomes, more than there are particles in the universe. Think of route optimization for logistics companies, which scales (super)exponentially with the number of stops. But there are also tons of scientific applications like molecular simulation (for drug development) and numerical simulations in quantum chemistry, biology or for physical systems. The latter includes simulations of quantum mechanical systems with non-trivial interactions, such as the ones discussed in this thesis. Their current implementations on ordinary computers require approximate calculations and give only partial results.

Already in the 1982, Richard Feynman proposed the use of quantum mechanics for simulating our quantum mechanical world [1]. These quantum computers would employ the collective properties of quantum states, eg superposition, which we will discuss later on. This allows for simultaneous evaluation of the many possible outcomes, where a classical ordinary computer can only do one calculation at the time. The creation of a quantum computer would bring solutions to these exponentially hard problems within reach. There are many experimental proposals for quantum computers. Some prominent examples of devices in operation are Google's Sycamore [2], IBM's Q System One [3] and D-Wave Systems [4], all based on superconducting Josephson junctions [5]. However, none of these systems outperform the best classical computers, yet [6–8]. For the so called quantum speed-up, ie faster than classical algorithms, a quantum computer needs to meet several requirements, like scalability of the processing unit, stability of the information and freedom of initialization and manipulation [9, 10]. For an ordinary computer all these criteria are met, whereas all state-of-the-art quantum computers are lacking in at least one of these aspects.

The challenge lies in the delicacy of the quantum bits (or qubits), the smallest building block of a quantum computer, analogous to the bit in the classical computer. These quantum systems need multiple states (eg spin up and spin down) at exactly the same energy, a degeneracy of the ground state. Quantum mechanically the system can be forced into a superposition of these states. Coupling many of these superpositioned qubits into an entangled state describes an exponential number of classical states. To be more concrete, the number of classical states represented by n qubits is 2^n, showing the exponential growth. While a classical computer does only one calculation at the time, a quantum computer, does computations on all these states in unison. This scheme relies on the presumption that the qubit states remain at the same energy. Distortions, like impurities and proximity effects, can cause the states to split in energy, breaking the superposition, which loses the information stored on the computer.

One promising class of qubits less sensitive to these external factors are based on topological systems [11–16]. Continued experimental efforts manufacturing and manipulating these topological qubits revealed the challenging nature, although there have been some extraordinary successes [17–22]. In this thesis we hope to contribute to the theoretical understanding of these elusive devices.

Topological systems are quite novel in condensed matter physics. Usually particles form states of matter that can be classified based on symmetries of the bulk of the system using the powerful Landau theory [23]. In this framework phases and transitions among them are distinguished by local order parameters and spontaneous symmetry breaking.[a] In the 1980s, models appeared that could no longer be captured in the Landau paradigm. The experimentally realized integer quantum Hall (IQH) effect [24–26] could not be classified by symmetries of the bulk alone, but required intricate knowledge of the physics of the boundaries of the system. Also, the theoretical formulation of the fractional quantum Hall (FQH) effect [27] and the chiral spin liquid description of high temperature superconductors [28, 29] showed physical behaviour that could not be explained by spontaneous symmetry breaking. A new kind of robust order was necessary, topological order. Soon thereafter the first topological invariants were formulated [30] and a classification of topological systems and corresponding invariants followed suit, known as the tenfold way [31].

On a microscopic level a topological phase is characterized by long range entanglement. Macroscopically, topology can be recognized by a robust de-

[a] For instance separating liquid water from ice. Ice accommodates a lattice symmetry, however the continuous translational and rotational symmetry of water are broken.

generacy of the ground state, caused by the presence of zero energy modes at the surface of the system, eg edge currents for FQH [26, 32]. The non-locality of these modes makes the degenerate states robust against local perturbations, eg local magnetic field fluctuations, crystalline impurities etc. The degeneracy can only be broken by energetic processes, like a quantum phase transition. On the other side of such a transition usually lives a trivial phase, with only one ground state, lacking the degeneracy.[b]

An example of such a topological system is the model proposed by Kitaev in 2001 [11]. This effective 1D system is comprised of a quantum wire of spinless fermions (c_j), coupled to a 3D p-wave superconductor, see Figure 1.1. In the former, fermions can hop along the chain between sites, with an energy w. The latter induces a superconducting pairing Δ of the spinless fermions in the wire. There is an on-site/chemical potential μ, which will play the role of modulator between the topological and trivial phase.

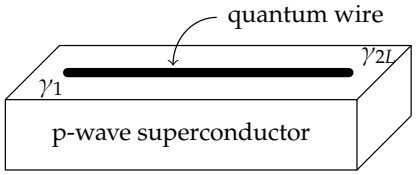

Figure 1.1: Proposal for experimental realization of Majorana zero modes in a quantum-wire-superconductor setup, from Ref. [11].

An intuitive picture arises with the introductions of Majorana fermions (γ_j). First proposed by Ettore Majorana [33], a complex fermion can artificially be decomposed in to two real Majoranas:

$$c_j = \gamma_{2j-1} + \mathrm{i}\gamma_{2j} \tag{1.1}$$

In this representation, the Hamiltonian[c] becomes simple, pictorially shown in Figure 1.2, where we have taken $\Delta = w$ for convenience. The circles denote the even site (white) and odd site (grey) Majorana fermions, coupled with alternating energies μ and w. Remember that, in reality, two neighbouring Majoranas form a fermion, as indicated by the rectangles.

Two limits are important to distinguish. With $\mu \gg w$ the Majoranas are bound into the original fermions (c_j), as the dotted bonds become irrelevant. The ground state is unique, with finite energy gap to the excited states and the

[b] This is by no means a complete discussion of topological systems. Only the necessary background is presented for understanding 1D topological chains, as they are the protagonist of this thesis.

[c] For the explicit form of the Hamiltonian, see Chapters 2 and 3.

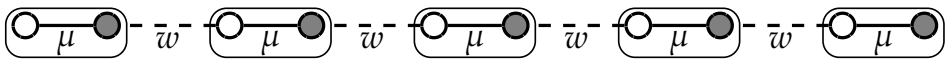

Figure 1.2: Pictorial representation of the Kitaev Hamiltonian with $L = 5$ fermions decomposed in $2L = 10$ Majorana fermions.

phase is trivial. However, for $\mu = 0$, the solid bonds disappear and the Majoranas bind with neighbours originally belonging to different fermions. In this quantum mechanical musical chairs, two Majoranas are left out, the first (white, γ_1) and last (grey, γ_{2L}). These are recombined into a long-ranged complex fermion, decoupled from the system. In other words, the energy of the system does not depend on the presence or absence of this long-ranged fermion. These edge Majoranas therefore have evident name: Majorana zero modes. Since this mode can be added free of (energy) charge, the ground state is twofold degenerate, two states at exactly the same energy.[d] Hence, this phase is topological. Moreover, the ground states are locally indistinguishable, making the topological phase extremely robust. Local disorder cannot hybridize the two [34–41], neither can small interactions [38, 39, 41–54]. Only approaching the transition at $\mu = w$ closes the macroscopic bulk gap, destroying the topological nature. Finally, the reality of the Majorana fermions gives them a great advantage, since it prevents decoherence due to dephasing [12].

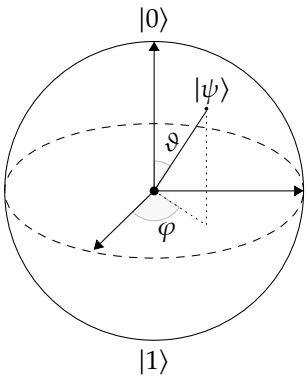

Figure 1.3: The Bloch sphere, the geometrical representation of any normalized pure state of a two-level quantum system.

These trademarks make the Majorana a candidate for a stable quantum bit. If we consider the two robust ground states without $|0\rangle$ and with the long-ranged fermion $|1\rangle$, we can obtain the superposition of the two as follows

$$|\psi\rangle = \cos(\vartheta/2)\,|0\rangle + e^{i\varphi}\sin(\vartheta/2)\,|1\rangle\,, \tag{1.2}$$

where the angles represent the degrees of freedom and are schematically shown

[d] Technically the energy difference is exponentially small, $\exp(-\Delta E L)$, where ΔE is the gap above the ground state. This vanishes extremely fast (away from transitions) with system size L.

on the Bloch sphere in Figure 1.3.[e] Manipulating these angles ϑ and φ is the basis of calculation in a quantum computer. This operation is done by quantum gates, microscopic components responsible for modulating one of more qubits. For Majorana qubits these manipulations arise from rotating Majoranas around each other in space, also known as braiding, denoted by s [14]. Pictorially, this is shown in Figure 1.4a. Braiding these Majorana qubits is an example of non-Abelian anyon braiding, for the non-commuting braid group. Alas, recent developments uncovered that these braid operations for Majoranas cannot quite cover the whole Bloch sphere [55, 56]. In other words, not all two-level states can be reached, which is one of requirements for a so-called universal quantum computer [9, 10].

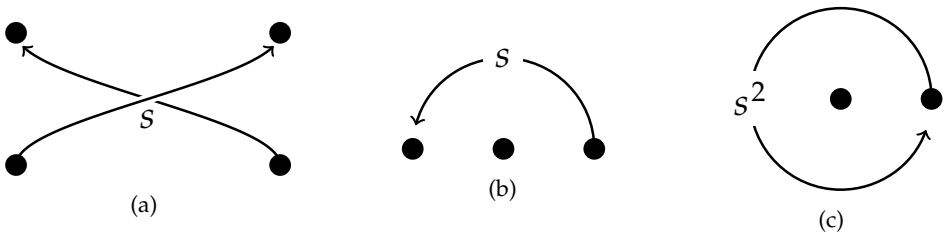

Figure 1.4: Braiding of two particles. The vertical axis of (a) represents time. In (b) the direction of time is along the path. Topologically the operations in (a) and (b) are equivalent. double braiding is shown in (c).

One route for resolving this obstacle leads through the other type of braiding, Abelian anyon braiding, the simpler of the two.[f] To understand this, we consider what happens when we apply the braid operator twice (s^2), bringing both particles back to their original position. Since we only worry about the relative movement of the particles, the operation in Figure 1.4b is equivalent to the winding in Figure 1.4a. The double braiding (s^2) is therefore shown in Figure 1.4c.

In 3D (or higher) this loop can simply be lifted over the the stationary particle and contracted to a point. That makes the double exchange trivial, indeed: $s^2 |\psi\rangle = |\psi\rangle$. A single exchange can therefore describe bosons: $s |\psi\rangle = |\psi\rangle$, or fermions: $s |\psi\rangle = -|\psi\rangle$, the only two types of particles allowed in 3D.

[e] The virtue of a quantum computer comes from the entanglement. Coupled qubits are not simply represented by Equation (1.2), but an rather a highly entangled state.

[f] Abelian anyon statistics are related to an Abelian group, like U(1). Hence non-Abelian anyon statistics are self-explanatory, with for instance the state (1.2) related to SU(2)

In 2D, the particle trajectory cannot be contracted into a point, without going through the other particle (which is forbidden). Therefore the double exchange is not necessarily trivial. States can obtain an arbitrary phase $s|\psi\rangle = e^{i\theta}|\psi\rangle$ from the exchange, such that $s^2|\psi\rangle = e^{2i\theta}|\psi\rangle$. For 0 and π we recover bosons and fermions, while generic θ defines fractional statistics. These particles were named "anyons" by Wilczek in 1982 [57], after they were predicted five years earlier by Leinaas and Myrheim [58]. The first anyon system was proposed theoretically in 1982 as well, when Tsui *et al.* formulated the fractional quantum Hall system [27]. In 2020 the first experimental evidence of fractional statistics was seen [59].

The path towards a new candidate for stable qubits follows these fractional statistics, in the form of parafermion, the fractional cousins of Majoranas. Originally proposed in statistical mechanics for understanding the Potts model (a spin-like lattice model), these parafermions are Abelian anyons [60]. Exchanging parafermions produces a phase of $\theta = \frac{2\pi}{m}$, with $m > 2$.[g] The symmetry group associated to these particles are the rotations of the m-polygon, isomorphic to $\mathbb{Z}_m$, see Figure 1.5. Therefore they are denoted by $\mathbb{Z}_m$ parafermions.

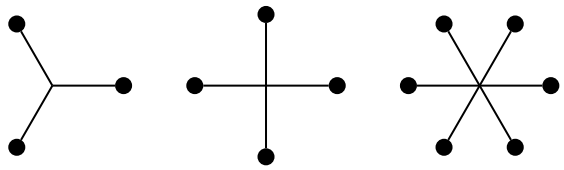

Figure 1.5: Three examples of eigenvalues on the unit circle of $\mathbb{Z}_m$ braid groups for $m = 3, 4, 6$.

Similar to the Kitaev chain for Majoranas, a so-called parafermion chains exist, with a trivial and topological phase [61]. Moreover, the topological phase features a robust m-fold degeneracy, protected by a non-local symmetry.

Even though there have been only a handful discussions on direct parafermion braiding, they would have similar shortcomings as Majoranas. They cannot be used for a universal quantum computer, since braiding parafermions would not cover the whole Bloch sphere [62]. Nevertheless, recently it was shown that parafermions can be manipulated to form Fibonacci anyons [62, 63]. For Fi-

[g] For $m = 2$ we recover Majorana fermions. Parafermions are hence a generalization of Majoranas.

bonacci anyons a braiding procedure is known that yields a universal quantum computer [16].

Here we will leave the discussion concerning quantum computing, as this thesis focusses on the theoretical discussion of the low energy behaviour (close to T = 0 K) of Majorana and parafermion systems. A detailed mathematical discussion of the parafermions is given in the relevant chapters.

Experimental proposals for parafermions are based on fractional quantum Hall (FQH) systems [16, 56, 64]. The edge currents of FQH experience fractional statistics. These currents can be captured as parafermions by decorating the edge with heterostructures (usually ferromagnets and superconductors). For a detailed discussion, see Section 5.3. First steps toward realizing parafermion excitations experimentally have been shown in Refs. [65–67].

Theoretically, parafermions pose new challenges compared to Majoranas. The unusual statistics limit the analytical tools at our disposal. Even the simplest (hermitian) parafermion chain cannot be solved exactly by means applicable to bilinear boson or fermion systems [61]. In other words, there are no free parafermions, any system behaves as an interacting one.[h] There are, however, still some analytical approaches for understanding parafermion systems.

First of all, there exists a mapping from a parafermion chain to the 2D Potts model, by virtue of the Fradkin–Kadanoff transformation [60] and transfer matrix formalism [71]. This model was studied extensively, with the help of statistical mechanics [72–75] and conformal field theory [76–79]. Valuable results can be translated back to parafermion language, offering a starting point for further research.

Moreover, in some particular cases there are some more analytical arms that can be twisted. While the whole spectrum might remain elusive, in the ground state(s) can be obtained exactly. Which is valuable, since we are interested in the T $\approx$ 0 K behaviour. These so-called frustration free lines help paint a bright partial picture. Also, in some limiting cases perturbative expansions shed light on the physical background of the systems in question. Finally, conformal field theory (CFT) and bosonization allowed for a better understanding of certain transitions and critical phases.

When all analytical options are depleted, we still have a very powerful numerical tool at our disposal. In obtaining the results in this thesis we have leaned heavily on Density Matrix Renormalization Group (DMRG) calcula-

[h] There are non-hermitian parafermion systems that is "free", since they can be written in a bilinear form [68–70].

tions [80, 81]. This 1D algorithm approximates the many body Hilbert space based on entanglement arguments and is widely used in the study of fermion- and spin(-like) strongly correlated systems. For an overview, see Ref. [81]

With these tools at our disposal, we have attacked several problems concerning parafermions. We have studied the topological phases in multiple models, adding potential heterogeneity and interactions to the Kitaev chain, considering four site interactions for the $\mathbb{Z}_3$ parafermion chain and describing classes of $\mathbb{Z}_m$ models with topological nature. In this quest, we have encountered several other interesting phases the parafermions can form, leading to many new open questions.

1.1 Outline

This thesis can be roughly separated into two parts. Chapters 2 and 3 discuss examples of frustration free systems. In Chapter 2 we observe that the zero modes and degeneracy in the Kitaev chain survive in the presence of an alternating chemical potential and interactions. Chapter 3 discusses an overarching approach for finding frustration free models, by a applying a conjugation method proposed by Witten [82]. Besides the interacting Kitaev chain and several $\mathbb{Z}_m$ parafermion models, also the q-deformed XXZ and AKLT model are revisited using this method.

In Chapters 4, 5, 6 we discuss several phase diagrams of parafermion systems. Chapter 4 is dedicated to $\mathbb{Z}_3$ Fock parafermions, showing the different critical phases that appear for this exotic system. Fock parafermions are to parafermions what fermions are to Majoranas, adding a notion of particle filling. In Chapter 5 an extension of the $\mathbb{Z}_3$-parafermion chain is discussed, including four-parafermion interactions. This is inspired by both an experimental proposal and a generalization of Coulomb interactions. We encounter several XXZ like phases, two gapped ferro- and anti-ferromagnetic phases and a Luttinger liquid phase. Finally, this discussion is continued in Chapter 6 for large interactions. This regime is not fully understood, yet show some novel interesting phases.

2 Exact ground states for interacting Kitaev chains

This chapter is based on: J. Wouters, H. Katsura and D. Schuricht, *Exact ground states for interacting Kitaev chains*, Physical Review B 98(11), 155119 (2018). J.W. performed most of the calculations and all numerical simulations, discussed the results and contributed to the final version of the manuscript.

We introduce a frustration-free, one-dimensional model of spinless fermions with hopping, p-wave superconducting pairing and alternating chemical potentials. The model possesses two exactly degenerate ground states even for finite system sizes. We present analytical results for the strong Majorana zero modes, the phase diagram and the topological order. Furthermore, we generalise our results to include interactions.

2.1 Introduction

Majorana fermions have attracted a lot of attention over the last two decades. Motivated by their anticipated future role [83, 84] in quantum computing applications, systems supporting Majorana zero modes have been widely studied in condensed-matter physics, culminating in recent experiments [20, 85–90] on superconductor-semiconductor nanowire systems.

The prime example of a model possessing Majorana zero modes is the Kitaev chain [11]. It describes spinless fermions on a tight-binding chain with open boundary conditions, which are subject to p-wave superconducting pairing with fermionic parity as symmetry operator. Depending on the parameters, the system will be either in its trivial or its topological phase. The latter is marked by a two-fold degenerate ground state, with corresponding zero-energy modes in the insulating gap. The zero modes are hermitian and normalisable, localised at the boundaries of the chain, commute with the Hamiltonian and anti-commute with fermion parity operator, making them Majorana edge zero modes [61].

Furthermore, because the two ground states live in the two different symmetry sectors, hybridisation is exponentially suppressed, hence the fermionic parity is protected by topology. Theoretical works on disorder [34–41], dimerization [52, 53, 91, 92] and interactions [38, 39, 41–54] have shown that the topological phase is very robust against various perturbations. Furthermore, via the non-local Jordan–Wigner transformation, the Kitaev chain can be mapped to a transverse-field Ising/XY chain, with the mentioned perturbations leading to more general spin-1/2 spin chains.

In this chapter we propose an inhomogeneous modification to the Kitaev chain, for which the zero modes and ground state obtain special properties. It turns out that the Majorana mode energy in this model becomes exactly zero, even for finite lattice sizes. This is in contrast with the generic Kitaev chain in its topological phase, where the energy decays exponentially with the length of the system. Moreover, we can obtain the ground states in a simple product form. The latter is equivalent to the model being frustration-free, meaning all local Hamiltonians are simultaneously minimised when projected onto the ground-state subspace. We will elaborate more on this notion later in this chapter. Well known frustration-free models are the AKLT chain [93, 94] and the Kitaev toric code [12]. There has also been progress concerning spin chains/Majorana models [49, 95]. An overview of homogeneous frustration-free XYZ/interacting-Majorana chains was given in Ref. [96].

Furthermore, we also introduce an interacting frustration-free model. This is an extension of the non-interacting inhomogeneous Kitaev chain, obtained by exploiting the local fermion-parity invariance. For this interacting model, we derive the ground-state energy analytically and give an estimate on the spectral gap. The exact ground states are inherited from the non-interacting model, which gives the opportunity to analytically compute zero-temperature correlation functions.

This chapter is organised as follows: In Section 2.2 we introduce the non-interacting model with alternating chemical potentials. We discuss in detail its properties, including the construction of the exact ground states, strong zero modes, phase diagram and topological order. In Section 2.3 we briefly discuss the construction of exact strong zero modes in the system with completely inhomogeneous chemical potentials. Finally, in Section 2.4 we return to the alternating setup but include interactions. The exact, two-fold degenerate ground state of the resulting model is calculated and the phase diagram is obtained, before we end with a conclusion. Technical details of our derivations are deferred to several appendices.

2.2 Non-interacting model

We begin by introducing the non-interacting model and discussing its properties in detail. Interactions will be added in Section 2.4.

2.2.1 Hamiltonian

We consider an open chain of length L supporting spinless fermions. The creation and annihilation operators on site j are given by $c_j^\dagger$ and c_j respectively, satisfying canonical anti-commutation relations $\{c_i, c_j\} = \{c_i^\dagger, c_j^\dagger\} = 0$ and $\{c_i, c_j^\dagger\} = \delta_{ij}$. The number operator on site j is defined as $n_j = c_j^\dagger c_j$. The Hamiltonian of the non-interacting model is given by

$$\begin{aligned} H &= -\sum_{j=1}^{L-1} \left[t(c_j^\dagger c_{j+1} + c_{j+1}^\dagger c_j) + \Delta(c_j^\dagger c_{j+1}^\dagger + c_{j+1} c_j) \right] \\ &\quad - \sum_{j=1}^{L} q_j(2n_j - 1) + S, \end{aligned} \tag{2.1}$$

$$S = \frac{1}{2}\left[q_1(2n_1 - 1) + q_L(2n_L - 1) \right], \tag{2.2}$$

where t and Δ are the hopping and pairing energies respectively. For later use we introduce the parametrisation

$$t = \frac{\eta + \eta^{-1}}{2}, \quad \Delta = \frac{\eta - \eta^{-1}}{2}, \tag{2.3}$$

which effectively removes the overall energy scale and thus reduces the number of parameters by one. An overall scale can be reintroduced, not changing anything qualitatively in the rest of the chapter. Furthermore, q_j denotes a chemical potential at lattice site j. Except for Section 2.3 we will consider the alternating setup

$$q_j = \begin{cases} q, & \text{if } j \text{ odd}, \\ q^{-1}, & \text{if } j \text{ even}. \end{cases} \tag{2.4}$$

Finally we note that the surface term S alters the chemical potential on the edges. This allows us to rewrite Equation (2.1) as sum of local Hamiltonians

$$H = \sum_{j=1}^{L-1} h_j, \tag{2.5}$$

$$h_j = -t(c_j^\dagger c_{j+1} + c_{j+1}^\dagger c_j) - \Delta(c_j^\dagger c_{j+1}^\dagger + c_{j+1} c_j) - \frac{q_j}{2}(2n_j - 1) - \frac{q_{j+1}}{2}(2n_{j+1} - 1). \tag{2.6}$$

The homogeneous system (i.e., q_j constant) is equivalent to the non-interacting point of the model studied in Ref. [49].

For simplicity, we will only consider even system lengths. Furthermore, we can assume $q > 0$ and $\eta > 0$, since charge conjugation [$c_j \to (-1)^j c_j^\dagger$] is equivalent to $q \to -q$ while $\eta \to -\eta$ can be achieved by $c_j \to (-1)^j c_j$. Moreover, we can restrict q and η to be larger than 1, because inversion ($c_j \to i c_{L-j+1}$) induces $q \to q^{-1}$ and $c_j \to i c_j$ induces $\eta \to \eta^{-1}$.

The total fermion number $F = \sum_j n_j = \sum_j c_j^\dagger c_j$ is not conserved by the Hamiltonian. However, the fermionic parity, i.e., the fermion number modulo two is a symmetry of the model,

$$[H, (-1)^F] = 0, \tag{2.7}$$

where $(-1)^F$ is the fermionic parity operator.

2.2.2 Exact ground states

In general the h_j's cannot be diagonalised simultaneously, because $[h_j, h_{j+1}] \neq 0$. However, progress can be made in the frustration-free case. This occurs if there exists a subspace, the ground-state space, with projector G_0, such that every h_j is minimised when projected onto this space, i.e., $h_j G_0 = \epsilon_0 G_0$ with ϵ_0 being the smallest eigenvalue of h_j. The ground states of the full Hamiltonian H minimise each h_j independently and the Hamiltonian H is said to be frustration-free. There are many examples of frustration-free models, possibly the most well known are the AKLT chain [93, 94] and the Kitaev toric code [12]. An extensive discussion on frustration-free systems was recently given by Jevtic and Barnett [96]. They give a systematic derivation of spin chain models with a factorised ground state, which support Majorana zero modes.

In this section we will show that the model (2.1) is frustration-free. The

determination of the ground-state subspace requires to minimise every local Hamiltonian, so we start by considering the two-site problem. The four states for this subsystem are $|\circ\circ\rangle = |\text{vac}\rangle$, $|\bullet\circ\rangle = c_j^\dagger |\text{vac}\rangle$, $|\circ\bullet\rangle = c_{j+1}^\dagger |\text{vac}\rangle$ and $|\bullet\bullet\rangle = c_j^\dagger c_{j+1}^\dagger |\text{vac}\rangle$, where $|\text{vac}\rangle$ denotes the vacuum state on the lattice sites j and $j+1$. The local Hamiltonians also preserve fermionic parity, so we can split system in an even and an odd sector,

$$h_j^e = -\frac{1}{2}\begin{pmatrix} q_j + q_j^{-1} & \eta - \eta^{-1} \\ \eta - \eta^{-1} & -q_j - q_j^{-1} \end{pmatrix}, \tag{2.8}$$

$$h_j^o = -\frac{1}{2}\begin{pmatrix} q_j - q_j^{-1} & \eta + \eta^{-1} \\ \eta + \eta^{-1} & -q_j + q_j^{-1} \end{pmatrix}, \tag{2.9}$$

which act on the basis $\{|\bullet\bullet\rangle, |\circ\circ\rangle\}$ and $\{|\bullet\circ\rangle, |\circ\bullet\rangle\}$ respectively. For both sectors the eigenvalues are given by $\epsilon_\pm = \pm\frac{1}{2}\mathcal{N}$, with $\mathcal{N} = \sqrt{q^2 + q^{-2} + \eta^2 + \eta^{-2}}$. The corresponding eigenstates with energy ϵ_- are

$$|\psi_j^e\rangle = \left(\frac{\mathcal{N} + q_j + q_j^{-1}}{\eta - \eta^{-1}}\right)|\bullet\bullet\rangle + |\circ\circ\rangle, \tag{2.10}$$

$$|\psi_j^o\rangle = \left(\frac{\mathcal{N} + q_j - q_j^{-1}}{\eta + \eta^{-1}}\right)|\bullet\circ\rangle + |\circ\bullet\rangle. \tag{2.11}$$

We note that any linear combination of these eigenstates minimises the local Hamiltonian h_j.

In order to find the ground state of the full system we first look for linear combinations of the eigenstates $|\psi_j^{e,o}\rangle$ that can be written as a product of single-site states. Making the ansatz

$$|\psi_{2k-1}^e\rangle \pm x_1 |\psi_{2k-1}^o\rangle = (x_0 c_{2k-1}^\dagger \pm 1)(x_1 c_{2k}^\dagger \pm 1)|\text{vac}\rangle, \tag{2.12}$$

$$|\psi_{2k}^e\rangle \pm x_0 |\psi_{2k}^o\rangle = (x_1 c_{2k}^\dagger \pm 1)(x_0 c_{2k+1}^\dagger \pm 1)|\text{vac}\rangle, \tag{2.13}$$

where we distinguish between even and odd sites because of the alternating

nature of the model, the coefficients are found to be

$$(x_0)^2 = \frac{\mathcal{N} + q + q^{-1}}{\eta + \eta^{-1}} \frac{\mathcal{N} + q - q^{-1}}{\eta - \eta^{-1}}, \tag{2.14}$$

$$(x_1)^2 = \frac{\eta + \eta^{-1}}{\eta - \eta^{-1}} \frac{\mathcal{N} + q + q^{-1}}{\mathcal{N} + q - q^{-1}}. \tag{2.15}$$

Now, since h_j commutes with $x_{0,1}c_k^\dagger \pm 1$ for $k \neq j, j+1$, the ground states minimising all local Hamiltonians and consequently the full system are

$$|\Psi^\pm\rangle = \prod_{k=1}^{L/2} (x_0 c_{2k-1}^\dagger \pm 1)(x_1 c_{2k}^\dagger \pm 1) \, |\mathrm{vac}\rangle \tag{2.16}$$

with ground-state energy

$$E_0 = -\frac{L-1}{2}\mathcal{N}. \tag{2.17}$$

Note that for $\eta = 1$ the ground state becomes non-degenerate, as both x_0 and x_1 diverge and the ground state is a fully filled state. In Section 2.2.3 we will see that the system possesses strong zero modes supporting the two-fold degeneracy in the ground state. Moreover, the zero modes indicate that there are no more linearly independent ground states, i.e., the ground-state subspace is two-dimensional.

At this point we have to note that the model in question is non-interacting, hence finding the ground state is always possible. However, this specific factorised form is reserved for only a small class of models. An alternative, more direct approach for finding the ground states is discussed in Appendix 2.A. There the notion of Lindblad operators is employed to verify the states in Equation (2.16) span the full ground-state subspace, further explored in Chapter 3 as well.

As noted above, the Hamiltonian (2.1) preserves fermionic parity. However, $|\Psi^\pm\rangle$ belong neither to the even nor the odd parity sector. More explicitly, because $(-1)^F(x_{0,1}c_k^\dagger \pm 1) = -(x_{0,1}c_k^\dagger \mp 1)(-1)^F$, the action of the fermionic parity on the ground states is $(-1)^F |\Psi^\pm\rangle = |\Psi^\mp\rangle$. Also, the states are not orthogonal.

However, the linear combinations

$$|\Psi^e\rangle = \frac{1}{\sqrt{2(N+M)}}\left(|\Psi^+\rangle + |\Psi^-\rangle\right), \tag{2.18}$$

$$|\Psi^o\rangle = \frac{1}{\sqrt{2(N-M)}}\left(|\Psi^+\rangle - |\Psi^-\rangle\right), \tag{2.19}$$

belong to the even and odd sector, respectively, and thus are orthogonal to each other. The coefficients that normalise the states are

$$N := \langle\Psi^\pm|\Psi^\pm\rangle = \left[(x_0^2+1)(x_1^2+1)\right]^{L/2}, \tag{2.20}$$

$$M := \langle\Psi^\mp|\Psi^\pm\rangle = \left[(x_0^2-1)(x_1^2-1)\right]^{L/2}, \tag{2.21}$$

which satisfy $N/M = \eta^L$.

The ground states (2.18) and (2.19) are locally indistinguishable, as can be seen as follows: [49] Consider any local operators with an even (O_e) and odd (O_o) number of fermion creation an annihilation operators, supported on a sublattice $1 < j_1 < \ldots < j_k < L$, such that $j_k - j_1 = \ell - 1$. Immediately, we note that $\langle\Psi^e|O_o|\Psi^e\rangle = \langle\Psi^o|O_o|\Psi^o\rangle = 0$, since O_o changes the fermionic parity of the states, while $|\Psi^{e,o}\rangle$ belong respectively to the even or odd sector. Furthermore, the even local operators we can bound as (see Appendix 2.B)

$$|\,\langle\Psi^e|O_e|\Psi^e\rangle - \langle\Psi^o|O_e|\Psi^o\rangle\,| \leq K\|O_e\|\,e^{-L/\xi}, \tag{2.22}$$

where$\|O_e\|$ is the operator norm [as defined in Equation (2.92)], K is a constant, small compared to $e^{L/\xi}$, and

$$\xi = \frac{1}{\ln[\max(\eta,\eta^{-1})]} > 0 \tag{2.23}$$

is the correlation length. Hence it is not possible to distinguish the two ground states (2.18) and (2.19) by measuring local expectation values in a thermodynamically large system.

Finally let us rewrite the system (2.1) in the form of a spin chain using the Jordan–Wigner transformation

$$\begin{aligned} c_j &= \prod_{k=1}^{j-1} \left(-\sigma_k^z\right) \frac{\sigma_j^x - i\sigma_j^y}{2}, \\ c_j^\dagger &= \prod_{k=1}^{j-1} \left(-\sigma_k^z\right) \frac{\sigma_j^x + i\sigma_j^y}{2}, \end{aligned} \tag{2.24}$$

with σ^i for $i = x, y, z$ denoting the Pauli matrices. Plugging this in into Equation (2.6) results in a XY chain in a transverse field,

$$h_j = -\frac{1}{2}(\eta\sigma_j^x\sigma_{j+1}^x + \eta^{-1}\sigma_j^y\sigma_{j+1}^y + q_j\sigma_j^z + q_j^{-1}\sigma_{j+1}^z). \tag{2.25}$$

Now it can be confirmed along the lines of Refs. [97] and [98] that the system is frustration-free for all values of η and q.

2.2.3 Strong zero modes

As we saw in the previous section, the model has a two-fold degenerate ground state. This is reminiscent of the two ground states of the Kitaev chain in its topological phase. The major difference is that due to the specific tuning of the edge chemical potential the ground states of the model (2.1) are perfectly degenerate and uncoupled for all system sizes. On the other hand, in a generic non-interacting Kitaev model, the coupling between the ground states decays exponentially with the length of the system [11].

The perfect degeneracy of the ground states in the system (2.1) suggests that there exists a single-particle mode T_0 with zero energy, mapping one ground state to the other, i.e., $|\Psi^o\rangle \propto T_0 |\Psi^e\rangle$. This mode must anti-commute with the fermionic parity operator, ($\{(-1)^F, T_0\} = 0$), mapping one parity sector to the other. Also it has to commute at least with the ground-state part of the Hamiltonian. This is what is sometimes called a "weak" zero mode [99].

In fact, since we are dealing with a non-interacting problem, the last property can be extended to the full Hilbert space, i.e., the zero mode commutes with the full Hamiltonian, $[H, T_0] = 0$. Furthermore, due to particle-hole symmetry these zero modes are necessarily Majorana modes ($T_0^\dagger = T_0$). In this section we will derive explicit expressions for these modes, called *strong Majorana zero*

modes, satisfying the following properties [61]:

1. $T_0^\dagger = T_0$,
2. $\{(-1)^F, T_0\} = 0$,
3. $[H, T_0] = 0$,
4. $T_0^\dagger T_0 = T_0^2 = 1$.

To do so, we first split the spinless complex fermions into two Majorana fermions $a_j = a_j^\dagger$ and $b_j = b_j^\dagger$ per lattice site in the usual fashion,

$$c_j = \frac{a_j - ib_j}{2}, \quad c_j^\dagger = \frac{a_j + ib_j}{2}. \tag{2.26}$$

The particular choice of the hopping and superconducting parameters becomes clear in the Majorana representation, in which the local Hamiltonian becomes

$$h_j = -\frac{i}{2}(\eta b_j a_{j+1} - \eta^{-1} a_j b_{j+1} - q_j a_j b_j - q_j^{-1} a_{j+1} b_{j+1}). \tag{2.27}$$

Requiring condition 3, or equivalently $[h_j, T_0] = 0$ for all j, we find two zero modes of the form

$$T_0^a = \alpha \sum_{j=1}^{L/2} \frac{1}{\eta^{2(j-1)}} \left(a_{2j-1} - \frac{q}{\eta} a_{2j} \right), \tag{2.28}$$

$$T_0^b = \beta \sum_{j=1}^{L/2} \eta^{2(j-1)} \left(b_{2j-1} - q\eta b_{2j} \right), \tag{2.29}$$

where α and β are normalisation factors fixed by condition 4. Note that by construction they also satisfy the first two requirements above. Thus T_0^a and T_0^b are indeed strong zero modes. We stress that these zero modes are exact even for finite system sizes, in contrast to the modes in a generic non-interacting Kitaev chain.

Let us also comment on the localisation of the zero modes T_0^a and T_0^b. Obviously they decay with η and η^{-1} respectively, localising them at one of the edges. For $\eta > 1$, T_0^a is localised at the left ($j = 1$) boundary, while T_0^b lives at the right edge ($j = L$). For $\eta < 1$ the situation is reversed. Thus for all $\eta \neq 1$

we have two strong zero modes localised at the opposite boundaries. At $\eta = 1$ both modes are delocalised and the ground state becomes singly degenerate.

Finally, in Appendix 2.C we discuss the action of the zero modes on the ground states. As one would expect the zero modes map one ground state to the other, i.e., $T_0^{a,b} |\Psi^e\rangle = |\Psi^o\rangle$. This confirms that the ground states are in a different fermion parity sector, since the Majorana zero modes change the parity by 1.

2.2.4 Phase Diagram

In the previous section we derived the existence of exact strong zero modes, supported by the two-fold degeneracy of the ground state. This hints towards a topological superconductor region in the phase diagram. Also there appears to be a phase transition at $\eta = 1$. In this section we will derive the spectrum to confirm this picture by examining the gap throughout the phase diagram. We have to note that, even though we are interested in finite-size systems allowing for the presence of edge effects, here we will be considering the gap in the thermodynamic limit, as only in this limit the system can become truly gapless. In this section we are interested in the bulk gap and bulk phase transition.

With the local Hamiltonian in the Majorana language (2.27) and recalling the alternating chemical potential (2.4), the Hamiltonian can be brought into matrix form

$$H = \frac{i}{2} \sum_{j,k=1}^{L} a_j B_{jk} b_k, \tag{2.30}$$

$$B = \begin{pmatrix} q & \eta^{-1} & & & & \\ \eta & 2q^{-1} & \eta^{-1} & & & \\ & \ddots & \ddots & \ddots & & \\ & & \eta & 2q & \eta^{-1} \\ & & & \eta & q^{-1} \end{pmatrix}. \tag{2.31}$$

The $L \times L$ matrix B is non-hermitian, and is not necessarily diagonalisable. However, $BB^\top$ is hermitian and the eigenvalues are $(2\epsilon_k)^2$, with ϵ_k the single-particle energies of the model. Diagonalising the pentadiagonal $BB^\top$ is quite troublesome. Fortunately, we can construct a symmetric tridiagonal matrix C,

such that $BB^\top = C^2$, with

$$C = \frac{1}{\mathcal{N}} \begin{pmatrix} \gamma_1 & \delta^{-1} & & & & & \\ \delta^{-1} & \gamma_- & \delta & & & & \\ & \delta & \gamma_+ & \delta^{-1} & & & \\ & & \ddots & \ddots & \ddots & & \\ & & & \delta & \gamma_+ & \delta^{-1} & \\ & & & & \delta^{-1} & \gamma_L \end{pmatrix}, \tag{2.32}$$

where

$$\begin{aligned} \gamma_\pm &= \eta^2 + \eta^{-2} + 2q^{\pm 2}, & \gamma_1 &= q^{-2} + \eta^2, \\ \delta &= q\eta^{-1} + q^{-1}\eta, & \gamma_L &= q^2 + \eta^{-2}. \end{aligned} \tag{2.33}$$

The matrix C can be diagonalised analytically, see Appendix 2.D. For $k = \frac{2\pi n}{L}$ with $n = 1, 2, \ldots, \frac{L}{2} - 1$ we find the eigenvalues

$$\epsilon_k^\pm = \frac{1}{2}\left(\mathcal{N} \pm \sqrt{q^2 + q^{-2} + 2\cos k}\right). \tag{2.34}$$

Furthermore, there are two additional modes with energies

$$\epsilon_0^- = 0, \quad \epsilon_0^+ = \frac{1}{2}\mathcal{N}. \tag{2.35}$$

Note that all eigenvalues are non-negative, because $BB^\top$ is positive semidefinite. The smallest non-zero eigenvalue is

$$\epsilon_{k=2\pi/L}^- = \frac{1}{2}\left(\mathcal{N} - (q + q^{-1}) + \frac{k^2}{2(q + q^{-1})}\right) + O(k^4), \tag{2.36}$$

which gives a spectral gap in the thermodynamic limit ($L \to \infty$) of

$$\Delta E = \frac{1}{2}\left[\mathcal{N} - (q + q^{-1})\right]. \tag{2.37}$$

From Equation (2.37) we see that the gap only vanishes at $\eta = 1$ indicating the phase transition. This is depicted in the q-η phase diagram in Figure 2.1. At the phase transition the low-energy spectrum is quadratic in k, putting the

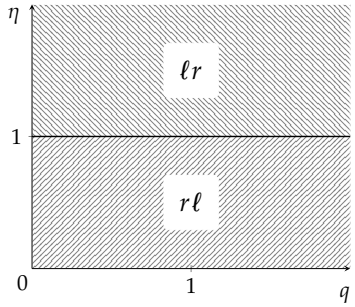

Figure 2.1: Phase diagram for the non-interacting model in $q-\eta$ plane. The localisation of the zero modes is indicated in the white squares, where ℓ and r refer to the left (near site 1) and right (near site L) edges. The first letter denotes the location of T_0^a, the second of T_0^b. In Figure 2.2 a cut along $q = 1$ (the homogeneous system) is shown in the phase space of the Kitaev parameters (μ, Δ).

critical model out of reach for conformal field theories. To clarify the nature of the phase transition, we consider Figure 2.2. In this figure we show a cut of Figure 2.1 along $q = 1$ (the homogeneous point) projected onto the μ-Δ space, i.e., using the conventional Kitaev parameters [100]. The dashed lines represent the Ising and XX transitions. The solid line depicts the cut along $q = 1$. Clearly, the phase transition at $\eta = 1$ occurs at the crossing of the Ising and XX line. As we discuss in Appendix 2.E, for general q this crossing can be identified as a transition in the Dzhaparidze-Nersesyan-Pokrovsky-Talapov (DN-PT) universality class [101–103]. Figure 2.1 also shows the localisation of the zero modes given by ℓ and r in each region, where the first letter corresponds to T_0^a and the second to T_0^b.

2.2.5 Topological order

We have discussed the presence of zero modes, the double degeneracy of the ground state, and the spectral gap. We also concluded that the ground states cannot be distinguished by local measurements. These properties do not come by surprise, because of the tight connection to the Kitaev chain. Specifically, at $q = 1$ the bulk model (2.1) reduces to the Kitaev chain, which will be in its topological phase for all $\eta \neq 1$. It is then easy to see that we can adiabatically change the system away from $q = 1$. Starting at $q = 1$ for $\eta > 1$, we can

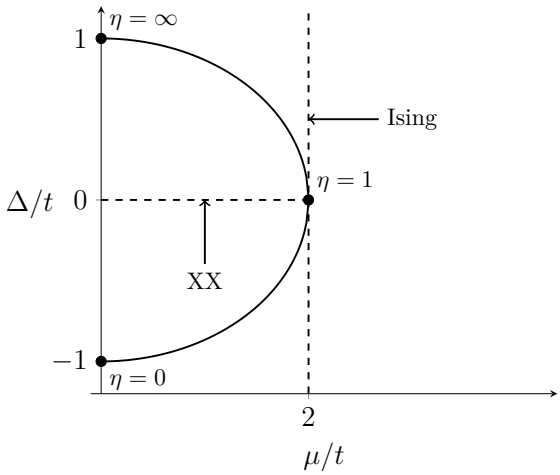

Figure 2.2: Cut along $q = 1$ in Figure 2.1 embedded in the Δ/t-μ/t phase space for the conventional Kitaev chain. The dashed lines represent the Ising and XX phase transitions. The solid line is the cut along $q = 1$. At the phase transition ($\eta = 1$) the cut passes through the intersection of the Ising and XX transition lines, where the spectrum becomes quadratic at small momenta. Adapted from Ref. [100].

make a smooth path to any other $\eta' > 1$ and $q > 0$ without closing the gap (see Figure 2.1), thus remaining in the topological phase. The same argument applies to all $\eta < 1$.

To support this statement, we consider two topological invariants: the $\mathbb{Z}_2$ invariant[104–106] for class D topological superconductors, and, since we do not explicitly break time reversal symmetry, the $\mathbb{Z}$ invariant[51, 107] for class BDI.

$\mathbb{Z}_2$ invariant: The fermionic parity of the closed system with twisted boundary conditions (TBC) is related to the topological properties of the open system. In general twisted boundary conditions are implemented by adding the boundary Hamiltonian

$$\begin{aligned} h_{\text{bound}} = &- \Phi\left[t\left(e^{i\varphi_1}c_L^\dagger c_1 + \text{h.c.}\right) - \Delta\left(e^{i\varphi_2}c_L^\dagger c_1^\dagger + \text{h.c.}\right)\right] \\ &- \frac{q_1}{2}(2n_1 - 1) - \frac{q_L}{2}(2n_L - 1). \end{aligned} \tag{2.38}$$

Recall that t and Δ are given by Equation (2.3). The open system corresponds

to $\Phi = 0$. For $\Phi = 1$ we find periodic boundary conditions (PBCs) for $(\varphi_1, \varphi_2) = (0, 0)$, and anti-periodic boundary conditions (APBCs) for $(\varphi_1, \varphi_2) = (\pi, \pi)$. In Ref. [106] it was shown that a different fermionic parity for the ground states for PBCs and APBCs corresponds to the topological phase, while equal fermionic parity corresponds to the trivial phase. In Appendix 2.F we show that the ground states for PBCs and APBCs are

$$|\Psi^{\mathrm{PBC}}\rangle = |\Psi^o\rangle\,, \qquad |\Psi^{\mathrm{APBC}}\rangle = |\Psi^e\rangle\,. \tag{2.39}$$

The parity of $|\Psi^e\rangle$ is $+1$ and the parity of $|\Psi^o\rangle$ is -1, which confirms the existence of the topological phase for all $\eta \neq 1$.

$\mathbb{Z}$ *invariant:* Using the second invariant we will be able to directly link the topological phase in Figure 2.1 to the topological phase in the conventional Kitaev chain [11].

In Ref. [107] it was shown that for a model in class BDI there exists a $\mathbb{Z}$ invariant in the form of a winding number

$$W = -\frac{i}{\pi}\int_{k=0}^{k=\pi} \frac{\mathrm{d}z(k)}{z(k)}, \tag{2.40}$$

where $z = \det(A(k))/|\det(A(k))|$. The matrix $A(k)$ is related to the rotated BdG Hamiltonian in k-space

$$U\mathcal{H}(k)U^\dagger = \begin{pmatrix} 0 & A(k) \\ A^\top(-k) & 0 \end{pmatrix}. \tag{2.41}$$

From the periodic alternating model [i.e. $(\varphi_1, \varphi_2) = (0, 0)$ and $\Phi = 1$ in Equation (2.38)] we obtain

$$A_q(k) = -\begin{pmatrix} q & t\cos(k) + i\Delta\sin(k) \\ t\cos(k) + i\Delta\sin(k) & q^{-1} \end{pmatrix}, \tag{2.42}$$

where the q-subscript refers to the alternating model. Direct evaluation now yields

$$W_q = \begin{cases} 1, & t > 1, \\ 0, & t < 1. \end{cases} \tag{2.43}$$

For the gapped regions ($\eta \neq 1$) the system is in the upper case, hence topological. The phase transition $\eta = 1$ corresponds to $t = 1$, where W is not well defined.

We can also reach this conclusion indirectly, by realising that $\det[A_q(k)]$ does not dependent on q. In fact, if one would calculate $A_{\mathrm{Kit}}(k)$ for the conventional homogeneous Kitaev chain, but viewed with a two site unit cell, one would find

$$\det[A_q(k)] = \det[A_{\mathrm{Kit}}(k)]. \tag{2.44}$$

Consequently, also $W_q = W_{\mathrm{kit}}$. This relates the topological phase for general q to the topological phase for the conventional Kitaev chain. Finally we note that the two invariants are related by the fact that the $\mathbb{Z}_2$ invariant is just the parity of the $\mathbb{Z}$ invariant [107].

2.3 Fully inhomogeneous model

In this section we briefly discuss a model with more general couplings than the alternating setup (2.4). Specifically, we consider completely inhomogeneous couplings η_j and q_j, i.e., the local Hamiltonian takes the form

$$h_j = -\frac{i}{2}(\eta_j b_j a_{j+1} - \eta_j^{-1} a_j b_{j+1} - q_j a_j b_j - q_j^{-1} a_{j+1} b_{j+1}). \tag{2.45}$$

From the most general ansatz for Majorana zero modes,

$$T_0^a = \sum_{j=1}^{L} \alpha_j a_j, \qquad T_0^b = \sum_{j=1}^{L} \beta_j b_j, \tag{2.46}$$

one finds by requiring $[h_j, T_0^{a,b}] = 0$ for all j that the coefficients have to satisfy the recursion relations

$$\alpha_{j+1} = -\frac{q_j}{\eta_j}\alpha_j, \qquad \beta_{j+1} = -q_j \eta_j \beta_j. \tag{2.47}$$

The constants α_1 and β_1 are fixed by the normalisation. We note that the localisation of the modes is not clear a priori.

As a trivial but instructive special case one can consider the homogeneous model with $q_j = q$ and $\eta_j = \eta$. This model was originally studied by Hinrichsen and Rittenberg [108–110] in the context of deformations of XY spin chains. In fact, they continued the work done by Saleur [111], who discussed a spin chain model corresponding to the homogeneous fermionic model introduced in Equation (2.45) with $\eta = 1$.

In the homogeneous setup Hinrichsen and Rittenberg showed that the zero modes simplify to

$$T^a = \sqrt{\frac{1-(q/\eta)^2}{1-(q/\eta)^{2L}}} \sum_{j=1}^{L} \left(-\frac{q}{\eta}\right)^{j-1} a_j, \tag{2.48}$$

$$T^b = \sqrt{\frac{1-(q\eta)^2}{1-(q\eta)^{2L}}} \sum_{j=1}^{L} \left(-q\eta\right)^{j-1} b_j. \tag{2.49}$$

Depending on the parameters the modes are localised on the same or opposite edges. The phase diagram can be deduced from the single-particle energies [110]

$$\Lambda_k = \sqrt{\frac{(q\eta^{-1}-e^{ik})(q\eta^{-1}-e^{-ik})(q\eta-e^{ik})(q\eta-e^{-ik})}{4q^2}} \tag{2.50}$$

for $k = \frac{2\pi n}{L}$ with $n = 1, \ldots, L-1$, which imply that the spectral gap closes for $\eta = q$ or $\eta = q^{-1}$. The phase diagram and the localisation of the Majorana zero modes are shown in Figure 2.3.

The gapless lines split the phase space into four regions, each with a different edge mode localisation. To understand which regions are considered topological, we look at the bulk-boundary correspondence such that we can neglect the surface terms. Without the fine tuned surface chemical potential the model reduces to the Kitaev chain, the phase transition in the Kitaev chain directly corresponds to the transitions are $\eta = q$ and $\eta = q^{-1}$. The resulting topological phases are shown as shaded regions in Figure 2.3. They are characterised by the appearance of Majorana zero modes at opposite edges. On the other hand, in the trivial phases the zero modes appear on the same edge and are thus not protected against local perturbations.

We note that the homogeneous model has a richer phase diagram than the model with alternating chemical potential we considered in Section 2.2. However, we stress that the homogeneous model is in general not frustration-free.

2.4 Interacting model

In this section we add interactions to the model from Section 2.2. By a special construction we will make the model interacting while keeping the ground

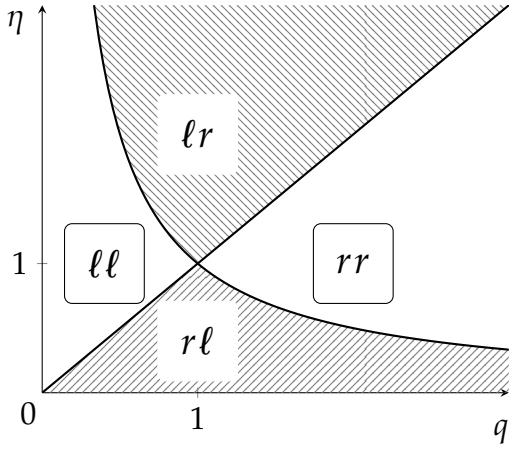

Figure 2.3: Phase diagram for the homogeneous model (2.45) with $\eta_j = \eta$ and $q_j = q$. The shaded region shows the topological phase, characterised by the existence of Majorana zero modes on opposite edges. The notation is as in Figure 2.1.

states in the disentangled form (2.16). Consequently, the interacting model will also prove to be frustration-free. There have been recent developments on frustration-free interacting spinless fermion models [49, 96]. We will show that in a specific limit we retrieve the model in Ref. [49]. Moreover, the two-fold degenerate ground state provides us with the notion of a *weak* zero modes [112]. In the last part of this section we will discuss the phase diagram of the interacting model, giving more insight in the topological order.

2.4.1 Hamiltonian

Recall that the non-interacting system left the fermionic parity invariant, allowing us to split the local Hamiltonian in even- and odd-parity parts [cf. Equations (2.8, 2.9)],

$$h_j = h_j^e P_j^e + h_j^o P_j^o, \tag{2.51}$$

where $P_j^{e,o}$ project onto the even/odd fermion parity sectors of the two-site Hilbert space at lattice sites j and $j+1$. We can define two semi-projectors

($Q^2 = c$, with c not necessarily 1), one in each sector, via

$$Q_j^{e,o} = \left(h_j^{e,o} + \frac{\mathcal{N}}{2}\right) P_j^{e,o}, \tag{2.52}$$

such that Equation (2.51) becomes

$$h_j = Q_j^e + Q_j^o - \frac{\mathcal{N}}{2}. \tag{2.53}$$

The semi-projectors (2.52) annihilate the ground states (2.16). In terms of fermionic operators they are explicitly expressed as

$$\begin{aligned} Q_j^e &= -\frac{\eta - \eta^{-1}}{2}(c_j^\dagger c_{j+1}^\dagger + c_{j+1}c_j) - \frac{q_j + q_j^{-1}}{2}(n_j + n_{j+1} - 1) \\ &\quad + \frac{\mathcal{N}}{4}\left[1 + (2n_j - 1)(2n_{j+1} - 1)\right], \end{aligned} \tag{2.54}$$

$$\begin{aligned} Q_j^o &= -\frac{\eta + \eta^{-1}}{2}(c_j^\dagger c_{j+1} + c_{j+1}^\dagger c_j) - \frac{q_j - q_j^{-1}}{2}(n_j - n_{j+1}) \\ &\quad + \frac{\mathcal{N}}{4}\left[1 - (2n_j - 1)(2n_{j+1} - 1)\right]. \end{aligned} \tag{2.55}$$

In particular, we see that the projectors (2.52) both contain a density-density interaction term, which drops out when considering the combination (2.53).

On the other hand, the existence of the density-density interaction in $Q_j^{e,o}$ points to a way to construct a frustration-free, interacting system. We set

$$\begin{aligned} H^{\text{int}} &= \sum_j h_j^{\text{int}}, \\ h_j^{\text{int}} &= \sqrt{2}\left[\cos\phi\, Q_j^e + \sin\phi\, Q_j^o\right] - \mathcal{N}\frac{\cos(\phi - \frac{\pi}{4})}{2}, \end{aligned} \tag{2.56}$$

where the parameter ϕ is restricted to $0 < \phi < \pi/2$. The non-interacting model corresponds to the choice $\phi = \pi/4$. We stress that by construction the two factorised states Equation (2.16) are the exact ground states of (2.56) with energy

$$E_0 = -\frac{(L-1)\cos(\phi - \frac{\pi}{4})}{2}\mathcal{N}. \tag{2.57}$$

Moreover, H^{int} is frustration-free, and for $q = 1$ it reduces to the model discussed in Ref. [49].

Again it is instructive to make the link to spin chains. By applying the Jordan–Wigner transformation (2.24) we obtain the XYZ chain in an alternating magnetic field

$$H^{\text{int}} = -\frac{1}{2}\sum_{j=1}^{L-1}\left(J_x\sigma_j^x\sigma_{j+1}^x + J_y\sigma_j^y\sigma_{j+1}^y + J_z\sigma_j^z\sigma_{j+1}^z\right) - \sum_{j=1}^{L} B_j\sigma_j^z, \tag{2.58}$$

where

$$J_x = \rho\eta + \varrho\eta^{-1}, \quad J_y = \rho\eta^{-1} + \varrho\eta, \quad J_z = \varrho\mathcal{N}, \tag{2.59}$$

with $\rho = \cos(\phi - \pi/4)$ and $\varrho = \sin(\phi - \pi/4)$, and

$$B_j = \begin{cases} B_0 = \rho q - \varrho q^{-1}, & \text{if } j \text{ odd}, \\ B_1 = \rho q^{-1} - \varrho q, & \text{if } j \text{ even}. \end{cases} \tag{2.60}$$

It turns out that these parameters satisfy the following condition

$$B_0 B_1 = J_z^2 + J_x J_y - J_z\sqrt{(J_x + J_y)^2 + (B_0 - B_1)^2}. \tag{2.61}$$

This shows great resemblance to the frustration-free condition for homogeneous XYZ chains provided by Refs. [97] and [98], in which case the condition becomes $B^2 = (J_x - J_z)(J_y - J_z)$. Thus it seems that the frustration-free condition in the alternating case is indeed given by Equation (2.61).

It is illustrative to return to the language of the interacting Kitaev chain

$$\begin{aligned} H = &-\sum_j \left[t(c_j^\dagger c_{j+1} + c_{j+1}^\dagger c_j) + \Delta(c_j^\dagger c_{j+1}^\dagger + c_{j+1}c_j)\right] \\ &- \frac{1}{2}\sum_j \mu_j(2n_j - 1) + U\sum_j (2n_j - 1)(2n_{j+1} - 1), \end{aligned} \tag{2.62}$$

where the parameters t, Δ, μ_j and U are non-trivial functions of q, η and ϕ. The chemical potential alternates between the values

$$\mu_j = \begin{cases} \mu_0 = \mu_0(q, \eta, \phi), & \text{if } j \text{ odd}, \\ \mu_1 = \mu_1(q, \eta, \phi), & \text{if } j \text{ even}. \end{cases} \tag{2.63}$$

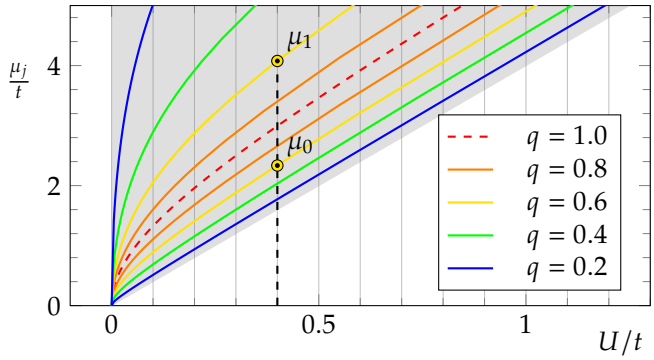

Figure 2.4: Frustration-free lines in $U - \mu$ space for $t = \Delta$. The Peschel–Emery line [49, 113] for the homogeneous case is given by the red dashed line. The other lines depict the alternating model. For every q the two chemical potentials in the system are given as a function of the interaction U. As an example $q = 0.6$ and $U = 0.4$ is explicitly shown, the two chemical potentials are indicated by the two yellow dots. The vertical lines are guides to the eye, each U relates to two μ_j's.

The condition of the model to be frustration-free results in relations between the parameters t, Δ, $\mu_{0,1}$ and U. For example, in Figure 2.4 we set $t = \Delta$ which fixes the function $\eta(\phi)$, which in turn determines the chemical potential and interaction as functions of q and ϕ, i.e., $\mu_{0,1}(q, \phi)$ and $U(q, \phi)$. Inverting the latter relation we obtain the conditions on the chemical potentials $\mu_{0,1}(q, U)$ for the model to become frustration-free, which is plotted in Figure 2.4 for different values of q. One way to view this result is that given an interaction strength U and the chemical potential μ_0 on the odd sites we can determine the inhomogeneity parameter q and thus the chemical potential μ_1 on the even sites. In the homogeneous case $q = 1$ we recover the Peschel–Emery line [49, 113]. In the limit $q \to 0$ one of the chemical potentials diverges, and the other approaches $4U$.

2.4.2 Weak zero modes

In general, if the ground state is degenerate one can always find operators mapping one ground state to the other. Some interacting systems allow for strong zero modes, commuting with the full Hamiltonian [114–116]. However, in general interactions destroy this feature and only the commutation within the low-energy sector remains. For the system (2.56) we already know the exact

form of the zero modes, because for $|\Psi^{e,o}\rangle$ we showed that $T_0^{a,b}|\Psi^e\rangle = |\Psi^o\rangle$ (see Appendix 2.C). However, in the interacting model we have $[H^{\text{int}}, T_0^{a,b}] \neq 0$, thus the modes $T_0^{a,b}$ are weak zero modes as defined in Ref. [112].

2.4.3 Phase Diagram

In this section we discuss the phase diagram of the interacting model (2.56). Without interactions it was possible to obtain exact results for the ground-state energy density and the spectral gap. When adding interactions generically one loses the analytical expressions for the observables and the only rescue lies in numerical tools. However, due to the specific construction for the interacting model, the ground-state energy can still be found analytically as we saw in Equation (2.57). For the spectral gap there is no analytic solution. Nevertheless, we can find lower and upper bounds for the gap by using the min-max principle [117]. This will give an indication for the gapped and gapless regions in phase space. To confirm these results, and fill in the remaining blanks we also perform a numerical analysis.

We start by discussing the bounds on the spectral gap. Recall that the local Hamiltonians are given by

$$h_j^{\text{int}} = \sqrt{2}\left[\cos\phi\, Q_j^e + \sin\phi\, Q_j^o\right]. \tag{2.64}$$

We are not concerned with the constant term, because we are interested in the energy gap. Since $Q^{e,o}$ are projection operators, they are positive semidefinite. We introduce the notion of operator inequality as: $A \geq B$ if $A - B$ is positive semidefinite. Two cases have to be distinguished: (i) $0 < \phi < \pi/4$ and (ii) $\pi/4 < \phi < \pi/2$. In case (i), we have

$$\sqrt{2}\sin\phi\,(Q_j^e + Q_j^o) \leq h_j^{\text{int}} \leq \sqrt{2}\cos\phi\,(Q_j^e + Q_j^o). \tag{2.65}$$

From Equation (2.51) we recognise that $Q_j^e + Q_j^o$ is nothing but a local Hamiltonian of the non-interacting model (up to a constant shift). This allows us to write

$$\sqrt{2}\sin\phi\, H \leq H^{\text{int}} \leq \sqrt{2}\cos\phi\, H, \tag{2.66}$$

where $H^{\text{int}} = \sum_{j=1}^{L-1} h_j^{\text{int}}$. Then, the min-max principle tells us that [117]

$$\sqrt{2}\sin\phi\, E_n \leq E_n^{\text{int}} \leq \sqrt{2}\cos\phi\, E_n, \tag{2.67}$$

where E_n and E_n^{int} ($n = 1, 2, 3, \ldots$) are nth eigenvalue of H and H^{int}, respectively. Since the interacting and the non-interacting Hamiltonians share the same ground states annihilated by all $Q_j^{e,o}$, we have

$$\sqrt{2}\sin\phi\,\Delta E \leq \Delta E^{\text{int}} \leq \sqrt{2}\cos\phi\,\Delta E, \tag{2.68}$$

where $\Delta E = E_3$ is the energy gap of the non-interacting system introduced in Equation (2.37), while $\Delta E^{\text{int}} = E_3^{\text{int}}$ is the one of the interacting system. Repeating the same argument, we find that the gap in case (ii) is bounded as

$$\sqrt{2}\cos\phi\,\Delta E \leq \Delta E^{\text{int}} \leq \sqrt{2}\sin\phi\,\Delta E. \tag{2.69}$$

Concluding, by using the min-max principle we have found upper and lower bounds on the gap energy for the interacting system.

From these bounds we can already draw several conclusions. First of all for $\eta \neq 1$ and $\phi \neq 0, \pi/2$ the system is gapped. The lower bound is finite, since both $\sin\phi, \cos\phi$ and ΔE are positive. Also, for $\eta = 1$ the gap has to close, independent of the interaction (governed by ϕ). Approaching this point both the upper and lower bound vanish, since both are proportional to ΔE (the non-interacting gap). In the following part we will discuss numerical results to confirm these statements. Moreover, there are two boundaries ($\phi = 0, \pi/2$), that cannot be addressed by the above reasoning. At these points the lower bound vanishes, while the upper bound is finite. We will come back to these special points below.

We use a density-matrix renormalisation group (DMRG) algorithm to explore the low-energy spectrum in parameter space [80, 81, 118]. Using finite-size scaling we obtained ground-state energy and spectral gap in the thermodynamic limit. Examples of these results (for $q = 2$) are shown in Figures 2.5 and 2.6. The top figures show that the exact and numerical findings for the ground-state energy match perfectly.

The bottom panel of Figure 2.5 shows the numerical results for the energy gap ΔE between the ground states and the first excited state. For the non-interacting case ($\phi = \pi/4$) also the analytic result is depicted by the solid blue line. For the interacting cases the dashed (dotted) line depicts the lower (upper) bound on the gap energy, confirming that the gap lies between the two bounds. As expected, for all interaction parameters ϕ the system only becomes gapless at $\eta = 1$. This we can clearly see in the inset, where the gap is depicted on

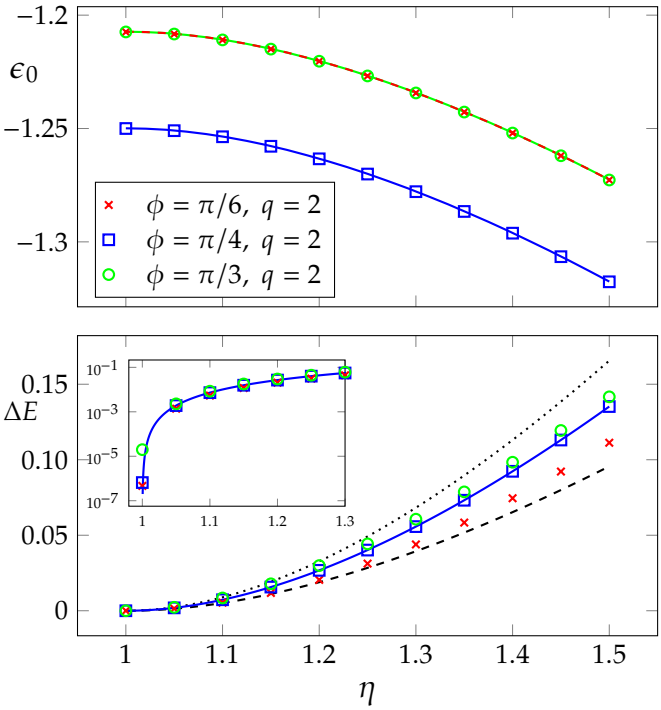

Figure 2.5: Ground-state energy per lattice site, $\epsilon_0 = E_0/L$, (top panel) and spectral gap (bottom panel) as a function of η obtained numerically (DMRG, bond dimension $D = 16$, results for system sizes $L = 40, 80, \ldots, 160$ extrapolated to the thermodynamic limit) for $q = 2$ and for three values for the interaction parameter ϕ. The non-interacting $\phi = \pi/4$ results are depicted by blue squares, the two interacting cases $\phi = \pi/6, \pi/3$ by red crosses and green circles respectively. In the top panel, the analytical results for ground-state energy are shown as solid lines [see Equation (2.57), red and green are overlapping]. In the bottom panel, the analytical spectral gap for $\phi = \pi/4$ is shown as the blue line [Equation (2.37)]. The inset shows the same results on a log scale, to emphasize the gap closing at $\eta = 1$. The lower and upper band are depicted by respectively the dashed and dotted line [Equations (2.68, 2.69)].

a logarithmic scale.[a] Also, the lower panel of Figure 2.6 confirms that, away from $\eta = 1$, the gap does not close for $0 < \phi < \pi/2$. From Figure 2.6 we can

[a] Here we have to note that the predicted gap at $\eta = 1$ vanishes, however the DMRG can never truly reach zero, due to the diverging entanglement at critical points. This is the only numerical point lying outside the bounds.

also deduce what happens when approaching the extremal cases $\phi = 0$ and $\phi = \pi/2$. The bounds do not converge (to zero), nevertheless, the gap closes when approaching either boundary.

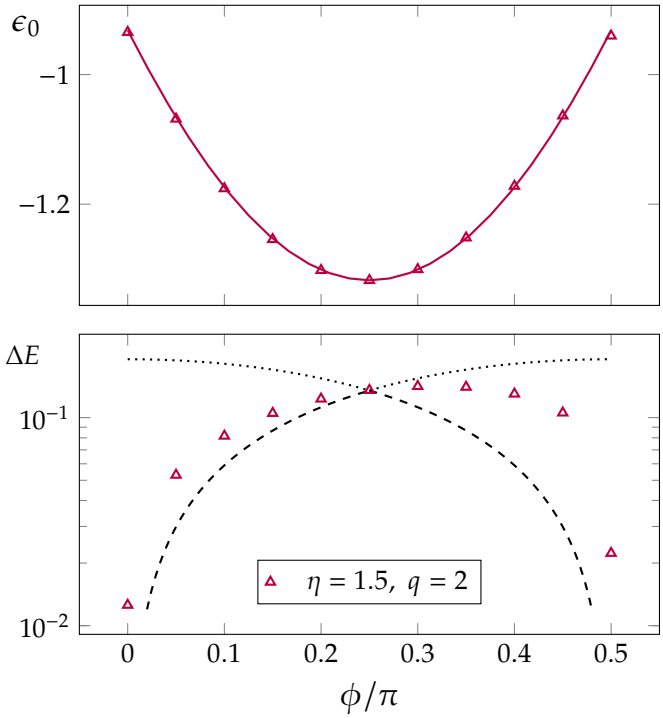

Figure 2.6: Ground-state energy per lattice site, $\epsilon_0 = E_0/L$, (top panel) and spectral gap (bottom panel) as a function of ϕ obtained numerically for $q = 2$ and $\eta = 1.5$. The purple triangles depict the DMRG results, for the ϵ_0 also the analytical results are shown by the solid line [Equation (2.57)]. The lower and upper band are depicted by respectively the dashed and dotted line [Equations (2.68, 2.69)]. The DMRG calculations were performed with the parameters of Figure 2.5.

The phase diagram of the interacting model is shown in Figure 2.7. The solid line represents the phase transition, which, as we argue in Appendix 2.E, is in the DN-PT universality class (like the non-interacting model) [103]. At the dashed lines the ground state becomes highly degenerate due to additional symmetry. We stress that the phase diagram is independent on the inhomogeneity parameter q.

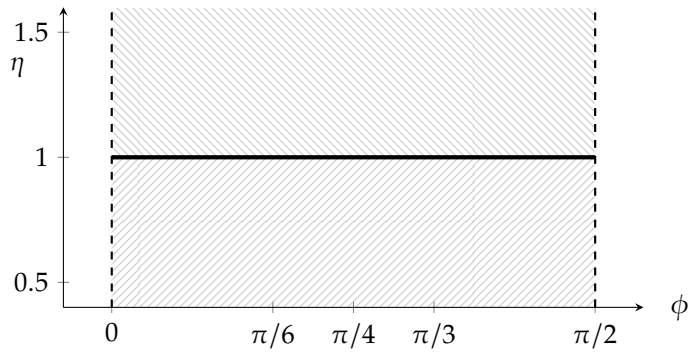

Figure 2.7: Phase diagram of the interacting model (2.56) in $\eta - \phi$ plane. The solid black line denotes a phase transition in the DN-PT universality class, while at the dashed black lines the ground state becomes highly degenerate due to additional symmetry (see main text). The phase diagram is independent of the inhomogeneity parameter q.

Finally, let us discuss what happens for $\phi = 0, \pi/2$. In the phase diagram Figure 2.7 they correspond to the dashed black lines. For these specific parameters only the even or odd two-site projector [Equation (2.52)] is present in the Hamiltonian. As we will see, this induces an additional symmetry in the low-energy sector, which in turn raises the ground-state degeneracy to $L + 1$. Here we explicitly show the construction of the ground states for $\phi = \pi/2$, the derivation for $\phi = 0$ is similar. We consider two different cases $q = 1$ and $q \neq 1$.

Case 1: $q = 1$: The local Hamiltonian reduces to the isotropic Heisenberg term if we rewrite the model in spin language using Equation (2.24),

$$h_j^{\text{int}} = -\frac{\eta + \eta^{-1}}{2\sqrt{2}} \left[\sigma_j^x \sigma_{j+1}^x + \sigma_j^y \sigma_{j+1}^y + \sigma_j^z \sigma_{j+1}^z \right]. \tag{2.70}$$

The Hamiltonian possesses an sl_2-symmetry generated by

$$\mathcal{S}^z = \sum_j \sigma_j^z, \qquad \mathcal{S}^\pm = \sum_k \sigma_j^\pm, \tag{2.71}$$

where $\sigma^\pm = \frac{\sigma^x \pm i\sigma^y}{2}$. If we define the fully polarised state $|\Uparrow\rangle = |\uparrow\uparrow \ldots \uparrow\rangle$, then the ground states are given by

$$|\Psi_p\rangle = (\mathcal{S}^-)^p \, |\Uparrow\rangle \,, \quad p = 0, 1, \ldots, L, \tag{2.72}$$

which are the $L+1$ states with $S_{\text{tot}} = L/2$.

Case 2: $q \neq 1$: The model can be represented as an XXZ chain with alternating magnetic field,

$$h_j^{\text{int}} = -\frac{\mathcal{N}}{2\sqrt{2}}\left[\frac{\eta+\eta^{-1}}{\mathcal{N}}\left(\sigma_j^x\sigma_{j+1}^x + \sigma_j^y\sigma_{j+1}^y\right) + \sigma_j^z\sigma_{j+1}^z + \frac{q_j - q_j^{-1}}{\mathcal{N}}\left(\sigma_j^z - \sigma_{j+1}^z\right) - 1\right], \tag{2.73}$$

where we have shifted the spectrum such that we have a zero-energy ground state. We note in passing that the model shows great resemblance to the XXZ model studied in Ref. [119], which supports $\mathrm{U}_q(\mathrm{sl}_2)$ symmetry. In that case the ground state is also $L+1$-fold degenerate. However, because of the quantum group symmetry, the excited states also have additional degeneracies which are not observed in the spectrum of Equation (2.73). Nevertheless, we can still construct the lowering operator analogous to $\mathcal{S}^-$ in Equation (2.71) to derive the $L+1$ ground states.

Note that the polarised state $|\Uparrow\rangle$ is still a ground state. We can define a lowering operator

$$\tilde{\mathcal{S}}^- = \sum_j g_j \sigma_j^-, \qquad g_j = \begin{cases} \sqrt{1 - \frac{q-q^{-1}}{\mathcal{N}}}, & j \text{ odd}, \\ \sqrt{1 + \frac{q-q^{-1}}{\mathcal{N}}}, & j \text{ even}. \end{cases} \tag{2.74}$$

The coefficients g_j have been obtained recursively ensuring that $h_j \tilde{\mathcal{S}}^- |\Uparrow\rangle = 0$. Since $(\sigma_j^-)^2 = 0$ we see that $(\tilde{\mathcal{S}}^-)^{L+1} = 0$. Furthermore, it turns out that

$$|\Psi_p\rangle = (\tilde{\mathcal{S}}^-)^p |\Uparrow\rangle \tag{2.75}$$

for $p = 0, 1, \ldots, L$ are ground states. The ground states $(\tilde{\mathcal{S}}^-)^p |\Uparrow\rangle$ are non-vanishing. This is because, away from the phase transition ($\eta = 1$), the coefficients g_j are strictly positive, hence there is no destructive interference for $p \leq L$, when acting on a single state ($|\Uparrow\rangle$).

We can check that the Hamiltonian still leaves

$$S^z = \mathcal{S}^z/2 \tag{2.76}$$

invariant. Since $|\Psi_p\rangle$ belongs to the $S^z = L/2 - p$ sector, the ground states are

linearly independent. Details of the construction of this operator and the proof of Equation (2.75) are given in Appendix 2.G.

2.5 Conclusion

In this chapter we have investigated frustration-free topological systems. Specifically, we studied non-interacting and interacting generalisations of the Kitaev chain, with alternating chemical potential on the lattice sites. Both introduced models possess two exactly degenerate ground states of product form. This allowed us to determine exactly the Majorana zero modes mapping the ground states onto each other. Only in the non-interacting case, these modes commute with the full Hamiltonian, making them *strong* zero modes. We stress that due to a fine-tuned boundary term all our results are exact even for finite systems, which is in contrast to the generic Kitaev chain where the Majorana edge mode energy only vanishes exponentially with the system length. For the non-interacting model we have shown that there is a finite energy gap above the ground states, except at the phase transition ($\eta = 1$) given by the zero-pairing limit. Hence there exists a smooth path connecting the inhomogeneous model to the (homogeneous) Kitaev chain, proving that both are in the same topological phase. Also, we have shown both analytically and numerically that the interacting model remains gapped in a certain region, implying that the interacting model is in the same topological phase as the corresponding non-interacting model.

In the future it would be interesting to investigate whether frustration-free models can also be constructed for genuinely interacting systems like $\mathbb{Z}_n$ clock models [120–124]. It would also be interesting to generalise our interacting model to include non-hermiticity. In a recent work, it was shown that a non-hermitian one-dimensional spinless p-wave superconductor can support complex edge modes in addition to Majorana zero modes [125]. These give rise to a purely imaginary shift in energy. Future work could be dedicated to discussing a non-hermitian extension of the models discussed in this chapter.

2.A Lindblad operators

An alternative approach in finding the ground states of the non-interacting Hamiltonian is by virtue of Lindblad operators. Less steps are required for deriving that $|\Psi^{\pm}\rangle$ are the ground states of H, it is, however, a less transparent

method. A similar approach has been used by Tanaka [126], who discussed a more general model with interaction, which includes as a special case the non-interacting model.

Lindblad operators L_j are defined in the context of non-equilibrium dynamics and govern the dissipation in the system [127–130]. For certain states $|D\rangle$, called dark states in the quantum optics literature, this dissipation term vanishes, which is expressed in terms of the Lindblad operators as

$$L_j |D\rangle = 0. \tag{2.77}$$

Here we leave the dissipation picture and use the notion of dark states to define

$$L_j = \sqrt{g}\left(x_j^{-1} c_j - x_j c_j^\dagger - x_{j+1}^{-1} c_{j+1} - x_{j+1} c_{j+1}^\dagger\right), \tag{2.78}$$

where $g = \frac{\eta^2 - \eta^{-2}}{\mathcal{N}}$ and $x_j = x_0$ (x_1) for j odd (even). One can now easily see that the dark states of L_j are given by $|\Psi^\pm\rangle$ as defined in Equation (2.16). Furthermore, the Lindblad operators are chosen such that

$$H = \sum_j h_j, \qquad h_j = L_j^\dagger L_j - \frac{\mathcal{N}}{2}, \tag{2.79}$$

with h_j the non-interacting Hamiltonian in Equation (2.6). Hence we have found two ground states of the Hamiltonian. In the following we will drop the overall constant $\mathcal{N}/2$.

Assuming that we have no knowledge of the ground state degeneracy from zero modes or the like, we still have to show that we have found all ground states. This can be done by Witten's conjugation argument: [82, 131]. The model we are interested in has at least a two-fold degenerate ground state and is given by

$$H = \sum_j L_j^\dagger L_j. \tag{2.80}$$

Now consider an invertible matrix $\mathcal{M}$, then we can define $\tilde{L}_j = \mathcal{M} L_j \mathcal{M}^{-1}$ such that

$$\tilde{H} = \sum_j \tilde{L}_j^\dagger \tilde{L}_j \tag{2.81}$$

has the same number of ground states as H. If we choose

$$\mathcal{M} = [1 + (x_0^{-1} - 1)n_1][1 + (x_1^{-1} - 1)n_2] \dots [1 + (x_1^{-1} - 1)n_L] \tag{2.82}$$

then $\tilde{L}_j = \sqrt{g}\left(c_j - c_j^\dagger - c_{j+1} - c_{j+1}^\dagger\right)$ and the conjugated Hamiltonian becomes

$$\tilde{H} = -2g \sum_j \left[c_j^\dagger c_{j+1} + c_{j+1}^\dagger c_j + c_{j+1} c_j + c_j^\dagger c_{j+1}^\dagger\right], \tag{2.83}$$

which is nothing but the Kitaev chain in the limit $t = \Delta$ and $\mu = 0$, which clearly has two ground states.

2.B Local operator and correlation length

In order to determine the correlation length, we calculate the equal-time Green function $G^{e,o}(i,j) = \langle \Psi^{e,o} | c_i^\dagger c_j | \Psi^{e,o} \rangle$. Note that $G^{e,o}$ does depend on the specific i and j and not only on the distance, because translational invariance is broken. If we define $d = |i - j|$, the Green function can be written as

$$G^{e,o}(i,j) = \frac{x_i x_j}{(1 - x_i^4)(1 - x_j^4)} \left[\frac{\eta^{-d}}{1 \pm \eta^L} + \frac{\eta^d}{1 \pm \eta^{-L}}\right], \tag{2.84}$$

where the upper sign corresponds to G^e and the lower to G^o. Furthermore, $x_i = x_0$ for i odd and $x_i = x_1$ for i even, with $x_{0,1}$ defined in Equations (2.14, 2.15), and we have used the identity

$$\frac{x_0^2 + 1}{x_0^2 - 1} \frac{x_1^2 + 1}{x_1^2 - 1} = \eta^2. \tag{2.85}$$

For large L the Green function is proportional to

$$G^{e,o}(i,j) \propto \begin{cases} \eta^d & \eta < 1, \\ \eta^{-d} & \eta > 1, \end{cases} \tag{2.86}$$

which scales as $e^{-d/\xi}$ with the correlation length

$$\xi = \frac{1}{\log[\max(\eta, \eta^{-1})]}. \tag{2.87}$$

We note that ξ diverges at the phase transition ($\eta = 1$).

Next we show that the difference between the expectation values of an even local operator O_e with respect to $|\Psi^e\rangle$ and $|\Psi^o\rangle$ satisfies the bound (2.22). First we recognise that for an even local operator O_e

$$\left[O_e, (-1)^F\right] = 0, \tag{2.88}$$

and recall that $|\Psi^-\rangle = (-1)^F |\Psi^+\rangle$. Therefore we can already infer that

$$\langle\Psi^-|O_e|\Psi^-\rangle = \langle\Psi^+|O_e|\Psi^+\rangle\,, \tag{2.89}$$
$$\langle\Psi^-|O_e|\Psi^+\rangle = \langle\Psi^+|O_e|\Psi^-\rangle\,. \tag{2.90}$$

This simplifies the left-hand side of Equation (2.22) to

$$\begin{aligned}\frac{|N\langle\Psi^+|O_e|\Psi^-\rangle - M\langle\Psi^+|O_e|\Psi^+\rangle|}{|N^2-M^2|} &\leq \frac{N|\langle\Psi^+|O_e|\Psi^-\rangle| + M|\langle\Psi^+|O_e|\Psi^+\rangle|}{|N^2-M^2|} \\ &\leq \frac{\|O_e\|\,|NM+N|\langle\Psi^+|O_e|\Psi^-\rangle|}{|N^2-M^2|},\end{aligned} \tag{2.91}$$

where N and M are given by Equations (2.20, 2.21) respectively. Here $\|O_e\|$ is the operator norm defined as

$$\|O_e\| := \inf\{c \;:\; \big\|A\,|\phi\rangle\big\| \leq c\big\||\phi\rangle\big\| \text{ for all } |\phi\rangle \in \mathbb{C}^{\otimes L}\}. \tag{2.92}$$

In the last line we have resolved one of the two correlators. The other one is more involved. In the following we will derive an upper bound for $|\langle\Psi^+|O_e|\Psi^-\rangle|$, which becomes a bit intricate because of the inhomogeneous nature of the system. The estimation hinges on the fact that O_e is a local operator with a support on ℓ sites.

First of all, notice that there are $L-\ell$ sites for which $|\Psi^\pm\rangle$ commutes with O_e, therefore we can reduce

$$\langle\Psi^+|O_e|\Psi^-\rangle = C_1\left[(x_0^2-1)(x_1^2-1)\right]^{\frac{L}{2}-\lfloor\frac{\ell}{2}+1\rfloor}\langle\tilde{\Psi}^+|O_e|\tilde{\Psi}^-\rangle\,, \tag{2.93}$$

where

$$C_1 = \max(x_0^2+1, x_0^2-1)\max(x_1^2+1, x_1^2-1), \tag{2.94}$$

and $\lfloor\cdot\rfloor$ is the floor function. Both the constant and the floor are a result of the alternating pattern in the model. They only contribute marginally to

magnitude, but for completeness we will keep them in. Furthermore, $\tilde{\Psi}^{\pm}$ are the ground states restricted on sites $i \in [j_1, j_k]$.

Using the Schwarz's inequality we obtain

$$\begin{aligned} |\langle\tilde{\Psi}^{+}|O_e|\tilde{\Psi}^{-}\rangle|^2 &\leq \langle\tilde{\Psi}^{+}|\tilde{\Psi}^{+}\rangle\langle\tilde{\Psi}^{-}|O_e^{\dagger}O_e|\tilde{\Psi}^{-}\rangle \\ &\leq \left(C_2\left[(x_0^2+1)(x_1^2+1)\right]^{\lfloor\frac{\ell}{2}\rfloor}\|O_e\|\right)^2, \end{aligned} \tag{2.95}$$

with

$$C_2 = \max(x_0^2+1,1)\max(x_1^2+1,1). \tag{2.96}$$

Plugging this all in yields

$$\begin{aligned} N|\langle\Psi^{+}|O_e|\Psi^{-}\rangle| &\leq NMC_3\left(\frac{(x_0^2+1)(x_1^2+1)}{(x_0^2-1)(x_1^2-1)}\right)^{\lfloor\ell/2\rfloor}\|O_e\| \\ &= NMC_3\eta^{2\lfloor\ell/2\rfloor}\|O_e\|, \end{aligned} \tag{2.97}$$

using Equation (2.85) and defining $C_3 = \frac{C_1C_2}{(x_0^2-1)(x_1^2-1)}$. Hence we find

$$\begin{aligned} |\langle\Psi^{e}|O_e|\Psi^{e}\rangle - \langle\Psi^{o}|O_e|\Psi^{o}\rangle| &\leq \frac{(1+C_3\eta^{2\lfloor\ell/2\rfloor})\|O_e\|}{|\eta^L-\eta^{-L}|} \\ &\approx (1+C_3\eta^{2\lfloor\ell/2\rfloor})\|O_e\|\,e^{-L/\xi}, \end{aligned} \tag{2.98}$$

where we have used $N/M = \eta^L$ and ξ is defined in Equation (2.87). For $\eta \neq 1$ and $l \ll L$ (i.e., O_e local) the numerator is small compared to $e^{L/\xi}$. Hence Equation (2.98) vanishes for large systems.

2.C Action of zero modes

In this appendix we will explicitly derive that T_0^a (analogously one can show this for T_0^b) maps one ground state to the other, i.e., $T_0^a|\Psi^e\rangle \propto |\Psi^o\rangle$.

Before we proceed with the derivation let us note that

$$\frac{x_1(x_0^2-1)}{x_1^2+1} = x_0 q\eta^{-1}, \tag{2.99}$$

which we will need later on.

Suppose $|\Psi^e\rangle = \sum_j \lambda_j a_j |\Psi^o\rangle$, then $\langle\Psi^o|a_j|\Psi^e\rangle = \lambda_j$, because $a_j^2 = 1$. Here we have assumed $\langle\Psi^o|a_j a_k|\Psi^o\rangle = 0$ for $j \neq k$, which is true because $\langle\Psi^\pm|a_j a_k|\Psi^\pm\rangle = \langle\Psi^\pm|a_j a_k|\Psi^\mp\rangle = 0$ due to the specific construction of the ground states.

And we define the shorthand notation $|(\pm)_j\rangle = (x_j c_j^\dagger \pm 1)|\text{vac}\rangle$ (with $x_j = x_{0,1}$ depending on parity), such that for instance $|\Psi^+\rangle = |(+ + \ldots +)\rangle$. Using this notation

$$c_j |\Psi^\pm\rangle = (-1)^{j-1} |(\mp \mp \ldots \mp)\rangle (x_j) |\text{vac}\rangle_j |(\pm \pm \ldots \pm)\rangle , \tag{2.100}$$

$$c_j^\dagger |\Psi^\pm\rangle = (-1)^{j-1} |(\mp \mp \ldots \mp)\rangle (\pm c_j^\dagger) |\text{vac}\rangle_j |(\pm \pm \ldots \pm)\rangle , \tag{2.101}$$

which in turn yields

$$\langle\Psi^\pm|c_j|\Psi^\pm\rangle = \langle\Psi^\pm|c_j^\dagger|\Psi^\pm\rangle = \pm x_j (-1)^{j-1} \prod_{k=1}^{j-1}(x_k^2 - 1) \prod_{l=j+1}^{L}(x_l^2 + 1), \tag{2.102}$$

$$\langle\Psi^\mp|c_j|\Psi^\pm\rangle = -\langle\Psi^\mp|c_j^\dagger|\Psi^\pm\rangle = \mp x_j (-1)^{j-1} \prod_{k=1}^{j-1}(x_k^2 + 1) \prod_{l=j+1}^{L}(x_l^2 - 1). \tag{2.103}$$

Recall that $a_j = c_j + c_j^\dagger$ (from Equation (2.26)) and $|\Psi^{e,o}\rangle = \frac{1}{\sqrt{2(N \pm M)}} \left(|\Psi^+\rangle \pm |\Psi^-\rangle\right)$ (from Equations (2.18, 2.19)) such that

$$\begin{aligned}\langle\Psi^o|\, a_j \,|\Psi^e\rangle &= \frac{2x_j(-1)^{j-1}}{\sqrt{N^2 - M^2}} \prod_{k=1}^{j-1}(x_k^2 - 1) \prod_{l=j+1}^{L}(x_l^2 + 1) \\ &= \frac{2x_j(-1)^{j-1}}{\sqrt{N^2 - M^2}} \frac{N}{x_j^2 + 1} \prod_{k=1}^{j-1} \frac{x_k^2 - 1}{x_k^2 + 1}.\end{aligned} \tag{2.104}$$

If j is odd then

$$\begin{aligned}\lambda_j &= \frac{2}{\sqrt{1 - \eta^{-2L}}} \frac{x_0}{x_0^2 + 1} \left(-\sqrt{\frac{(x_0^2 - 1)(x_1^2 - 1)}{(x_0^2 + 1)(x_1^2 + 1)}} \right)^{j-1} \\ &= \frac{2}{\sqrt{1 - \eta^{-2L}}} \frac{x_0}{x_0^2 + 1} \left(-\eta^{-1} \right)^{j-1},\end{aligned} \tag{2.105}$$

using Equation (2.85). For even j we get

$$\begin{aligned}\lambda_j &= -\frac{2}{\sqrt{1-\eta^{-2L}}}\frac{1}{x_0^2+1}\frac{x_1(x_0^2-1)}{x_1^2+1}\left(-\eta^{-1}\right)^{j-2} \\ &= \frac{2}{\sqrt{1-\eta^{-2L}}}\frac{x_0}{x_0^2+1}\left[-q\eta^{-1}\left(-\eta^{-1}\right)^{j-2}\right],\end{aligned} \tag{2.106}$$

using Equation (2.99). Comparing these results to Equation (2.28) we conclude that $\lambda_j = K\alpha_j$, for some constant K. Finally, we check that the λ_j's are normalised correctly:

$$\langle \Psi^e | \Psi^e \rangle = \sum_j \lambda_j^2 = \frac{4x_0^2}{(x_0^2+1)^2}\frac{\eta^2+q^2}{\eta^2-\eta^{-2}}. \tag{2.107}$$

By simply plugging in x_0 one can verify that this equals unity. Hence T_0^a maps one ground state to the other, up to an overall phase. For T_0^b one can do a similar derivation.

2.D Spectrum

In this appendix we derive the spectrum for the non-interacting model. The first eigenvalue we have already encountered, since there is a zero-energy mode in the system. The other eigenvalues we find by diagonalising C in Equation (2.32). We use the following ansatz for the eigenstates of C:

$$T_k^a(2l-1) = \alpha e^{ik(2l-1)} + \bar{\alpha} e^{-ik(2l-1)}, \tag{2.108}$$

$$T_k^a(2l) = \beta e^{ik(2l)} + \bar{\beta} e^{-ik(2l)}. \tag{2.109}$$

Note that we have taken this two-site periodicity, suitable for the diagonalisation of the Hamiltonian with the alternating chemical potential. Using this ansatz we obtain the following equations for the bulk spectrum

$$\begin{pmatrix} \gamma_+ - 2\epsilon(k) & \delta e^{-ik} + \delta^{-1} e^{ik} \\ \delta e^{ik} + \delta^{-1} e^{-ik} & \gamma_- - 2\epsilon(k) \end{pmatrix} \begin{pmatrix} \alpha \\ \beta \end{pmatrix} = 0, \tag{2.110}$$

which is satisfied if the determinant of the matrix vanishes, resulting in the following eigenvalues

$$\epsilon^{\pm}(k) = \frac{1}{2}\left(\mathcal{N} \pm \sqrt{q^2 + q^{-2} + 2\cos(k)}\right). \tag{2.111}$$

It is important to note that we have not yet specified anything for k. If the system were periodic, we would find $k = \frac{2\pi n}{L}$ for $n \in \{0, \ldots, \frac{L}{2} - 1\}$.

In the open system to find a constraint on k we have to study the boundary conditions. To do so we return to $C^2 = BB^\top$, because it offers four boundary equations, which we need to set the four free parameters (α,$\bar{\alpha}$,β,$\bar{\beta}$):

$$\begin{pmatrix} \delta^{-2} + \gamma_1^2 - \epsilon^2 & (\gamma_1 + \gamma_-)\delta^{-1} & 1 & 0 \\ (\gamma_1 + \gamma_-)\delta^{-1} & \delta^{-2} + \delta^2 + \gamma_-^2 - \epsilon^2 & (\gamma_+ + \gamma_-)\delta & 1 \end{pmatrix} \begin{pmatrix} T(1) \\ T(2) \\ T(3) \\ T(4) \end{pmatrix} = 0, \tag{2.112}$$

$$\begin{pmatrix} 1 & (\gamma_+ + \gamma_-)\delta & \delta^{-2} + \delta^2 + \gamma_+^2 - \epsilon^2 & (\gamma_+ + \gamma_L)\delta^{-1} \\ 0 & 1 & (\gamma_+ + \gamma_L)\delta^{-1} & \delta^{-2} + \gamma_L^2 - \epsilon^2 \end{pmatrix} \begin{pmatrix} T(L-3) \\ T(L-2) \\ T(L-1) \\ T(L) \end{pmatrix} = 0, \tag{2.113}$$

where we have dropped the super- (a) and subscript (k) for brevity. Plugging in the ansatz gives a 4×4 matrix. The determinant of this matrix vanishes when $k = \frac{2\pi n}{L}$ with $n \in \{1, \ldots, \frac{L}{2} - 1\}$. For $k = 0$ the determinant also vanishes, but that occurs because the ansatz eigenfunction becomes trivial. Therefore, we can only determine $2(L/2-1) = L-2$ eigenvalues from C directly. Adding the zero mode gives us $L-1$ eigenvalues. It turns out we can construct the remaining mode explicitly. The following Majorana modes satisfy $[H, T^{a,b}_{\mathcal{N}/2}] = \pm\frac{\mathcal{N}}{2}T^{a,b}_{\mathcal{N}/2}$:

$$T^a_{\mathcal{N}/2} = \alpha_1 \sum_{j=1}^{L/2} \left(-q^{-2}\right)^{j-1} \left(a_{2j-1} + \frac{\eta}{q} a_{2j}\right), \tag{2.114}$$

$$T^b_{\mathcal{N}/2} = \beta_1 \sum_{j=1}^{L/2} \left(-q^{-2}\right)^{j-1} \left(b_{2j-1} + \frac{1}{q\eta} b_{2j}\right), \tag{2.115}$$

therefore the final eigenvalue is $\mathcal{N}/2$.

2.E Phase transition

Here we show that the phase transition at $\eta = 1$ is in the DN-PT universality class. First we will address the non-interacting problem, and then also consider the interactions. We use the results for the staggered XXZ chain

$$H = -\frac{1}{2}\sum_{j=1}^{L}\left[\sigma_j^x\sigma_{j+1}^x + \sigma_j^y\sigma_{j+1}^y + \Delta\sigma_j^z\sigma_{j+1}^z + 2(h + (-1)^j h_s)\sigma_j^z\right]. \tag{2.116}$$

In Ref. [103] it was shown that there is a DN-PT phase transition at

$$h = \sqrt{h_s^2 + 1} - \Delta. \tag{2.117}$$

For the non-interacting model with PBCs, then we can read from Equation (2.25) that at criticality [$\eta = 1$, recall Equation (2.4)]

$$\left.\begin{array}{ll} h - h_s & = q \\ h + h_s & = q^{-1} \end{array}\right\} \Rightarrow \begin{array}{ll} h & = (q^{-1} + q)/2, \\ h_s & = (q^{-1} - q)/2. \end{array} \tag{2.118}$$

Thus with $J = 1$ and $\Delta = 0$ we see that Equation (2.117) is satisfied, i.e., the model is precisely at the DN-PT transition. Similarly, when including interaction the phase transition still occurs at $\eta = 1$. From Equations (2.58-2.60) we can derive that

$$\begin{aligned} h &= \cot\phi\ (q^{-1} + q), \\ \Delta &= (\cot\phi - 1)(q^{-1} + q), \\ h_s &= q^{-1} - q, \end{aligned} \tag{2.119}$$

where an overall factor of $\sqrt{2}\sin(\phi)$ has been taken out. Thus the condition (2.117) is also satisfied for the interacting model.

2.F Ground state for PBCs and APBCs

Following Appendix D in Ref. [106] we derive the ground states for PBCs and APBCs. From Equation (2.16) we define

$$A_L^{\pm} = \prod_{k=1}^{L/2}(x_0 c_{2k-1}^\dagger \pm 1)(x_1 c_{2k}^\dagger \pm 1), \tag{2.120}$$

such that $|\Psi^{\pm}\rangle = A^{\pm}|\text{vac}\rangle$. Subsequently

$$A_L^e = A_L^+ + A_L^-, \qquad A_L^o = A_L^+ - A_L^-, \tag{2.121}$$

which implies $|\Psi^{e,o}\rangle = \frac{1}{\sqrt{2(N\pm M)}} A^{e,o}|\text{vac}\rangle$.

We will now prove that $|\Psi^o\rangle$ $\left(|\Psi^e\rangle\right)$ is the ground state for PBCs (APBCs). The open chain we studied in section 2.2 is closed by adding a boundary term, as we saw in Equation (2.38). For PBCs and APBCs we can identify

$$h_{\text{bound}} = h_L \tag{2.122}$$

with h_L as in Equation (2.6), which acts on site L and $L+1 \equiv 1$. For PBCs we can identify $c_{L+1} = c_1$. Therefore, h_{bound} is minimised by $(x_1 c_L^\dagger \pm 1)(x_0 c_1^\dagger \pm 1) f(c_2^\dagger, \ldots, c_{L-1}^\dagger)$, where f is some polynomial. Rewriting

$$A_L^{\pm} = A_{L-1}^{\pm} x_1 c_L^\dagger \pm A_{L-1}^{\pm} = -x_1 c_L^\dagger A_{L-1}^{\mp} \pm A_{L-1}^{\pm}, \tag{2.123}$$

brings $c_L^\dagger$ next to $c_1^\dagger$. Next we note that

$$\begin{aligned} A_L^o &= (x_1 c_L^\dagger + 1) A_{L-1}^+ - (x_1 c_L^\dagger - 1) A_{L-1}^- && (2.124)\\ &= (x_1 c_L^\dagger + 1)(x_0 c_1^\dagger + 1)(\ldots) - (x_1 c_L^\dagger - 1)(x_0 c_1^\dagger - 1)(\ldots), && (2.125) \end{aligned}$$

with $(\ldots)$ some polynomial in $c_2^\dagger, \ldots, c_{L-1}^\dagger$. Therefore $A_L^o|\text{vac}\rangle$ minimises h_{bound}, so the ground state for PBCs is $|\Psi^o\rangle$.

For APBCs $c_{L+1}^\dagger = -c_1^\dagger$, so h_{bound} is minimised by $(x_1 c_L^\dagger \pm 1)(-x_0 c_1^\dagger \pm 1) f(c_2^\dagger, \ldots, c_{L-1}^\dagger)$. Using Equation (2.123) we recognise

$$\begin{aligned} A_L^e &= -(x_1 c_L^\dagger - 1) A_{L-1}^+ - (x_1 c_L^\dagger + 1) A_{L-1}^- && (2.126)\\ &= -(x_1 c_L^\dagger - 1)(x_0 c_1^\dagger + 1)(\ldots) - (x_1 c_L^\dagger + 1)(x_0 c_1^\dagger - 1)(\ldots), \end{aligned}$$

concluding that $|\Psi^e\rangle$ is the ground state for APBCs.

2.G Odd projector

In this appendix we derive the ground states of the Hamiltonian in Equation (2.73). It is known that there are $L+1$ unique ground states [132, 133]. For notational convenience we rewrite

$$h_j^{\text{int}} = -\mathcal{N}\left[\cos(\theta_j)\left(\sigma_j^x\sigma_{j+1}^x + \sigma_j^y\sigma_{j+1}^y\right) + \sigma_j^z\sigma_{j+1}^z + \sin(\theta_j)\left(\sigma_j^z - \sigma_{j+1}^z\right) - 1\right], \tag{2.127}$$

where we used that

$$\cos(\theta_j)^2 + \sin(\theta_j)^2 = \frac{(\eta+\eta^{-1})^2 + (q_j - q_j^{-1})^2}{\mathcal{N}^2} = 1.$$

One can easily check that the polarised state $|\Uparrow\rangle$ is one of the ground states of the system, $H|\Uparrow\rangle = 0$. We claim that all the ground states are given by

$$|\Psi_p\rangle = (\tilde{\mathcal{S}}^-)^p |\Uparrow\rangle, \tag{2.128}$$

for $p = 0, 1, \ldots, L$ with $\tilde{\mathcal{S}}^-$ defined in Equation (2.74), such that $H|\Psi_p\rangle = 0$.

In order to prove this statement we need the following two conditions:

$$H\tilde{\mathcal{S}}^-|\Uparrow\rangle = [H, \tilde{\mathcal{S}}^-]|\Uparrow\rangle = 0, \tag{2.129}$$

$$[[H, \tilde{\mathcal{S}}^-], \tilde{\mathcal{S}}^-] = 0. \tag{2.130}$$

To derive this, we plug Equation (2.74) into Equation (2.129) resulting in the following constraint on g_j:

$$g_j \cos(\theta_j) = g_{j+1}(1 - \sin(\theta_j)), \tag{2.131}$$

is satisfied by

$$g_{j+1} = \frac{1+\sin(\theta_j)}{\cos(\theta_j)} g_j = \frac{\mathcal{N} + q_j - q_j^{-1}}{\eta + \eta^{-1}} g_j. \tag{2.132}$$

Choosing $g_1 = \sqrt{1 - \frac{q-q^{-1}}{N}}$ results in Equation (2.74), which proves Equation (2.129). Finally, simply writing out the commutator

$$[[h_j, g_j\sigma_j^z + g_{j+1}\sigma_{j+1}^z], g_j\sigma_j^z + g_{j+1}\sigma_{j+1}^z], \tag{2.133}$$

and plugging in g_j verifies Equation (2.130).

Now suppose $|\Psi_p\rangle$ and $|\Psi_{p+1}\rangle$ are ground states of H. For $p = 0$ this is true, because of $H|\Uparrow\rangle = 0$ and Equation (2.129). Using Equation (2.130):

$$\begin{aligned} 0 &= [[H, \tilde{\mathcal{S}}^-], \tilde{\mathcal{S}}^-]\,|\Psi_p\rangle \\ &= \left(H(\tilde{\mathcal{S}}^-)^2 - 2\tilde{\mathcal{S}}^- H\tilde{\mathcal{S}}^- + (\tilde{\mathcal{S}}^-)^2 H\right)|\Psi_p\rangle \\ &= H\,|\Psi_{p+2}\rangle - 2\tilde{\mathcal{S}}^- H\,|\Psi_{p+1}\rangle + (\tilde{\mathcal{S}}^-)^2 H\,|\Psi_p\rangle \\ &= H\,|\Psi_{p+2}\rangle\,. \end{aligned} \tag{2.134}$$

Hence also $|\Psi_{p+2}\rangle$ is a zero-energy ground state of H, and therefore by induction all $|\Psi_p\rangle$ are ground states. Next, we note that $(\sigma_j^-)^2 = 0$, and therefore $(\tilde{\mathcal{S}}^-)^{L+1} = 0$, allowing for finite $(\mathcal{S}^-)^p$ for $p = 0, 1, \ldots, L$.

Finally, we have to prove that (a) all $|\Psi_p\rangle$ exist and (b) we have found a complete ground-state basis.

(a): For the first point we note that $g_j > 0$ for all j, therefore $(\mathcal{S}^-)^p$ is a non-negative matrix and $(\mathcal{S}^-)^p \neq 0$ for $p \leq L$. Hence, the states $|\Psi_p\rangle$ are non-trivial (i.e., $\big\||\Psi_p\rangle\big\| > 0$).

(b): For the second point we observe that $S^z\,|\Psi_p\rangle = (L/2-p)\,|\Psi_p\rangle$, with S^z as in Equation (2.76). In other words, all $|\Psi_p\rangle$ belong to different S^z sectors. Proving the completeness is equivalent to showing that the ground state $|\Psi_p\rangle$ is the unique ground state in the respective S^z sector. Given that S^z commutes with the Hamiltonian, the Hamiltonian matrix ($\mathcal{H}$) becomes block diagonal in the S^z basis. Each block ($\mathcal{H}_p$) corresponds to a fixed S^z sector. In Equation (2.127) we note that only the $\cos(\theta_j)$ terms gives rise to off-diagonal terms in $\mathcal{H}_p$, with a strictly negative coefficient $-(\eta + \eta^{-1})$. Because $\sigma_j^x\sigma_{j+1}^x + \sigma_j^y\sigma_{j+1}^y$ corresponds to a non-negative matrix, the off-diagonal elements of the matrix are non-positive. Note that we are allowed to add a constant term, making the full matrix non-positive. Since $\mathcal{H}_p$ is hermitian, irreducible and non-positive, the Perron-Frobenius theorem tells us that the ground state is non-degenerate [134]. ■

3 Frustration-free models from Witten's conjugation

This chapter is based on: J. Wouters, H. Katsura and D. Schuricht, *Interrelations among frustration-free models via Witten's conjugation*, SciPost Physics Core 4(4), 027 (2021). J.W. performed all calculations, except for Sections 3.3.3 and 3.3.4 which were in conjunction with H.K. Moreover, J.W. performed numerical simulations, discussed the results and contributed to the final version of the manuscript.

We apply Witten's conjugation argument [82] to spin chains, where it allows us to derive frustration-free systems and their exact ground states from known results. We particularly focus on $\mathbb{Z}_p$-symmetric models, with the Kitaev and Peschel–Emery line of the axial next-nearest neighbour Ising (ANNNI) chain being the simplest examples. The approach allows us to treat two $\mathbb{Z}_3$-invariant frustration-free parafermion chains, recently derived by Iemini et al. [120] and Mahyaeh and Ardonne [124] in a unified framework. We derive several other frustration-free models and their exact ground states, including $\mathbb{Z}_4$- and $\mathbb{Z}_6$-symmetric generalisations of the frustration-free ANNNI chain.

3.1 Introduction

Strongly correlated quantum systems are notoriously hard to study. Even when restricted to one spatial dimension the applicability of analytical methods is rather limited. Notable exceptions are provided by systems like the quantum Ising or XY spin chain that can be mapped to effectively non-interacting models [135], thus allowing the determination of the full spectrum by elementary means. A second class of systems is provided by integrable models [136]. They also allow the determination of the full energy spectrum, although more sophisticated methods like the algebraic Bethe ansatz [137, 138] have to be employed and simple results in a closed form are usually not available. A third

type of systems are so-called frustration-free models [139]. These are distinguished by the fact that the ground-state manifold can be given in an exact, closed form. In this chapter we will discuss such frustration-free models and present an overarching framework connecting many of them.

One of the first frustration-free models was described by Peschel and Emery [113]. They realised that for a constrained set of couplings the ground state of the axial next-nearest neighbour Ising (ANNNI) [140] model takes the simple form of a product state, thus facilitating the straightforward calculation of correlation functions. Along this Peschel–Emery line the model can be viewed as a deformation of the trivial ferromagnetic Ising model. Several generalisations to other two-dimensional models including the three-state Potts model were discovered in the following [141–144]. Recently, frustration-free models of this type have been investigated in the context of Majorana zero modes [49, 96, 145] by employing the original results of Peschel and Emery.

Another famous example of a frustration-free model is the Affleck–Kennedy–Lieb–Tasaki (AKLT) chain [93, 94, 139], which was originally devised in the context of the Haldane conjecture for integer spin chains [146–148]. The idea to construct a parent Hamiltonian was subsequently used to construct further frustration-free models like the q-deformed AKLT model [149, 150], valence bond solids with general Lie group symmetries [151–155], or supersymmetric systems [156, 157]. As the ground state of the AKLT model can be written as a compact matrix product state it has served as the starting point for the development of the general theory of matrix product and tensor network states [158–163] and their application in numerical simulations [81, 164] as well as the classification of quantum phases and their symmetry protections [165–169].

Our investigation was motivated in particular by two recent works by Iemini et al. [120] and Mahyaeh and Ardonne [124]. They constructed two different, frustration-free $\mathbb{Z}_3$-clock models. The motivation for these studies was given by their relation to parafermions, thus naturally generalising Majorana zero modes to $\mathbb{Z}_3$-symmetric systems [61]. Like in the case of the Peschel–Emery line discussed above, both models can be viewed as deformations of a simple classical system, in this case the three-state zero-bias Potts chain. One of our main results is to reformulate both models in a unified framework, thus treating them on an equal footing and clarifying their relation (illustrated in Figure 3.3).

This will be achieved by applying Witten's conjugation argument [82, 131], originally introduced for supersymmetric systems, to spin chains. Starting from a simple model with known ground-state manifold, we derive interacting deformations as well as their exact ground states. The explicit construction

then allows the calculation of correlation functions and, in some cases, the proof of the existence of an energy gap. We will apply this line of argument to $\mathbb{Z}_p$-symmetric systems, with the two specific $\mathbb{Z}_3$-symmetric models mentioned above analysed in detail. Furthermore, we construct several new frustration-free models, including generalisations of the Peschel–Emery line to $\mathbb{Z}_4$- and $\mathbb{Z}_6$-symmetric systems.

In this context we note that a method very similar to the Witten conjugation has been applied in the field of matrix product states to construct frustration-free models from the respective parent Hamiltonians [166, 167, 170, 171]. The framework of matrix product (or generalised valence bond solid) states also allows for the calculation of correlation functions, and provides the starting point to prove the existence of an energy gap for the corresponding parent Hamiltonians. These proofs are based either on the martingale method [172] or finite-size criteria [158, 173–175]. The latter link the energy gap of a finite-size system to a lower bound on the energy gap in the thermodynamic limit. The first work following such an approach was done by Knabe [176], who used exact diagonalisation on finite-size systems to obtain a lower bound for the energy gap in the spin-1 AKLT model. We will use this approach to obtain bounds for the energy gaps of several models considered in this chapter. We note that our proofs can in principle be extended by using more advanced methods [172, 174], however, the obtained bounds are physically less practical as we discuss for instance for the model in Section 3.6.5. In order to keep our discussion less abstract, we thus take a more explicit approach not relying on matrix product states in the following but note that many of the results we present below can be rephrased in such terms.

This chapter is organised as follows: In the next section we discuss Witten's conjugation argument and tailor it to frustration-free spin chains. Section 3.3 recalls some known families of frustration-free models that are rederived using the deformation approach. In Section 3.4 we introduce the necessary notations to discuss $\mathbb{Z}_p$-symmetric clock models. In Sections 3.5 and 3.6 we analyse two types of deformations, in particular covering the models introduced in References [120, 124] in the special case $p = 3$. In addition, we consider several frustration-free $\mathbb{Z}_p$-models. While Witten's conjugation argument applied here ensures the form of the ground state, it does not guarantee the existence of an energy gap. Therefore, in the appendix we apply Knabe's method [176] to obtain lower bounds for the energy gap for some of the considered models.

3.2 Conjugation argument

Originally [82] Witten introduced his conjugation argument in the context of supersymmetric quantum mechanical models. More specifically he discussed, given a supersymmetric Hamiltonian H, how to construct an inequivalent Hamiltonian $\tilde{H}$ with the same number of zero-energy states. In this section we recall this argument, already tailoring the notation to the spin-chain systems we will discuss in the following sections. For completeness we recall Witten's original argument in Appendix 3.A.

We consider a lattice with a finite-dimensional Hilbert space for each of the lattice sites. More specifically, in this work we restrict ourselves to one-dimensional chains with open boundary conditions, and assume the local Hamiltonian to act non-trivially on neighbouring sites only. We note, however, that the argument presented here is applicable more generally, for example, to periodic boundary conditions, higher-dimensional lattices or longer-ranged models. Coming back to our setup, we consider a Hamiltonian of the form

$$H = \sum_{j=1}^{N-1} H_{j,j+1} = \sum_{j=1}^{N-1} L_{j,j+1}^{\dagger} L_{j,j+1}, \tag{3.1}$$

where each term[a] $H_{j,j+1} = L_{j,j+1}^{\dagger} L_{j,j+1}$ acts non-trivially on the neighbouring lattice sites j and $j+1$ only, and is positive semi-definite, $\langle\Psi| H_{j,j+1} |\Psi\rangle \geq 0$ for all $|\Psi\rangle$. Consequently, the ground-state manifold G is spanned by $|\Psi_1\rangle, \ldots, |\Psi_n\rangle$, $1 \leq n$, with $L_{j,j+1} |\Psi_i\rangle = 0$ for all j; in other words, G is the intersection of the kernels of the operators $L_{j,j+1}$, $G = \bigcap_j \ker(L_{j,j+1})$.

The representation (3.1) now allows us to say something about the ground states of a deformed/conjugated Hamiltonian. Consider an invertible operator M_j that acts non-trivially on the local Hilbert space of lattice site j only, with which we define an invertible operator acting non-trivially on the whole chain via $M = \prod_j M_j$. Using this operator we can write down the conjugated operators as

$$\tilde{L}_{j,j+1} = M L_{j,j+1} M^{-1} = M_j M_{j+1} L_{j,j+1} M_{j+1}^{-1} M_j^{-1}, \tag{3.2}$$

where we used $[L_{j,j+1}, M_k] = 0$ for $k \neq j, j+1$.

[a] We use capital letters to denote operators acting on the Hilbert space of the full chain, with subindices indicating on which lattice sites they act non-trivially.

Now the deformed/conjugated local Hamiltonian is given by

$$\tilde{H} = \sum_{j=1}^{N-1} \tilde{H}_{j,j+1} = \sum_{j=1}^{N-1} \tilde{L}_{j,j+1}^{\dagger} C_{j,j+1} \tilde{L}_{j,j+1}, \tag{3.3}$$

where we have introduced the hermitian operator $C_{j,j+1}$ as additional degrees of freedom in the construction. The operator $C_{j,j+1} = K_{j,j+1}^{\dagger} K_{j,j+1}$ is assumed to be positive definite, $\langle\Psi| C_{j,j+1} |\Psi\rangle > 0$ for all $|\Psi\rangle$, and thus invertible. The product form of M and the locality of $C_{j,j+1}$ and $L_{j,j+1}$ ensure that the resulting Hamiltonian is still local. Note that in general there is no unique annihilation operator $L_{j,j+1}$. Later in this section we will discuss the interplay between the freedom of $C_{j,j+1}$, $L_{j,j+1}$ and M_j.

In this setting we can now prove the following theorem (see Reference [82] and Appendix 3.A for the original supersymmetric case):

Theorem 1. *The ground-state manifold $\tilde{G}$ of the conjugated Hamiltonian $\tilde{H}$ is given by $\tilde{G} = \mathrm{span}\{M |\Psi_1\rangle, \ldots, M |\Psi_n\rangle\}$, thus the ground-state degeneracies of H and $\tilde{H}$ are identical.*

We note that the states $M |\Psi_i\rangle$ do not form an orthonormal basis, but since M is invertible the states $\{M |\Psi_1\rangle, \ldots, M |\Psi_n\rangle\}$ are linearly independent.

Proof. First we show that since $C_{j,j+1}$ is positive definite we have $\ker(\tilde{H}) = \bigcap_j \ker(\tilde{L}_{j,j+1})$. The proof is simple: Note that a priori $\bigcap_j \ker(\tilde{L}_{j,j+1}) \subseteq \ker(\tilde{H})$. Now suppose $|\Psi\rangle \in \ker(\tilde{H})$, ie, $\tilde{H} |\Psi\rangle = 0$, then

$$\langle\Psi| \tilde{H} |\Psi\rangle = \sum_j \langle\Psi| \tilde{L}_{j,j+1}^{\dagger} C_{j,j+1} \tilde{L}_{j,j+1} |\Psi\rangle = \sum_j \left\| K_{j,j+1} \tilde{L}_{j,j+1} |\Psi\rangle \right\|^2 = 0. \tag{3.4}$$

This implies $K_{j,j+1} \tilde{L}_{j,j+1} |\Psi\rangle = 0$ for all j, and consequently $K_{j,j+1}^{\dagger} K_{j,j+1} \tilde{L}_{j,j+1} |\Psi\rangle = 0$. Since $C_{j,j+1} = K_{j,j+1}^{\dagger} K_{j,j+1}$ is invertible we deduce $\tilde{L}_{j,j+1} |\Psi\rangle = 0$ for all j. Thus we have shown that $|\Psi\rangle \in \bigcap_j \ker(\tilde{L}_{j,j+1})$, which implies $\ker(\tilde{H}) \subseteq \bigcap_j \ker(\tilde{L}_{j,j+1})$.

Second we have to show $\bigcap_j \ker(\tilde{L}_{j,j+1}) = \tilde{G}$. Note that for all $1 \leq j \leq N-1$ and $1 \leq i \leq n$ we have

$$\tilde{L}_{j,j+1} M |\Psi_i\rangle = M L_{j,j+1} |\Psi_i\rangle = 0, \tag{3.5}$$

yielding $\tilde{G} \subseteq \bigcap_j \ker(\tilde{L}_{j,j+1})$.

Conversely, suppose $|\tilde{\Psi}\rangle \in \bigcap_j \ker(\tilde{L}_{j,j+1})$, then for all $1 \leq j \leq N-1$ we find

$$\tilde{L}_{j,j+1} |\tilde{\Psi}\rangle = M L_{j,j+1} M^{-1} |\tilde{\Psi}\rangle = 0, \tag{3.6}$$

from which we conclude that $M^{-1} |\tilde{\Psi}\rangle \in \bigcap_j \ker(L_{j,j+1})$. Consequently we can expand the state as $M^{-1} |\tilde{\Psi}\rangle = \sum_i a_i |\Psi_i\rangle$ with suitable $a_i \in \mathbb{C}$, resulting in

$$|\tilde{\Psi}\rangle = \sum_{i=1}^{n} a_i M |\Psi_i\rangle \in \tilde{G}. \tag{3.7}$$

Therefore $\bigcap_j \ker(\tilde{L}_{j,j+1}) \subseteq \tilde{G}$, which together with the above implies $\bigcap_j \ker(\tilde{L}_{j,j+1}) = \tilde{G}$.

Finally, we note that since $\tilde{H}$ is positive semi-definite, its ground-state manifold is given by its kernel (provided it is non-zero), thus resulting in $\tilde{G} = \ker(\tilde{H})$ as had to be shown. □

We stress that the theorem above provides a direct way to determine the ground-state degeneracy of the deformed Hamiltonian. On the other hand, the theorem does not make any statement about the energy gap above the ground-state manifold or the excited states of the model. Thus, in Appendix 3.B we will discuss a separate approach to prove the existence of a finite energy gap for some specific models.

Before applying the theorem to the construction of spin chain models, let us discuss the degree of freedom in the choices for $L_{j,j+1}$, $C_{j,j+1}$ and M_j. First, assuming a local Hilbert space of dimension p, we have the freedom to perform a local basis transformation[b] v_j, with $v_j \in \mathrm{U}(p)$, at each lattice site j. Under this the operators M_j transform as

$$M_j \to V_j M_j V_j^\dagger, \quad V_j = 1 \otimes \ldots \otimes 1 \otimes v_j \otimes 1 \otimes \ldots \otimes 1, \tag{3.8}$$

and accordingly

$$L_{j,j+1} \to V_j V_{j+1} L_{j,j+1} V_j^\dagger V_{j+1}^\dagger, \quad C_{j,j+1} \to V_j V_{j+1} C_{j,j+1} V_j^\dagger V_{j+1}^\dagger. \tag{3.9}$$

Using this we can always choose a suitable basis in the local Hilbert spaces to

[b] We use small letters to denote operators acting on the Hilbert space of one or two lattice sites.

simplify M_j. Second, recalling that the deformed local Hamiltonian is given by

$$\tilde{H}_{j,j+1} = (M^\dagger)^{-1} L^\dagger_{j,j+1} M^\dagger C_{j,j+1} M L_{j,j+1} M^{-1}, \tag{3.10}$$

we can also perform a transformation on the bonds between lattice sites j and $j+1$ with $u_{j,j+1} \in \mathrm{U}(p^2)$. Specifically setting

$$L_{j,j+1} \to U_{j,j+1} L_{j,j+1}, \quad C_{j,j+1} \to (M^\dagger)^{-1} U_{j,j+1} M^\dagger C_{j,j+1} M U^\dagger_{j,j+1} M^{-1}, \tag{3.11}$$

where

$$U_{j,j+1} = 1 \otimes \ldots \otimes 1 \otimes u_{j,j+1} \otimes 1 \otimes \ldots \otimes 1, \tag{3.12}$$

we see that the local Hamiltonian remains invariant. In the examples in the following sections we will use these freedoms to simplify $L_{j,j+1}$.

3.3 Frustration-free models revisited

In this section we will revisit several known frustration-free models within the framework of Witten's conjugation. We first consider two spin-1/2 models: the XY model [97, 98, 177] with transverse magnetic field and the ANNNI model [49, 113]. Then we review the q-deformed XXZ chain [119, 178, 179], and finally we consider the q-deformed AKLT model [149, 150].

3.3.1 XY chain in transverse magnetic field

We rederive the frustration-free line for the XY model in a magnetic field. Our starting point is the classical Ising chain (which is equivalent to the Kitaev/Majorana chain [11] in the decoupling limit),

$$H_{j,j+1} = 2 - 2\sigma^x_j \sigma^x_{j+1} \tag{3.13}$$

with the exact ground states

$$|\Psi_\pm\rangle = \frac{1}{2^{N/2}} \bigotimes_j \left(|\uparrow\rangle_j \pm |\downarrow\rangle_j \right), \tag{3.14}$$

where $|\uparrow\rangle_j$ and $|\downarrow\rangle_j$ denote the eigenstates of σ^z_j with eigenvalues ± 1. We are looking for models that have a $\mathbb{Z}_2$-symmetry generated by $\prod_j \sigma^z_j$. We choose

M_j diagonal, real and positive, thus there is only one independent parameter in M_j,

$$M_j = 1 \otimes \ldots \otimes 1 \otimes m_j \otimes 1 \otimes \ldots \otimes 1, \quad m_j = \begin{pmatrix} 1 & \\ & r \end{pmatrix}, \quad 0 < r < \infty. \tag{3.15}$$

The operator m_j acts at lattice site j only, with the matrix representation given in the basis $\{|\uparrow\rangle_j, |\downarrow\rangle_j\}$. Hence the deformed ground states are

$$|\tilde{\Psi}_\pm\rangle = M\,|\Psi_\pm\rangle\,. \tag{3.16}$$

Note that the states above are not orthogonal. Orthonormal ground states are instead given by

$$|\tilde{\Phi}_\pm\rangle = \frac{1}{N_\pm}\big(M\,|\Psi_+\rangle \pm M\,|\Psi_-\rangle\big) \tag{3.17}$$

with suitable normalisations $N_\pm$. If we take

$$L_{j,j+1} = \sigma_j^x - \sigma_{j+1}^x, \quad C_{j,j+1} = 1, \tag{3.18}$$

the deformation (3.3) gives the frustration-free line for the Kitaev chain[11], ie, the Jordan–Wigner transform of the XY chain with magnetic field

$$\tilde{H}^{(1)}_{j,j+1} = -J_x\sigma_j^x\sigma_{j+1}^x - J_y\sigma_j^y\sigma_{j+1}^y + \frac{B^{(1)}}{2}(\sigma_j^z + \sigma_{j+1}^z) + \epsilon, \tag{3.19}$$

with the parameters

$$J_x = \frac{(r + r^{-1})^2}{2}, \quad J_y = \frac{(r - r^{-1})^2}{2}, \quad B^{(1)} = r^2 - r^{-2}, \quad \epsilon = r^2 + r^{-2}, \tag{3.20}$$

which correspond to the parameters on the Barouch–McCoy circle [177]. Due to Theorem 1 the model $\tilde{H}^{(1)} = \sum_j \tilde{H}^{(1)}_{j,j+1}$ possesses a two-fold degenerate ground state. In Section 3.5.3 we will discuss the $\mathbb{Z}_3$-generalisation [120] of this model. Section 3.5 will be dedicated to generalise the construction to arbitrary $\mathbb{Z}_p$-symmetry.

3.3.2 ANNNI model

For the second example we obtain an interacting parent Hamiltonian of (3.16) by choosing

$$C_{j,j+1} = \frac{r^2}{2} M_j^{-2} M_{j+1}^{-2}, \tag{3.21}$$

which acts non-trivially on the neighbouring lattice sites j and $j+1$, with M_j and L_j as in Section 3.3.1. The resulting deformed local Hamiltonian is the ANNNI model

$$\tilde{H}^{(2)}_{j,j+1} = -\sigma^x_j \sigma^x_{j+1} + J_z \sigma^z_j \sigma^z_{j+1} + \frac{B^{(2)}}{2}\left(\sigma^z_j + \sigma^z_{j+1}\right) + \epsilon, \tag{3.22}$$

with

$$J_z = \frac{(r - r^{-1})^2}{4}, \quad B^{(2)} = \frac{r^2 - r^{-2}}{2}, \quad \epsilon = \frac{(r + r^{-1})^2}{4}. \tag{3.23}$$

The frustration-free line rediscovered here is the well-known Peschel–Emery line [49, 113] defined by the relation $B^{(2)} = 2\sqrt{J_z(1+J_z)}$. The exact two-fold ground-state degeneracy of $\tilde{H}^{(2)} = \sum_j \tilde{H}^{(2)}_{j,j+1}$ is assured by Theorem 1. In Section 3.6.1 we discuss the $\mathbb{Z}_3$-generalisation [124] of this setup, while in Section 3.6.4 we extend the construction to $\mathbb{Z}_4$-symmetry.

By construction the models (3.19) and (3.22) share the same ground states. Thus their combination is also a parent Hamiltonian,

$$\tilde{H}_{j,j+1} = \alpha_1 \tilde{H}^{(1)}_{j,j+1} + \alpha_2 \tilde{H}^{(2)}_{j,j+1}, \tag{3.24}$$

as long as $\alpha_i \geq 0$. The parameters in the resulting spin model reproduce the frustration-free condition for the XYZ model [95, 97, 98]. Furthermore, the existence of an energy gap above the ground states for (3.24) has been proven [49]. We also note that the construction above can be extended to inhomogeneous magnetic fields, in particular with an alternating bias [145], or higher-dimensional systems [180, 181]. Finally, we note that the states (3.16) allow a straightforward calculation of correlation functions. For example, the two-point function of the Ising order parameter is independently of the separation $j - j'$ given by [177]

$$\frac{\langle \tilde{\Psi}_\pm | \sigma^x_j \sigma^x_{j'} | \tilde{\Psi}_\pm \rangle}{\langle \tilde{\Psi}_\pm | \tilde{\Psi}_\pm \rangle} = \frac{4}{(r + r^{-1})^2}, \tag{3.25}$$

which simplifies to unity at the Ising point ($r = 1$) as expected.

3.3.3 q-deformed XXZ chain

As a third example we show that the XXX chain and the q-deformed XXZ chain are related via Witten's conjugation. We start with the local Hamiltonian of the spin-1/2 XXX Heisenberg chain

$$H_{j,j+1} = 1 - \left(\sigma_j^x \sigma_{j+1}^x + \sigma_j^y \sigma_{j+1}^y + \sigma_j^z \sigma_{j+1}^z\right). \tag{3.26}$$

We first note that the local Hamiltonian satisfies $(H_{j,j+1})^2 = 4H_{j,j+1}$, which means that the operators $H_{j,j+1}/4$ act as projectors. Thus we can write

$$\frac{1}{4} H_{j,j+1} = |\mathrm{sing}\rangle_{j,j+1}\langle \mathrm{sing}|_{j,j+1} \tag{3.27}$$

with[c] $|\mathrm{sing}\rangle_{j,j+1} = (|\uparrow\rangle_j |\downarrow\rangle_{j+1} - |\downarrow\rangle_j |\uparrow\rangle_{j+1})/\sqrt{2}$ denoting the singlet state on the lattice sites j and $j+1$. On all other lattice sites $H_{j,j+1}$ acts trivially. To make the link to the notion introduced above we write

$$\frac{1}{4} H_{j,j+1} = L_{j,j+1}^\dagger L_{j,j+1}, \quad L_{j,j+1} = |\uparrow\rangle_j |\downarrow\rangle_{j+1} \langle \mathrm{sing}|_{j,j+1}. \tag{3.28}$$

Next we consider the generators of $\mathrm{U}_q(\mathrm{sl}_2)$ [182]

$$q^{S^z}, \quad S_q^\pm = \sum_{j=1}^N q^{\sigma_1^z/2} \cdots q^{\sigma_{j-1}^z/2}\, \sigma_j^\pm\, q^{-\sigma_{j+1}^z/2} \cdots q^{-\sigma_N^z/2}, \tag{3.29}$$

where we assume $q \in \mathbb{R}$, $q > 0$, and

$$S^z = \frac{1}{2}\sum_{j=1}^N \sigma_j^z, \quad \sigma_j^\pm = \frac{\sigma_j^x \pm \mathrm{i}\sigma_j^y}{2}. \tag{3.30}$$

These generators satisfy the algebra

$$q^{S^z} S_q^\pm q^{-S^z} = q^{\pm 1} S_q^\pm, \quad [S_q^+, S_q^-] = \frac{q^{2S^z} - q^{-2S^z}}{q - q^{-1}}, \tag{3.31}$$

which reduce to the standard relations among the generators of SU(2) in the limit $q \to 1$.

[c] For the tensor product of states on neighbouring lattice sites we use the short-hand notation $|\uparrow\rangle_j |\downarrow\rangle_{j+1} = |\uparrow\rangle_j \otimes |\downarrow\rangle_{j+1}$ and so on.

In order to proceed, we next define the operator M via

$$M(q) = q^{-\sigma_1^z/2} \cdots q^{-j\sigma_j^z/2} \cdots q^{-N\sigma_N^z/2}, \tag{3.32}$$

with the inverse given by

$$M(q)^{-1} = q^{\sigma_1^z/2} \cdots q^{j\sigma_j^z/2} \cdots q^{N\sigma_N^z/2}. \tag{3.33}$$

With this one gets

$$\tilde{L}_{j,j+1} = M(q) L_{j,j+1} M(q)^{-1} = \sqrt{\frac{1+q^2}{2}} \, |\uparrow\rangle_j \, |\downarrow\rangle_{j+1} \, \langle \mathrm{sing}(q)|_{j,j+1}, \tag{3.34}$$

where the q-deformed singlet state is given by

$$|\mathrm{sing}(q)\rangle_{j,j+1} = \frac{1}{\sqrt{q+q^{-1}}} (q^{-1/2} \, |\uparrow\rangle_j \, |\downarrow\rangle_{j+1} - q^{1/2} \, |\downarrow\rangle_j \, |\uparrow\rangle_{j+1}). \tag{3.35}$$

Thus we obtain

$$\tilde{L}^\dagger_{j,j+1} \tilde{L}_{j,j+1} = \frac{1+q^2}{2} |\mathrm{sing}(q)\rangle_{j,j+1} \langle \mathrm{sing}(q)|_{j,j+1}, \tag{3.36}$$

which is manifestly $\mathrm{U}_q(\mathrm{sl}_2)$ invariant as it is the projection onto the q-deformed singlet state on the bond $(j, j+1)$. A straightforward calculation choosing $C_{j,j+1} = 1$ shows that

$$\frac{1}{4} \tilde{H}_{j,j+1} = \tilde{L}^\dagger_{j,j+1} \tilde{L}_{j,j+1} \tag{3.37}$$

$$= -\frac{q}{4} \left[\sigma_j^x \sigma_{j+1}^x + \sigma_j^y \sigma_{j+1}^y + \frac{q+q^{-1}}{2} \left(\sigma_j^z \sigma_{j+1}^z - 1 \right) + \frac{q-q^{-1}}{2} \left(\sigma_j^z - \sigma_{j+1}^z \right) \right], \tag{3.38}$$

which, up to the prefactor q, is the local Hamiltonian of the q-deformed XXZ chain [119, 178, 179, 182].

After deriving the Hamiltonian, let us consider the ground states in more detail. The ground states of the Heisenberg chain (3.26) are given by[d]

$$(S_1^-)^i \, |\Uparrow\rangle \,, \quad i = 0, 1, \ldots, N, \quad \text{with} \quad |\Uparrow\rangle = |\uparrow \cdots \uparrow\rangle \,. \tag{3.39}$$

[d] We note that the subscript refers to the deformation parameter, ie, $S_1^- \equiv S^-_{q=1}$.

According to Theorem 1 the ground states of the q-deformed model read

$$M(q)\,(S_1^-)^i\,|\Uparrow\rangle \propto (\tilde{S}_1^-)^i\,|\Uparrow\rangle \quad \text{with} \quad \tilde{S}_1^- = M(q)S_1^-M(q)^{-1} = \sum_{j=1}^{N} q^j \sigma_j^-. \tag{3.40}$$

However, the $\mathrm{U}_q(\mathrm{sl}_2)$ algebra dictates that the ground-state manifold is spanned by

$$(S_q^-)^i\,|\Uparrow\rangle\,. \tag{3.41}$$

By induction we will show that there is a correspondence (up to normalisation) between these sets of states, ie,

$$(S_q^-)^i\,|\Uparrow\rangle \propto (\tilde{S}_1^-)^i\,|\Uparrow\rangle\,. \tag{3.42}$$

Obviously this relation holds for $i = 0$. Now suppose that (3.42) is true up to $i-1$. If we write

$$S_q^{\pm} = q^{-S^z \pm \frac{1}{2}} \sum_{j=1}^{N} q^{\sigma_1^z} \cdots q^{\sigma_{j-1}^z}\, \sigma_j^{\pm}, \tag{3.43}$$

then

$$(S_q^-)^i\,|\Uparrow\rangle \propto S_q^-(\tilde{S}_1^-)^{i-1}\,|\Uparrow\rangle = (i-1)!S_q^- \sum_{j_1<\cdots<j_{i-1}} q^{j_1+\cdots+j_{i-1}} \sigma_{j_1}^- \cdots \sigma_{j_{i-1}}^-\,|\Uparrow\rangle \tag{3.44}$$

$$= (i-1)!q^{-\frac{N+1}{2}} \frac{q^i - q^{-i}}{q-q^{-1}} \sum_{j_1<\cdots<j_i} q^{j_1+\cdots+j_i} \sigma_{j_1}^- \cdots \sigma_{j_i}^-\,|\Uparrow\rangle \tag{3.45}$$

$$= \frac{q^{-\frac{N+1}{2}}}{i} \frac{q^i - q^{-i}}{q-q^{-1}} (\tilde{S}_1^-)^i\,|\Uparrow\rangle\,, \tag{3.46}$$

where the precise prefactor is in fact irrelevant for our purpose. This shows that the relation (3.42) is indeed fulfilled, and thus that the ground states of the q-deformed model are given by $M(q)\,(S_1^-)^i\,|\Uparrow\rangle$.

3.3.4 q-deformed AKLT chain

Arguably one of the most prominent frustration-free models is the AKLT chain [93, 94, 139]. Even though the ground state of this system is a matrix product state, we will see that we can still employ the tools outlined above to derive its q-deformed generalisation [149, 150, 183].

We start with the original AKLT chain written as

$$H = \sum_j H_{j,j+1}, \quad H_{j,j+1} \equiv \sum_{m=-2}^{2} |\psi_m\rangle_{j,j+1} \langle\psi_m|_{j,j+1}\,, \tag{3.47}$$

where $H_{j,j+1}$ is the projector onto the subspace of total spin-2 on the neighbouring lattice sites j and $j+1$. It can be written in terms of the corresponding eigenstates $|\psi_m\rangle_{j,j+1}$ and acts trivially on all other lattice sites. The eigenstates are given by

$$\begin{aligned}
&|\psi_2\rangle_{j,j+1} = |+\rangle_j |+\rangle_{j+1}\,, \quad |\psi_1\rangle_{j,j+1} = 1/\sqrt{2}\left(|+\rangle_j |0\rangle_{j+1} + |0\rangle_j |+\rangle_{j+1}\right),\\
&|\psi_0\rangle_{j,j+1} = 1/\sqrt{6}\left(|+\rangle_j |-\rangle_{j+1} + |-\rangle_j |+\rangle_{j+1} + 2\,|0\rangle_j |0\rangle_{j+1}\right),\\
&|\psi_{-1}\rangle_{j,j+1} = 1/\sqrt{2}\left(|0\rangle_j |-\rangle_{j+1} + |-\rangle_j |0\rangle_{j+1}\right), \quad |\psi_{-2}\rangle_{j,j+1} = |-\rangle_j |-\rangle_{j+1}\,,
\end{aligned} \tag{3.48}$$

with $|\pm\rangle_j$, $|0\rangle_j$ denoting the eigenstates of the spin-1 operator S_j^z at a given lattice site j. Note that since $H_{j,j+1}$ is a projector, we can match our convention by simply setting $L_{j,j+1} = H_{j,j+1}$. For the deformation we choose ($q \in \mathbb{R}$, $q > 0$)

$$M(q) = \prod_j M_j(q), \qquad M_j(q) = q^{-2jS_j^z} \left(\frac{q+q^{-1}}{2}\right)^{(S_j^z)^2/2}. \tag{3.49}$$

and we define q-deformed states

$$\begin{aligned}
&|\tilde{\psi}_2^q\rangle_{j,j+1} = |+\rangle_j |+\rangle_{j+1}\,, \quad |\tilde{\psi}_1^q\rangle_{j,j+1} = \frac{1}{\sqrt{1+q^4}}\left(|+\rangle_j |0\rangle_{j+1} + q^2\,|0\rangle_j |+\rangle_{j+1}\right),\\
&|\tilde{\psi}_0^q\rangle_{j,j+1} = \frac{q^{-2}\,|+\rangle_j |-\rangle_{j+1} + q^2\,|-\rangle_j |+\rangle_{j+1} + (q+q^{-1})\,|0\rangle_j |0\rangle_{j+1}}{\sqrt{q^4+q^{-4}+(q+q^{-1})^2}},\\
&|\tilde{\psi}_{-1}^q\rangle_{j,j+1} = \frac{1}{\sqrt{1+q^4}}\left(|0\rangle_j |-\rangle_{j+1} + q^2\,|-\rangle_j |0\rangle_{j+1}\right), \quad |\tilde{\psi}_{-2}^q\rangle_{j,j+1} = |-\rangle_j |-\rangle_{j+1}\,.
\end{aligned} \tag{3.50}$$

We then work out that the conjugated annihilation operator $\tilde{L}_{j,j+1}$ is given by

$$\begin{aligned}\tilde{L}_{j,j+1} \equiv & |\tilde{\psi}_2^{q^{-1}}\rangle_{j,j+1} \langle\tilde{\psi}_2^{q}|_{j,j+1} + |\tilde{\psi}_{-2}^{q^{-1}}\rangle_{j,j+1} \langle\tilde{\psi}_{-2}^{q}|_{j,j+1} \\ & + a(q)\left(|\tilde{\psi}_1^{q^{-1}}\rangle_{j,j+1} \langle\tilde{\psi}_1^{q}|_{j,j+1} + |\tilde{\psi}_{-1}^{q^{-1}}\rangle_{j,j+1} \langle\tilde{\psi}_{-1}^{q}|_{j,j+1}\right) + b(q)\,|\tilde{\phi}_0\rangle_{j,j+1} \langle\tilde{\psi}_0^{q}|_{j,j+1}\end{aligned} \tag{3.51}$$

with the auxiliary state

$$|\tilde{\phi}_0\rangle_{j,j+1} = q^2\,|+\rangle_j\,|-\rangle_{j+1} + q^{-2}\,|-\rangle_j\,|+\rangle_{j+1} + \frac{4}{q+q^{-1}}\,|0\rangle_j\,|0\rangle_{j+1} \tag{3.52}$$

and the parameters

$$a(q) = \frac{q^2+q^{-2}}{2}, \quad b(q) = \frac{(q^2+q^{-2})(q^2+q^{-2}+1)}{6}. \tag{3.53}$$

Now we choose $C_{j,j+1}$ as

$$\begin{aligned}C_{j,j+1} = & |\tilde{\psi}_2^{q^{-1}}\rangle_{j,j+1} \langle\tilde{\psi}_2^{q^{-1}}|_{j,j+1} + |\tilde{\psi}_{-2}^{q^{-1}}\rangle_{j,j+1} \langle\tilde{\psi}_{-2}^{q^{-1}}|_{j,j+1} \\ & + \frac{1}{a(q)^2}\left(|\tilde{\psi}_1^{q^{-1}}\rangle_{j,j+1} \langle\tilde{\psi}_1^{q^{-1}}|_{j,j+1} + |\tilde{\psi}_{-1}^{q^{-1}}\rangle_{j,j+1} \langle\tilde{\psi}_{-1}^{q^{-1}}|_{j,j+1}\right) \\ & + \frac{1}{b(q)^2}\,|\tilde{\phi}_0\rangle_{j,j+1} \langle\tilde{\phi}_0|_{j,j+1},\end{aligned} \tag{3.54}$$

such that the deformed local Hamiltonian becomes the projector

$$\tilde{H}_{j,j+1} = \tilde{L}_{j,j+1}^{\dagger} C_{j,j+1} \tilde{L}_{j,j+1} \equiv \sum_{m=-2}^{2} |\tilde{\psi}_m^{q}\rangle_{j,j+1} \langle\tilde{\psi}_m^{q}|_{j,j+1}\,. \tag{3.55}$$

Hence we obtain the q-deformed AKLT model [149, 150, 183].

The above result shows the deformation at the level of the Hamiltonian. Let us also look explicitly at the ground state. The four ground states of the undeformed AKLT chain can be written in the matrix product state representation as

$$\begin{pmatrix} |\Psi_{\mathrm{AKLT}}^{1,1}\rangle & |\Psi_{\mathrm{AKLT}}^{1,2}\rangle \\ |\Psi_{\mathrm{AKLT}}^{2,1}\rangle & |\Psi_{\mathrm{AKLT}}^{2,2}\rangle \end{pmatrix} = A_1 \cdots A_L, \text{ with } A_j = \begin{pmatrix} |0\rangle_j & -\sqrt{2}\,|+\rangle_j \\ \sqrt{2}\,|-\rangle_j & -\,|0\rangle_j \end{pmatrix}. \tag{3.56}$$

According to Theorem 1, the ground state of the q-deformed model is generated by the matrix

$$\tilde{A}_j = \begin{pmatrix} |0\rangle_j & -q^{-2j}\sqrt{q+q^{-1}}\,|+\rangle_j \\ q^{2j}\sqrt{q+q^{-1}}\,|-\rangle_j & -|0\rangle_j \end{pmatrix}. \tag{3.57}$$

Generically a matrix product state is defined up to a gauge freedom. If we take

$$f_{j-1,j} = \begin{pmatrix} q^j & \\ & q^{-(j-1)} \end{pmatrix}, \tag{3.58}$$

we can redefine the matrix representation as

$$\tilde{A}_j^{\mathrm{tr}} = f_{j-1,j}\tilde{A}_j f_{j,j+1}^{-1} = \begin{pmatrix} q^{-1}|0\rangle_j & -\sqrt{q+q^{-1}}\,|+\rangle_j \\ \sqrt{q+q^{-1}}\,|-\rangle_j & -q\,|0\rangle_j \end{pmatrix}, \tag{3.59}$$

which is identical to the one given in References [150, 183] for the ground state of the q-deformed AKLT chain.

Finally we note that a similar derivation to the one presented in this section can be used to relate the AKLT chain (3.47) to a frustration-free point in the (representation) symmetry protected phase of S_3-invariant chains recently studied by O'Brien et al. [184].

3.4 Introduction to $\mathbb{Z}_p$-clock models

The rest of the chapter considers $\mathbb{Z}_p$-clock models, and frustration-free systems of this type. Therefore, let us first briefly review the $\mathbb{Z}_p$-clock algebra. Consider a local p-dimensional Hilbert space and two local operators σ and τ satisfying

$$\sigma^p = \tau^p = 1, \quad \sigma^{p-1} = \sigma^\dagger, \quad \tau^{p-1} = \tau^\dagger, \quad \sigma\tau = \omega\tau\sigma, \tag{3.60}$$

where $\omega = \exp(2\pi\mathrm{i}/p)$ is the pth root of unity. Denoting the eigenstates of σ and τ by $|\sigma, i\rangle$ and $|\tau, i\rangle$ with $i = 0, \ldots, p-1$ respectively, the action of the operators is given by

$$\sigma\,|\sigma, i\rangle = \omega^i\,|\sigma, i\rangle\,, \quad \tau\,|\sigma, i\rangle = |\sigma, i+1\rangle\,, \tag{3.61}$$

$$\tau\,|\tau, i\rangle = \omega^i\,|\tau, i\rangle\,, \quad \sigma\,|\tau, i\rangle = |\tau, i-1\rangle\,, \tag{3.62}$$

where $i \pm 1$ has to be taken modulo p. The states $|\sigma, i\rangle$ can be represented in terms of the states $|\tau, i\rangle$ as

$$|\sigma, i\rangle = \frac{1}{\sqrt{p}} \left(|\tau, 0\rangle + \omega^i |\tau, 1\rangle + \cdots + \omega^{(p-1)i} |\tau, p-1\rangle \right). \tag{3.63}$$

The Potts/clock model is a generalisation of the Ising model. Here we start with the counterpart of the classical Ising chain (3.13), namely the classical Potts model, whose local Hamiltonian is given by

$$H_{j,j+1} = 2 - \sigma_j \sigma_{j+1}^\dagger - \sigma_j^\dagger \sigma_{j+1}, \tag{3.64}$$

where σ_j and τ_j denote the operators σ and τ introduced above, now acting non-trivially on the local Hilbert space of site j. The classical Potts model possesses a p-fold degenerate ground state

$$|\Psi_i\rangle = \bigotimes_j |\sigma, i\rangle_j \tag{3.65}$$

with $|\sigma, i\rangle_j$ denoting the eigenstates of σ_j. Furthermore, the system has an energy gap above the ground states.

Finally, we note that the clock operators σ_j and τ_j have a parafermionic dual by virtue of the Fradkin–Kadanoff transformation [60], which is the generalisation of the Jordan–Wigner transformation to $\mathbb{Z}_p$-symmetry. The resulting parafermions can be regarded as generalisation of Majorana fermions [61].

We can already discuss the most general form of deformation that we consider in the rest of the chapter. So far the only requirement for M_j is the invertibility. In this work we restrict ourselves to models that preserve $\mathbb{Z}_p$-symmetry generated by

$$\omega^P = \prod_j \tau_j. \tag{3.66}$$

Since M has to commute with ω^P, the local operator m_j has to be diagonal in the τ-basis, ie,

$$m_j = \begin{pmatrix} \alpha_0 & & & \\ & \alpha_1 & & \\ & & \ddots & \\ & & & \alpha_{p-1} \end{pmatrix} = \frac{1}{p} \sum_{k,l=0}^{p-1} \alpha_k \omega^{-kl} \tau^l \tag{3.67}$$

for $\alpha_k \in \mathbb{C}$. Note that we can take out an overall scaling factor, so we end up with $p-1$ independent complex coefficients α_k/α_0, $k = 1, \ldots, p-1$. For now we will leave it in the most general form. In line with the cyclicity of the algebra, the coefficients α_k are also defined modulo p,

$$\alpha_k = \alpha_{k \bmod p}, \tag{3.68}$$

for instance $\alpha_{-k} = \alpha_{p-k}$. Later we will see that in specific examples we get more constraints on the coefficients α_k.

Starting with the ground states (3.65) we obtain the deformed states by acting with the operator $M = \prod_j M_j = \bigotimes_j m_j$, ie,

$$|\tilde{\Psi}_i\rangle = M\,|\Psi_i\rangle = \bigotimes_j m_j\,|\sigma, i\rangle_j\,. \tag{3.69}$$

This form immediately allows us to calculate correlation functions. For example, the two-point function of the order parameter σ becomes

$$\left|\frac{\langle\tilde{\Psi}_i|\sigma_j\sigma_{j'}^\dagger|\tilde{\Psi}_i\rangle}{\langle\tilde{\Psi}_i|\tilde{\Psi}_i\rangle}\right| = \frac{|\sum_k \alpha_k^*\alpha_{k+1}|^2}{(\sum_k |\alpha_k|^2)^2} \leq 1, \tag{3.70}$$

where the upper bound is obtained by virtue of the Schwarz inequality. Other correlation functions can be obtained in a similar way. In the following sections we will derive the parent Hamiltonian for the deformed ground states.

3.5 Frustration-free $\mathbb{Z}_p$-generalisations of the XY chain

In this section we generalise the $\mathbb{Z}_2$-XY chain discussed in Section 3.3.1 to arbitrary $\mathbb{Z}_p$-symmetry. Specifically we use the term XY in the sense that we take $L_{j,j+1}$ and $C_{j,j+1}$ of the following form

$$L_{j,j+1} = \sigma_j - \sigma_{j+1}, \quad C_{j,j+1} = 1. \tag{3.71}$$

Furthermore, we require the resulting model to possess ω^P-symmetry, which fixes m_j to be given by (3.67). In the case $p = 3$ we recover a model recently studied by Iemini et al. [120], see Section 3.5.2.

For the choices (3.67) and (3.71) it is straightforward to work out the conjugated Hamiltonian (we set $\alpha_{-1} \equiv \alpha_{p-1}$ to lighten the notation). First,

$$\tilde{L}_{j,j+1} = \frac{1}{p} \sum_{k,l=0}^{p-1} \frac{\alpha_{k-1}}{\alpha_k} \omega^{-kl} \left(\sigma_j \tau_j^l - \sigma_{j+1} \tau_{j+1}^l \right), \tag{3.72}$$

where we used [see Equation (3.60)]

$$M_j \sigma_j M_j^{-1} = \frac{1}{p^2} \sum_{k,k',l,l'} \frac{\alpha_k}{\alpha_{k'}} \omega^{-(k+1)l-k'l'} \sigma_j \tau_j^{l+l'} = \frac{1}{p} \sum_{k,l=0}^{p-1} \frac{\alpha_{k-1}}{\alpha_k} \omega^{-kl} \sigma_j \tau_j^l. \tag{3.73}$$

With (3.72) the conjugated local Hamiltonian then becomes

$$\begin{aligned} \tilde{H}_{j,j+1} &= \frac{1}{p^2} \sum_{k,k',l,l'} \frac{\alpha_{k-1}^*}{\alpha_k^*} \frac{\alpha_{k'-1}}{\alpha_{k'}} \omega^{kl-k'l'} \left[\left(\tau_j^{l'-l} + \tau_{j+1}^{l'-l} \right) - \left(\tau_j^{-l} \sigma_j^\dagger \sigma_{j+1} \tau_{j+1}^{l'} + \text{h.c.} \right) \right] \\ &= - \left(B_j^\dagger \sigma_j^\dagger \sigma_{j+1} B_{j+1} + \text{h.c.} \right) + \sum_{l=0}^{p-1} \gamma_l \left(\tau_j^l + \tau_{j+1}^l \right), \end{aligned} \tag{3.74}$$

where

$$B_j = \sum_{l=0}^{p-1} \beta_l \tau_j^l, \quad \beta_l = \frac{1}{p} \sum_{k=0}^{p-1} \frac{\alpha_{k-1}}{\alpha_k} \omega^{-kl}, \quad \gamma_l = \frac{1}{p} \sum_{k=0}^{p-1} \left| \frac{\alpha_{k-1}}{\alpha_k} \right|^2 \omega^{-kl}. \tag{3.75}$$

Admittedly this form is not yet very insightful. Thus in the following sections we will consider specific cases for which the Hamiltonian simplifies.

3.5.1 $\mathbb{Z}_p$-XY model: most general real coefficients

One simplification occurs with the requirement that the coefficients β_l and γ_l are real. For odd p this implies the following conditions (we set $\alpha_0 = r_0 = 1$ due to the freedom in the overall scaling of m_j)

$$\alpha_k = \begin{cases} e^{\mathrm{i}\theta_k} r_k, & k = 1, \ldots, \frac{p-1}{2}, \\ e^{\mathrm{i}\theta_{p-k-1}} \frac{r_{(p-1)/2}^2}{r_{p-k-1}}, & k = \frac{p+1}{2}, \ldots, p-1, \end{cases} \tag{3.76}$$

for $r_1, \ldots, r_{(p-1)/2} > 0$ and $\theta_1, \ldots, \theta_{(p-1)/2} \in [0, 2\pi)$.

Similarly, for p even β_l and γ_l are real provided

$$\alpha_k = \begin{cases} e^{\mathrm{i}\theta_k} r_k, & k = 1, \ldots, \frac{p}{2} - 1, \\ \pm e^{\mathrm{i}\theta_{p-k-1}} \frac{s}{r_{p-k-1}}, & k = \frac{p}{2}, \ldots, p-1, \end{cases} \tag{3.77}$$

for $r_1, \ldots, r_{p/2-1}, s > 0$ and $\theta_1, \ldots, \theta_{p/2-1} \in [0, 2\pi)$.

3.5.2 $\mathbb{Z}_p$-XY model: compact form with real coefficients

In order to obtain a compact form for the Hamiltonian (3.74) the results from the section can be further specified. Taking $\alpha_k = r^k$ with $r \in \mathbb{R}\backslash\{0\}$ such that the ratio between consecutive α_k is constant, we obtain for the coefficients

$$\beta_l = \frac{1}{pr}\left(r^p + p\delta_{l,0} - 1\right), \quad \gamma_l = \frac{1}{pr^2}\left(r^{2p} + p\delta_{l,0} - 1\right). \tag{3.78}$$

Thus the local Hamiltonian simplifies to

$$\tilde{H}_{j,j+1} = \epsilon - \left[\left(1 + b\sum_{l=1}^{p-1}\tau_j^l\right)\sigma_j^\dagger\sigma_{j+1}\left(1 + b\sum_{l=1}^{p-1}\tau_{j+1}^l\right) + \text{h.c.}\right] - \frac{f}{2}\sum_{l=1}^{p-1}\left(\tau_j^l + \tau_{j+1}^l\right), \tag{3.79}$$

with

$$b = \frac{r^p - 1}{r^p + p - 1}, \quad f = \frac{2p(1 - r^{2p})}{(r^p + p - 1)^2}, \quad \epsilon = \frac{p(r^{2p} + p - 1)}{(r^p + p - 1)^2}, \tag{3.80}$$

where we have done a multiplicative rescaling to set the coupling of $\sigma_j^\dagger\sigma_{j+1}$ to -1. For $p = 2$ the model simplifies to the XY model (3.19) discussed in Section 3.3.1.

We note that for odd p the model parameters depend on the sign of r, while for even p the coefficients only contain even powers of r. The latter suggests that there are two sets of ground states for the same Hamiltonian,

$$|\tilde{\Psi}_i^+\rangle = M(r)\,|\Psi_i\rangle\,, \quad |\tilde{\Psi}_i^-\rangle = M(-r)\,|\Psi_i\rangle\,. \tag{3.81}$$

However, from the expansion we recognise

$$|\tilde{\Psi}_i^-\rangle = |\tilde{\Psi}_{i+p/2}^+\rangle\,, \tag{3.82}$$

so both $M(r)$ and $M(-r)$ provide the same set of ground states. Moreover, the physical properties do not change under $r \to 1/r$. We can see this from $m_j = \mathrm{diag}(1, r, \ldots, r^n) \to \mathrm{diag}(1, r^{-1}, \ldots, r^{-n}) \propto \mathrm{diag}(r^n, r^{n-1}, \ldots, 1)$. The latter is related to the original m_j by a conjugation and cyclic rotation of the basis, hence the physical properties remain invariant.

Finally we note that for $p = 3$ and $r > 0$ we reproduce the model introduced by Iemini et al. [120]. There the authors also derive the positive-definite form (3.3) by the use of Fock parafermions [185]. Using elementary methods, in Appendix 3.B.2 we show that the model possesses a finite energy gap for $0.5695 \lesssim r \lesssim 1/0.5695 \approx 1.7560$, thus confirming the corresponding numerical results [120]. We note that our proof does not exclude the existence of an energy gap outside this interval, which can be extended by improving our analysis or using alternative methods [158, 172, 174]. We note, however, that special care has to be taken regarding the treatment of the boundary conditions.

3.5.3 $\mathbb{Z}_3$-XY model: real coefficients from complex deformation

Our construction allows us to directly generalise the model discussed above. From Section 3.5.1 we see that for $p = 3$ there is an additional freedom in the choice of m_j in the form of a complex phase, ie, we can choose

$$m_j = \begin{pmatrix} 1 & & \\ & e^{\mathrm{i}\theta} r & \\ & & r^2 \end{pmatrix}, \tag{3.83}$$

which results in

$$\tilde{H}_{j,j+1} = \epsilon - \left[\left(1 + b^+ \tau_j + b^- \tau_j^\dagger\right) \sigma_j^\dagger \sigma_{j+1} \left(1 + b^- \tau_{j+1} + b^+ \tau_{j+1}^\dagger\right) + \frac{f}{2} \left(\tau_j + \tau_{j+1}\right) + \mathrm{h.c.} \right] \tag{3.84}$$

with the parameters

$$f = \frac{6(1 - r^6)}{(r^3 + 2\cos\theta)^2}, \quad b^\pm = \frac{r^3 - \cos\theta \pm \sqrt{3}\sin\theta}{r^3 + 2\cos\theta}, \quad \epsilon = \frac{6(r^6 + 2)}{(r^3 + 2\cos\theta)^2}. \tag{3.85}$$

For $\theta = 0$ we recover the model studied in Reference [120]. We note that the parameters (3.85) possess a divergence at $r = \sqrt[3]{-2\cos\theta}$ provided $\theta \in [\frac{\pi}{2}, \frac{3\pi}{2}]$. This divergence is an artefact of fixing the prefactor of the $-\sigma_j^\dagger \sigma_{j+1}$-term to unity, it can be removed by rescaling the Hamiltonian by $(r^3 + 2\cos\theta)^2$.

3.6 Frustration-free $\mathbb{Z}_p$-generalisations of the ANNNI model

In this section we construct $\mathbb{Z}_p$-invariant generalisations of the ANNNI model (see Section 3.3.2), for which we will use the term[e] axial next-nearest neighbour Potts (ANNNP) model [144]. More specifically, we consider $\mathbb{Z}_p$-invariant Hamiltonians where besides the classical Potts term $\sigma_j\sigma_{j+1}^\dagger + \sigma_j^\dagger\sigma_{j+1}$ only terms of the form $\tau_j^l\tau_{j+1}^{l'}$ with $l, l' = 0, \ldots, p-1$ appear. In particular, there are no terms containing products of σ- and τ-operators.

First we will derive some general results following from this simple set of rules. Then we discuss several specific examples. We take m_j to be defined by (3.67) and $L_{j,j+1} = \sigma_j - \sigma_{j+1}$ as before. Furthermore, generalising (3.21) we set $C_{j,j+1} = K_jK_{j+1}$, where K_j acts non-trivially at lattice site j with the matrix k_j. Now making the ansatz (in the τ-basis)

$$k_j = \operatorname{diag}\left(\frac{\alpha_1}{\alpha_0}, \frac{\alpha_2}{\alpha_1}, \ldots, \frac{\alpha_{p-1}}{\alpha_{p-2}}, \frac{\alpha_0}{\alpha_{p-1}}\right), \tag{3.86}$$

and recalling that $C_{j,j+1}$ has to be hermitian and positive definite, we deduce that the α_k have to be real and positive (we set $\alpha_0 = 1$). From the form above we also deduce that the following identity holds, $K_jM_j\sigma_jM_j^{-1} = \sigma_j$. Hence we find for the deformed local Hamiltonian

$$\begin{aligned}\tilde{H}_{j,j+1} &= \tilde{L}_{j,j+1}^\dagger K_jK_{j+1}\tilde{L}_{j,j+1} = \tilde{L}_{j,j+1}^\dagger\left(\sigma_jK_{j+1} - K_j\sigma_{j+1}\right)\\ &= \left(M_j^{-1}\sigma_j^\dagger M_j - M_{j+1}^{-1}\sigma_{j+1}^\dagger M_{j+1}\right)\left(\sigma_jK_{j+1} - K_j\sigma_{j+1}\right)\\ &= -\left(\sigma_j\sigma_{j+1}^\dagger + \sigma_j^\dagger\sigma_{j+1}\right) + \left(M_j^{-1}\sigma_j^\dagger M_j\sigma_jK_{j+1} + K_jM_{j+1}^{-1}\sigma_{j+1}^\dagger M_{j+1}\sigma_{j+1}\right).\end{aligned} \tag{3.87}$$

Here the first two terms represent the classical Potts model. Note that, both M_j and K_j are diagonal in the τ-basis and can therefore be expanded in powers of τ_j.

$$M_j^{-1}\sigma_j^\dagger M_j\sigma_j = \sum_l \Delta_l\tau_j^l, \quad K_j = \sum_l \Gamma_l\tau_j^l, \tag{3.88}$$

[e] Alternatively, since the models will be written in terms of the clock operators, we could use the term axial next-nearest neighbour clock (ANNNC) model [186].

where we introduced the abbreviations

$$\Delta_l = \frac{1}{p}\sum_k \frac{\alpha_{k-1}}{\alpha_k}\omega^{-kl}, \quad \Gamma_l = \frac{1}{p}\sum_k \frac{\alpha_{k+1}}{\alpha_k}\omega^{-kl}. \tag{3.89}$$

Hence, the last two terms in (3.87) only produce contributions of the form $\tau_j^l \tau_{j+1}^{l'}$, as was intended. We will not write down the explicit expansion, since it is tedious and not insightful. Instead, in the next sections we will discuss several explicit examples. Doing so we obtain a general complex $\mathbb{Z}_3$-ANNNP model. Furthermore, we rediscover the known frustration-free line [124, 144] in the $\mathbb{Z}_3$ case, with purely real coefficients. Finally, we discuss a frustration-free line for $p = 2q$ even, of which the original ANNNI model (3.22) is the simplest representative and $\mathbb{Z}_4$- and $\mathbb{Z}_6$-ANNNP examples are given below.

3.6.1 $\mathbb{Z}_3$-ANNNP model: with complex coefficients

The simplest non-trivial example (besides ANNNI) we can derive with this construction is the $\mathbb{Z}_3$-ANNNP. The most general deformation for $\mathbb{Z}_3$ is

$$m_j = \begin{pmatrix} 1 & & \\ & r & \\ & & s \end{pmatrix}, \tag{3.90}$$

with the corresponding $C_{j,j+1}$ determined by (3.86). The deformed Hamiltonian takes the simple form

$$\tilde{H} = -\sum_j \left[\sigma_j \sigma_{j+1}^\dagger + \frac{f}{2}(\tau_j + \tau_{j+1}) + g_1 \tau_j \tau_{j+1} + g_2 \tau_j \tau_{j+1}^\dagger + \text{h.c.}\right] + \epsilon, \tag{3.91}$$

which is also the quantum limit of the axial next-nearest neighbour Potts model [144]. Since the operators σ_j and τ_j are not self-adjoint, more terms and coefficients than in the original ANNNI model (3.22) appear. The similarity with the ANNNI model is exemplified by the following identifications:

ANNNI model		$\mathbb{Z}_3$-ANNNP model
$\sigma_j^x \sigma_{j+1}^x$	$\to$	$\sigma_j \sigma_{j+1}^\dagger$
σ_j^z	$\to$	τ_j
$\sigma_j^z \sigma_{j+1}^z$	$\to$	$\tau_j \tau_{j+1},\ \tau_j \tau_{j+1}^\dagger$

The coefficients generated by the deformation (3.90) are in general complex

$$f = \frac{2}{9}\left[2\left(rs + \omega\frac{r}{s^2} + \bar{\omega}\frac{s}{r^2}\right) - \left(\frac{1}{rs} + \bar{\omega}\frac{r^2}{s} + \omega\frac{s^2}{r}\right)\right], \tag{3.92}$$

$$g_1 = -\frac{2}{9}\left[\omega\left(\frac{r^2}{s} + \frac{s}{r^2}\right) + \bar{\omega}\left(\frac{s^2}{r} + \frac{r}{s^2}\right) + rs + \frac{1}{rs}\right], \tag{3.93}$$

$$g_2 = \frac{1}{9}\left[3 + \left(\frac{1}{rs} + \frac{s^2}{r} + \frac{r^2}{s}\right) - 2\left(rs + \frac{s}{r^2} + \frac{r}{s^2}\right)\right]. \tag{3.94}$$

Even though there is some elegance in the generality of this model, these complex coefficients are not very practical. Therefore in the next sub-sections we discuss two specific cases.

$\mathbb{Z}_3$-ANNNP model: real coefficients reproducing Reference [124]

The first example features purely real coefficients. This model was originally obtained by direct calculation by Mahyaeh and Ardonne [124]. We rediscover it by considering the deformation (3.90) with $s = r$, ie,

$$m_j = \begin{pmatrix} 1 & & \\ & r & \\ & & r \end{pmatrix}, \quad L_{j,j+1} = \sigma_j - \sigma_{j+1}, \quad C_{j,j+1} = K_j K_{j+1}, \quad k_j = \begin{pmatrix} r & & \\ & 1 & \\ & & r^{-1} \end{pmatrix}, \tag{3.95}$$

such that the coefficients become

$$f = \frac{2(1+2r)(1-r^3)}{9r^2}, \quad \epsilon = \frac{2(1+r+r^2)^2}{9r^2}, \tag{3.96}$$

$$g_1 = -\frac{2(1-r)^2(1+r+r^2)}{9r^2}, \quad g_2 = \frac{(1-r)^2(1-2r-2r^2)}{9r^2}. \tag{3.97}$$

The exact ground states originally constructed in Reference [124] follow by direct application of Theorem 1. Furthermore, in Appendix 3.B.2 we prove that the model possesses an energy gap above these ground states at least in the interval $\sqrt{\frac{3}{2}\sqrt{2} - 2} \approx 0.3483 \lesssim r \lesssim 3.9912$. Finally we note that for

$r = (\sqrt{3}-1)/2 \approx 0.366$ the model (3.91) simplifies as the parameter g_2 vanishes.

$\mathbb{Z}_3$-ANNNP with ground state deformation of $\mathbb{Z}_3$-XY model

For the second example we consider the deformation that we encountered before for $\mathbb{Z}_3$-XY, namely $s = r^2$,

$$m_j = \begin{pmatrix} 1 & & \\ & r & \\ & & r^2 \end{pmatrix}. \tag{3.98}$$

Thus the deformed ground states are identical to the ones for $\theta = 0$ discussed in Section 3.5.3. However, due to the non-trivial choice for $C_{j,j+1}$ the Hamiltonian will differ, specifically we obtain (3.91) with the coefficients

$$f = \bar{\omega}\frac{(1-r^3)\left[(1-r^3)+3\sqrt{3}\mathrm{i}(1+r^3)\right]}{9r^3}, \quad g_1 = -2\omega g_2, \quad g_2 = -\frac{(1-r^3)^2}{9r^3}. \tag{3.99}$$

The coefficient g_1 can be chosen to be real via a gauge transformation, ie, a permutation of diagonal elements of m_j.

3.6.2 $\mathbb{Z}_p$-ANNNP model: most general real coefficients

For general $\mathbb{Z}_p$ we discuss the case when all coefficients take real values. From (3.88) and (3.89) we recognise that the coefficient of $\tau_j^l \tau_{j+1}^{l'}$ is $\Delta_l \Gamma_{l'} + \Gamma_l \Delta_{l'}$. This is real for example if $\Gamma_l^* = \Delta_l$, which yields the constraints (recall that $\alpha_k > 0$)

$$\alpha_{-k} \equiv \alpha_{p-k} = \alpha_k \tag{3.100}$$

for all k. Thus there are $(p-1)/2$ real degrees of freedom for p odd and $p/2$ for p even. The expansion is still not in a compact form. In Section 3.6.3 we will discuss a Hamiltonian with a compact form for p even. For p odd we did not obtain a simple compact form, except for the case $p = 3$ discussed in the next section.

The condition (3.100) has another consequence. Under charge conjugation

$$\sigma_j \to \sigma_j^\dagger, \quad \tau_j \to \tau_j^\dagger, \tag{3.101}$$

we see that

$$M_j^{-1}\sigma_j^\dagger M_j\sigma_j \to K_j, \quad K_j \to M_j^{-1}\sigma_j^\dagger M_j\sigma_j. \tag{3.102}$$

In this particular case the Hamiltonian (3.87) is invariant under charge conjugation, and together with the $\mathbb{Z}_p$-symmetry generated by ω^P, the full symmetry group is the dihedral group D_p [187, 188]. Note that for $p = 3$ the dihedral group is isomorphic to the symmetric group S_3 of all permutations.

3.6.3 $\mathbb{Z}_{2q}$-ANNNP model: compact form with real coefficients

For even $p = 2q$ it is possible to construct a model depending on a single parameter which possesses real coefficients and a simple closed form. We start with

$$m_j = \mathrm{diag}(1, r, \ldots, r^{q-1}, r^q, r^{q-1}, \ldots, r), \quad k_j = \mathrm{diag}(r, \ldots, r, r^{-1}, \ldots, r^{-1}). \tag{3.103}$$

Using Equation (3.67) we see that

$$M_j^{-1}\sigma_j^\dagger M_j\sigma_j = \sum_{l=0}^{p-1}\left[r^{-1} + (-1)^l r\right]\theta^q(l)\tau_j^l, \tag{3.104}$$

$$K_j = \sum_{l=0}^{p-1}(-\omega)^l\left[r^{-1} + (-1)^l r\right]\theta^q(l)\tau_j^l, \tag{3.105}$$

where

$$\theta^q(l) = \frac{1}{2q}\sum_{k=1}^{q}\omega^{-kl} = \begin{cases} \frac{1}{2}, & \text{if } l = 0, \\ 0, & \text{if } l \text{ even} \neq 0, \\ \frac{1}{2q}\sum_{k=1}^{q}\omega^{-kl}, & \text{if } l \text{ odd}. \end{cases} \tag{3.106}$$

Note that both (3.104) and (3.105) only contribute odd powers of τ (or the identity), hence the last two terms in (3.87) can only give odd powers of τ_j-

operators. The full expression becomes

$$M_j^{-1}\sigma_j^\dagger M_j\sigma_j k_{j+1} + k_j M_{j+1}^{-1}\sigma_{j+1}^\dagger M_{j+1}\sigma_{j+1} = \sum_{l,l'}\left[(-\omega)^l + (-\omega)^{l'}\right]\left[r^{-1} + (-1)^l r\right]\left[r^{-1} + (-1)^{l'} r\right]\theta^q(l)\theta^q(l')\tau_j^l\tau_{j+1}^{l'}. \tag{3.107}$$

Let us consider the different terms individually. First, the term with $l = l' = 0$ turns into an energy shift given by

$$\epsilon = \frac{(r + r^{-1})^2}{2}. \tag{3.108}$$

Second, the terms with $l = 0$ or $l' = 0$ turn into a magnetic-field term of the form $-\frac{f}{2}(\tau_j^l + \tau_{j+1}^l)$ for odd l, with the prefactor given by

$$f = -(r^{-2} - r^2)(1 - \omega^l)\theta^q(l) = \frac{r^2 - r^{-2}}{2q}\sum_{k=1}^{q}\left(\omega^{-kl} - \omega^{-(k-1)l}\right) = \frac{r^{-2} - r^2}{q}. \tag{3.109}$$

Finally, the remaining terms with $l, l' \neq 0'$ yield the terms $U_{ll'}\tau_j^l\tau_{j+1}^{l'}$ with

$$U_{ll'} = -\left(\omega^l + \omega^{l'}\right)\left(r - r^{-1}\right)^2\theta^q(l)\theta^q(l'). \tag{3.110}$$

Note that $\left[\omega^l\theta^q(l)\theta^q(l')\right]^* = \omega^{l'}\theta^q(l)\theta^q(l')$ and therefore $U_{ll'}^* = U_{ll'} = U_{l'l}$, such that the full local Hamiltonian becomes

$$\tilde{H}_{j,j+1} = -\left(\sigma_j\sigma_{j+1}^\dagger + \sigma_j^\dagger\sigma_{j+1}\right) - \frac{f}{2}\sum_{\substack{l=1\\ l\,\text{odd}}}^{p-1}\left(\tau_j^l + \tau_{j+1}^l\right) + \sum_{\substack{l,l'=1\\ l,l'\,\text{odd}}}^{p-1} U_{ll'}\tau_j^l\tau_{j+1}^{l'} + \epsilon. \tag{3.111}$$

We note that the Hamiltonian for even p is invariant under $r \to 1/r$ and $\tau \to -\tau$.

3.6.4 $\mathbb{Z}_4$-ANNNP model

The first new non-trivial example originating from the construction of the previous section is obtained for $p = 4$. In this case the local Hamiltonian

becomes remarkably simple

$$\tilde{H}_{j,j+1} = -\left[\sigma_j\sigma_{j+1}^\dagger + \frac{f}{2}(\tau_j + \tau_{j+1}) - U\tau_j\tau_{j+1} + \text{h.c.}\right] + \epsilon \tag{3.112}$$

with the parameters

$$f = \frac{r^{-2} - r^2}{2}, \quad U = \frac{(r - r^{-1})^2}{4}, \quad \epsilon = \frac{(r + r^{-1})^2}{2}. \tag{3.113}$$

Note the absence of terms like τ_j^2, $\tau_j\tau_{j+1}^2$ and $\tau_j\tau_{j+1}^\dagger$, in contrast to the frustration-free $\mathbb{Z}_3$-ANNNP model (3.91). The correlation functions of the four-fold degenerate ground states $|\tilde{\Psi}_i\rangle$ are identical to the ones in the ANNNI model, see Equation (3.25),

$$\left|\frac{\langle\tilde{\Psi}_i|\sigma_j\sigma_{j'}^\dagger|\tilde{\Psi}_i\rangle}{\langle\tilde{\Psi}_i|\tilde{\Psi}_i\rangle}\right| = \frac{4}{(r + r^{-1})^2}, \tag{3.114}$$

In Appendix 3.B.3 we prove that the model (3.112) possesses an energy gap $\tilde{\Delta}$ above the ground states. More specifically, we show that the lower bound for the gap in the thermodynamic limit is given by $\frac{4\min(r^2,r^{-2})}{r^2+r^{-2}} \leq \tilde{\Delta}$. For completeness in Figure 3.1 we compare this to numerical results for the energy gap. The latter were obtained by extrapolating finite-size data from system sizes $L = 64, 76, 88, 100$ to $L \to \infty$, with the finite-size results being calculated by employing the density matrix renormalisation group (DMRG) method [81, 118] using the TeNPy [189] library.

Closer inspection of the parameters (3.113) shows that they satisfy the relation $f = 2\sqrt{U(1+U)}$, which is identical to the relation along the Peschel–Emery line in the ANNNI model. This points towards a closer relation between the models (3.112) and (3.22), which we discuss in the following. In fact, even away from the frustration-free line one can map the $\mathbb{Z}_4$-ANNNP chain to two decoupled ANNNI chains. For simplicity we consider an infinitely long system (ie, we ignore the boundary conditions) and drop the constant energy shift ϵ; thus (3.112) turns into the Hamiltonian

$$H_{\text{ANNNP}} = -\sum_j \left(\sigma_j\sigma_{j+1}^\dagger + f\tau_j - U\tau_j\tau_{j+1} + \text{h.c.}\right). \tag{3.115}$$

Introducing the dual operators via

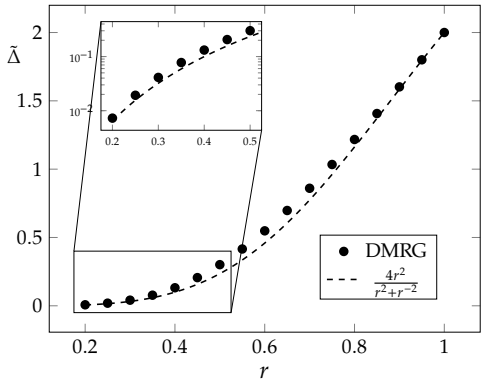

Figure 3.1: Energy gap $\tilde{\Delta}$ above the four-fold degenerate ground states $|\tilde{\Psi}_i\rangle$ of the frustration-free ANNNP model (3.112). The dots show the energy gap obtained by extrapolating the finite-size data for $L = 64, 76, 88, 100$ to the thermodynamic limit. The dashed line is the lower bound for the energy gap proven to exist in Appendix 3.B.3. Inset: Zoom in to small-r region, logarithmic scale.

$$\sigma_j^\dagger \sigma_{j+1} \to \tilde{\tau}_j, \quad \tau_j \to \tilde{\sigma}_{j-1}\tilde{\sigma}_j^\dagger, \tag{3.116}$$

which satisfy the clock algebra (3.60) with $p = 4$, we can rewrite this as

$$H_{\text{ANNNP}}^{\text{dual}} = -\sum_j \left(\tilde{\tau}_j + f\tilde{\sigma}_j\tilde{\sigma}_{j+1}^\dagger - U\tilde{\sigma}_j\tilde{\sigma}_{j+2}^\dagger + \text{h.c.}\right). \tag{3.117}$$

Next we introduce two sets of Pauli matrices $\sigma_{i,j}^{x/z}$, $i = 1, 2$, per lattice site j, and consider the mapping [188, 190, 191]

$$\tilde{\sigma}_j = e^{i\frac{\pi}{4}}\left(\frac{\sigma_{1,j}^x - i\sigma_{2,j}^x}{\sqrt{2}}\right), \quad \tilde{\tau}_j + \tilde{\tau}_j^\dagger = \sigma_{1,j}^z + \sigma_{2,j}^z. \tag{3.118}$$

From the second relation in (3.118) we can already infer that the $\tilde{\tau}_j$-terms are mapped to a transverse magnetic field on the Ising ladder. For the other terms, we use the following simple identity

$$\tilde{\sigma}_j\tilde{\sigma}_{j+j'}^\dagger + \text{h.c.} = \sigma_{1,j}^x\sigma_{1,j+j'}^x + \sigma_{2,j}^x\sigma_{2,j+j'}^x. \tag{3.119}$$

Thus the dual of the $\mathbb{Z}_4$-ANNNP model can be written as the sum of two

decoupled ANNNI chains

$$H^{\text{dual}}_{\text{ANNNP}} = H^{\text{dual}}_{\text{ANNNI},1} + H^{\text{dual}}_{\text{ANNNI},2} \tag{3.120}$$

with

$$H^{\text{dual}}_{\text{ANNNI},i} = -\sum_j \left(\sigma^z_{i,j} + f\sigma^x_{i,j}\sigma^x_{i,j+1} - U\sigma^x_{i,j}\sigma^x_{i,j+2}\right). \tag{3.121}$$

Performing another duality transformation (3.121) can be brought into the form (3.22) discussed in Section 3.3.2. The condition for the parameters f and U to be on the frustration-free line directly turns intro the Peschel–Emery line for the two ANNNI models.

3.6.5 $\mathbb{Z}_6$-ANNNP model

Interestingly, in the case $p = 6$ the deformation (3.103) leads to another rather simple model with the local Hamiltonian

$$\begin{aligned}\tilde{H}_{j,j+1} = -\Bigg[&\sigma_j\sigma^\dagger_{j+1} + \frac{f}{2}\left(\tau_j + \frac{1}{2}\tau^3_j + \tau_{j+1} + \frac{1}{2}\tau^3_{j+1}\right)\\ &-U\left(\tau_j\tau_{j+1} + \frac{1}{4}\tau_j\tau^3_{j+1} + \frac{1}{4}\tau^3_j\tau_{j+1} - \frac{1}{2}\tau_j\tau^\dagger_{j+1} + \frac{1}{8}\tau^3_j\tau^3_{j+1}\right) + \text{h.c.}\Bigg] + \epsilon,\end{aligned} \tag{3.122}$$

where the parameters are given by

$$f = \frac{r^{-2} - r^2}{3}, \quad U = \frac{2}{9}(r - r^{-1})^2, \quad \epsilon = \frac{(r + r^{-1})^2}{2}. \tag{3.123}$$

We note that even though the $\mathbb{Z}_6$-symmetry allows a wealth of terms of the form $\tau^l_j\tau^{l'}_{j+1}$, along the frustration-free line the relative prefactors of them are fixed to fairly simple values. In Figure 3.2 we show the energy gap above the six-fold degenerate ground state. The numerical results were obtained by extrapolation from finite-size data, they clearly indicate the existence of a finite energy gap along the frustration-free line. In addition, in Appendix 3.B.4 we prove that the model is gapped at least in the interval $0.5754 \lesssim r \lesssim 1/0.5754 \approx 1.7379$. We note in passing that using more advanced methods for open boundary conditions [174] it is possible to enlarge the region for which the existence of a finite energy gap can be proven. However, the obtained lower bounds are

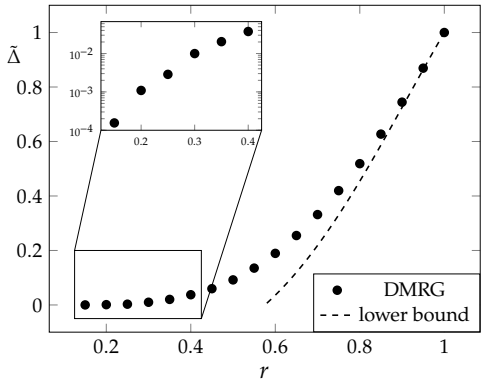

Figure 3.2: Energy gap $\tilde{\Delta}$ above the six-fold degenerate ground states of the frustration-free ANNNP model (3.122). The dots show the energy gap obtained by extrapolating the finite-size data for $L = 64, 76, 88, 100$ to the thermodynamic limit. The dashed line is the lower bound for the energy gap obtained in Appendix 3.B.4.

found to be quite small ($< 10^{-5}$).

3.7 Discussion

We have presented a constructive approach to understand and derive one-dimensional frustration-free spin models. Starting from a simple point, for example a classical system, we derived the corresponding frustration-free quantum models and their exact ground states. We have shown that many known frustration-free spin-1/2, spin-1 and $\mathbb{Z}_p$-clock models can be understood in this framework on an equal footing. Hence our approach provides an overarching framework for many frustration-free systems.

More specifically, the approach allowed us to connect two distinct frustration-free $\mathbb{Z}_3$-clock models recently introduced by Iemini et al. [120] and Mahyaeh and Ardonne [124]. As we have shown, both models can be interpreted as different deformations of the classical three-state Potts chain, see Figure 3.3 for an illustration of their relation. As a side remark, we analytically showed that the energy gap remains finite in a finite region around the classical point for both models. This in particular implies that both models (or their parafermion analogues) are in the same (topological) phase. Furthermore, we have constructed several new frustration-free $\mathbb{Z}_p$-clock models, including $\mathbb{Z}_4$- and $\mathbb{Z}_6$-generalisations of

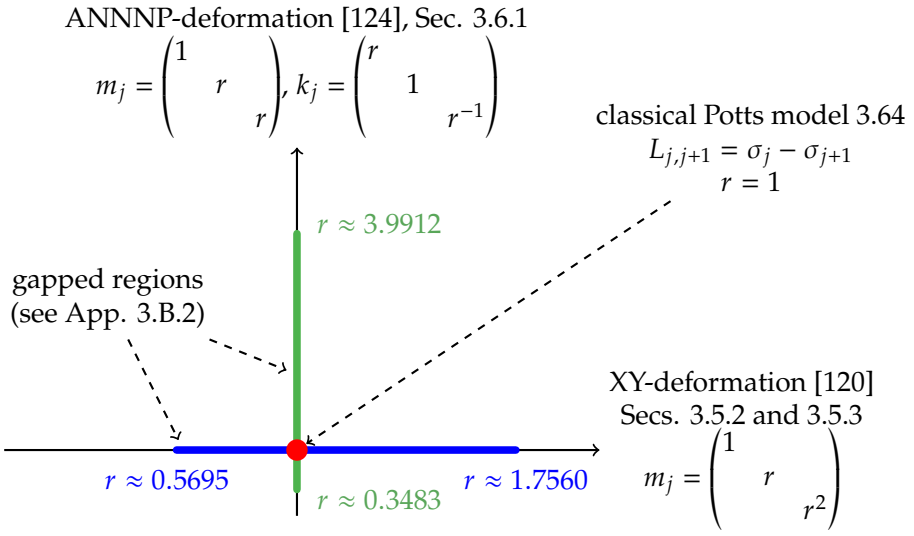

Figure 3.3: Schematic sketch of the relation between the two frustration-free $\mathbb{Z}_3$-clock models introduced by Iemini et al. [120] (see Sections 3.5.2 and 3.5.3) and Mahyaeh and Ardonne [124] (see Section 3.6.1). Both models can be obtained as deformations of the classical three-state Potts chain (red dot) using the local deformations m_j and central term k_j depending on the parameter r. The green lines indicate the regions in which the systems are proven to be gapped in Appendix 3.B.2. In particular, within this region the two models can be connected without closing the energy gap, implying that they are in the same phase.

the Peschel–Emery line of the original ANNNI chain.

We stress that the list of frustration-free clock models considered above is by no means extensive. On the contrary, the examples discussed here should be regarded as a proof of principle on how to apply the general construction. Several generalisations come to mind: First, one may consider chiral classical models [192, 193] as starting points in the deformation construction. However, since in this case the local Hamiltonians are no longer given by simple projectors, the deformed Hamiltonians so obtained may become quite complicated. Second, in this chapter we have kept the considered deformations to be homogeneous, a restriction that is not required by Theorem 1. Thus our results can be extended to inhomogeneous systems. Third, another generalisation would be to relax the requirement for the operator $C_{j,j+1}$ to be positive definite. In such a case, the ground states of the undeformed model are no longer trans-

formed into ground states of the new model. However, they will still be exact eigenstates, potentially in the middle of the spectrum, and thus may be relevant in the context of quantum many-body scars [194–199].

3.A Witten's conjugation argument

In this appendix we recall Witten's original conjugation argument on the ground-state degeneracy of supersymmetric Hamiltonians. Consider two supercharges Q and $Q^\dagger$ as well as a Hamiltonian H satisfying

$$Q^2 = (Q^\dagger)^2 = 0, \quad H = Q^\dagger Q + QQ^\dagger. \tag{3.124}$$

First we note that any zero-energy ground state $|\psi\rangle$ of H is annihilated by both Q and $Q^\dagger$. Furthermore, it is not possible to obtain $|\psi\rangle$ by action of Q, ie, $|\psi\rangle \neq Q|\phi\rangle$ for any state $|\phi\rangle$. (To see this assume $|\psi\rangle = Q|\phi\rangle$. But since $|\psi\rangle$ is a zero-energy ground state we have $0 = Q^\dagger|\psi\rangle = Q^\dagger Q|\phi\rangle$ which implies $\langle\phi|Q^\dagger Q|\phi\rangle = \|Q|\phi\rangle\|^2 = 0$ and thus $Q|\phi\rangle = 0$ in contradiction with the assumption that $|\psi\rangle$ is a ground state.)

Now let us consider the deformed/conjugated operators $\tilde{Q} = MQM^{-1}$, $\tilde{Q}^\dagger = (\tilde{Q})^\dagger$ and $\tilde{H} = \tilde{Q}^\dagger\tilde{Q} + \tilde{Q}\tilde{Q}^\dagger$ with M being invertible. Obviously, if $|\psi\rangle$ is a ground state of H, the deformed state $|\tilde{\psi}\rangle = M|\psi\rangle$ is annihilated by $\tilde{Q}$. Furthermore, $|\tilde{\psi}\rangle$ cannot be written as $|\tilde{\psi}\rangle = \tilde{Q}|\tilde{\phi}\rangle$ for any $|\tilde{\phi}\rangle$, since this would imply that $|\psi\rangle = QM^{-1}|\tilde{\phi}\rangle$ in contradiction with the assumption that $|\psi\rangle$ was a ground state of H. Thus $|\tilde{\psi}\rangle$ is a ground state of $\tilde{H}$ establishing a one-to-one correspondence between the ground-state manifolds of H and $\tilde{H}$.

3.B Energy gap of some $\mathbb{Z}_3$-, $\mathbb{Z}_4$- and $\mathbb{Z}_6$-models

The conjugation argument does only provide information about the ground-state manifold. In order to obtain information about the energy gap above it, additional techniques have to be employed. In Appendix 3.B.1 we recall Knabe's method [176], which was originally applied to the AKLT model with periodic boundary conditions. This is then applied in Appendices 3.B.2, 3.B.3 and 3.B.4 to prove the existence of an energy gap in specific $\mathbb{Z}_3$-, $\mathbb{Z}_4$-, and $\mathbb{Z}_6$-models.

3.B.1 Knabe's method

We consider a system with N sites, open boundary conditions and the Hamiltonian

$$H_N = \sum_{j=1}^{N-1} P_{j,j+1}, \tag{3.125}$$

with the $P_{j,j+1}$ two-site projection operators. We assume $\bigcap_j \ker(P_{j,j+1}) \neq \{0\}$, ie, the ground state is at zero energy, and denote the energy gap of H_N by Δ_N.

Theorem 2 (Knabe's method [176])**.** *For the projector Hamiltonian H_N the gap above the ground state (Δ_N) is bounded from below by*

$$\Delta_N \geq \frac{m-1}{m-2}\left(\min_{m'=2,\ldots,m}\{\Delta_{m'}\} - \frac{1}{m-1}\right), \tag{3.126}$$

where $\Delta_{m'}$ denotes the gap of the m'-site, sub-system Hamiltonian

$$h_{j,m'} = \sum_{k=j}^{j+m'-2} P_{k,k+1}. \tag{3.127}$$

Proof. Note that H_N is positive semi-definite, therefore $H_N^2 \geq \Delta_N H_N$. In other words, if we obtain the above inequality with Δ_N, the Theorem is proven. We have the analogous statement for $h_{j,m'}$, $h_{j,m'}^2 \geq \Delta_m h_{j,m'}$, and moreover realise that $P_{j,j+1}^2 = P_{j,j+1}$ and $[P_{j,j+1}, P_{k,k+1}] = 0$ for $|j-k| > 1$.

To prove the bound, we first expand H_N^2

$$H_N^2 = \sum_{j=1}^{N-1} h_{j,2}^2 + \sum_{m'=1}^{m-2}\sum_{j=1}^{N-m'-1}\left(h_{j,2}h_{j+m',2} + \text{h.c.}\right) + \sum_{|j-k|>m-2} h_{j,2}h_{k,2} \tag{3.128}$$

$$\geq H_N + \sum_{m'=1}^{m-2}\frac{m-m'-1}{m-2}\sum_{j=1}^{N-m'-1}\left(h_{j,2}h_{j+m',2} + \text{h.c.}\right), \tag{3.129}$$

with the second step following from the fact that $h_{j,2}h_{k,2}$ is positive semi-

definite for $|k-j|>1$. This can be further reduced to

$$H_N^2 \geq H_N + \frac{1}{m-2}\left[\sum_{j=1}^{N-m+1} h_{j,m}^2 + \sum_{m'=2}^{m-1}\left(h_{1,m'}^2 + h_{N-m'+1,m'}^2\right) - (m-1)H_N\right] \tag{3.130}$$

$$\geq \left(1-\frac{m-1}{m-2}\right)H_N + \frac{1}{m-2}\left[\Delta_m \sum_{j=1}^{N-m+1} h_{j,m} + \sum_{m'=2}^{m-1}\Delta_{m'}\left(h_{1,m'} + h_{N-m'+1,m'}\right)\right]. \tag{3.131}$$

Because we have the expansion

$$H_N = \frac{1}{m-1}\left[\sum_{j=1}^{N-m+1} h_{j,m} + \sum_{m'=2}^{m-1}\left(h_{1,m'} + h_{N-m'+1,m'}\right)\right] \tag{3.132}$$

and $\Delta_{m'} \leq 1$, the last term of (3.131) can be simplified to obtain

$$H_N^2 \geq -\frac{1}{m-2}H_N + \frac{m-1}{m-2}\min_{m'=2,\ldots,m}\{\Delta_{m'}\}H_N \tag{3.133}$$

$$= \frac{m-1}{m-2}\left(\min_{m'=2,\ldots,m}\{\Delta_{m'}\} - \frac{1}{m-1}\right)H_N. \tag{3.134}$$

This proves the Theorem with the lower bound
$\Delta_N \geq \frac{m-1}{m-2}\left(\min_{m'=2,\ldots,m}\{\Delta_{m'}\} - \frac{1}{m-1}\right)$. □

Remark 3. *Given that the models considered here can be viewed as parent Hamiltonians for matrix product ground states, one can apply more powerful tools [158, 172, 174] to prove the existence of energy gaps.*[f] *These methods allow one to extend the parameter regions with proven energy gaps. However, in some cases, Knabe's method gives us a better lower bound for an energy gap for fixed parameters. We also note that when analysing the energy gap, special care has to be taken regarding the treatment of different boundary conditions.*

[f] For example, for a so-called injective matrix product state one can prove that the corresponding parent Hamiltonian has a unique ground state and a finite energy gap [158, 159, 172]. However, most of the ground states we have looked at in this article do not qualify as injective (see, eg, Reference [96] for the ANNNI model), because of the degeneracy.

Note that the argument above assumes the Hamiltonian to be the sum of projectors. The systems studied in this chapter do not fit that picture. However, since they are frustration-free we can still obtain a bound using the following observation:

Corollary 4. *For a frustration-free model with an n-fold degenerate zero-energy ground state and a p-dimensional local Hilbert space, with $p^2 > n$, we can arrange the two-site eigenvalues $\tilde{\Delta}_2^k$ and normalised eigenstates $|\tilde{\psi}_k\rangle$ such that $\tilde{\Delta}_2^k \leq \tilde{\Delta}_2^l$ for $k < l$ and $\tilde{\Delta}_2^1, \ldots, \tilde{\Delta}_2^n = 0$. Then two-site Hamiltonian can be bounded from below as follows,*

$$\begin{aligned}\tilde{H}_{j,j+1} &= \sum_{k=n+1}^{p^2} \tilde{\Delta}_2^k |\tilde{\psi}_k\rangle \langle\tilde{\psi}_k| = \tilde{\Delta}_2^{n+1} \sum_{k=n+1}^{p^2} |\tilde{\psi}_k\rangle \langle\tilde{\psi}_k| + \sum_{k=n+1}^{p^2} \left(\tilde{\Delta}_2^k - \tilde{\Delta}_2^{n+1}\right) |\tilde{\psi}_k\rangle \langle\tilde{\psi}_k| \\ &\geq \tilde{\Delta}_2^{n+1} P_{j,j+1} = \tilde{\Delta}_2 P_{j,j+1}, \end{aligned} \tag{3.135}$$

with the gap $\tilde{\Delta}_2 = \tilde{\Delta}_2^{n+1}$ of the frustration-free Hamiltonian $\tilde{H}_{j,j+1}$ and $P_{j,j+1}$ denoting the projector onto the space orthogonal to its ground-state manifold. The min-max theorem [117] then implies for the gap $\tilde{\Delta}_N$ of the frustration-free model on N sites

$$\tilde{\Delta}_N \geq \tilde{\Delta}_2 \Delta_N. \tag{3.136}$$

Thus in order to prove that a frustration-free Hamiltonian possesses an energy gap $\tilde{\Delta}$ above its ground states in the thermodynamic limit, we proceed as follows: (i) We consider projectors $P_{j,j+1}$ onto the space orthogonal to the local ground states on the lattice sites j and $j+1$ and determine the gap Δ_2 above these ground states. (ii) From that we construct the auxiliary m-site Hamiltonian $h_{1,m} = \sum_{j=1}^{m} P_{j,j+1}$ and determine its energy gap Δ_m. (iii) If this gap satisfies $\min_{m'=2,\ldots,m} \{\Delta_{m'}\} > 1/(m-1)$, then the auxiliary N-site Hamiltonian H_N will have a gap Δ_N satisfying (3.126). (iv) Due to (3.136) the gap $\tilde{\Delta}$ of the original frustration-free Hamiltonian is bounded from below by

$$\tilde{\Delta} = \lim_{N\to\infty} \tilde{\Delta}_N \geq \lim_{N\to\infty} \tilde{\Delta}_2 \Delta_N \geq \tilde{\Delta}_2 \frac{m-1}{m-2} \left(\min_{m'=2,\ldots,m} \{\Delta_{m'}\} - \frac{1}{m-1} \right). \tag{3.137}$$

Every $m > 2$ gives a lower bound on the gap, so the supremum over subsystem sizes is also a lower bound. Usually, the bound increases for increasing m. Since the computation of Δ_m requires exact diagonalisation of a $p^m \times p^m$ matrix, the maximal feasible m is constrained by computational resources. In the following appendices we apply this line of argument to several models.

3.B.2 Gap in $\mathbb{Z}_3$-models

In order to treat both $\mathbb{Z}_3$-models (3.84) (for $\theta = 0$) and the models discussed in Section 3.6.1 within the same framework, we consider the general, diagonal deformation with

$$m_j = \begin{pmatrix} 1 & & \\ & r & \\ & & s \end{pmatrix}, \tag{3.138}$$

where $r, s > 0$. For each point in the (r, s)-plane we get a lower bound on the thermodynamic gap by means of (3.126), provided that for some feasible m the relevant energy gap of the auxiliary m-site Hamiltonian satisfies $\min_{m'=2,\dots,m} \{\Delta_{m'}\} > 1/(m-1)$. Computational resources allow us to go up to $m = 7$. In Figure 3.4 we have depicted the maximal lower bound for $m = 3, \dots, 7$ in the (r, s)-plane obtained from this. Note that this is a lower bound for the gap of the auxiliary projector Hamiltonian. For a particular parent Hamiltonian like (3.84) and (3.91), the true gap depends on the local gap $\tilde{\Delta}_2$. As long as the local parent Hamiltonian has the same degeneracy as the local auxiliary Hamiltonian it is gapped for the same parameter regime, by virtue of (3.137). We only consider the triangle $s \leq r \leq 1$, since due to the dihedral symmetry of the model there is a six-fold symmetry in the (r, s)-plane. The red line denotes the boundary of the region that is definitively gapped, ie, for all points above this line in the (r, s)-plane it is assured that the full system is gapped in the thermodynamic limit. The blue and green lines correspond to the ground states of (3.84) (for $\theta = 0$) and (3.91), respectively, with the black star indicating the model (3.91) at the special point $g_2 = 0$. Given the six-fold symmetry in the (r, s)-plane, we have to be careful how to display the green $(1, r, r)$ and blue $(1, r, r^2)$ lines. For the blue line, note that $(1, r, r^2) \simeq (r^{-2}, r^{-1}, 1)$, since the Hamiltonian is invariant under rescaling of M. Also the freedom in the form of the dihedral symmetry lets us write $(1, r, r^2) \simeq (1, r^{-1}, r^{-2})$, permuting the entries. Hence the blue line for $r > 1$, maps to the blue line for $r < 1$ under the symmetry. Using the same reasoning for the green line we obtain $(1, r, r) \simeq (r^{-1}, 1, 1) \simeq (1, 1, r^{-1})$, mapping $(1, r, r)$ for $r > 1$ to $(1, 1, s)$ for $s = r^{-1}$.

Let us zoom in on the two lines $s = r^2$ and $s = r$ that correspond to the ground states of (3.84) and (3.91) respectively. In Table 3.1 we list the lower and upper limit $r^{\text{low,up}}$ for the gapped region for different sub-system sizes m. For $s = r^2$ the upper limit is simply $r^{\text{up}} = 1/r^{\text{low}}$, as follows from the symmetry discussed above. As m increases we see that the region increases in both directions.

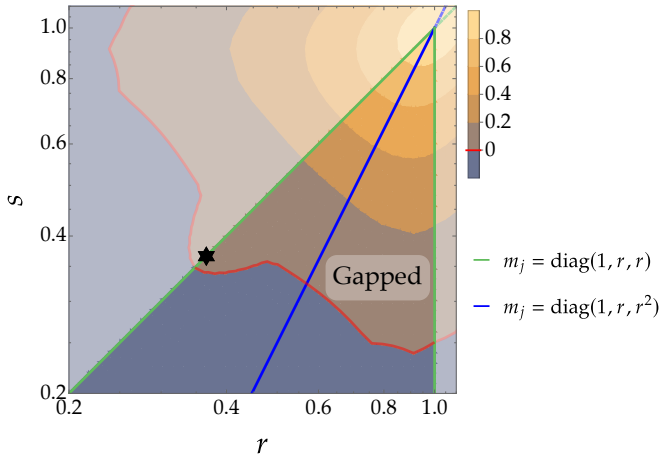

Figure 3.4: Log-log contour plot for the deformation in Equation (3.138) of the lower bound $\max_{m=3,\ldots,7} \frac{m-1}{m-2}\left(\min_{m'=2,\ldots,m}\{\Delta_{m'}\} - \frac{1}{m-1}\right)$. For a finite lower bound the system is gapped in the thermodynamic limit $N \to \infty$, ie, all points above the red line yield gapped systems. The blue and green lines correspond to the ground states of (3.84) (for $\theta = 0$) and (3.91), respectively. The star is the special point with $g_2 = 0$.

On the other hand, for $s = r$ something peculiar occurs. The lower limit r^{low} is significantly better for $m = 3$ than for $m = 4, \ldots, 7$. This lower limit has the exact value of $r^{\text{low}} = 2^{1/4} - 2^{-1/4} = \sqrt{\frac{3}{2}\sqrt{2} - 2} \approx 0.3483$ The upper limit, on the other hand, does become more informative as m increases.

In total we deduce that the full system (3.84) (for $\theta = 0$) is gapped in the thermodynamic limit for $0.5695 \lesssim r \lesssim 1/0.5695$ and (3.91) for $0.3483 \lesssim r \lesssim 3.9912$. In particular this implies that in this parameter regime the models can be adiabatically connected to the classical model obtained for $r = s = 1$ as sketched in Figure 3.3.

3.B.3 Gap in $\mathbb{Z}_4$-ANNNP model

We can apply the same method to analyse the gap of the $\mathbb{Z}_4$-ANNNP model (3.112). For this model it is sufficient to consider $m = 3$, since

$$\Delta_3 = \frac{1}{2} + \frac{\min(r^2, r^{-2})}{r^2 + r^{-2}}, \tag{3.139}$$

	$s = r^2$ ($\mathbb{Z}_3$-XY model)		$s = r$ ($\mathbb{Z}_3$-ANNNP model)	
m	r^{low}	r^{up}	r^{low}	r^{up}
3	0.6337	1.5779	**0.3483**	2
4	0.6204	1.6119	0.4216	2.6796
5	0.6026	1.6595	0.4259	3.0146
6	0.5853	1.7086	0.4200	3.6233
7	**0.5695**	**1.7560**	0.4116	**3.9912**

Table 3.1: Lower and upper limit $r^{\text{low,up}}$ for the gapped regions of the $\mathbb{Z}_3$-XY model (3.84) and $\mathbb{Z}_3$-ANNNP model (3.91) as deduced from different sub-system sizes m. The bold values indicate the extremal values which are stated in the main text.

which is strictly larger than $1/2$ for $0 < r < \infty$. Thus we deduce for the gap in the thermodynamic limit

$$\tilde{\Delta} \geq \frac{4 \min(r^2, r^{-2})}{r^2 + r^{-2}}. \tag{3.140}$$

Instead of using Corollary 4, the lower bound (3.140) can also be obtained from the mapping to two decoupled ANNNI chains, together with the lower bound for the energy gap along the Peschel–Emery line of the ANNNI chain obtained in Reference [49].

3.B.4 Gap in $\mathbb{Z}_6$-ANNNP model

For the $\mathbb{Z}_6$-ANNNP model (3.122) the condition of $\Delta_3 > 1/2$ shows that the model is gapped at least in the interval $0.5754 \lesssim r \lesssim 1/0.5754$, where we have used the invariance of the model under $r \to 1/r$. The region does not improve for $m = 4, 5$ and higher sub-systems sizes are not accessible with our current resources.

4 Phase diagram of tight-binding $\mathbb{Z}_3$-Fock parafermion chain

This chapter is based on: I. Mahyaeh, J. Wouters and D. Schuricht, *Phase diagram of the $\mathbb{Z}_3$-Fock parafermion chain with pair hopping*, SciPost Physics Core 3(2), 011 (2020). I.M. and J.W. together performed the calculations and numerical simulations, discussed the results and contributed to the final version of the manuscript.

We study a tight binding model of $\mathbb{Z}_3$-Fock parafermions with single-particle and pairhopping terms. The phase diagram has four different phases: a gapped phase, a gapless phase with central charge $c = 2$, and two gapless phases with central charge $c = 1$. We characterise each phase by analysing the energy gap, entanglement entropy and different correlation functions. The numerical simulations are complemented by analytical arguments.

4.1 Introduction

Usually, particles come in two flavours: bosons, satisfying commutation relations $\Psi(x_1, x_2) = \Psi(x_2, x_1)$ and fermions, with anti-commutation $\Psi(x_1, x_2) = -\Psi(x_2, x_1)$. In 2D a third class of (quasi-)particles can exist, known as anyons [57, 200], satisfying a fractional relation $\Psi(x_1, x_2) = e^{i\theta}\Psi(x_2, x_1)$ [58]. These non-trivial statistics stem from the 2D braid group, different from 3D (and higher), since intertwined exchange paths cannot be contracted to points in 2D [201].

Anyonic statistics arise for instance in fractional quantum Hall (FQH) systems, where the vortex excitations have and anyonic nature [202–204]. There are several proposals to capture the fractional modes on 1D interfaces of FQH systems [16, 56, 64]. The appearing 1D quasi modes are generally called parafermions. Historically these parafermions were introduced [60] to analyse clock models. Recently they have attracted attention for generalizing Majoranas. After Kitaev's seminal paper [11], the study of Majorana systems has

taken off. The edge modes in the Kitaev chain have become a prototypical example of 1D topological physics. The Majoranas in Kitaev's descriptions, decompose spinless fermions into real particles, sharing the fermionic statistics. Parafermions form the natural extension following fractional statistics [60, 61].

$$\gamma_j^p = \mathbf{1}, \qquad \gamma_j^\dagger = \gamma_j^{p-1}, \qquad \gamma_j\gamma_k = \omega^{\mathrm{sgn}(k-j)}\gamma_k\gamma_j, \tag{4.1}$$

where $\omega = \exp(2\pi\mathrm{i}/p)$, for general $p \geq 2$. Note that this simplifies Majorana algebra for $p = 2$, where in particular the reality condition $\gamma_j^\dagger = \gamma_j$ is satisfied.

With the Fradkin–Kadanoff transformation [60] these parafermions are related to clock variables

$$\gamma_{2j-1} = \left(\prod_{k<j}\tau_k\right)\sigma_j, \qquad \gamma_{2j} = \omega^{(p-1)/2}\gamma_{2j-1}\tau_j, \tag{4.2}$$

The clock operators generalize the Pauli matrices, with fractionality appearing in the algebra

$$\sigma_j^p = \tau_j^p = 1, \quad \sigma_j^\dagger = \sigma_j^{p-1}, \quad \tau_j^\dagger = \tau_j^{p-1}, \tag{4.3}$$

$$\sigma_j\tau_j = e^{2\pi\mathrm{i}/p}\tau_j\sigma_j, \quad \sigma_i\tau_j = \tau_j\sigma_i \quad \text{for } i \neq j. \tag{4.4}$$

The most notable clock system is the Potts model, generalizing the transverse field Ising chain

$$H_{\text{Potts}} = -J\sum_j\left(\sigma_j^\dagger\sigma_{j+1} + \sigma_{j+1}^\dagger\sigma_j\right) - f\sum_j\left(\tau_j^\dagger + \tau_j\right) \tag{4.5}$$

As the Majoranas helped to interpret the topological nature of the fermionic dual of the Ising model, so do parafermions offer a interpretation of the topology of the Potts model. Due to the fractionality, the edge modes are not as stable as in the Kitaev case, and often only appear as *weak* zero modes [61, 115, 188, 205]. However, the fractional nature of the parafermions gives rise to p-fold degeneracy in these topological systems.

While parafermions have proven useful in statistical mechanics and the study of edge zero modes, they possess a huge drawback. Due to the relations (4.1) it is not possible to interpret $\gamma_j^\dagger$ as a particle creation operator at site j. Very recently this limitation was overcome by Cobanera and Ortiz [185] who introduced the

so-called Fock parafermions (FPFs). Here the term “Fock" refers to the fact that the newly introduced operators $F_j^\dagger$ and F_j can be interpreted as creation and annihilation operators for particles, which act on a Fock space in the sense that a definite number of particles at lattice site j can be defined (see next section for the detailed definition). Hence FPFs constitute particles with anyonic and fractional exclusion statistics and thus provide the ideal framework to study the consequences of generalised quantum statistics on the properties of many-particle systems. In this work we will specifically investigate which types of many-particle states of FPFs exist in one-dimensional systems.

A first step in this direction has been taken very recently by Rossini et al. [206], who studied a tight-binding chain of FPFs simply hopping between neighbouring sites. For $p = 3$ (the case we will restrict ourselves) they uncovered a gapped phase reminiscent of a Mott insulator at unit filling, while at all other fillings a gapless anyonic Luttinger phase [207] emerged. In our work we will extend these results by generalising the simple hopping model to include also coherent hopping of two-particle pairs, which is possible as two FPFs may exist at the same lattice site. As a consequence of the pair hopping two additional phases appear in the phase diagram (see Figure 4.1): A second Luttinger phase (labelled R) and, between the two Luttinger phases, a gapless phase with central charge $c = 2$ (labelled M).

This chapter is organised as follows. In the next section we review the construction of FPFs. In Section 4.3 we define the model and present its phase diagram, the main result of this chapter. In Section 4.4 we explain the implementation of the numerical simulations, while in Section 4.5 we present our detailed results and analysis of the phase diagram. We conclude with a discussion in Section 4.6.

4.2 Fock parafermions

In this section we discuss Fock parafermions as introduced by Cobanera and Ortiz [185]. They appear as particle-like excitations constructed from parafermions in the same way as spinless fermions are obtained from Majorana fermions. To be more specific, let us start with the discussing the concept of parafermions [60, 61], which can be viewed as a fractional generalization of Majorana fermions.

Consider a set of $2L$ parafermion operators γ_j satisfying

$$\gamma_j\gamma_k = \omega^{\mathrm{sgn}(k-j)}\gamma_k\gamma_j, \qquad \omega = \exp\left(\frac{2\pi\mathrm{i}}{p}\right), \tag{4.6}$$

with integer $p \geq 2$. For $p = 2$ we obtain the simple anti-commutation relations of Majorana fermions, but for $p > 2$ the parafermions are neither commuting nor anti-commuting. The other relations fixing the algebra are

$$\gamma_j^{p-1} = \gamma_j^\dagger, \qquad \gamma_j^p = \mathbf{1}, \tag{4.7}$$

in which $\mathbf{1}$ is the identity operator. An explicit realisation is provided by (4.2).

As for Majoranas, for parafermions there is no notion of filling, ie, there are no highest and lowest weight states as we see from Equation (4.7). However, for Majorana fermions this can be remedied by introducing spinless Dirac fermions via

$$c_j = \frac{1}{2}(\gamma_{2j-1} + \mathrm{i}\gamma_{2j}), \qquad c_j^\dagger = \frac{1}{2}(\gamma_{2j-1} - \mathrm{i}\gamma_{2j}), \tag{4.8}$$

which then allow a direct interpretation as particle annihilation and creation operators.

In Reference [185] a similar particle description was introduced for parafermions. These so-called FPF operators are defined as

$$F_j = \frac{p-1}{p}\gamma_{2j-1} - \frac{1}{p}\sum_{m=1}^{p-1}\omega^{m(m+p)/2}\gamma_{2j-1}^{m+1}\gamma_{2j}^{\dagger m}. \tag{4.9}$$

They possess anyonic commutation relations on different sites,

$$F_jF_k = \omega^{\mathrm{sgn}(k-j)}F_kF_j, \qquad F_j^\dagger F_k = \omega^{-\mathrm{sgn}(k-j)}F_kF_j^\dagger, \qquad j \neq k, \tag{4.10}$$

which implies that their statistical angle is given by $\theta = 2\pi/p$, while on-site they satisfy

$$F_j^p = 0, \qquad F_j^{\dagger m}F_j^m + F_j^{p-m}F_j^{\dagger(p-m)} = \mathbf{1}, \quad m = 1, \ldots, p-1. \tag{4.11}$$

The Fock space can be constructed by acting with the creation operators on the vacuum state,

$$|n_1, n_2, \ldots, n_L\rangle = F_1^{\dagger n_1}F_2^{\dagger n_2}\ldots F_L^{\dagger n_L}|0\rangle. \tag{4.12}$$

Note that due to the first relation in (4.11) the highest possible filling on each site is $p-1$, thus generalising the usual Pauli principle. Furthermore, we can indeed define the number operator,

$$N_j = \sum_{m=1}^{p-1} F_j^{\dagger m} F_j^m, \tag{4.13}$$

which obeys the usual algebra with creation and annihilation operators,

$$\left[N_j, F_j^\dagger\right] = F_j^\dagger, \qquad \left[N_j, F_j\right] = -F_j, \tag{4.14}$$

and acts as follows on the Fock states as

$$N_j \left|n_1, n_2, \ldots, n_L\right\rangle = n_j \left|n_1, n_2, \ldots, n_L\right\rangle. \tag{4.15}$$

Finally we note that for $p = 4$ the FPF operators can be linked to spinful fermions via a non-linear relation [208]. However, in our work we will not use this since we focus exclusively on the case $p = 3$ in the following.

4.3 The model and its phase diagram

In this section we introduce the model and its symmetries and present its phase diagram, the main result of this chapter. We discuss the observables and correlation functions which will be used to analyse the different phases in Section 4.5.

Having introduced the operators creating and annihilating FPFs in the previous section, we are now in the position to define the model which we will study in this chapter. We restrict ourselves to the simplest non-trivial case of $p = 3$ and consider the one-dimensional Hamiltonian

$$H(g) = -t \sum_{j=1}^{L-1} \left[(1-g) F_j^\dagger F_{j+1} + g F_j^{\dagger 2} F_{j+1}^2 + \text{h.c.}\right]. \tag{4.16}$$

Throughout our work we set $t = 1$ and use it as the energy unit. The parameter g is restricted to the interval $0 \leq g \leq 1$, interpolating between the extreme cases of pure single-particle hopping and pure coherent pair hopping. The latter is allowed due to the possibility of having two FPFs at the same lattice

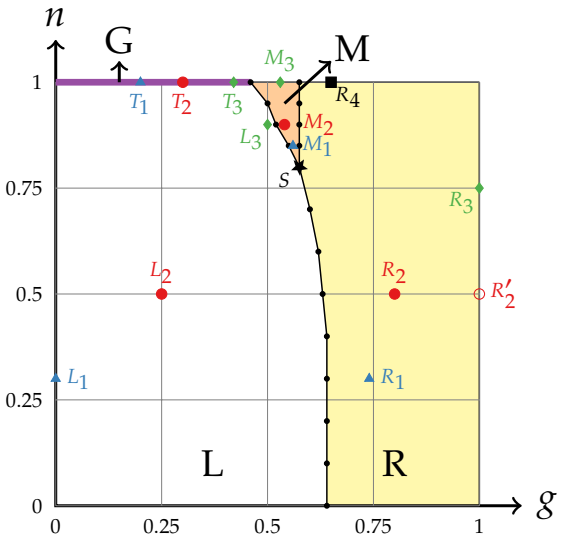

Figure 4.1: The phase diagram of the model (4.16). We identified four phases: the left (L) phase (white region), the right (R) phase (yellow), the middle (M) phase (orange) and the gapped (G) phase (thick violet line at unit filling $n = 1$). The properties of the phases are summarised in Table 4.1. The detailed analyses at the coloured points ($L_{1,2,3}$ etc.) are presented in Section 4.5. The black star, $S \simeq (0.58, 0.80)$, indicates the point where the three phases, L, R and M, meet. The phase transitions have been determined at the black dots; for fixed n the estimated uncertainty is of the order of $\Delta g = 0.01$. The transition between the L and R phase seems to be second order.

site. We consider a one-dimensional chain of L lattice sites with free boundary conditions.

We note that the three-state quantum Potts chain (4.5) can in principle also be written in terms of FPFs. However, the resulting expression is much more complicated that the hopping Hamiltonian (4.16), containing for example terms that break the particle-number conservation.

The model (4.16) with $g = 0$, ie, the case of pure single-particle hopping, was studied by Rossini et al. [206]. They showed that there exists a Mott-like phase at unit filling, ie, if there are L FPFs in total, while at all other filling fractions the model is gapless and can be described by an anyonic Luttinger liquid [207]. The aim of our work is to extend the analysis to $g \neq 0$ and study the effect of the additional pair hopping on the phase diagram.

phase	energy gap	c	$G_1(r)$	$G_2(r)$
L	gapless	1	$\sim r^{-2/3}$	$\sim r^{-\alpha_2(g,n)}$
R	gapless	1	0	$\sim r^{-13/18}$
M	gapless	2	$\sim r^{-\alpha_1'(g,n)}$	$\sim r^{-\alpha_2'(g,n)}$
G	gapped	-	$\sim \exp\left[-r/\xi_1(g)\right]$	$\sim \exp\left[-r/\xi_2(g)\right]$

Table 4.1: Summary of the properties of the four phases in Figure 4.1. The central charge c is obtained from the fit of the EE to the CC formula (4.17). In the L and R phase we obtain the value $c = 1$ up to about 1%. In the M phase the deviation from $c = 2$ is slightly larger, as indicated in the inset of Figure 4.7a.

Coming back to the Hamiltonian (4.16), we observe a U(1) symmetry which results in the conservation of the total number of particles, $N = \sum_{j=1}^{L} N_j$, as can be checked using Equation (4.14). Moreover the model is invariant under the particle-hole transformation $F_j \to F_j^\dagger$. The proof is presented in Appendix 4.A. This implies that, although the Hilbert space can have states with at most $N = 2L$ particles, it is sufficient to restrict the study to those with $N \leq L$. Since we are interested in the thermodynamic limit, the relevant quantity would rather be the density or the filling defined by $n = N/L$. Therefore we will present the results for $0 < n \leq 1$.

Our main result is the phase diagram of the model (4.16) which is presented in Figure 4.1. The phase diagram consists of four phases: the left phase (white region in Figure 4.1, which will be indicated by L throughout the paper), the right phase (yellow region, indicated by R), the middle phase (orange region, indicated by M) and the gapped phase (the thick violet line at $n = 1$, indicated by G). To characterise and distinguish different phases we look into different properties and observables: the energy gap, the entanglement entropy and two-point correlation functions. The results of this characterisation are summarised in Table 4.1: we find two gapless phases (L and R) that allow a Luttinger liquid description ($c = 1$) which are distinguished by the different power-law behaviour of the correlation functions, another gapless phase (M) with central charge $c = 2$, and a gapped phase (G) which can be regarded as the extension of the anyonic Mott-like phase to $g \neq 0$. A detailed discussion of the four phases is given in Section 4.5.

Studying the energy difference between the ground state and the first excited state, $\delta(L) = E_1(L) - E_0(L)$, as a function of system size, L, is a classical way of determining whether the model is gapped. For a gapped system this difference will converge to a finite value while for a gapless system it converges to zero as L^{-z}, where z is the dynamical critical exponent. For a gapless system in one dimension which can be described by a conformal field theory (CFT) the dynamical critical exponent is $z = 1$ [76, 78]. The scaling behaviour of entanglement entropy (EE), $S(l)$, as a function of subsystem size, l, is another probe to separate different phases from each other. For a gapped phase the EE saturates to a constant value. For a gapless system, however, the EE grows with the subsystem size. For an open chain at criticality with an underlying CFT, one can read off the central charge, c, using the Calabrese-Cardy (CC) formula [209, 210],

$$S(l) = \frac{c}{6} \log \left[\frac{L}{\pi} \sin \left(\frac{\pi l}{L} \right) \right] + S_0, \tag{4.17}$$

in which S_0 is a non-universal constant. Finally, correlation functions play an essential role in our understanding of the phases. In a gapped phase a typical two-point correlation function decays exponentially as a function of distance with a correlation length of the order of the inverse gap. For a gapless system, however, the two-point correlation functions show power-law behaviour. Hence, following Reference [206], we will also study the two-point correlation functions of FPF operators

$$G_1(r) = \left| \left\langle F^\dagger_{\frac{L}{2}-\frac{r}{2}} F_{\frac{L}{2}+\frac{r}{2}} \right\rangle \right|, \qquad G_2(r) = \left| \left\langle (F^\dagger)^2_{\frac{L}{2}-\frac{r}{2}} F^2_{\frac{L}{2}+\frac{r}{2}} \right\rangle \right|. \tag{4.18}$$

We measure the correlations between two lattice sites of distance r which are symmetrically distributed around the middle of the chain. This is to minimise the finite-size effects from the edges.

The analysis of the phases using the tools discussed above we will be presented in Section 4.5. In addition, in some cases it is also possible to employ analytical methods like bosonisation [211, 212], which for example allows us to obtain an effective Luttinger liquid description in the L and R phases. Before presenting the detailed results for the phase diagram we will briefly discuss the implementation of our numerical simulations in the next section.

4.4 The implementation for numerical studies

To study the model numerically we performed density matrix renormalisation group (DMRG) simulations [81, 118] using the ALPS [213–215] and TeNPy [189] libraries and checked that the obtained results are the same. To implement the model for performing DMRG and bosonisation we use the Fradkin–Kadanoff transformation [60],

$$F_j = \left(\prod_{k=1}^{j-1} U_k\right) B_j, \tag{4.19}$$

where

$$U_k = \mathbf{1} \otimes \cdots \otimes \underbrace{U}_{k} \otimes \cdots \otimes \mathbf{1}, \qquad U = \begin{pmatrix} 1 & 0 & 0 \\ 0 & \omega & 0 \\ 0 & 0 & \omega^2 \end{pmatrix}, \tag{4.20}$$

$$B_j = \mathbf{1} \otimes \cdots \otimes \underbrace{B}_{j} \otimes \cdots \otimes \mathbf{1}, \qquad B = \begin{pmatrix} 0 & 1 & 0 \\ 0 & 0 & 1 \\ 0 & 0 & 0 \end{pmatrix}. \tag{4.21}$$

The matrix representations of the local operators U and B are given in the local basis where the clock operator τ is diagonal, ie, $U = \tau$. The operators acting on different sites commute while the on-site algebra is given by

$$B_j U_j = \omega U_j B_j. \tag{4.22}$$

Applying this transformation together with the resulting relation $B_j^{\dagger 2} U_j^2 = B_j^{\dagger 2}$, the Hamiltonian (4.16) becomes

$$H(g) = -t \sum_{j=1}^{L-1} \left[(1-g) B_j^\dagger U_j B_{j+1} + g B_j^{\dagger 2} B_{j+1}^2 + \text{h.c.} \right], \tag{4.23}$$

which is local and consists of bosonic degrees of freedom only. Hence it can be easily implemented for the DMRG calculation.

The DMRG simulations for the entanglement entropy and the correlation functions were performed for a chain of size $L = 240$, our default system size. To find the central charge of the gapless phases using the CC formula or its modified variation, as it will be later introduced, we dropped the first and the last ten sites to stay away form finite-size effects due to the edges. The data

for the correlation functions will be presented for $r \in [10 - L/2]$ and the same interval will be used for the fittings. For the finite-size scaling of the energy gap we use a range of system sizes, usually between $L = 64$ and $L = 240$. The DMRG was performed with the bond dimension $\chi = 500$ in the L, R and G phases, and $\chi = 800 - 1000$ in the M phase. The number of sweeps which is needed for the convergence varies and depends on the parameters. The typical number of sweeps in the L, R and G phases is between 20 and 50. In the M phase, however, 40 to 60 sweeps were done. Each sweep consists of minimisation from the first site to the very last one and then from the last site back to the first one.

4.5 The results

In this section we present the detailed results of our numerical and analytical study of the phase diagram. The specific values of the parameters at which we present numerical data are indicated by coloured points in Figure 4.1. We will use the same colour to present the EE and correlation functions G_1 and G_2 for each one of these points.

4.5.1 The L phase

Rossini et al. [206] studied the model (4.16) for the special case of $g = 0$ and various filling fractions n. They found that the model is gapless for any filling $n < 1$ and well described by an anyonic Luttinger liquid [207] with Luttinger parameter $K = p/2$ such that the correlation functions decay as power laws $G_1(r) \sim r^{-\alpha_1}$ with $\alpha_1 = 2/p$ and $G_2(r) \sim r^{-\alpha_2}$ with $\alpha_2 = 4\alpha_1$. Although the numerical results of Reference [206] match very well with the theoretical predictions derived by Calabrese and Mintchev [207] for G_1, there are discrepancies between the theory and the numerics for G_2. Our numerical and analytical results show that the properties of the model at $g = 0$ extend to a finite region with $g > 0$.

The results of the numerical calculations in the L phase are shown at the points $L_1 = (g, n) = (0, 0.3)$, $L_2 = (0.25, 0.5)$ and $L_3 = (0.5, 0.9)$. These points were selected to show the typical behaviour. The L phase, which is depicted as a white region in Figure 4.1, is found to be gapless with the central charge $c = 1$, as is confirmed by the fit of the EE shown in Figure 4.2a to the CC formula. In Figure 4.2b we show the energy difference $\delta(L) = E_1(L) - E_0(L)$ at the point L_2 and system sizes $L \in [64 - 176]$. We used a power-law function for

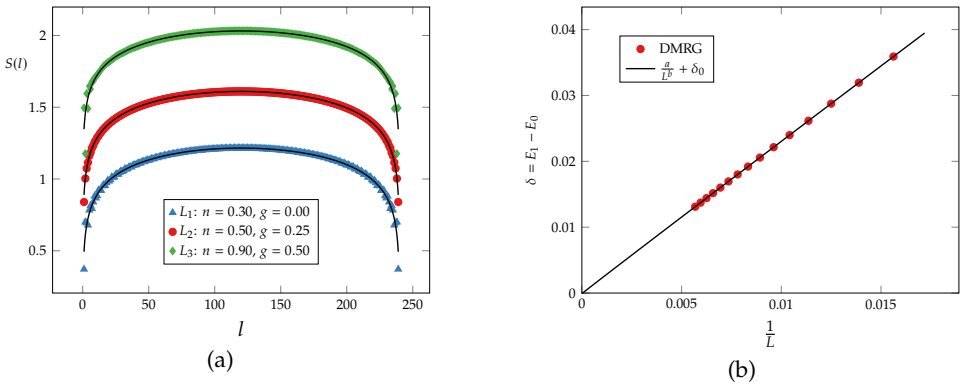

Figure 4.2: EE and gap for the points L_1, L_2 and L_3 in the L phase. (a) EE as a function of subsystem size l for a chain of size $L = 240$. The solid lines are the CC formula with $c = 1$. We have shifted the red points by 0.2 and the green points by 0.4 for visibility. (b) The energy difference between the first excited state and the ground state at the point L_2 as a function of $1/L$ for $L \in [64 - 176]$. The fitting parameters for the solid line are $b \approx 0.99$ and $\delta_0 \simeq 10^{-4}$, thus indicating a gapless phase.

the fitting, $\delta(L) = a/L^b + \delta_0$, which gave us $b \approx 0.99$ and $\delta_0 \simeq 10^{-4}$. Therefore we can conclude that the dynamical critical exponent is given by $z = 1$, which confirms that the low-energy physics can be described by a CFT.

In Figure 4.3 we present the two-point correlation functions $G_1(r)$ and $G_2(r)$ for the same three points in the L phase. The correlation function $G_1(r)$ shows a power-law behaviour, $G_1(r) \sim r^{-\alpha_1}$ with $\alpha_1 \approx 2/3$, as it was the case for $g = 0$. In addition we observe weak oscillations with a wave number q_1 that takes the values $q_1 \approx 0.95$ at L_1 and $q_1 \approx 1.57$ at L_2, while at L_3 we were not able to determine q_1 with sufficient accuracy. The origin of these oscillations seems to involve doubly-occupied sites, as is indicated by comparison to the bosonisation treatment (see below). The result on the correlation function G_2 shows a power-law decay too, $G_2(r) \sim r^{-\alpha_2}$, but the exponent α_2 depends on both the pairwise hopping, g, and the filling fraction, n, as it is indicated in the inset.

In the following we provide an argument for our finding of $G_1(r) \sim r^{-2/3}$ based on a bosonisation [211, 212] treatment. Or starting point is the observation that the probability to have two particles at the same site is strongly suppressed throughout the L phase. For example, at the point L_2 the prob-

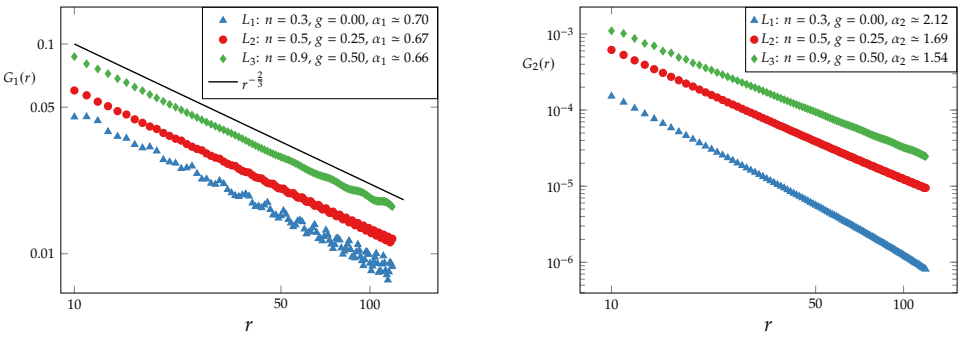

(a) (b)

Figure 4.3: Correlation functions at the three points L_1, L_2 and L_3 in the L phase. (a) $G_1(r)$ as function of r. To avoid mixing the data points, we multiplied $G_1(r)$ for the point L_3 by 1.5. For comparison $r^{-2/3}$ as derived in (4.35) is also plotted. (b) $G_2(r)$ as function of r. We fitted a power law with exponent α_2, the obtained values are given in the legend. We note that both correlation functions show a power-law decay, and that $G_2(r) \ll G_1(r)$ at small r consistent with the strongly suppressed probability to find two particles at the same site.

ability of having an empty site, a site with one particle and a site with two particles are $P(0) \simeq 0.54$, $P(1) \simeq 0.42$ and $P(2) \simeq 0.04$, respectively. Therefore one can argue that it is reasonable to project the model to the local Hilbert space with at most one particle at a given site, and thus drop the second term in the Hamiltonian. Using this projection, we can identify the operator B_j in the subspace spanned by $|0\rangle$ and $|1\rangle$ with the raising spin-1/2 operator σ_j^+,

$$B_j \to \sigma_j^+ = \begin{pmatrix} 0 & 1 \\ 0 & 0 \end{pmatrix}, \tag{4.24}$$

and simplify $G_1(r)$ to

$$G_1(r) = \left|\left\langle F_0^\dagger F_r \right\rangle\right| = \left|\left\langle B_0^\dagger U_0 U_1 \cdots U_{r-1} B_r \right\rangle\right| \sim \left|\left\langle \sigma_0^- U_0^{(p)} U_1^{(p)} \cdots U_{r-1}^{(p)} \sigma_r^+ \right\rangle\right|, \tag{4.25}$$

in which

$$U_k^{(p)} = \mathbf{1} \otimes \cdots \otimes \underbrace{U^{(p)}}_{k} \otimes \cdots \otimes \mathbf{1}, \qquad U^{(p)} = \begin{pmatrix} 1 & 0 \\ 0 & \omega \end{pmatrix}. \tag{4.26}$$

Due to the projection we are left with two states per site. We can use a Jordan–Wigner (JW) transformation and relate the spin-1/2 operators to a set of spinless fermions, ψ_j,

$$\sigma_j^z = 2n_j - 1, \qquad \sigma_j^+ = e^{\mathrm{i}\pi \sum_{k<j} n_k} \psi_j^\dagger, \qquad n_j = \psi_j^\dagger \psi_j, \tag{4.27}$$

where the ψ_j satisfy $\{\psi_i, \psi_j\} = 0$ and $\{\psi_i, \psi_j^\dagger\} = \delta_{ij}$. Applying the JW transformation to $G_1(r)$ and rewriting the matrix $U^{(p)}$ we obtain

$$G_1(r) \sim \left| \left\langle \sigma_0^- U_0^{(p)} U_1^{(p)} \cdots U_{r-1}^{(p)} \sigma_r^+ \right\rangle \right| = \left| \left\langle \sigma_0^- \left[\prod_{k=0}^{r-1} e^{\mathrm{i}\frac{2\pi}{3}(1-n_k)} \right] \sigma_r^+ \right\rangle \right| \tag{4.28}$$

$$= e^{\mathrm{i}\frac{2\pi}{3} r} \left| \left\langle \psi_0 \, e^{-\mathrm{i}\frac{2\pi}{3} \sum_{k=0}^{r-1} n_k} e^{\mathrm{i}\pi \sum_{l=0}^{r-1} n_l} \, \psi_r^\dagger \right\rangle \right| = \omega^r \left| \left\langle \psi_0 \, e^{\mathrm{i}\frac{\pi}{3} \sum_{k=0}^{r-1} n_k} \, \psi_r^\dagger \right\rangle \right|. \tag{4.29}$$

Assuming that the fermions have a Fermi surface, we can linearise around the two resulting Fermi points $k = \pm k_\mathrm{F}$,

$$\psi_j = \sqrt{a} \left[e^{\mathrm{i}k_\mathrm{F} x} \psi_+(x) + e^{-\mathrm{i}k_\mathrm{F} x} \psi_-(x) \right], \tag{4.30}$$

where a denotes the lattice constant and $x = ja$ the spatial coordinate that will be treated as a continuous variable. In addition we use the bosonisation dictionary [211, 212],

$$\psi_\pm(x) = \frac{1}{\sqrt{2\pi\alpha}} e^{\mathrm{i}\sqrt{\pi}\left[\pm\phi(x) - \theta(x)\right]}, \tag{4.31}$$

in which α^{-1} is the momentum cut-off, and $\phi(x)$ and $\theta(x)$ are dual fields that satisfy the commutation relation $\left[\phi(x), \theta(y)\right] = \mathrm{i}\Theta(y - x)$, with $\Theta(x)$ being the Heaviside step function. To continue we recall that for bosonisation normal ordering is necessary. Hence for the density operator we use $n_k =: n_k : + \bar{n}$, in which $\bar{n}$ is the average density on each site in the ground state and $: n_k := \partial_x \phi / \sqrt{\pi}$. Furthermore, assuming that the interactions are incorporated via a Luttinger parameter K we rescale the bosonic fields as $\phi(x) \to \sqrt{K}\phi(x)$,

$\theta(x) \to \theta(x)/\sqrt{K}$ to bring the correlation function into the standard form

$$G_1(r) \sim \left| \left\langle \left[e^{\mathrm{i}\sqrt{\pi}\left[\sqrt{K}\phi(0) - \frac{\theta(0)}{\sqrt{K}}\right]} + e^{-\mathrm{i}\sqrt{\pi}\left[\sqrt{K}\phi(0) + \frac{\theta(0)}{\sqrt{K}}\right]} \right] e^{\mathrm{i}\frac{\sqrt{\pi K}}{3}\left[\phi(r) - \phi(0)\right]} \right.$$
$$\left. \times \left[e^{-\mathrm{i}\sqrt{\pi}\left[\sqrt{K}\phi(r) - \frac{\theta(r)}{\sqrt{K}}\right]} e^{-\mathrm{i}k_{\mathrm{F}}r} + e^{\mathrm{i}\sqrt{\pi}\left[\sqrt{K}\phi(r) + \frac{\theta(r)}{\sqrt{K}}\right]} e^{\mathrm{i}k_{\mathrm{F}}r} \right] \right\rangle \Bigg|. \tag{4.32}$$

Using the Wick theorem, the neutrality condition for vertex operators, and

$$\left\langle e^{\mathrm{i}\beta\left[\phi(r) - \phi(0)\right]} \right\rangle = \left\langle e^{\mathrm{i}\beta\left[\theta(r) - \theta(0)\right]} \right\rangle = \left(\frac{\alpha^2}{\alpha^2 + r^2} \right)^{\frac{\beta^2}{4\pi}} \tag{4.33}$$

we get

$$G_1(r) \sim A_1 \left(\frac{1}{r} \right)^{\frac{1}{2K} + \frac{2}{9}K} \left[1 + \cos\left(2k_{\mathrm{F}}r\right) \left(\frac{\alpha}{r} \right)^{\frac{2}{3}K} \right], \tag{4.34}$$

where we have limited ourselves to the two leading terms at large separations, and A_1 is a non-universal constant. For $K > 0$ the first term in $G_1(r)$ decays slower than the second one and thus is dominant at large separations. Hence we conclude that at large r

$$G_1(r) \sim r^{-\frac{1}{2K} - \frac{2}{9}K} \sim r^{-\frac{2}{3}}, \tag{4.35}$$

where in the last step we have used that for the free anyon gas [206, 207] the Luttinger parameter K is related to the statistical parameter $\kappa = \theta/\pi$ via $K = 1/\kappa = 3/2$. We stress that we have derived the result (4.35) from the microscopic model (4.16), thereby linking it to the phenomenological theory applied by Calabrese and Mintchev [207]. In particular, our line of argument shows why the anyonic Luttinger model indeed provides a good description of the L phase. We note, however, that the oscillations in $G_1(r)$ observed in Figure 4.3a are not adequately described by the second term in (4.34). Thus they are not captured by the line of argument presented above, which hints at the importance of doubly-occupied sites. Moreover, the behaviour $G_2(r) \sim r^{-\alpha_2}$ cannot be described by the bosonisation approach, as obviously doubly occupancy will be relevant for this correlation function. We do not have a clear understanding yet how the oscillations in $G_1(r)$ or the power-law scaling of $G_2(r)$, in particular the exponent α_2, relate to the filling n and the parameter g.

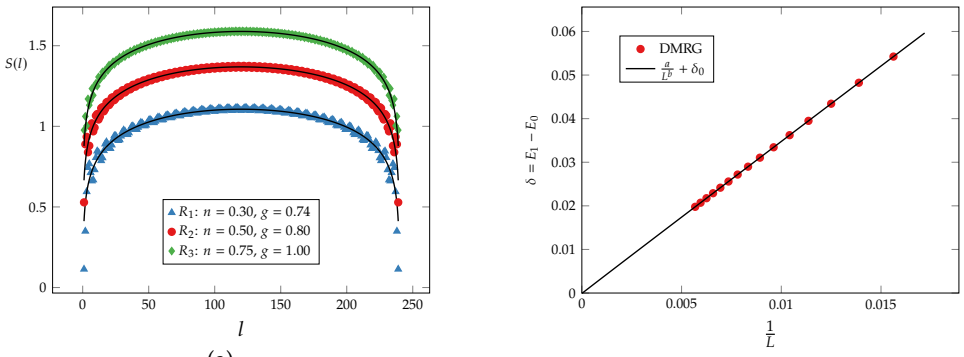

(a) (b)

Figure 4.4: EE and energy gap for three points R_1, R_2 and R_3 in the R phase. (a) EE as a function of subsystem size l. The solid lines are the CC formula with $c = 1$. We have shifted the red points by 0.2 and the green points by 0.4 for visibility. (b) Energy gap above the ground state at the point R_2. The fitting parameters for the solid line are $b \approx 0.99$ and $\delta_0 \simeq 10^{-4}$, again indicating a gapless phase.

4.5.2 The R phase

The parameter g controls the relative strength of single-particle and pair-hopping amplitudes. By increasing g for the filling $n \lesssim 0.8$ the system directly enters the R phase (yellow region in Figure 4.1) from the L phase. For larger filling, $0.8 \lesssim n < 1$, there exists a phase with the central charge $c \approx 2$ between the L phase and the R phase. This M phase will be discussed in Section 4.5.3. The point where the three phases L, R and M meet is located at $S \simeq (0.58, 0.80)$ and marked with a black star in the phase diagram.

In this section we present details on the R phase. Numerical results are shown for the selected points $R_1 = (0.74, 0.3)$, $R_2 = (0.8, 0.5)$ and $R_3 = (1, 0.75)$. The EE and energy gap at these three points are given in Figure 4.4. We conclude that also the R phase is gapless with central charge $c = 1$. More precisely, the energy gap scales as $\delta(L) = a/L^b + \delta_0$ with $b \approx 0.99$ and $\delta_0 = 10^{-4}$, thus the dynamical critical exponent is given by $z = 1$.

The difference between the L and R phase shows up only when considering the correlation functions. In the R phase the correlation function $G_1(r)$ decays exponentially as a function of distance r, $G_1(r) \sim \exp(-r/\xi_1)$, with a correlation length, ξ_1, of the order of a few lattice constants. Away from the phase transition one even finds $\xi_1 \sim a$, ie, the correlation function essentially vanishes. This

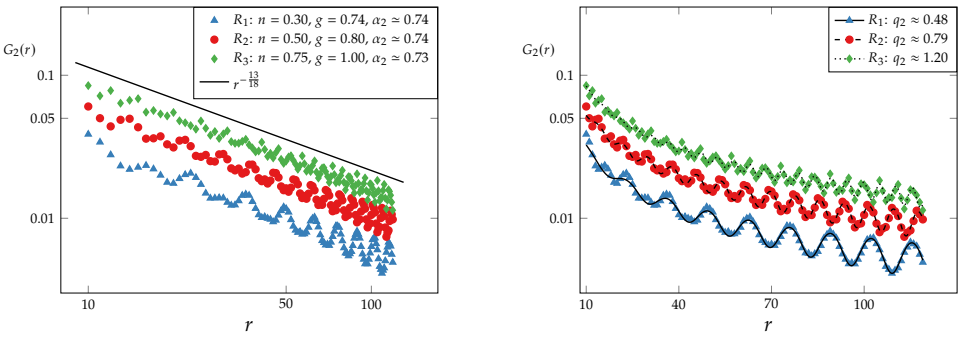

Figure 4.5: The correlation function $G_2(r)$ is plotted as function of r for the three points R_1, R_2 and R_3 in the R phase. To avoid mixing the data points, we multiplied $G_2(r)$ by 1.5 and 2 for the red and green data points, respectively. (a) For comparison we plot the prediction (4.40) as solid line. (b) We fitted the data with sub-leading oscillations decaying as a power law, ie, $G_2(r) = A_2 r^{-\frac{13}{18}} + A_2' r^{-\beta_2} \cos(q_2 r + \phi_2)$. The resulting wave numbers q_2 are given in the legend. For the point R_3 the wave length $2\pi/q_2 \approx 5$ becomes rather short, increasing the uncertainty in the fit. The accuracy of the fit for the exponent β_2 was not sufficient to obtain reliable results.

finding can be understood by noting that deep in the R phase the probability of having one particle on a site is generally much smaller than having two particles or an empty site. For instance, at the point R_2 the probability of having an empty site, a site with one particle and a site with two particles are $P(0) \simeq 0.24$, $P(1) \simeq 0.01$ and $P(2) \simeq 0.75$, respectively. In the special case of $g = 1$ we even find $P(1) = 0$ in the ground state. This can be understood from the Hamiltonian $H(1)$, in which only the operators F_j^2 or $F_j^{\dagger 2}$ appear, which both annihilate the one-particle state. So the on-site one-particle sector decouples and does not play a crucial role on the low-energy physics.

We can use this information from the numerics and assume that in the R phase the low-energy physics can be captured by the second term in the Hamiltonian only, ie, we approximate

$$H_{\mathrm{R}}^{(p)}(g) = -t\,g \sum_{j=1}^{L-1} F_j^{\dagger 2} F_{j+1}^2 + \text{h.c.} = -t\,g \sum_{j=1}^{L-1} B_j^{\dagger 2} B_{j+1}^2 + \text{h.c.}. \tag{4.36}$$

Following our line of argument used above for the L phase we project the Hamiltonian onto the space with empty or doubly occupied on-site subspaces $|0\rangle$ and $|2\rangle$, respectively. Hence we can identify the operator B_j^2 with the raising spin-1/2 operator σ_j^+ in this subspace,

$$B_j^2 \to \sigma_j^+ = \begin{pmatrix} 0 & 1 \\ 0 & 0 \end{pmatrix}, \tag{4.37}$$

which gives rise to the XX-Hamiltonian,

$$H_{\mathrm{R}}^{(p)}(g) = -tg \sum_{j=1}^{L-1} \sigma_j^- \sigma_{j+1}^+ + \text{h.c.}. \tag{4.38}$$

This projected Hamiltonian is quite fruitful. First of all we note that it is well-known that the XX-model is gapless and can be described with the bosonic CFT with the central charge $c = 1$[76, 78]. Moreover, we can calculate $G_2(r)$ in the same way that we calculated $G_1(r)$ in the L phase,

$$G_2(r) = \left| \left\langle F_0^{\dagger 2} F_r^2 \right\rangle \right| = \left| \left\langle B_0^{\dagger 2} U_0^2 U_1^2 \cdots U_{r-1}^2 B_r^2 \right\rangle \right|. \tag{4.39}$$

Using the definition of the matrix U, we see that the projection of U^2 onto the subspace spanned by $|0\rangle$ and $|2\rangle$ has the same form as the matrix $U^{(p)}$ in Equation (4.26). Therefore the calculation we presented for the correlation function $G_1(r)$ in Section 4.5.1 can be directly applied to the correlation function $G_2(r)$ in the R phase. Furthermore, since the XX-model is a free theory it seems reasonable to set the Luttinger parameter to its non-interacting value, $K = 1$. As a result we finally arrive at the prediction

$$G_2(r) \sim r^{-\frac{1}{2}-\frac{2}{9}} = r^{-\frac{13}{18}}. \tag{4.40}$$

In Figure 4.5 we present the correlation function $G_2(r)$ for the three points $R_{1,2,3}$ deep in the R phase. The agreement between the numerical results and the simple prediction (4.40) from LL theory is quite good. On top of the power-law decay we observe oscillations with a wave number q_2. As can be seen from the fitted values given in the legend of Figure 4.5b, the wave number strongly depends on the filling fraction n. On the other hand, we determined the wave number at the point $R_2' = (1, 0.5)$ to be $q_2 \approx 0.8$, indicating that there

seems to be no (strong) dependence on the parameter g. This is also consistent with results obtained along the cut $(g, 0.3)$ for $0.6 \leq g \leq 0.7$ (not shown, see Figure 4.12 for the energy along this cut) which show essentially constant wave numbers for both $G_1(r)$ and $G_2(r)$ within the phases L and R.[a] Furthermore, the oscillations seem not to be described by the first correction to (4.40), ie, they are not captured by the Luttinger-liquid description of $G_2(r)$. Thus at the moment we lack a clear understanding of the oscillations.

Finally we note that there are subtleties in the R phase at the filling $n = 1$. In Figure 4.6 we present the EE and the pair correlation function $G_2(r)$ for the point $R_4 = (0.65, 1)$. The correlation function $G_1(r)$ vanishes, as it is the case throughout the R phase. Due to the bifurcation in the EE profile, in order to find the central charge we use the modified CC formula[216, 217],

$$S(l) = \frac{c}{6} \log \left[\frac{L}{\pi} \sin \left(\frac{\pi l}{L} \right) \right] + S_0 + \frac{a_1 + a_2 \cos(\pi l)}{\left[\frac{L}{\pi} \sin \left(\frac{\pi l}{L} \right) \right]^b}, \tag{4.41}$$

in which a_1, a_2 and b are new fitting parameters in addition to the central charge c and the constant S_0. Using the modified CC formula we get the central charge $c = 1$ for the filling $n = 1$ in the R phase, just as was obtained for lower fillings. The same bifurcation also appears in the correlation function $G_2(r)$. Therefore, in order to extract a power law we picked the upper part of the data for fitting with the result $G_2(r) \sim r^{-0.78}$, which is still quite close to the prediction $13/18 \approx 0.72$ we obtained deep in the R phase from bosonisation. The difference between the prediction and the numerical value could be due to the fit to the upper part of data and the fact that at this point $P(1) \simeq 0.1$, which means that the local state $|1\rangle$ plays a more important role than it does deep in the R phase.

4.5.3 The M phase

For sufficiently large filling fractions, $0.8 < n \leq 1$, another gapless phase between the L and R phases exists. This M phase is indicated as the orange region in the phase diagram, Figure 4.1. The M phase is found to be gapless with central charge $c = 2$, as can be deduced from the fit of the CC formula

[a] Incidentally we observe that for a fixed filling fraction n the wave numbers are approximately related by $q_1 \approx 2q_2$, both at $n = 0.3$ and $n = 0.5$.

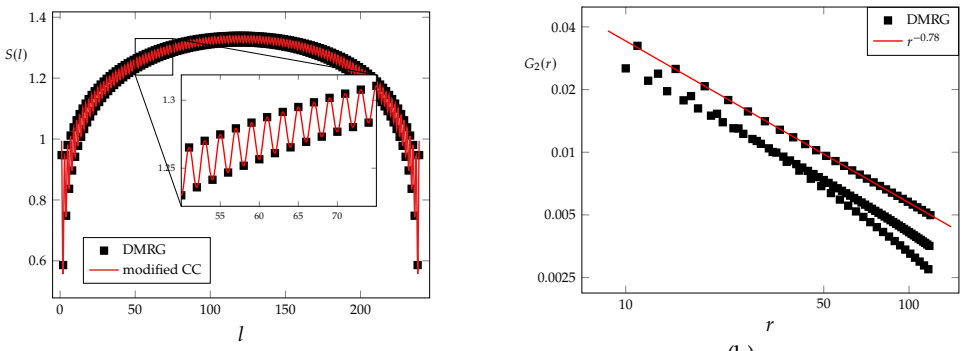

(a) (b)

Figure 4.6: EE and the correlation function $G_2(r)$ at the point $R_4 = (0.65, 1)$. (a) The EE as a function of subsystem size l together with a fit of the modified CC formula (4.41). We find $c = 1$ and $b = 0.78$. The inset shows the bifurcation of the data points between even and odd l. (b) The correlation function $G_2(r)$ together with a fit (red solid line) to the upper branch of the data.

(4.17) to the EE calculated at the points $M_1 = (0.56, 0.85)$, $M_2 = (0.54, 0.9)$ and $M_3 = (0.53, 1)$ shown in Figure 4.7a. Verifying the CFT prediction regarding the scaling of the low-lying energy levels, $\delta(L) \sim 1/L$, turned out to be a hard task. This could be due to two issues: The M phase is a fairly small region, therefore any chosen point is quite close to the phase boundaries with the L and the R phases. This in turn demands very large system sizes. In addition, the high central charge $c = 2$ and oscillatory features suggest that larger bond dimensions are required. In Figure 4.7b we present our results for the energy gap at the point M_3, system sizes $L \in [16 - 120]$ and bond dimension $\chi = 1000$. While we observe a strongly fluctuating dependence on the system size, the results clearly indicate a vanishing of the energy gap in the thermodynamic limit.

The two-point correlation functions $G_1(r)$ and $G_2(r)$ are presented in Figure 4.8. They both show a power-law behaviour as it is expected from CFT. The correlation function $G_1(r)$ is quite smooth and behaves as $G_1(r) \sim r^{-\alpha_1}$ with an exponent $\alpha_1 \simeq 0.75 - 0.8$. Although ripples and fluctuations in the correlation functions $G_2(r)$ are clearly visible, it still has a power-law trend, $G_2(r) \sim r^{-\alpha_2}$ with $\alpha_2 \simeq 1.1$. Since in the M phase all three states at each site play a role, it is not clear at this point whether one can relate the properties of this phase to a Luttinger liquid picture.

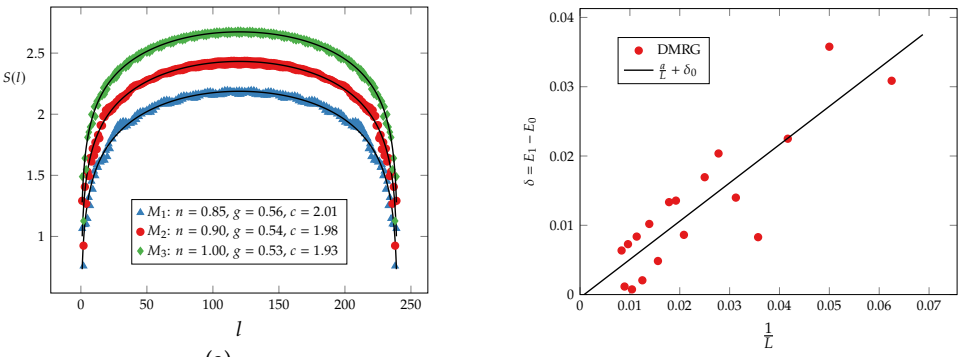

(a) (b)

Figure 4.7: (a) EE as a function of subsystem size l for the points M_1, M_2 and M_3 in the M phase. The fits are performed with the CC formula (4.17), giving a central charge of $c \approx 2$. We have shifted the red points by 0.2 and the green points by 0.4 for visibility. (b) Energy gap above the ground state at the point M_3. The fitting parameters for the solid line are $b \approx 1$ and $\delta_0 \simeq 10^{-4}$.

The location of the M phase between the L and R phases suggest the following interpretation: In the M phase one has two sets of gapless bosonic modes, which is supported by its central charge $c = 1 + 1 = 2$. A priori we do not see a reason why these two theories should have the same effective velocity.[b] Now, when crossing the phase boundary to the L phase, a gap opens in one of the bosonic theories (which is naively related to pair excitations), while when going to the R phase the other theory develops a gap (naively related to single-particle excitations).

4.5.4 The G phase

Finally we consider the gapped G phase indicated by a thick violet line in Figure 4.1. This phase was identified by Rossini et al. [206] at $g = 0$ and interpreted as an anyonic Mott-like phase. Our analysis reveals that this phase extends to finite values of g with the transition to the gapless M phase located at $g \simeq 0.45$. Using DMRG we numerically calculated the energy gap as a function of system size, $\Delta(L)$, and used a power-law fit to extract the gap $\Delta = \Delta(g)$ in the

[b] The situation is reminiscent to the one-dimensional Hubbard model away from half filling [218], and might be similar to the $c = 3/2$ phase recently discussed in Reference [219].

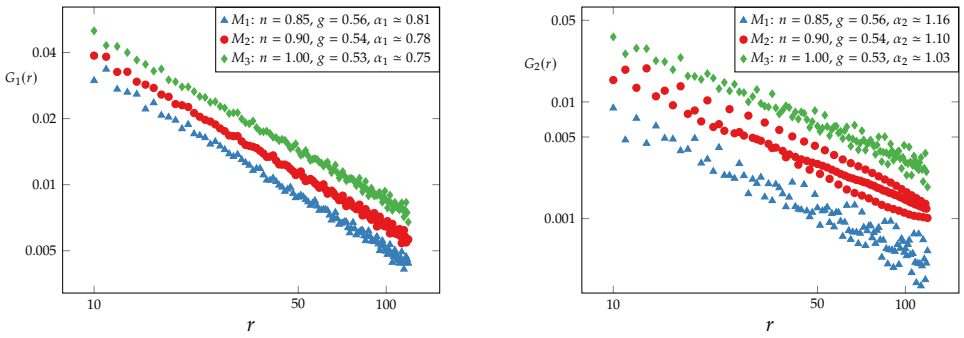

Figure 4.8: The correlation functions $G_1(r)$ and $G_2(r)$ for the three points, M_1, M_2 and M_3, in the M phase are plotted in (a) and (b), respectively. To avoid mixing the data points, $G_1(r)$ for the point M_3 was multiplied by 1.2, $G_2(r)$ for M_2 was multiplied by 2.5 and $G_2(r)$ for M_3 was multiplied by 3.2. For both correlation functions we fitted power laws with exponents $\alpha_{1,2}$, the obtained values are given in the legends.

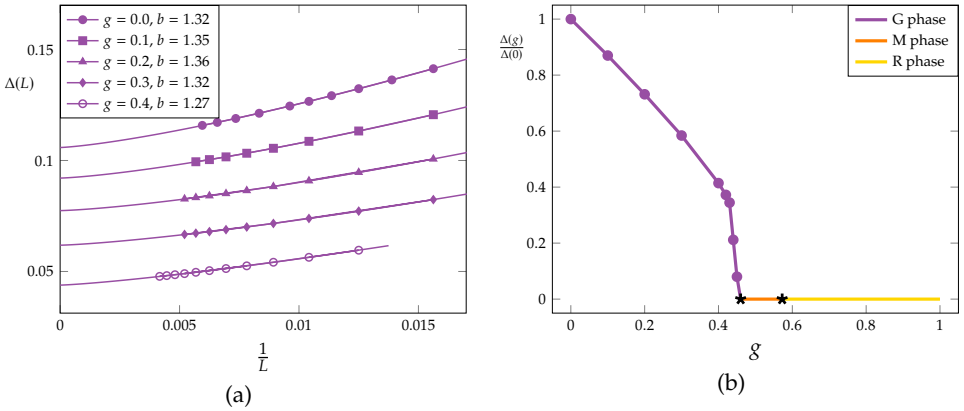

Figure 4.9: (a) Finite-size scaling of the energy gap, $\Delta(L)$, as a function of system size $L \in [64 - 240]$ at several points in the G phase. (b) Rescaled energy gap in the thermodynamic limit, $\Delta(g)/\Delta(0)$, as a function of g. The orange and the yellow lines correspond to the M and the R phases, respectively, while the stars indicate the transition points.

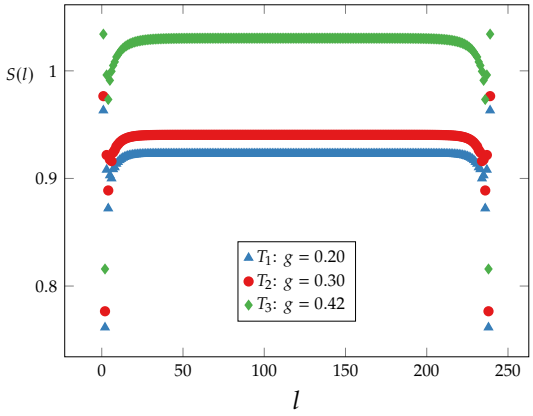

Figure 4.10: EE as a function of the subsystem size l for three points T_1, T_2 and T_3 in the G phase. We note that in the middle of the chain the EE takes a constant value indicating a finite correlation length [209].

thermodynamic limit via

$$\Delta(L) = \frac{a}{L^b} + \Delta. \tag{4.42}$$

The finite-size data and fits as well as the g-dependence of the extracted gap $\Delta(g)$ are presented in Figure 4.9. For convenience we rescaled the gap with its value at $g = 0$, namely $\Delta(0) = 0.106\,t$.

We have calculated the EE and correlation functions at the points $T_1 = (0.2, 1)$, $T_2 = (0.3, 1)$ and $T_3 = (0.42, 1)$ in the G phase. The data are shown in Figures 4.10 and 4.11, respectively. The EE saturates quite quickly as a function of subsystem size l to a constant value, which is indicative of a finite correlation length [209]. This is also supported by the behaviour of the correlation functions, which show an exponential decay with power-law corrections,

$$G_i(r) = A_i r^{-\beta_i} \exp(-r/\xi_i), \quad i = 1, 2. \tag{4.43}$$

The obtained fitting parameters are given in Figure 4.11. The correlations lengths are much smaller than system size, usually of the order 10-20 lattice constants.

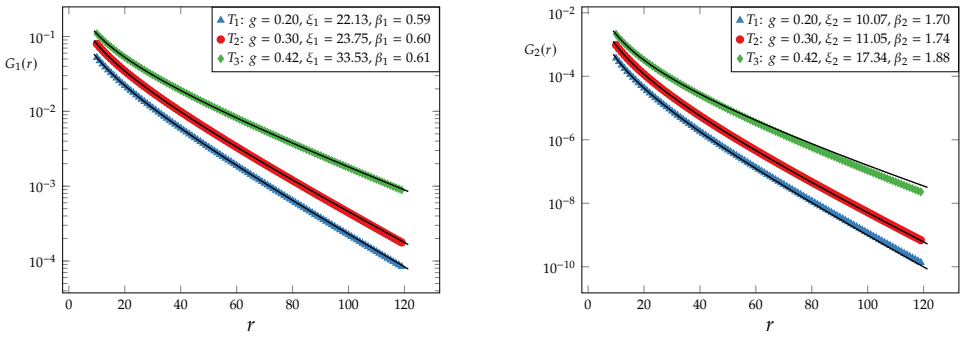

(a) (b)

Figure 4.11: The correlation functions $G_1(r)$ and $G_2(r)$ for the three points T_1, T_2 and T_3 in the G phase are plotted in (a) and (b), respectively. To avoid mixing the data points, $G_1(r)$ for T_2 was multiplied by 1.5, $G_1(r)$ for T_3 was multiplied by 2, $G_2(r)$ for T_2 was multiplied by 2.5 and $G_2(r)$ for T_3 was multiplied by 4.5. We note that both correlation functions show an exponential decay at large distances, as indicated by the fitted functions (4.43) shown as solid lines.

4.5.5 On the nature of the transitions

So far we focussed on the properties of the individual phases. In this section we will examine the nature of the transitions between them by studying the ground-state energy and its derivatives together with the information we gathered so far.

The transition between the L and the R phases

First we consider the phase transition between the two gapless phases with the central charge $c = 1$, namely the L phase and the R phase. As discussed above, these two phases are best distinguished by the behaviour of the correlation functions and in particular by the vanishing of $G_1(r)$ in the R phase. To further investigate the nature of the transition we calculated the ground-state energy $E(g)$ at a fixed filling. For example, in Figure 4.12 we show $E(g)$ and its first and second derivatives with respect to g at the filling $n = 0.3$. We see that while the energy and its first derivative are smooth and continuous, there exists a divergence in the second derivative $\frac{\partial^2 E}{\partial g^2}$ at $g_c \simeq 0.64$. This value is identical to the one extracted from the change of the behaviour in $G_1(r)$. We have checked

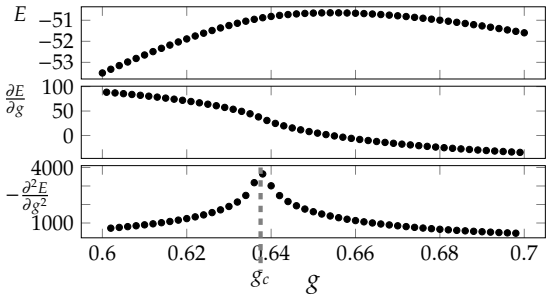

Figure 4.12: Ground-state energy $E(g)$ as well as its first and second order derivatives with respect to the parameter g but at fixed filling $n = 0.3$. We observe a divergence in $\frac{\partial^2 E}{\partial g^2}$ at $g_c \simeq 0.64$ indicating the existence of a second-order phase transition between the L and R phase.

the presence of the two phases down to the filling $n = 0.1$. The transition parameter $g_c(n) = 0.64$ is the same within the accuracy of our numerics for the fillings $0.1 \leq n \leq 0.4$, therefore in Figure 4.1 we extrapolate it down to $n = 0$. In summary, we conclude that the L and R phases are separated by a phase transition that seems to be of second order, but that future work is required to obtain a complete characterisation.

The transitions to the M phase

For the transition between the M phase and the L and R phases, we studied again the ground-state energy and its first and second derivatives (not shown). While the energy and its first derivative are smooth within our precision, the second order derivative is smooth in the L and the R phases but quite fluctuating and spiky within the M phase. This may be related to the presence of fluctuations as it was recently observed in the incommensurate phase of the Kitaev–Hubbard model [220].

For the phase transitions at $n = 1$ between the M phase and G phase we performed a scaling analysis. For systems of size $L \in [64 - 100]$ we numerically calculated the energy difference between the first excited state and the ground state, $\Delta(L, g) = E_1(L, g) - E_0(L, g)$. As it is presented in Figure 4.13a the quantity $L^z \Delta$ with $z = 1$ for various system sizes cross at $g_c \simeq 0.45$. This value is consistent with the critical parameter g_c obtained from the EE. Figure 4.13b also shows that by scaling the g-axis as $L^{1/\nu}(g - g_c)$ with $\nu = 1$ all the data close to the transition collapse to a single curve. Thus we conclude that our

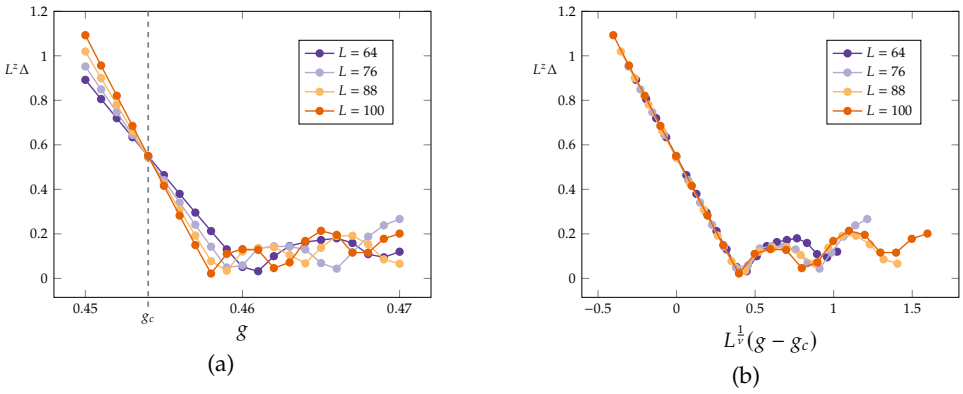

Figure 4.13: (a) The energy gap at $n = 1$ scaled with the system size, $L\Delta(L, g)$, indicates a phase transition at $g_c \simeq 0.45$. (b) The scaling collapse of data using the critical exponents $z = \nu = 1$.

results are consistent with the existence of a second-order transition. We note, however, that reasonable scaling collapse of the data is still obtained if z is varied provided ν is adapted appropriately.

4.6 Conclusion and outlook

In this work we studied a one-dimensional model for FPFs with $p = 3$, which contained single-particle and coherent pair-hopping terms between nearest-neighbour sites. Using a combination of numerical simulations and analytical arguments we determined the phase diagram as a function of the relative strength between the two hopping terms and the filling fraction, ie, the number of FPFs per lattice site. We identified four different phases: two distinct gapless Luttinger phases with central charge $c = 1$, one gapless phase with $c = 2$, and one gapped phase. All phases were characterised by the energy gap, entanglement entropy and behaviour of two-point correlation functions. While we were able to locate the phase transitions accurately, their complete characterisation had to be left for future studies.

Our work can be seen as a step towards the general understanding of the many-particle states of FPFs, or more broadly towards a better understanding of the manifestations of anyonic statistics in many-particle phases. Of course there are many open directions for future research: First, it would be very interesting to analyse the effects of extensions to the simple model (4.16), for

example by including additional complex phases. These are known [221, 222] to have drastic effects on the phase diagram of parafermionic models, and can be crucial for the existence of edge zero modes [61]. Similarly, the addition of BCS-like terms will break the particle number conservation and thus is expected to support additional phases in the phase diagram. Second, studying the properties of FPFs with $p > 3$ is of interest. So far only the pure hopping model (ie, $g = 0$) for $p = 6$ was studied by Rossini et al. [206], who pointed out analogies with counter-propagating boundary modes in the $\nu = 1/3$ Laughlin state. Third, it would be of general interest to establish possible experimental realisations of FPFs, for example based on structures combining quantum Hall systems and superconductors, quantum Hall bilayers, or two-dimensional topological insulators [112].

4.A Proof of "particle-hole" symmetry

In this section we prove that it is sufficient to study the model for $0 < n \leq 1$. First of all note that the number operator for FPFs,

$$N_j = \mathbf{1} \otimes \cdots \otimes \underbrace{N}_{j} \otimes \cdots \otimes \mathbf{1}\,, \qquad N = \begin{pmatrix} 0 & 0 & 0 \\ 0 & 1 & 0 \\ 0 & 0 & 2 \end{pmatrix}, \tag{4.44}$$

can be rewritten in terms of the bosonic operators (4.21) as

$$N_j = F_j^{\dagger 2} F_j^2 + F_j^\dagger F_j = B_j^{\dagger 2} B_j^2 + B_j^\dagger B_j. \tag{4.45}$$

We now perform the transformation

$$U_j \to U_j^\dagger, \qquad B_j \to B_j^\dagger, \tag{4.46}$$

which preserves the bosonic algebra (4.22). From Equation (4.19) one can see that this transformation corresponds to $F_j \to F_j^\dagger$. Applying it to N_j we get for the particle density

$$N_j \to B_j^2 B_j^{\dagger 2} + B_j B_j^\dagger = \mathbf{2} - N_j \quad \Rightarrow \quad n = \frac{1}{L} \sum_{j=1}^{L} N_j \to 2 - n. \tag{4.47}$$

The action of (4.46) on the Hamiltonian (4.23) is given by

$$H(g) = -t(1-g)\sum_{j=1}^{L-1}\left(B_j^\dagger U_j B_{j+1} + U_j^\dagger B_j B_{j+1}^\dagger\right) - tg\sum_{j=1}^{L-1}\left(B_j^{\dagger 2}B_{j+1}^2 + B_j^2 B_{j+1}^{\dagger 2}\right) \tag{4.48}$$

$$\to -t(1-g)\sum_{j=1}^{L-1}\left(B_j U_j^\dagger B_{j+1}^\dagger + U_j B_j^\dagger B_{j+1}\right) - tg\sum_{j=1}^{L-1}\left(B_j^2 B_{j+1}^{\dagger 2} + B_j^{\dagger 2}B_{j+1}^2\right) \tag{4.49}$$

$$= -t(1-g)\sum_{j=1}^{L-1}\left(\omega B_j^\dagger U_j B_{j+1} + \bar{\omega} U_j^\dagger B_j B_{j+1}^\dagger\right) - tg\sum_{j=1}^{L-1}\left(B_j^{\dagger 2}B_{j+1}^2 + B_j^2 B_{j+1}^{\dagger 2}\right). \tag{4.50}$$

We recall that we can choose other representations for the matrix U in Equation (4.20) as long as it satisfies the requirements $U^3 = \mathbf{1}$ and $U^2 = U^\dagger$. Thus we can redefine U_j as $\tilde{U}_j = \omega U_j$, which still satisfies the algebra (4.22) with the B_j's. Therefore Equation (4.50) can be rewritten in terms of $\tilde{U}_j$ and then retrieves its original form (4.48).

Note that although the model (4.16) can be defined for any $p \geq 3$, its bosonic representation (4.23) was written specifically for the case of $p = 3$. Hence our proof is also restricted to this case.

5 Phase diagram of a parafermion chain with four site interactions

This chapter is based on: J. Wouters, F. Hassler, H. Katsura and D. Schuricht, *Phase diagram of an extended parafermion chain*, arXiv:2106.15823 (2021) currently under review at SciPost Physics Core. A revised version has been uploaded to arXiv. J.W. performed all calculations, except for Section 5.3, and numerical simulations, discussed the results and contributed to the final version of the manuscript.

We study the phase diagram of an extended parafermion chain, which, in addition to terms coupling parafermions on neighbouring sites, also possesses terms involving four sites. Via a Fradkin—Kadanoff transformation the parafermion chain is shown to be equivalent to the non-chiral $\mathbb{Z}_3$ axial next-nearest neighbour Potts model. We discuss a possible experimental realisation using heteronanostructures. The phase diagram contains several gapped phases, including a topological phase where the system possesses three (nearly) degenerate ground states, and a gapless Luttinger-liquid phase.

5.1 Introduction

The properties, experimental realisations and potential applications of Majorana fermions in condensed-matter systems have been studied to a great extent in the past two decades. In a seminal work Kitaev [11] introduced, amongst other things, a one-dimensional toy model of spinless fermions and showed that the phase diagram contained a topological phase where Majorana zero modes are localised at the edges. This Majorana chain is equivalent to the well-known quantum Ising chain (see, eg, Fendley [61]). The topological and trivial phases of the Majorana chain correspond to the ferromagnetic and paramagnetic phases of the Ising model, separated by a transition described by a conformal field theory (CFT) [76, 78] with central charge $c = 1/2$. Several

extensions of this toy model have been studied, like the inclusion of disorder [36, 37, 223], interactions [42, 44–46, 48, 49, 224], or both [40, 41, 225, 226]. Without disorder, the interacting Majorana chain is equivalent to the axial next-nearest neighbour Ising (ANNNI) model [113, 140]. Besides the topological and trivial phases, already present in the absence of interactions, this model also possesses an incommensurate charge density wave phase as well as a Mott insulating phase [44, 45, 227–229].

The Majorana/quantum Ising chain possesses a $\mathbb{Z}_2$-symmetry. An obvious path for generalisation is given by considering $\mathbb{Z}_3$-symmetric[a] systems, which in turn leads to parafermions [60]. In the corresponding parafermion chain the $\mathbb{Z}_3$-symmetry turns out to be less restrictive than the $\mathbb{Z}_2$-symmetry of its Majorana cousin, for example, the breaking of time-reversal and spatial parity symmetry via chiral interactions is allowed. The parafermion chain is equivalent [61] to the $\mathbb{Z}_3$-clock model, which, in the non-chiral case, simplifies to the three-state quantum Potts chain [230]. The latter possesses an ordered phase with three-fold degenerate ground state, which is separated from a paramagnetic phase by a quantum phase transition described by a CFT with central charge $c = 4/5$. In addition, the chiral model possesses an incommensurate phase [192, 221, 222]. Interestingly, the transition between the ordered and paramagnetic phases in the non-chiral model is no longer described by a CFT [222]. In the parafermion description the ordered phase is topological, possessing zero-energy modes linked to the degeneracy of the ground state [61, 115, 188, 205]. In addition to the chiral interactions, the $\mathbb{Z}_3$-symmetry allows several extensions of the parafermion chain, which correspond to the terms coupling parafermions beyond neighbouring sites [124, 231–233]. The equivalent clock models can be viewed as $\mathbb{Z}_3$-generalisations of the ANNNI model. It is interesting to note that for specific parameters these clock models become frustration free [124, 145], implying that the degenerate ground states can be constructed explicitly. This behaviour generalises the well-known frustration-free Peschel–Emery line [113] of the ANNNI model.

In this work we focus on a specific extension of the parafermion chain, which, in addition to terms coupling parafermions on neighbouring sites, also possesses terms involving four sites next to each other. In terms of clock variables our model becomes the non-chiral $\mathbb{Z}_3$ axial next-nearest neighbour Potts (ANNNP) model [144]. Our specific choice is motivated by a possible experimental realisation of this extended parafermion chain using heterostructures

[a] The generalisation to arbitrary $\mathbb{Z}_n$-symmetry is straightforward, however, in this chapter we will restrict ourselves to $n = 3$.

containing ferromagnets, superconductors and fractional quantum Hall states. We provide a detailed characterisation of the phase diagram of our model (shown in Figure 5.2), which, for moderate strengths of the extension, contains four gapped phases: the topological and trivial phases already present in the pure parafermion chain, and two phases showing antiferromagnetic and ferromagnetic Ising-type order. In addition, we identify a critical Luttinger-liquid phase with central charge $c = 1$. The latter as well as the two Ising-type phases can be linked to the physics of the spin-1/2 XXZ Heisenberg chain. Furthermore, we provide evidence that the topological phase is pinched between the Luttinger-liquid phase and the ferromagnetic Ising phase.

This chapter is organised as follows: In the next section we define the extended parafermion chain. In Section 5.3 we discuss a proposal to experimentally realise it in heteronanostructures, thus motivating our specific choice of the considered extension. We then link the extended parafermion chain to the non-chiral ANNNP model, which provides the starting point for our further analysis. In Section 5.5 we give a qualitative discussion of the phase diagram, whose details are elaborated on in Sections 5.6 and 5.7. We then give a brief outlook on the phase diagram at stronger extension parameters, followed by a concluding discussion of our results in Section 5.8. The appendix contains further details of our analysis, including a discussion of duality transformations, additional supporting numerical results, and details of the mapping to the effective XXZ chain.

5.2 Extended parafermion chain

In this chapter we are investigating the phase diagram of a one-dimensional parafermionic system which can be viewed as an extension of the parafermion chain [61, 205] by terms coupling parafermions on four neighbouring sites. Specifically, we consider an open chain of length $2L$. At each lattice site we define parafermion operators χ_l, $l = 1, \ldots, 2L$, satisfying

$$\chi_l^3 = 1, \quad \chi_l^\dagger = \chi_l^2, \quad \chi_l\chi_m = \omega^{\mathrm{sgn}(m-l)}\chi_m\chi_l \quad \text{for } m \neq l, \qquad \omega = e^{2\pi \mathrm{i}/3}, \tag{5.1}$$

which can be regarded as direct generalisation of Majorana fermions. Using this the Hamiltonian of the extended parafermion chain can be written as

$$H = -J\sum_{j=1}^{L-1}\chi_{2j}\chi_{2j+1}^\dagger - f\sum_{j=1}^{L}\chi_{2j-1}^\dagger\chi_{2j} + U\sum_{j=1}^{L-1}\chi_{2j-1}^\dagger\chi_{2j}\chi_{2j+1}^\dagger\chi_{2j+2} + \text{h.c.}. \tag{5.2}$$

The parameters J, f and U are assumed to be real[b], making the model non-chiral. Unless it is stated otherwise, we set $J = 1$. In the absence of the last term, ie, $U = 0$, this model is known as the parafermion chain [61, 205]. The term $\propto U$ corresponds to an extension involving four neighbouring sites. One thus might be tempted to call the model (5.2) "interacting parafermion chain", however, due to the non-trivial relations (5.1) the model is not quadratically solvable even for $U = 0$. We note that a similar extension to the parafermion chain has been studied by Milsted et al. [186] and Zhang et al. [232]. The former focussed on the $\mathbb{Z}_6$ variant of Equation (5.2), while the latter discussed the $\mathbb{Z}_3$ model in a different parameter regime.[c] For $f = U = 0$ we recognise that χ_1 and χ_{2L} decouple from the system and form a non-local zero-energy edge mode that generates a three-fold degeneracy throughout the whole spectrum. This degeneracy is protected by the non-local $\mathbb{Z}_3$-symmetry $\omega^P = \prod_j (\chi^\dagger_{2j-1}\chi_{2j})$. Contrary to the Majorana chain, these exact modes disappear when going away from the classical point. While the ground state might retain its degeneracy, the degenerate excited states hybridise and thus split in energy [61, 115, 188, 205], ie, the zero modes cease to commute with the full Hamiltonian. The region around the classical point where the ground state remains (approximately) degenerate is called the topological phase.

Before analysing the phase diagram of the extended parafermion chain (5.2), in the next section we present a proposal to experimentally realise the model using heterostructures containing ferromagnets, superconductors and fractional quantum Hall states.

5.3 Proposal for experimental realisation

Recently, there have been several proposals put forward that allow to realise parafermionic bound states by cleverly constraining the fractionalised edge states of two-dimensional interacting systems [16, 56, 64]. To fix the ideas, we discuss the set-up described by Ref. [64] in more detail. Its starting point are helical edge states of a fractional quantum spin Hall state at filling factor $\nu = 1/m$. Such an edge configuration can also be realised at the interface of two fractional quantum Hall states with g-factors of opposite signs [56].

[b] Complex parameters would lead to chiral interactions, which in turn break spatial parity and time-reversal symmetry.

[c] The Hamiltonian in [232] is related to (5.2) via a duality transformation as discussed in Appendix 5.A.

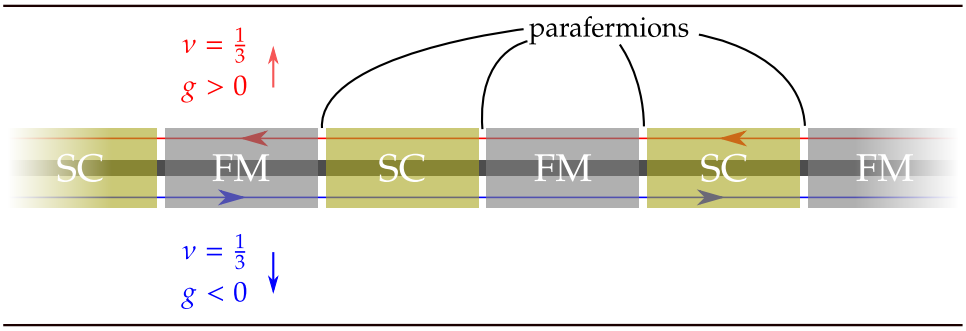

Figure 5.1: Schematic display of a fractional quantum Hall system with appearing effective parafermion degrees of freedom. The alternating placement of superconductors (SC) and ferromagnets (FM) traps the edge modes. These trapped modes obey the $\mathbb{Z}_6$-parafermion algebra.

Independent of the realisation, the low-energy degrees of freedom are counter-propagating modes of fractionalised electrons with charge $e^* = e/m$ and spin $1/m$ (in units of the electron spin), see Figure 5.1.

There are two (dual) ways of opening a gap in these edge states. Coupling them to a (s-wave) superconductor (SC) allows a transfer of charge $2e$ to and from the superconducting condensate. The electric charge eQ_j on the j-th superconducting island can thus assume the values

$$eQ_j = 0, \frac{e}{m}, \frac{2e}{m}, \ldots, \frac{(2m-1)e}{m} \pmod{2e}. \tag{5.3}$$

The (clock) operator describing the charge is thus given by $e^{\mathrm{i}\pi Q_j}$ and commutes with the Hamiltonian [64].

The second way to open a gap is via backscattering. This involves a change of the spin which can be achieved by coupling the edge state to a ferromagnetic (FM) insulator. The spin S_j in the j-th ferromagnetic region may assume the values

$$S_j = 0, \frac{1}{m}, \frac{2}{m}, \ldots, \frac{(2m-1)}{m} \pmod{2} \tag{5.4}$$

due to the fact that the ferromagnet serves as a reservoir of spins in units of 2. Note that the backscattering leads to the formation of an insulating phase and correspondingly the charge vanishes in the FM segments. The corresponding

clock operators satisfy

$$e^{\mathrm{i}\pi S_j} e^{\mathrm{i}\pi Q_k} = e^{\mathrm{i}\frac{\pi}{m}(\delta_{j,k+1}-\delta_{j,k})} e^{\mathrm{i}\pi Q_k} e^{\mathrm{i}\pi S_j}, \tag{5.5}$$

displaying the fractional statistics. Using the algebra in Equation (5.5) the SC and FM operators can be represented by the parafermion modes on the interfaces,

$$\chi_{2j}\chi_{2j-1}^{\dagger} = e^{\mathrm{i}\pi Q_j}, \quad \chi_{2j+1}\chi_{2j}^{\dagger} = e^{\mathrm{i}\pi S_j}. \tag{5.6}$$

With this procedure only $\mathbb{Z}_{2m}$-parafermions can be realised natively while we concentrate on the case $\mathbb{Z}_3$ in this work. Note however that starting from $\mathbb{Z}_6$ ($m = 3$), $\mathbb{Z}_3$-parafermions naturally emerge by allowing for fluctuations of the gauge field with restricted dynamics [234]. An alternative experimental avenue to the $\mathbb{Z}_3$-parafermions is the spin-unpolarised $\nu = 2/3$-state [16].

The entrapment of the parafermions is not perfect and exchange processes through the FMs and SCs couple the parafermions. Tunnelling of a fractional charge e^* through the FM segments is described by the operator $e^{\mathrm{i}\pi S_j}$ and yields the term

$$H_J = -J \sum_j \left(e^{\mathrm{i}\theta} e^{\mathrm{i}\pi S_j} + \text{h.c.} \right), \tag{5.7}$$

with some coupling $Je^{\mathrm{i}\theta}$. In general the coupling is complex, for the purpose of this chapter, we will set $\theta = 0$. Moreover, we set $J = 1$, fixing the overall energy scale.

Charging effects on the small mesoscopic islands perturbatively can only involve the operator $e^{\mathrm{i}\pi Q_j}$. The charging effects are due to the Aharonov–Casher phase of a superconducting vortex encircling the island. The charging energy assumes the form

$$H_f = -\sum_j \left(f e^{\mathrm{i}\pi Q_j} + \text{h.c.} \right), \tag{5.8}$$

where f can be made real by an appropriate gate voltage. This term is due to the self-capacitance of the island. The terms (5.7) and (5.8) realise the (dual of) $\mathbb{Z}_3$-Potts model studied in Ref. [61]. This is the parafermionic analogue of the Kitaev chain [11].

Following Reference [45], we argue that the charging effects due to cross-capacitances between adjacent islands are important. They are described by the term

$$H_U = U \sum_j \left(e^{\mathrm{i}\pi(Q_j+Q_{j+1})} + \text{h.c.} \right), \tag{5.9}$$

with $U \in \mathbb{R}$ due to the Aharonov–Casher effect encircling two adjacent islands. We note that the realisation proposed here will generically lead to the regime $|U| \lesssim |f|$. With the relation (5.6), the effective Hamiltonian $H_J + H_f + H_U$ maps to (5.2) whose phase diagram we will investigate in the following.

5.4 ANNNP MODEL

The analysis of the phase diagram of the extended parafermion chain will be fostered by mapping it to the equivalent non-chiral $\mathbb{Z}_3$ ANNNP model [144]. The latter generalises the quantum Potts chain by including an additional coupling term, which is reminiscent to the addition of a transverse interaction term when generalising the quantum Ising chain to the ANNNI model [113, 140].

We begin with the Fradkin–Kadanoff transformation [60]

$$\chi_{2j-1} = \left(\prod_{k=1}^{j-1} \tau_k \right) \sigma_j, \quad \chi_{2j} = \left(\prod_{k=1}^{j-1} \tau_k \right) \sigma_j \tau_j = \chi_{2j-1} \tau_j, \tag{5.10}$$

which relates the $2L$ parafermion operators χ_l to clock operators σ_j and τ_j, $j = 1, \ldots, L$. These clock operators commute off-site,

$$[\tau_i, \tau_j] = [\sigma_i, \sigma_j] = [\tau_i, \sigma_j] = 0, \quad i \neq j, \tag{5.11}$$

while on the same lattice site they satisfy

$$\sigma_j^3 = \tau_j^3 = 1, \quad \sigma_j^\dagger = \sigma_j^2, \quad \tau_j^\dagger = \tau_j^2, \quad \sigma_j \tau_j = \omega \tau_j \sigma_j, \quad \omega = e^{2\pi \mathrm{i}/3}. \tag{5.12}$$

An explicit matrix representation for the clock operators on an individual lattice site is given by

$$\tau = \begin{pmatrix} 1 & & \\ & \omega & \\ & & \omega^2 \end{pmatrix}, \quad \sigma = \begin{pmatrix} & 1 & \\ & & 1 \\ 1 & & \end{pmatrix}. \tag{5.13}$$

In terms of the clock operators the extended parafermion chain (5.2) becomes

$$H = -J \sum_{j=1}^{L-1} \sigma_j \sigma_{j+1}^\dagger - f \sum_{j=1}^{L} \tau_j + U \sum_{j=1}^{L-1} \tau_j \tau_{j+1} + \text{h.c.} \tag{5.14}$$

with $J = 1$. We note that the ANNNP model resides on a chain of length L, ie, there has been an effective halving of the system size. The non-local $\mathbb{Z}_3$-symmetry[d] of the Hamiltonian is generated by $\omega^P = \prod_j \tau_j$. On the clock variables the spatial parity transformation acts as [221] $P\sigma_j P = \sigma_{L-j+1}$, $P\tau_j P = \tau_{L-j+1}$, while time reversal is implemented via $T\sigma_j T = \sigma_j$, $T\tau_j T = \tau_j^\dagger$ together with complex conjugation of scalars. This shows that indeed for real parameters J, f and U the system is time-reversal and parity invariant. At $U = 0$ the model reduces to the quantum Potts chain [230], which possesses a critical point at $f = 1$ described by a CFT with central charge $c = 4/5$ [76, 78]. At $f = 0$ we obtain the classical (ferromagnetic) Potts model, which has a three-fold degenerate ground state.

5.5 Phase diagram

The phase diagram of the extended parafermion chain/$\mathbb{Z}_3$-ANNNP model for weak to moderate values of U is shown in Figure 5.2. The discussion concerning large U can be found in Chapter 6. The phases and transitions were studied using a combination of numerical simulations, conformal field theory [76, 78] and perturbative arguments. For the numerics we used the TeNPy implementation [189] of the density matrix renormalisation group (DMRG) algorithm [81, 118]. First the rough topography of the phase diagram was obtained from an inexpensive DMRG calculation, see Figure 5.12 of the supporting numerical results in Appendix 5.B. Then the detailed properties of the phases and transitions were investigated, as is discussed in Sections 5.6 and 5.7.

We see that the model displays a variety of phases. The top half of the phase diagram ($f \geq 0$) resembles the picture for the ANNNI model [45, 49], with two gapped phases separated by a critical line. The ground state of the paramagnetic phase is singly degenerate, while the $\mathbb{Z}_3$-ordered phase has

[d] We note in passing that the model (5.14) possesses an additional $\mathbb{Z}_2$-symmetry $\sigma_j \to \sigma_j^\dagger$, $\tau_j \to \tau_j^\dagger$ which enlarges the $\mathbb{Z}_3$-symmetry to a full S_3-symmetry [188].

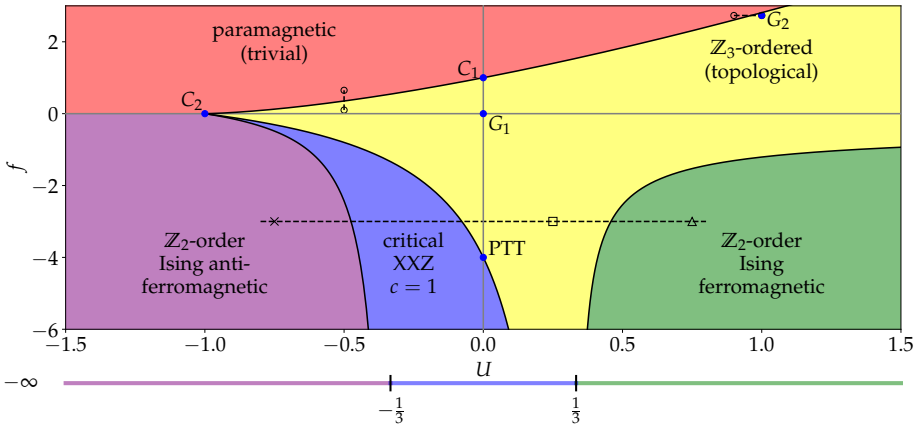

Figure 5.2: Phase diagram of the extended parafermion chain/$\mathbb{Z}_3$-ANNNP model. We distinguish the following four gapped phases: a paramagnetic phase (red), a topological phase (yellow), an Ising antiferromagnetic (purple) and an Ising ferromagnetic (green) phase. Furthermore, we identify a critical $c = 1$ XXZ like phase (violet) with central charge $c = 1$. We also indicate the transition points C_1 and C_2 corresponding to specific conformal field theories, the points G_1 and G_2 at which the model becomes frustration-free and thus allows an exact description of the ground state, and a Pokrovsky–Talapov transition (PTT) [221]. The dashed lines indicate cuts along which detailed results are shown in Figures 5.3, 5.4, and 5.9b (with the corresponding symbols for marked points).

a threefold degenerate ground state. The latter is due to approximate zero-energy parafermion modes, which explains the term "topological phase". The top half of the phase diagram is discussed in detail in Section 5.6

In contrast to the ANNNI model, the $\mathbb{Z}_3$-ANNNP model is not invariant under $f \to -f$ (which is a consequence of the $\mathbb{Z}_2$-symmetry of the ANNNI model). The lack of this invariance is manifest in the phase diagram, which shows four phases for $f < 0$: the topological phase, a gapped antiferromagnetic phase, a critical XXZ phase, and a ferromagnetic phase. The latter three can be related to the physics of the XXZ chain in the limit $f \to -\infty$, which predicts the transitions to be at $U = \pm 1/3$. The detailed description of these phases is given in Section 5.7.

5.6 Upper half of the phase diagram ($f \geq 0$)

Given that the $\mathbb{Z}_3$-ANNNP model is not integrable, the applicability of analytical methods is limited. Still, the quantum Potts model ($U = 0$) is well understood due to its relation to the two-dimensional classical Potts model. Two topologically distinct phases are separated by a quantum phase transition at $f = 1$ (C_1 in Figure 5.2) described by a CFT with central charge $c = 4/5$. The two distinct phases can be characterised by analysing the limiting cases $f \to \infty$ and $f = 0$ respectively.

In the limit $f \to \infty$ the ground state is unique and given by a product state

$$|\Psi_0\rangle = |0\rangle_\tau^{\otimes L}\,, \tag{5.15}$$

where $|i\rangle_\tau$, $i = 0, 1, 2$, span the space of eigenstates of τ,

$$\tau\,|i\rangle_\tau = \omega^i\,|i\rangle_\tau\,. \tag{5.16}$$

In the parafermionic language this is identified as the trivial phase due to the absence of boundary modes. The whole phase denoted as paramagnetic in Figure 5.2 is adiabatically connected to this limit, in particular, it possesses a unique ground state with an energy gap above it. Explicit numerical evidence for the gap at a representative point ($U = -1$, $f = 1$) is shown in Figure 5.13(a) of Appendix 5.B.2.

The nature of the $\mathbb{Z}_3$-ordered phase is obvious from studying the $f = 0$ point (G_1). Here the threefold degenerate ground state is given by

$$|\Phi_0^i\rangle = |i\rangle_\sigma^{\otimes L} \qquad \text{for } i = 0, 1, 2, \tag{5.17}$$

where $|i\rangle_\sigma$ span the space of eigenstates of σ,

$$\sigma\,|i\rangle_\sigma = \omega^i\,|i\rangle_\sigma\,. \tag{5.18}$$

The parafermion dual of this system is topological, with edge states χ_1 and χ_{2L}.

Recent progress on frustration-free models allows us to analytically discuss one additional point in the topological phase. In Ref. [124] it was shown that at $U = 1$, $f = 1 + \sqrt{3}$ the model is frustration free (point G_2), enabling the construction of the exact ground states. Furthermore, this point is adiabatically (ie, without closing the energy gap) connected to the classical Potts model (G_1) [145]. In fact, the points G_1 and G_2 lie on a frustration free line of a more

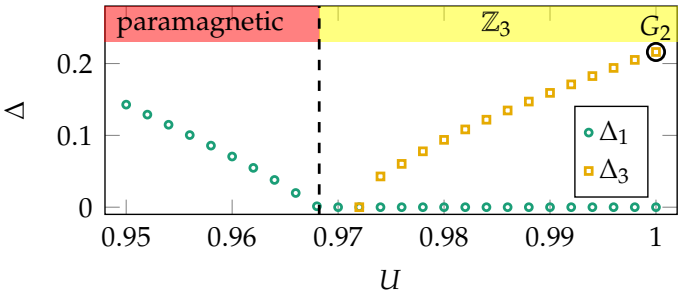

Figure 5.3: Energy gaps Δ_n between the ground state and the nth eigenstate obtained from finite-size scaling as a function of U for fixed $f = 1 + \sqrt{3}$ (see dashed line close to G_2 in Figure 5.2). In the $\mathbb{Z}_3$-ordered phase we observe the threefold degeneracy of the ground state ($\Delta_1 = \Delta_2 = 0$) with a finite gap above it ($\Delta_3 > 0$). In contrast, in the paramagnetic phase the ground state is unique ($\Delta_1 > 0$). The transition (determined with the methods discussed in Section 5.6.1) is located at $U_c \approx 0.97$. The gap Δ_3 is very small close to the transition.

general Hamiltonian, obtained from (5.14) by adding a term $\propto (\tau_j \tau_{j+1}^\dagger + \text{h.c.})$ with a suitable prefactor. The situation is reminiscent to the Peschel–Emery line in the ANNNI model [49, 113]. The numerically calculated energy gaps shown in Figure 5.3 confirm that at G_2 the model indeed possesses a threefold degenerate ground state. The model is gapped down to the transition to the paramagnetic phase at $U_c \approx 0.97$. Further numerical results presented in Appendix 5.B.2 [see Figure 5.13(b) for the point $U = f = 1$] show that the model is gapped with a threefold degenerate ground state throughout the topological phase.

Finally, a simplification occurs along the line $f = 0$. Performing two duality transformations (see Appendix 5.A for the details) we can bring the Hamiltonian in the following form

$$H = -\sum_{a=\mathrm{o,e}} \left[\sum_{j=1}^{L/2-2} \sigma_j^a (\sigma_{j+1}^a)^\dagger - U \sum_{j=1}^{L/2-1} \tau_j^a \right] + \text{h.c.}, \tag{5.19}$$

where we omitted the boundary terms. The result (5.19) represents two decoupled (o/e) quantum Potts chains. Consequently, at $U = -1$ the model possesses a second-order phase transition corresponding to a CFT with $c = 4/5+4/5 = 8/5$ (see also Reference [235]) depicted by C_2 in Figure 5.2, separating a trivial from a topological phase.

5.6.1 Potts transition in the vicinity of C_1

In this subsection we perform a more detailed analysis of the Potts transition. We begin with a scaling analysis of finite-size data, followed by a inspection of the vicinity of the point C_1.

Scaling analysis

In Figure 5.4 we show several observables along a cut at $U = -0.5$ (indicated by a dashed line in Figure 5.2). The numerical data were obtained for system sizes $L = 64, 70, \ldots, 100$.

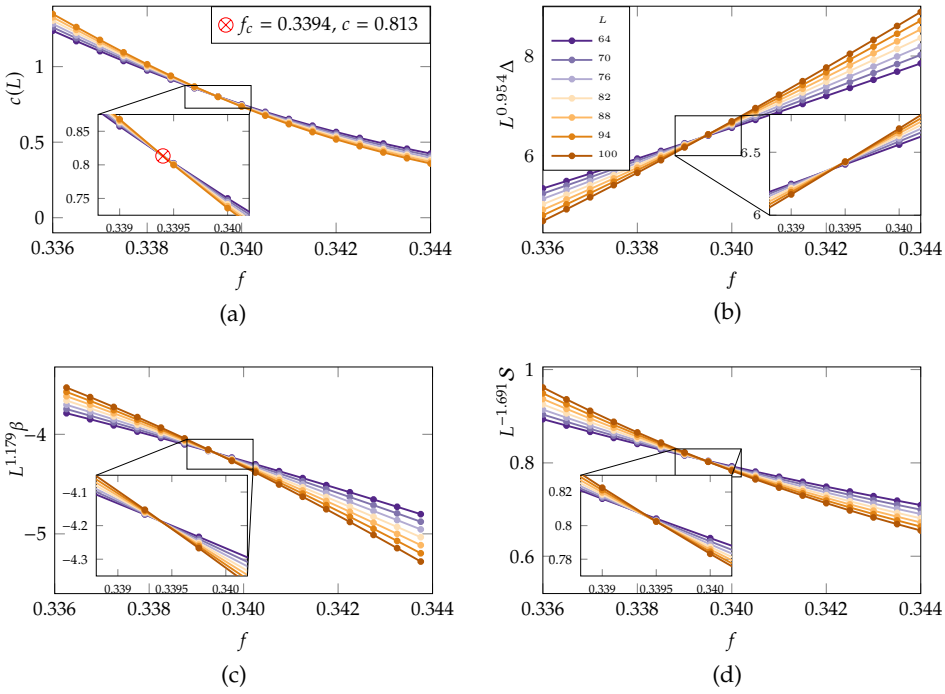

Figure 5.4: Finite-size results for $U = -0.5$, locating the transition at $f_c = 0.3394$ from the central charge (a) with $c \approx 0.813$ ($L_{\max} = 100$). From (b) we confirm the dynamical exponent is close to 1. From the Callan–Symanzik β function in (c) we derive $1/\nu \approx 1.179$ and the structure factor $\mathcal{S}$ gives $2 - \eta = 1.691$. The exponents in (b), (c) and (d) are obtained by requiring that the finite-size data are independent of L at the transition f_c.

First, we consider the entanglement entropy S. In a conformally invariant system this is predicted by the Calabrese–Cardy formula [209, 210]

$$S(L, l) = S_0 + \frac{c}{6} \log \left[\frac{L}{\pi} \sin \left(\frac{\pi l}{L} \right) \right], \tag{5.20}$$

with c being the central charge, l the bipartition length, and S_0 being a model-dependent constant. Setting $l = L/2$ we obtain the central cut entanglement entropy, for which we realise that

$$c = 6 \frac{S(L, L/2) - S(L_{\max}, L_{\max}/2)}{\log(L/L_{\max})}. \tag{5.21}$$

For a critical system the right-hand side of (5.21) is length (L) independent. Thus we can locate the transition as the point where the finite-size data collapse, obtaining the central charge in the process. From the entanglement-entropy results in Figure 5.4a we can infer that $f_c = 0.3394$ with $c \approx 0.813$, which is in good agreement with the predicted value of $c = 4/5$.

Second, we consider the energy gap whose scaling behaviour is given by [222, 236]

$$\Delta(L) = L^{-z} \tilde{\Delta}(L^{1/\nu} |f - f_c|) \tag{5.22}$$

with z being the dynamical exponent. The critical exponent ν governs the divergence of the correlation length $\xi \propto |f - f_c|^{-\nu}$. At the $f = f_c$ we find z by requiring $L^z \Delta(L)$ to be independent of L. From this ansatz we obtain $z \approx 0.954$ [see Figure 5.4b], in good agreement with the value $z = 1$ expected for a CFT.

Third, we consider the Callan–Symanzik function β [237]

$$\beta = \frac{\Delta}{\Delta - 2 \frac{\partial \Delta}{\partial \ln f}} \propto |f - f_c|, \tag{5.23}$$

which allows us to determine the critical exponent ν. The finite-size ansatz implies that $\beta(L)$ scales as $L^{-1/\nu}$. The CFT prediction for the Potts transition is determined from the scaling dimension of the perturbing field, in this case the energy operator E, to be

$$\nu = \frac{1}{2 - \Delta_E} = \frac{5}{6} \tag{5.24}$$

with $\Delta_E = 4/5$ for the critical Potts model [76]. From Figure 5.4c we get the numerical value $1/\nu = 1.179$, again close to the prediction.

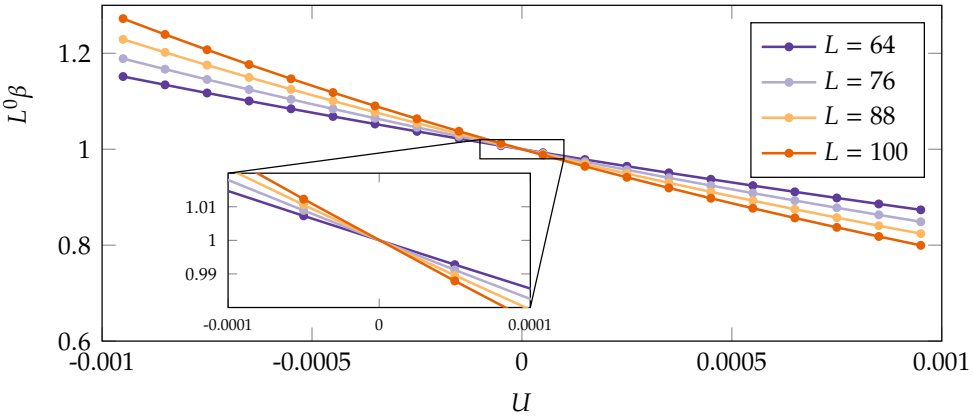

Figure 5.5: The Callan–Symanzik β function for the $U(\tau_j\tau_{j+1} + \text{h.c.})$ perturbation at C_1. The scaling at the transition is independent of the system size, $\propto L^0$, indicating that the perturbation is marginal.

Finally, the last critical exponent we can easily study is the scaling of the two-point correlation function $\Gamma(r) = \langle \sigma^\dagger_{i+r}\sigma_i\rangle \propto r^{-\eta}$ with $\langle . \rangle$ denoting the ground-state expectation value. From the finite-size scaling ansatz we see that the structure factor behaves as

$$\mathcal{S}(L) = \sum_{i,j}\langle \sigma_i\sigma^\dagger_j\rangle \propto L^{2-\eta}. \tag{5.25}$$

From the CFT description we recognise that η relates to the scaling dimension of the σ-field [76] $\eta = 4\Delta_\sigma = 4/15$. Consequently, the theoretical prediction is $2 - \eta = 26/15 \approx 1.7333$, with the numerical data in Figure 5.4d yielding the estimate $2 - \eta = 1.691$.

We obtained similar results for several points along the transition line depicted in Figure 5.2, indicating that the transition along the whole line is described by the Potts CFT with $c = 4/5$.

Perturbation around C_1

In general it is possible to link the lattice operators in the quantum Potts chain to scaling fields in the Potts CFT [79]. Unfortunately, for the $\tau_j\tau_{j+1}$-perturbation coupled to U, which is of interest here, the corresponding field expansion was not derived in Reference [79]. However, from numerical analysis we can obtain its scaling dimension Δ_U. The Callan–Symanzik function (5.23) in Figure 5.5

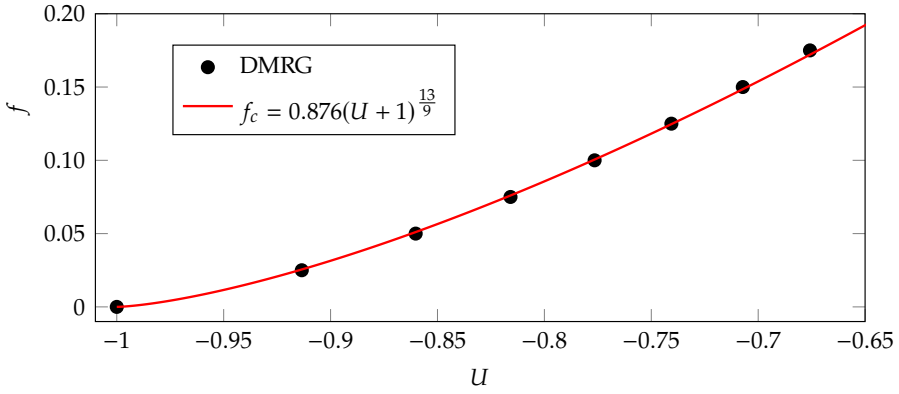

Figure 5.6: The phase boundary between the paramagnetic and topological phase. The dots are obtained with finite-size scaling from the DMRG calculation. The red line is the CFT prediction (5.29), with the prefactor obtained from a fit to the numerical data.

shows that the $\tau_j\tau_{j+1}$ perturbation at C_1 scales with $1/\nu = 0$, ie, is independent of the system size at the transition. From Equation (5.24) we conclude that the corresponding field has scaling dimension $\Delta_U = 2$ and is thus marginal.

The qualitative behaviour of the transition line close to C_1 is consistent with a simple mean-field argument. Decoupling the $U(\tau_j\tau_{j+1} + \text{h.c.})$ perturbation is tantamount to a shift in the on-site field term, $f \to f^* = f - 2\langle\tau_j\rangle U$; implying that the transition is shifted to $f_c = 1 + 2\langle\tau_j\rangle U$. Numerically we obtain $\langle\tau_j\rangle = 0.609 > 0$ at $U = 0$, in qualitative agreement with the positive slope of the transition between the trivial and topological phase.

5.6.2 Potts transition in the vicinity of C_2

Finally, let us look more closely at the phase transition in the vicinity of $U = -1$. As already discussed in relation to (5.19), using a duality transformation the model with $f = 0$ can be written as two copies of a quantum Potts chain, implying that the transition at $U = -1, f = 0$ possesses central charge $c = 8/5$. Now let us reinstate the f-term within the dual description, which results in the Hamiltonian (again dropping the boundary terms; for details see Appendix 5.A)

$$H = -\sum_{a=\mathrm{o,e}} \left[\sum_{j=1}^{L/2-2} \sigma_j^a (\sigma_{j+1}^a)^\dagger - U \sum_{j=1}^{L/2-1} \tau_j^a \right] - f \sum_{j=1}^{L/2-1} (\mu_j^{\mathrm{o}} \mu_j^{\mathrm{e}} + \mu_j^{\mathrm{e}} \mu_{j+1}^{\mathrm{o}}) + \mathrm{h.c.}, \quad (5.26)$$

Starting from the $U = -1, f = 0$, the perturbing fields related to the lattice operators are known to be [79]

$$(U+1)(E^{\mathrm{o}} + E^{\mathrm{e}}), \quad 2f\mu^{\mathrm{o}}\mu^{\mathrm{e}}, \quad (5.27)$$

which are the energy density and disorder fields respectively for each copies of the Potts chain. Both terms independently open up a gap, as can be seen in the phase diagram Figure 5.2. However, a proper combination of the perturbations will leave the system gapless, ie, there will be a gapless line $f_c(U)$. At first order in the couplings the renormalisation-group equations contain the scaling dimensions of the relevant fields $E^{\mathrm{o,e}}$ and $\mu^{\mathrm{o,e}}$

$$\partial_l (U+1) = (2 - \Delta_E)(U+1), \quad \partial_l f = (2 - \Delta_{\mu\mu}) f = (2 - 2\Delta_\mu) f, \quad (5.28)$$

with $\Delta_E = 4/5$ and $\Delta_\mu = 2/15$ [76]. At the phase transition neither flows to strong coupling, thus the scalings are necessarily proportional: $|f_c|^{\frac{1}{2-2\Delta_\mu}} \propto |U_c + 1|^{\frac{1}{2-\Delta_E}}$. Therefore, the transition follows a power law in the vicinity of $U_c = -1$ (see, eg, References [62, 220] for a similar line of argument),

$$|f_c| \propto |U+1|^{13/9}. \quad (5.29)$$

In Figure 5.6 we see that the numerically obtained transition points (black dots) are in very good agreement with the scaling prediction (red line). Thus the emerging picture is that under the perturbations (5.27) the $c = 8/5$ fixed point is unstable, with the flow along the line (5.29) being described by the Potts CFT with $c = 4/5$. This is also consistent with the fact that due to the c-theorem [76, 238] the central charge cannot increase under the renormalisation-group flow. We note in passing that such an analysis for the Ising transition in the ANNNI model shows similar behaviour, with the scaling exponent replaced by 7/4 [220].

5.7 Lower half of the phase diagram ($f < 0$)

The phase diagram of ANNNI model is symmetric around the f-axis due to the underlying $\mathbb{Z}_2$-symmetry of the model. In contrast, the ANNNP model

possesses a $\mathbb{Z}_3$-symmetry, which in turn breaks the symmetry of the phase diagram under $f \to -f$. While we have discussed above the phase digram in Figure 5.2 for $f > 0$, and seen that it looks very similar to the one of the ANNNI model, for $f < 0$ a completely different topography appears. It is the aim of this section to discuss the lower half of the phase diagram in detail.

5.7.1 Chiral clock model at $U = 0$

In the absence of the U-term the model (5.14) becomes a special case of the chiral $\mathbb{Z}_3$ clock model [61], whose phase diagram as a function of the chiral angles (ϕ, θ) was studied by Zhuang et al. [221]. More specifically, our model (5.14) at $U = 0, f < 0$ is equivalent to the chiral model at positive field strength and $\phi = \pi/3, \theta = 0$. The phase diagram for the latter shows a Pokrovsky–Talapov transition between the topological phase and a gapless, incommensurate phase with central charge $c = 1$. Using our conventions this translates into a transition from the topological phase to a gapless phase with $c = 1$ at $f_{\mathrm{PTT}} \approx -4$, in complete agreement with our numerical results shown in Figure 5.2.

5.7.2 Limit $f \to -\infty$: Effective XXZ model

We start the discussion by considering the limit $f \to -\infty$, in which the field term $-f(\tau_j + \tau_j^\dagger)$ in (5.14) becomes dominant. As the local eigenstates $|0\rangle_j, |1\rangle_j, |2\rangle_j$ have energies $-2f, f, f$, this limit projects onto the two local states $|1\rangle_j, |2\rangle_j$. This allows us to derive an effective spin-1/2 model, with the third state, $|0\rangle_j$, only appearing in virtual processes.

The remaining terms in (5.14) are treated perturbatively. The first-order contributions to the effective Hamiltonian are (see Appendix 5.C for derivation)

$$H_{\mathrm{eff}}^{(1)} = -\sum_j \left[\sigma_j^+ \sigma_{j+1}^- + \sigma_j^- \sigma_{j+1}^+ + \frac{3U}{2} \sigma_j^z \sigma_{j+1}^z \right], \tag{5.30}$$

where $\sigma_j^\pm = (\sigma_j^x \pm \mathrm{i}\sigma_j^y)/2$ with σ_j^a, $a = x, y, z$, denoting the Pauli matrices acting on lattice site j. Thus at leading order we recognise the spin-1/2 XXZ model with an U(1) symmetry generated by $\sum_j \sigma_j^z$. [We note that a similar argument was used in References [62, 239] to explain the appearance of critical $c = 1$ phases parafermion chains to the XY phase of (5.30).] For this integrable model, the phase diagram is well-known [211] and consists of an antiferromagnetic Ising phase for $3U < -1$, a ferromagnetic Ising phase $3U > 1$, and a Luttinger-

liquid phase with $c = 1$ in between. The Luttinger parameter of the critical phase is given by (at $f = -\infty$)

$$K = \frac{\pi}{2\arccos(3U)}. \tag{5.31}$$

Note that the ferromagnetic Heisenberg point ($U = 1/3$) is not described by a CFT, as the dispersion becomes quadratic, or equivalently Luttinger parameter diverges. The transition to the antiferromagnetic phase at $U = -1/3$ appears at $K = 1/2$, where a gap opens due to the relevance of perturbations to the Luttinger-liquid field theory. The effective model (5.30) provides a good approximation close to $f = -\infty$. The line under the phase diagram (Figure 5.2) indicates this limit.

The second-order contributions provide more information at finite $|f|$ (see Appendix 5.C for the details),

$$H^{(2)}_{\text{eff}} = \sum_j \left[\frac{1}{6f}(\sigma^+_j\sigma^-_{j+1} + \sigma^-_j\sigma^+_{j+1}) + \frac{1}{4f}\sigma^z_j\sigma^z_{j+1} \right. \tag{5.32}$$

$$\left. + \frac{1}{3f}(\sigma^+_j\sigma^-_{j+2} + \sigma^-_j\sigma^+_{j+2}) + \frac{2}{3f}(\sigma^+_j\sigma^+_{j+1}\sigma^+_{j+2} + \sigma^-_j\sigma^-_{j+1}\sigma^-_{j+2}) \right]. \tag{5.33}$$

In the absence of U, a similar expansion has been obtained in Reference [239] in the analysis of S_3-invariant spin chains [184]. In Reference [240], a similar effective description was found, discussing edge effects in fractional quantum Hall systems. The first two terms (5.32) only cause a shift of the XXZ parameters, which in turn shifts the locations of the phase transitions to

$$\text{AFM:} \quad U = -\frac{1}{3} + \frac{2}{9f}, \qquad \text{FM:} \quad U = \frac{1}{3} + \frac{1}{9f}. \tag{5.34}$$

We note that both transition points are shifted to the left, in agreement with the numerical results leading to the phase diagram. In addition, the Luttinger parameter will also acquire corrections to the leading result (5.31). The two three-site terms (5.33) need a more careful consideration: The first term is a next-nearest neighbour spin-flip term, conserving the U(1) symmetry. It has been shown that, for small perturbations, this terms only renormalises the XXZ parameters [241], leading to a further shift of the transition points on top of (5.34). The second term of (5.33) is more involved. It breaks the U(1) symmetry down to $\mathbb{Z}_3$, which is expected to open a gap. However, as we will show in the next section, for small perturbations the effect of this term

is barely visible. The reason for this is that within a bosonisation treatment this term has a scaling dimension of $\frac{9}{4K} + K$ (see Appendix 5.C.3), which is strictly larger than 2 for any K, meaning that in the Luttinger-liquid regime this term is irrelevant.[e] However, this line of argument is not applicable at the ferromagnetic Heisenberg point, since the model is not described by a CFT. A further analytical discussion is beyond the scope of this chapter, but we suspect that this term is responsible for the appearance of the $\mathbb{Z}_3$-ordered phase visible at finite $-f$. We note in passing that a similar U(1)-breaking term has been shown to lead to $\mathbb{Z}_3$-order in a dilute Bose gas [242], although the precise relation to our setup remains unclear.

Finally we note that the analysis presented above critically depends on the absence of chirality breaking in the original model (5.14). Introducing a chirality breaking term would, in the limit $f \to -\infty$, result in an additional, strong magnetic field term $\propto f \sum_j \sigma_j^z$ to be added to the effective Hamiltonian (5.30). This in turn would destroy the Luttinger-liquid phase as well as the antiferromagnetic and ferromagnetic Ising phases of the XXZ model and transform them into a trivial, paramagnetic phase.

5.7.3 DMRG results for finite $|f|$

The perturbative argument is only valid for sufficiently negative field strengths. In this section we discuss numerical results to connect this limit to the region with finite $|f|$.

In principle, the DMRG simulations allow for a straightforward calculation of the central charge from the entanglement entropy via the Calabrese–Cardy formula (5.20). However, as the entanglement entropy of the XXZ model is sensitive to finite-size effects, a modified relation was proposed [216] taking the finite-size oscillations into account,

$$S_{\mathrm{mod}}(L, l) = S(L, l) + \frac{a \cos(\pi l)}{\frac{L}{\pi} \sin\left(\frac{\pi l}{L}\right)}. \tag{5.35}$$

Furthermore, we study the correlation function

$$G(l) = \left| \langle \sigma_j^\dagger \sigma_{j+l} \rangle \right| \propto l^{-b}, \quad b = \frac{1}{2K}, \tag{5.36}$$

[e] This contradicts the conclusion in Refs. [239, 240], identifying this term as relevant (in some regime). We stress that the numerical evidence never showed any gap appearing as a result of this (small) perturbation, except at the isotropic point.

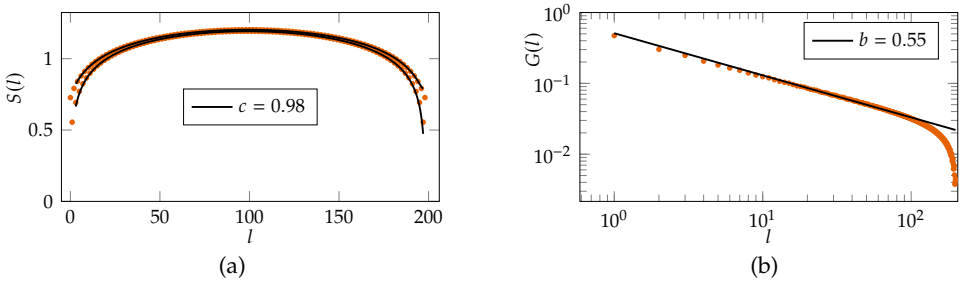

Figure 5.7: DMRG results (orange dots) for the $\mathbb{Z}_3$-ANNNP model for $U = -0.25$, $f = -3$ and $L = 200$. (a) Entanglement entropy, with the fitted prediction (5.35) (solid line). (b) Correlation function $G(l)$ with the corresponding power scaling l^{-b} (solid line).

for which we obtain the scaling exponent b from the XXZ description. With the spin-1/2 projection we recognise

$$\langle \sigma_j^\dagger \sigma_{j+l} \rangle = \langle \tilde{\sigma}_j^+ \tilde{\sigma}_{j+l}^- \rangle \quad \text{with} \quad \tilde{\sigma}^\pm = \mathrm{diag}(0, \sigma^\pm). \tag{5.37}$$

The scaling behaviour then follows from standard bosonization [211].

As an example Figure 5.7 shows fits of these predictions to numerical results for $U = -0.25$ and $f = -3$, confirming $c \approx 1$ in the critical XXZ region as well as determining the Luttinger parameter to be $K = 0.9$.

In Figure 5.8 we show the central charge (c) and the scaling exponent (b) for a cut along $f = -300$. The differently coloured circles correspond to the full $\mathbb{Z}_3$-ANNNP model (red) and the various XXZ perturbative approximations (first order in dark blue, second order without the U(1)-breaking term in light blue, second order with U(1)-breaking term in yellow). First of all, we note that the agreement of the results for the different models is remarkable, convincing us of the validity of the XXZ approximation for $f = -300$. Moreover, the results for the first- and second-order models conserving the U(1) symmetry are indistinguishable. This confirms that the next-nearest neighbour spin-flip term (5.33) is (marginally) irrelevant. Finally, around $U = 1/3$ there is some discrepancy between the different models, indicating that the U(1)-breaking term is important in this regime. Going away from $U = 1/3$, however, the U(1)-breaking term seems irrelevant as well.

We note that the results for both the $\mathbb{Z}_3$-ANNNP model as well as the XXZ approximations appear to show criticality even for $U < -1/3$. We attribute

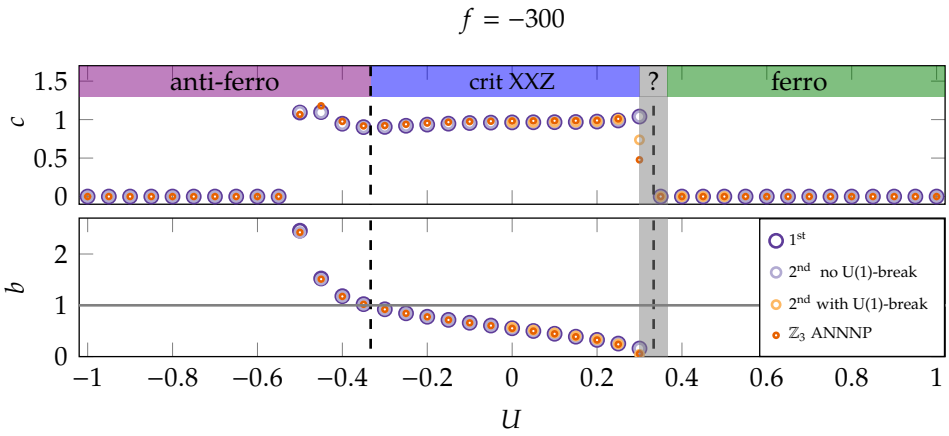

Figure 5.8: Numerical results for the different XXZ approximations (with and without the U(1)-breaking term) and the full $\mathbb{Z}_3$-ANNNP model for $L = 200$ at $f = -300$. The top panel shows the central charge from fitting to the Calabrese–Cardy formula (5.20). The bottom panel shows the power-law scaling for the correlation function $G(l)$. The solid horizontal line at $b = 1$ shows the scaling for the antiferromagnetic Heisenberg model. The vertical dashed lines indicate the transition points.

this to finite-size effects, since the corresponding antiferromagnetic transition in the XXZ model is of Kosterlitz–Thouless type for which the gap opens very slowly [211]. This makes the determination of the transition point from the central charge quite inaccurate. However, the antiferromagnetic transition is also characterised by the Luttinger parameter taking the value $K = 1/2$. We thus use the corresponding value for the scaling exponent ($b = 1$) to locate the transition, as is shown in the bottom panel of Figure 5.8.

We have already seen in Figure 5.8 that in the vicinity of the ferromagnetic transition at $U = 1/3$ the U(1)-breaking term seems to be important. To elaborate on this, we show the central charge and scaling exponents for smaller values of the field, $f = -30$ and $f = -3$, in the upper and middle panels of Figure 5.9. Indeed we observe that the XXZ chain without the U(1)-breaking term does not yield a satisfying description of the full ANNNP model. We also checked (results not shown) that the local state $|0\rangle_j$ is (almost) projected out even for $f = -3$, ie, the restriction of the local Hilbert space to two states is still reasonable. In general we observe that the effective XXZ description is less accurate around the ferromagnetic transition, in particular for $f = -3$ higher-order corrections seem to become important.

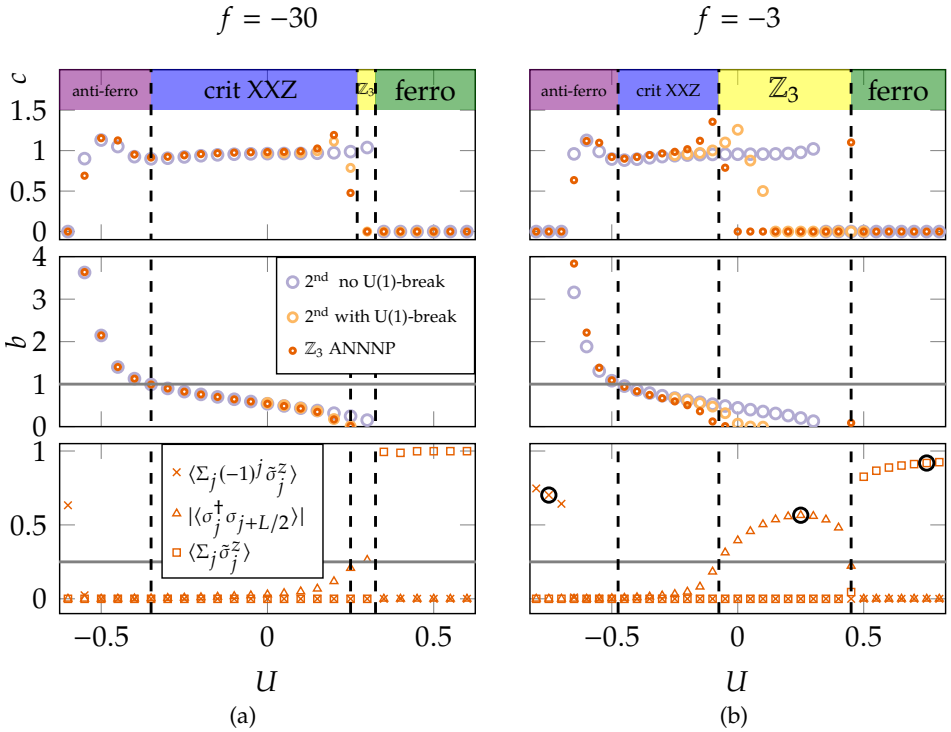

Figure 5.9: Numerical results for the different XXZ approximations (with and without the U(1)-breaking term) and the full $\mathbb{Z}_3$-ANNNP model for $L = 200$ for (a) $f = -30$ and (b) $f = -3$. The top and middle panels show the central charge and scaling exponent respectively; the solid horizontal lines at $b = 1$ indicate the value of the exponent at the antiferromagnetic transition. The bottom panels show the three order parameters introduced in (5.38). Here the solid horizontal line at $1/4$ indicates the value of the long-range order $G(L/2)$ for the ferromagnetic Heisenberg point. The vertical dashed lines indicate the transitions. The black circles highlight the points for which further results are shown in Figure 5.10.

In order to further characterise the gapped phases, we have calculated three order parameters in the full ANNNP model. The results are shown in the bottom panels of Figure 5.9. Specifically, we determined the $\mathbb{Z}_3$-embedded antiferromagnetic and ferromagnetic order parameters as well as the long-range $\mathbb{Z}_3$-order defined as

$$\left\langle\sum_j(-1)^j\tilde{\sigma}^z_j\right\rangle, \quad \left\langle\sum_j\tilde{\sigma}^z_j\right\rangle, \quad G(L/2) = \left|\langle\sigma^\dagger_j\sigma_{j+L/2}\rangle\right|. \tag{5.38}$$

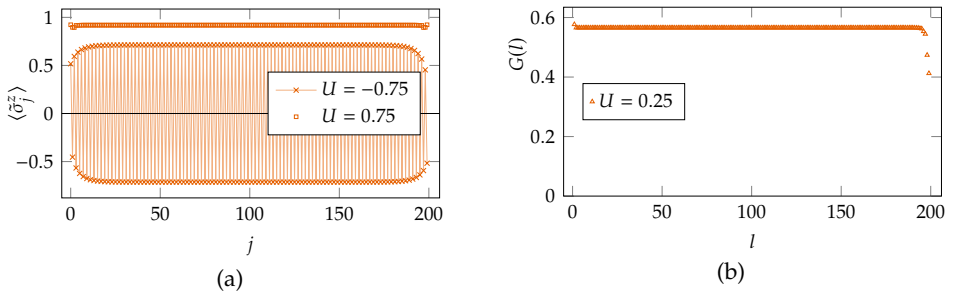

Figure 5.10: Example points displaying the respective order for the various gapped phases for $f = -3$. (a) The antiferromagnetic ($U = -0.75$) and ferromagnetic ($U = 0.75$) behaviour of the local magnetisation. (b) The correlation function (5.36) signalling $\mathbb{Z}_3$/topological order. All data for $L = 200$.

Here $\tilde{\sigma}_j^z = \mathrm{diag}(0, 1, -1)_\tau$ in the local eigenbasis of τ_j. In Figure 5.10 we show the order parameters for representative points in the different gapped phases, clearly confirming the nature of these phases as antiferromagnetic, ferromagnetic and $\mathbb{Z}_3$-long-range ordered, respectively. We note that the study of $G(L/2)$ is preferable over the short-range correlations $|\langle \sigma_j^\dagger \sigma_{j+1} \rangle|$, because the latter can be potentially close to 1 in the critical phase, while the long-range correlation decays with the system size (although with a power law). In contrast, $G(L/2)$ will become constant in the ferromagnetic regime, as can be seen exemplarily in Figure 5.10(b). We also note that the antiferromagnetic and ferromagnetic Ising phases have a two-fold degenerate ground state with a finite energy gap above; see Figure 5.14 in Appendix 5.B.2. On the other hand, in the critical XXZ phase shows an even-odd effect (Figure 5.15, Appendix 5.B.2).

Coming back to the bottom panels of Figure 5.9 we see that the three gapped phases can be well distinguished by the order parameters (5.38). This reveals the nature of the phases and can be used to locate the phase transitions. In particular, the transition between the $\mathbb{Z}_3$-ordered and ferromagnetic phases becomes clear from the crossover in the respective order parameters.

The transition from the Luttinger-liquid phase to the $\mathbb{Z}_3$-ordered phase is more subtle. For this we assume that the transition approaches the Heisenberg ferromagnet and recognise that the long-range order parameter is still finite in the critical phase. For the ferromagnetic Heisenberg model the extensive

ground-state manifold is spanned by

$$|\Psi_0^i\rangle = \frac{1}{\mathcal{N}}(S^-)^i\,|\uparrow\cdots\uparrow\rangle \qquad \text{for } i = 0,\ldots,L, \text{ with } S^- = \sum_{j=1}^{L}\sigma_j^-, \tag{5.39}$$

and $\mathcal{N}$ denoting the normalisation of the states. With some combinatorics, we obtain

$$\langle\Psi_0^i|\sigma_j^+\sigma_{j+l}^-|\Psi_0^i\rangle = i\frac{(L-2)!}{(L-i-1)!}\Big/\frac{L!}{(L-i)!} = \frac{i(L-i)}{L(L-1)} \tag{5.40}$$

Since our system is at half filling, $i = L/2$, the ferromagnetic transition in the thermodynamic limit is characterised by $\langle\sigma_j^\dagger\sigma_{j+L/2}\rangle = \langle\sigma_j^+\sigma_{j+L/2}^-\rangle = 1/4$ [with (5.37)]. Comparing this prediction to the numerical data allows us to locate the remaining transition, as can be seen in Figure 5.9. Note that the result coincides with the point at which $b \to 0$, since $K \to \infty$ as the system approaches the ferromagnetic transition.

Finally, from the topography of the phase diagram shown in Figure 5.12 in Appendix 5.B.1 we deduce that the antiferromagnetic region extends up to vanishing f, while the transition to $\mathbb{Z}_3$-ordered phase keeps the ferromagnetic region from touching the $f = 0$ axis (in the studied range for U). We also infer, in combination with the discussion above, that XXZ critical region extends up to $U = -1, f = 0$ where the critical point with $c = 8/5$ is located. We would like to stress that the vicinity of this point is very difficult to study numerically, since both the left and right transitions are rather soft. Similar difficulties were experienced in the vicinity of a multi-critical point in the ANNNI model [220].

5.7.4 Results along an almost frustration-free line

As discussed in Section 5.6 the model possesses two frustration-free points in the phase diagram, G_1 and G_2. These points are characterised by the fact that the local Hamiltonian

$$h_{j,j+1} = -\sigma_j\sigma_{j+1}^\dagger - \frac{f}{2}(\tau_j + \tau_{j+1}) + U\tau_j\tau_{j+1} + \text{h.c.} \tag{5.41}$$

has a threefold degenerate local ground state (one for each sector), and that all local Hamiltonians can be minimised simultaneously, giving a threefold degenerate ground state of the full system [124, 145].

While it is not possible to find further frustration-free points in the phase diagram, we can obtain an "almost frustration-free (AFF) line" by only requiring that the local Hamiltonian (5.41) has a threefold degenerate ground state. This yields the relation

$$U_{\mathrm{AFF}} = \frac{1}{2}\left[\frac{f}{2} - \sqrt{1 + \frac{f}{3} + \frac{f^2}{4}} + \sqrt{1 + f^2 - \frac{2f}{3}}\right], \tag{5.42}$$

of which the points G_1 and G_2 are special cases, see Figure 5.11 for a sketch. Away from these points the many-body ground states cannot be written as exact product states, however, there are product states that turn out to be very close to the true ground states. Let us define

$$|\Phi_k\rangle = \bigotimes_{j=1}^{L}\left(|0\rangle_j + \alpha\omega^k\,|1\rangle_j + \alpha\omega^{2k}\,|2\rangle_j\right), \quad \alpha = \frac{1}{4}\left[-2 - 3f + \sqrt{36 + 3f(4+3f)}\right], \tag{5.43}$$

for $k = 0, 1, 2$.

Note that these states are not orthonormal, so we consider the orthogonal basis

$$|\Psi_l^{\mathrm{approxGS}}\rangle = \frac{1}{N_l}\left[|\Phi_0\rangle + \omega^{-l}\,|\Phi_1\rangle + \omega^{-2l}\,|\Phi_2\rangle\right], \quad l = 0, 1, 2, \tag{5.44}$$

which are eigenstates of the symmetry operator $\omega^P = \prod_j \tau_j$ as well, with corresponding eigenvalues ω^l, displaying the $\mathbb{Z}_3$-ordered nature of the phase.

The overlap $|\langle\Psi_l^{\mathrm{approxGS}}|\Psi_l\rangle|$ of these approximate eigenstates with the numerical ground states is shown in Figure 5.11. We note that the overlap improves for decreasing f. For example, at $f = -10$ we obtain $|\langle\Psi_l^{\mathrm{approxGS}}|\Psi_l\rangle| \approx (0.9997)^L$, resulting in a 97% overlap for $L = 100$. Even though the approximate ground states are not exact eigenstates, their resemblance to the actual ground states strongly suggests that along the line (5.42) the system possesses a $\mathbb{Z}_3$-ordering. Obviously, for $f = 0$ we recover the trivial point G_1. In the other limit, $f \to -\infty$, the line approaches $U = 1/3$, thus exactly pinching in between the critical XXZ and Ising ferromagnetic regions. This suggests[f] that the $\mathbb{Z}_3$-ordered phase indeed connects to the ferromagnetic transition of the effective XXZ chain.

[f] We note that the approximate ground states (5.44) simplify in this limit to $\bigotimes_j(\omega^k\,|1\rangle_j + \omega^{2k}\,|2\rangle_j) \equiv \bigotimes_j(\omega^k\,|\uparrow\rangle_j + \omega^{2k}\,|\downarrow\rangle_j)$, which belong to the ground-state manifold of the ferromagnetic XXZ chain at $U = 1/3$.

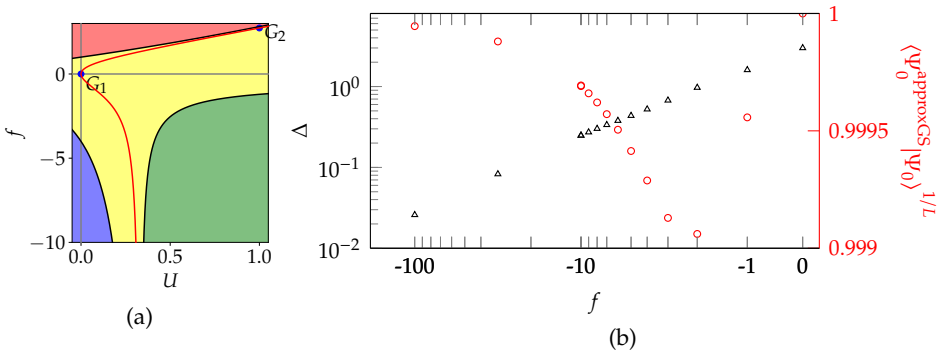

Figure 5.11: (a) The red line indicates the location of the almost frustration-free line (5.42) inside the topological (yellow) phase. (b) Energy gap Δ above the ground-state manifold and overlap $\langle \Psi_l^{\text{approxGS}} | \Psi_l \rangle$ along the almost frustration-free line. Both results were obtained by fitting the data for $L = 40, 45, \ldots, 60$.

5.8 Discussion

In this chapter we have studied an extended parafermion chain, which possessed terms coupling parafermions on four neighbouring sites. We mapped the model to the non-chiral $\mathbb{Z}_3$-ANNNP model via a Fradkin–Kadanoff transformation and analysed the phase diagram for weak to moderate couplings of the four-site term. By applying a combination of DMRG simulations, scaling arguments and analytical results in special limiting cases we identified four gapped phases: a topological phase possessing a three-fold degenerate ground state, a trivial (paramagnetic) phase as well as an antiferromagnetic and ferromagnetic Ising ordered phase. The latter two as well as an additional critical Luttinger-liquid phase can be connected to the well-known phase diagram of the XXZ Heisenberg chain. We provided evidence that the topological phase is pinched between the Luttinger-liquid phase and the ferromagnetic Ising phase and extends to the limit of arbitrarily negative field strengths f. Furthermore, we discussed a possible experimental realisation of the extended parafermion chain using hetero-nanostructures consisting of ferromagnets, superconductors and fractional quantum Hall states.

In this chapter we have omitted the large U regime, which is explored in Chapter 6 in great detail. There are several other directions for future studies: (i) The $\mathbb{Z}_3$-symmetry of the model (5.14) allows the inclusion of terms in addition to $U \sum_j (\tau_j \tau_{j+1} + \text{h.c.})$. For example, including a term $\sim \sum_j (\tau_j \tau_{j+1}^\dagger + \text{h.c.})$ allows the construction [124, 145] of a family of frustration-free models, of which the points

G_1 and G_2 in Figure 5.2 are just special cases. These frustration-free models could serve as starting point for an analytic study of the topological phase. We note that the addition of such a term is also feasible within the framework of the hetero-nanostructures discussed in Section 5.3. (ii) The properties of the parafermion chain critically depend on the chirality breaking in the model, see, eg, References [221, 222, 232] for studies of the phase diagram in chiral parafermion chains. Thus it would be natural to extend the model (5.14) by including chirality breaking, which, as indicated in Section 5.7.2, is expected to have a drastic effect on the phase diagram.

5.A Duality transformation

In this appendix we discuss the duality transformation of the Potts model (see, eg, Reference [243]), with extra care to treat the boundary terms. We start with the Hamiltonian (5.14)

$$H = -\sum_{j=1}^{L-1} \sigma_j \sigma_{j+1}^\dagger - f \sum_{j=1}^{L} \tau_j + U \sum_{j=1}^{L-1} \tau_j \tau_{j+1} + \text{h.c.} \tag{5.45}$$

Let us now apply the following transformation,

$$\nu_j = \sigma_j \sigma_{j+1}^\dagger, \quad \mu_j = \prod_{i \le j} \tau_i^\dagger \qquad \Leftrightarrow \qquad \sigma_j = \prod_{i<j} \nu_i^\dagger, \quad \tau_j = \mu_{j-1} \mu_j^\dagger, \tag{5.46}$$

with auxiliary operator $\sigma_1 = \nu_0^\dagger$ and the exception $\tau_1 = \mu_1^\dagger$. Note that ν_L is not defined, which is not a problem for the moment. Applying this, the dual Hamiltonian reads

$$H = -\sum_{j=1}^{L-2} \nu_j - f \sum_{j=1}^{L-1} \mu_j \mu_{j+1}^\dagger + U \sum_{j=1}^{L-2} \mu_j \mu_{j+2}^\dagger + B + \text{h.c.} \tag{5.47}$$

where $B = -\nu_{L-1} - f\mu_1^\dagger + U\mu_2^\dagger$. Up to boundary terms, for $U = 0$ we recognise that (5.45) and (5.47) are physically equivalent at $f = 1$, ie, the model is self-dual at this point in the thermodynamic limit. We note that the model (5.47) has been studied by[g] Zhang et al. [232] with a focus on the phase diagram in the presence of chirality breaking.

[g] The relation between the parameters in Equation (4) of Reference [232] and the ones in (5.47) is given by $h \to J \equiv 1$, $J \to f$ and $J' \to U$. In particular, the supercritical point corresponds in our convention to the limit $f = 2U$ with $U \to \infty$, indicating that the Potts transition between the trivial and topological phases extends to arbitrary large U.

Next, we turn off the perpendicular field, ie, we consider $f = 0$. The operators ν and μ can be split on the odd/even (o/e) sites to obtain

$$H = -\sum_{a=\mathrm{o,e}} \left[\sum_{j=1}^{L/2-1} \nu_j^a - U \sum_{j=1}^{L/2-1} \mu_j^a (\mu_{j+1}^a)^\dagger \right] + B + \text{h.c.}, \tag{5.48}$$

where $B = -\nu_{L/2}^{\mathrm{o}} + U(\mu_1^{\mathrm{e}})^\dagger$ contains the boundary terms. We recognise two decoupled Potts chains in their dual representation: For each chain we can do another duality transformation

$$\tau_j^a = \mu_j^a (\mu_{j+1}^a)^\dagger, \quad \sigma_j^a = \prod_{i \le j} (\nu_i^a)^\dagger \quad \Leftrightarrow \quad \mu_j^a = \prod_{i<j} (\tau_i^a)^\dagger, \quad \nu_j^a = \sigma_{j-1}^a (\sigma_j^a)^\dagger, \tag{5.49}$$

with auxiliary operator $\mu_1 = \tau_0^\dagger$ and the exception $\nu_1^a = (\sigma_1^a)^\dagger$. This gives

$$H = -\sum_{a=\mathrm{o,e}} \left[\sum_{j=1}^{L/2-2} \sigma_j^a (\sigma_{j+1}^a)^\dagger - U \sum_{j=1}^{L/2-1} \tau_j^a \right] + B + \text{h.c.} \tag{5.50}$$

with

$$B = -\left(\nu_{L/2}^{\mathrm{o}} - \nu_1^{\mathrm{e}} - \nu_1^{\mathrm{o}} \right) + U(\mu_1^{\mathrm{e}})^\dagger. \tag{5.51}$$

It is interesting to relate the original order parameter σ_j to the new operators σ_j^a,

$$\sigma_j = \begin{cases} \prod_{i<(j-1)/2} (\nu_i^{\mathrm{o}})^\dagger (\nu_i^{\mathrm{e}})^\dagger & = \sigma_{(j-1)/2}^{\mathrm{o}} \sigma_{(j-1)/2}^{\mathrm{e}}, \qquad j \text{ odd}, \\ \left[\prod_{i<j/2} (\nu_i^{\mathrm{o}})^\dagger (\nu_i^{\mathrm{e}})^\dagger \right] (\nu_{j/2}^{\mathrm{o}})^\dagger & = \sigma_{j/2-1}^{\mathrm{e}} \sigma_{j/2}^{\mathrm{o}}, \qquad j \text{ even}, \end{cases} \tag{5.52}$$

with the inverse relation given by

$$\sigma_j^a = \begin{cases} \prod_{i<j} \nu_{2i-1}^\dagger = \prod_{i<2j} (\sigma_i)^{(-1)^i}, & a = \mathrm{o}, \\ \prod_{i<j} \nu_{2i}^\dagger = \prod_{2<i<2j+1} (\sigma_i)^{-(-1)^i}, & a = \mathrm{e}. \end{cases} \tag{5.53}$$

Thus we see that the relation is non-local involving string operators. We also rewrite the symmetry operator, $\omega^P = \prod_j \tau_j = \mu_L^\dagger = (\mu_{L/2}^{\mathrm{e}})^\dagger = \prod_j \tau_j^{\mathrm{e}}$. For $f = 0$, the original Hamiltonian has another symmetry $\tilde{\omega}^P = \prod_j \sigma_j = \prod_{j,a} (\sigma_j^a)^\dagger$.

Finally, for completeness we reinstate the f-term for the second transformation. Even though the resulting lattice model is non-local in terms of the original operators σ and τ, the following expression will be useful in Section 5.6.2

$$H = -\sum_{a=\mathrm{o,e}} \left[\sum_{j=1}^{L/2-1} v_j^a - U \sum_{j=1}^{L/2-1} \mu_j^a (\mu_{j+1}^a)^\dagger \right] - \sum_{j=1}^{L/2-1} f \mu_j^{\mathrm{e}} \left[(\mu_j^{\mathrm{o}})^\dagger + (\mu_{j+1}^{\mathrm{o}})^\dagger \right] + B + \mathrm{h.c.} \tag{5.54}$$

with $B = -v_{L/2}^{\mathrm{o}} - f \left[(\mu_1^{\mathrm{o}})^\dagger + \mu_{L/2}^{\mathrm{o}} (\mu_{L/2}^{\mathrm{e}})^\dagger \right] + U (\mu_1^{\mathrm{e}})^\dagger$.

5.B Supporting numerical results

In this appendix we present additional numerical material to support certain points in the main text.

5.B.1 Rough topography of the phase diagram

The overall structure of the phase diagram presented in Section 5.5 was determined largely based on an inexpensive DMRG calculation, ie, for small systems ($L = 50 - 100$). The results of these calculations are shown in Figure 5.12. It displays the central-cut entanglement entropy and central charge. The entanglement entropy follows naturally from the DMRG calculation. With Schmidt decomposition we can write the ground state as

$$|\Psi\rangle = \sum_a s_a \, |\Psi_a^A\rangle \, |\Psi_a^B\rangle \,, \tag{5.55}$$

where A, B are the left and right subsystems, such that $L_A + L_B = L$ and $\sum_a s_a^2 = 1$. Also $|\Psi_a^A\rangle$ and $|\Psi_a^B\rangle$ form an orthonormal basis in their respective subspace. The reduced density matrix becomes

$$\rho_A = \mathrm{Tr}_B \rho = \sum_a s_a^2 \, |\Psi_a^A\rangle \, \langle \Psi_a^A| \,, \tag{5.56}$$

with the entanglement entropy given by [81]

$$S(L, L_A) = -\mathrm{Tr} \rho_A \log(\rho_A) = -\sum_a s_a^2 \log(s_a^2). \tag{5.57}$$

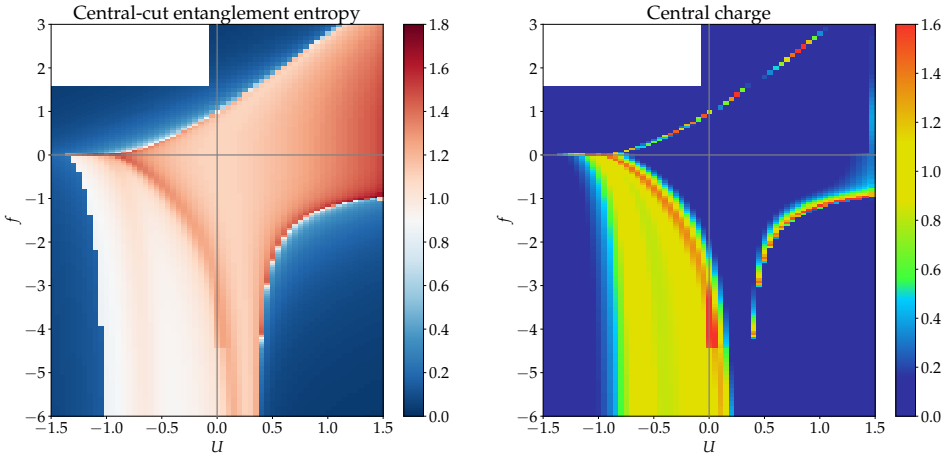

Figure 5.12: Rough topography of the phase diagram for the $\mathbb{Z}_3$-ANNNP model. The central-cut entanglement entropy and central charge results were obtained for small system sizes L =50–100 and low bond dimension in the parity sector 0. Even though the nature of the phases and transitions cannot be conclusively derived from these plots, it gives a good visual guide for the features to be studied in more detail.

The area law predicts that the entanglement entropy should be constant with respect to system size for gapped systems, which can be used as a first tool to identify gapped phases studying the central-cut entanglement entropy $S(L, L/2)$.

As an example, consider the unique product state (5.15) the central-cut entanglement entropy is simply given by $S = -1\log(1) = 0$. In the top left of the phase diagram in Figure 5.12a we find $S \approx 0$, indicating that this region is indeed connected to the trivial product state. On the other hand, for the $\mathbb{Z}_3$-ordered phase at $U = f = 0$, the ground state for each parity sector is a linear combination of the three degenerate ground states (5.17). Hence the central-cut entanglement entropy is given by $S = -\sum_{a=0}^{2} \frac{1}{3}\log(1/3) = \log(3) \approx 1.09$, which we observe throughout the topological phase. We note that the central-cut entanglement entropy can also be deceiving. For example, the ground states for the antiferromagnetic and ferromagnetic phases for $f < 0$ seem to be singly degenerate ($S = 0$), while they are in fact doubly degenerate with the two degenerate ground states lying in different symmetry sectors and the central-cut entanglement entropy vanishing in each of them.

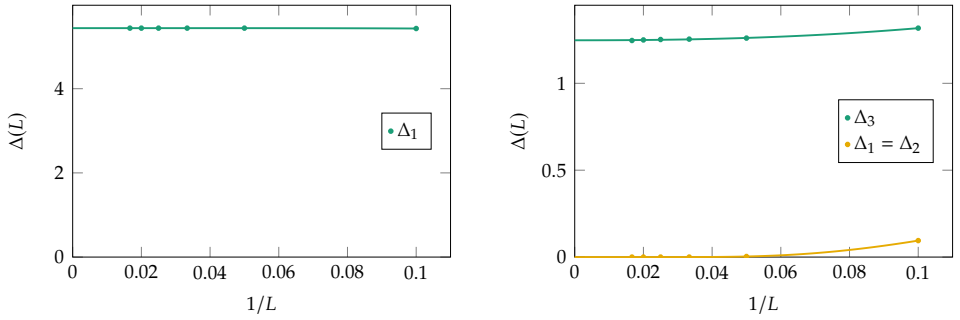

(a) Paramagnetic/trivial ($f = 1, U = -1$) (b) $\mathbb{Z}_3$-ordered/topological ($f = 1, U = 1$)

Figure 5.13: Energy gaps Δ_n between the nth energy eigenstate and the ground state, obtained from finite-size scaling for system sizes $L = 10, \ldots, 60$: (a) at $f = 1, U = -1$ in the paramagnetic/trivial phase, (b) at $f = U = 1$ in the $\mathbb{Z}_3$-ordered/topological phase.

In the critical regions the central-cut entanglement entropy is not a good indicator, since it diverges logarithmically with the system size. Instead, here we employ the central charge c obtained by fitting the entanglement entropy (5.57) to the Calabrese–Cardy formula [209, 210] (5.20). It is important to note that this fit only give a qualitative view. The central charge in Figure 5.12b(b) is often overestimated at points close to transitions, because at finite sizes the correlation lengths exceed the system size. Nevertheless, it shows the presence of a transition in the top left and bottom right. Moreover, there are several critical regions that can be identified, in particular the critical XXZ phase in the bottom left (see Section 5.7).

5.B.2 Finite-size scaling of energy gaps

Here we present data for the finite-size scaling in the gapped regions discussed in Sections 5.6 and 5.7. The plots in Figure 5.13 show the gap for the paramagnetic/trivial phase and $\mathbb{Z}_3$-ordered/topological phase. These confirm both the thermodynamic gaps and the respective degeneracies of the ground states.

In Figure 5.14 we show the finite-size scaling for the energy gap in the antiferromagnetic and ferromagnetic phase described in Section 5.7, showing that both are indeed gapped with a two-fold degeneracy.

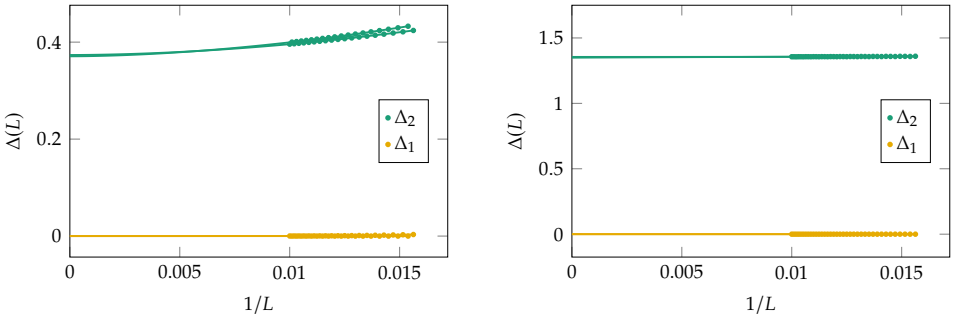

(a) Ising antiferromagnetic ($f = -3, U = -0.75$)

(b) Ising ferromagnetic ($f = -3, U = 0.75$)

Figure 5.14: Finite-size scaling of the energy gaps Δ_n for representative points in the Ising antiferromagnetic (a) as well as the Ising ferromagnetic (b) phase. Both DMRG results are for system sizes $L = 64, 65, \ldots, 100$. In both cases we find $\Delta_1 = 0$, showing that the ground states are two-fold degenerate, while $\Delta_2 > 0$ in the thermodynamic limit.

On the other hand, in Figure 5.15 we see that both the gap to the first and second excited states vanish at $U = -0.25, f = -3$, thus this point indeed belongs to a critical region. There is even-odd effect in the finite-size gap that we can explain from the effective XXZ description; for an extensive discussion see Reference [216]. For even chain lengths (and in the absence of a magnetic field) the ground state is unique with total spin $\langle S^z \rangle = \langle \sum_j \sigma_j^z \rangle = 0$. The first excited state is two-fold degenerate with $\langle S^z \rangle = \pm 1$, with the two states related by a global spin flip. On the other hand, for odd lengths the smallest magnetisation commensurate with the system is $\langle S^z \rangle = \pm \frac{1}{2}$, hence there is a double degeneracy of the ground states. We recognise this pattern in the finite-size scaling in Figure 5.15.

5.C Effective XXZ chains

In this appendix we derive the effective XXZ chain describing the limit $f \to -\infty$, which was presented in Section 5.7.2. We note that a similar expansion has been obtained in Reference [239].

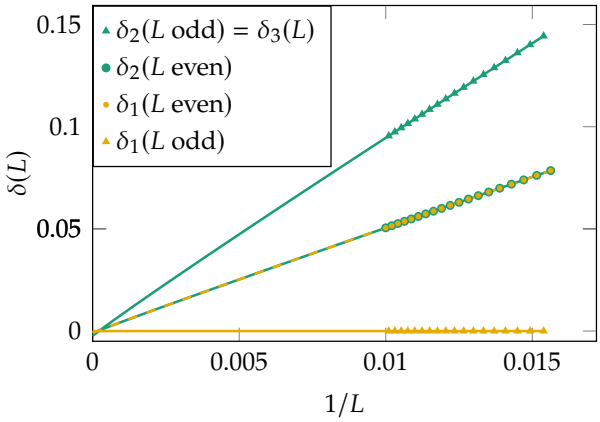

Figure 5.15: Finite-size scaling of the gap δ_n to the n-th excited states from system sizes $L = 64, 65, \ldots 100$ for the system in the critical XXZ phase ($U = -0.25$, $f = -3$).

5.C.1 First-order term

The eigenvalues of the local field term $-f(\tau_j + \tau_j^\dagger)$ are $-2f, f, f$ for the eigenstates $|0\rangle_j, |1\rangle_j, |2\rangle_j$ respectively. Thus for $f \to -\infty$ there will be a large energy gap between the state $|0\rangle_j$ and the states $|1\rangle_j, |2\rangle_j$, which allows us to project onto a local, two-dimensional Hilbert space. Let us denote the resulting projected many-body Hilbert space by $\mathcal{G}$, with the notation $|\Psi_i\rangle \in \mathcal{G}$ and $|\Phi_i\rangle \notin \mathcal{G}$, and the respective energies due to this leading term by E_{Ψ_i} and E_{Φ_i}. For the remaining terms we can write down an effective first-order Hamiltonian describing the action of $V^\sigma = \sum_j v_j^\sigma$, with $v_j^\sigma = -\sigma_j \sigma_{j+1}^\dagger - \sigma_j^\dagger \sigma_{j+1}$, ie, terms that represent $\langle \Psi_i | V^\sigma | \Psi_k \rangle$. If we view the operators as tensor products of 2×2 matrices acting on the local states $|1\rangle_j, |2\rangle_j$, we can write

$$-\sigma_j \sigma_{j+1}^\dagger - \sigma_j^\dagger \sigma_{j+1} = -\sigma_j^+ \sigma_{j+1}^- - \sigma_j^- \sigma_{j+1}^+, \tag{5.58}$$

with $\sigma_j^\pm$ being the effective spin-1/2 raising and lowering operators acting at site j, ie, $\sigma_j^+ = |1\rangle_j \langle 2|_j$ and $\sigma_j^- = |2\rangle_j \langle 1|_j$. Similarly, we have $\sigma_j^z = |1\rangle_j \langle 1|_j - |2\rangle_j \langle 2|_j$. Using this we recognise that

$$\tau_j = \omega^{\sigma_j^z} = -\frac{1}{2} + \mathrm{i}\frac{\sqrt{3}}{2}\sigma_j^z. \tag{5.59}$$

This allows us to rewrite the term $U\tau_j\tau_{j+1} + \text{h.c.}$ as

$$U\tau_j\tau_{j+1} + \text{h.c.} = -\frac{3U}{2}\sigma_j^z\sigma_{j+1}^z + \frac{U}{2}. \tag{5.60}$$

Taken together we thus deduce that at leading order the effective Hamiltonian describing the large $-f$ limit of the ANNNP model becomes

$$H_{\text{eff}}^{(1)} = -\sum_j \left[\sigma_j^+\sigma_{j+1}^- + \sigma_j^-\sigma_{j+1}^+ + \frac{3U}{2}\sigma_j^z\sigma_{j+1}^z\right]. \tag{5.61}$$

Hence the behaviour of the ANNNP model in this limit is governed by the XXZ Heisenberg chain, which is known to be critical for $|U| \leq 1/3$ with central charge $c = 1$ [211].

5.C.2 Second-order term

The second-order terms originate from perturbations of the form

$$\sum_k \frac{\langle\Psi_i|V^\sigma|\Phi_k\rangle\langle\Phi_k|V^\sigma|\Psi_l\rangle}{E_\Psi - E_{\Phi_k}}, \tag{5.62}$$

where $E_\Psi = E_{\Psi_i} = E_{\Psi_l}$ the unperturbed energies of the ground states. Let us start with the contributions to effective two-site terms. The diagonal terms read

$$\frac{\langle 12|v_j^\sigma|00\rangle\langle 00|v_j^\sigma|12\rangle}{E_\Psi - E_{\Phi_k}} = \frac{\langle 21|v_j^\sigma|00\rangle\langle 00|v_j^\sigma|21\rangle}{E_\Psi - E_{\Phi_k}} = \frac{1}{6f}, \tag{5.63}$$

$$\frac{\langle 11|v_j^\sigma|20\rangle\langle 20|v_j^\sigma|11\rangle}{E_\Psi - E_{\Phi_k}} + \frac{\langle 11|v_j^\sigma|02\rangle\langle 02|v_j^\sigma|11\rangle}{E_\Psi - E_{\Phi_k}} \tag{5.64}$$

$$= \frac{\langle 22|v_j^\sigma|10\rangle\langle 10|v_j^\sigma|22\rangle}{E_\Psi - E_{\Phi_k}} + \frac{\langle 22|v_j^\sigma|01\rangle\langle 01|v_j^\sigma|22\rangle}{E_\Psi - E_{\Phi_k}} = \frac{2}{3f}, \tag{5.65}$$

which can be summarised as $\frac{1}{4f}\sigma_j^z\sigma_{j+1}^z + \frac{1}{2f}$. Similarly, the off-diagonal two-site contribution is given by

$$\frac{\langle 12|v_j^\sigma|00\rangle\langle 00|v_j^\sigma|21\rangle}{E_\Psi - E_{\Phi_k}} = \frac{1}{6f}, \tag{5.66}$$

which becomes the spin-flip term $\frac{1}{6f}(\sigma_j^+\sigma_{j+1}^- + \sigma_j^-\sigma_{j+1}^+)$. Furthermore, there are three-site contributions such as

$$\frac{\langle 111|v_{j+1}^\sigma|102\rangle\,\langle 102|v_j^\sigma|222\rangle}{E_\Psi - E_{\Phi_k}} + \frac{\langle 111|v_j^\sigma|201\rangle\,\langle 201|v_{j+1}^\sigma|222\rangle}{E_\Psi - E_{\Phi_k}} = \frac{2}{3f}, \tag{5.67}$$

and its hermitian conjugate, which taken together become $\frac{2}{3f}(\sigma_j^+\sigma_{j+1}^+\sigma_{j+2}^+ + \sigma_j^-\sigma_{j+1}^-\sigma_{j+2}^-)$. This term breaks the U(1) symmetry of the XXZ chain, but preserves the $\mathbb{Z}_3$-symmetry.

Finally, there is a next-nearest neighbour hopping term,

$$\frac{\langle 112|v_j^\sigma|202\rangle\,\langle 202|v_{j+1}^\sigma|211\rangle}{E_\Psi - E_{\Phi_k}} = \frac{\langle 122|v_{j+1}^\sigma|101\rangle\,\langle 101|v_j^\sigma|221\rangle}{E_\Psi - E_{\Phi_k}} = \frac{1}{3f}, \tag{5.68}$$

which can be written as $\frac{1}{3f}(\sigma_j^+\sigma_{j+2}^- + \sigma_j^-\sigma_{j+2}^+)$. Taken together we arrive at the second-order Hamiltonian

$$\begin{aligned} H_{\text{eff}}^{(2)} = \sum_j \Bigg[&\frac{1}{6f}(\sigma_j^+\sigma_{j+1}^- + \sigma_j^-\sigma_{j+1}^+) + \frac{1}{4f}\sigma_j^z\sigma_{j+1}^z \\ &+ \frac{1}{3f}(\sigma_j^+\sigma_{j+2}^- + \sigma_j^-\sigma_{j+2}^+) + \frac{2}{3f}(\sigma_j^+\sigma_{j+1}^+\sigma_{j+2}^+ + \sigma_j^-\sigma_{j+1}^-\sigma_{j+2}^-)\Bigg]. \end{aligned} \tag{5.69}$$

5.C.3 U(1) breaking term

Following the bosonisation dictionary of Giamarchi [211] the low-energy behaviour of the XXZ model is governed by a Luttinger liquid

$$H = \frac{u}{2\pi}\int dx \left[K\left(\nabla\theta(x)\right)^2 + \frac{1}{K}\left(\nabla\phi(x)\right)^2\right], \tag{5.70}$$

with ϕ and θ being a bosonic field and its dual, and (at $f = -\infty$)

$$K = \frac{\pi}{2\arccos(3U)}, \quad u = \frac{1}{2 - 1/K}\sin\left[\pi\left(1 - 1/2K\right)\right] \tag{5.71}$$

denoting the Luttinger parameter and velocity respectively. The local spin-flip operators σ_j^+ are related to the bosonic field via [the Fermi momentum is given by $k_F = \pi/(2a)$]

$$\sigma_j^+ = \sqrt{a} S^+(x) = \frac{e^{-\mathrm{i}\theta(x)}}{\sqrt{2\pi}} \Big[(-1)^x + \cos(2\phi(x)) \Big], \tag{5.72}$$

where $x = ja$ with a being the lattice constant (which we set to one), and $S^+(x)$ the continuum operator related to σ_j^+. With this in mind the U(1)-breaking term in $H_{\text{eff}}^{(2)}$ will become a sum of terms of the form $e^{-\mathrm{i}a\theta(x) - \mathrm{i}b\phi(x)}$ with individual scaling dimensions $\Delta_{a,b} = \frac{a^2}{4K} + \frac{b^2 K}{4}$. Some of these terms will contain rapidly oscillating factors $(-1)^x$, which will thus not contribute in the continuum limit. The leading non-oscillating term turns out to possess the scaling dimension

$$\Delta_{+++} = \frac{9}{4K} + K, \tag{5.73}$$

which is strictly larger than 2 for any value of K. Thus we conclude that the term $\propto \sigma_j^+ \sigma_{j+1}^+ \sigma_{j+2}^+$ is irrelevant in the Luttinger-liquid regime.

6 Strong interaction for extended parafermion chain

This chapter contains unpublished results, continuing the investigation from Chapter 5.

In Chapter 5 we have encountered an extended parafermion/$\mathbb{Z}_3$-ANNNP chain. Besides the topological and trivial phases, present for the unaltered parafermion chain [61], the additional interaction gave rise to emergent XXZ phases. Nevertheless, the discussion was confined to small interactions, warranted by the experimental suggestions. Moreover, the phases and transitions for $U < 1.5$ are well understood.

In this chapter we present the findings for $U > 1.5$. These understanding of the large interaction regime is by no means comparable to the results in the previous chapter. However, the compelling nature of the phases and transitions justifies the discussion.

6.1 Introduction

For the ANNNI model [140, 144] large interactions give rise to new phases. Besides the usual topological and trivial phase, a critical incommensurate and insulating Mott phase appear [44, 45, 220, 227–229]. For the extended parafermion/$\mathbb{Z}_3$ ANNNP chain (see Equation (5.14) in Section 5.4) we encounter an even richer phase diagram, see Figure 6.1. The rough topography of the phase diagram was obtained from an inexpensive DMRG calculation, see Figure 6.7 of the supporting numerical results in Appendix 6.A. There appear several critical regions, with exotic nature. Besides a $c = 2$ line, which is related by duality to the XXZ phase in Section 5.7, there is an unknown $c = 1$ phase for $f < 0$ and an intricate XXZ like phase related to large U, f. Certain areas are left grey, because our data was not conclusive here. This came mostly down to

a lack of computing power, when dealing with highly critical phases. Part of the discussion in Reference [232] also considered this corner of the phase diagram, albeit in a different parametrization and focussing mainly on the $f \to \infty$ regime. However, the extend and nature of their critical region (for $U, f > 1$) is equivalent. Also for the analogous $\mathbb{Z}_6$-ANNNP chain a comparable critical phase has been found in this regime in Ref. [186].

In this chapter we discuss the findings into this elaborate part of the parameter space. By virtue of duality transformations discussed in Appendix 5.A we recognize XXZ behaviour along $f = 0$, further discussed in Section 6.2. Moreover for $f \gg 1$, there is a correspondence to another XXZ chain, that shows an intricate even-odd effect, as described in Sections 6.3, 6.4 and 6.5. Finally, we elaborate on the grey transition regions in Section 6.6.

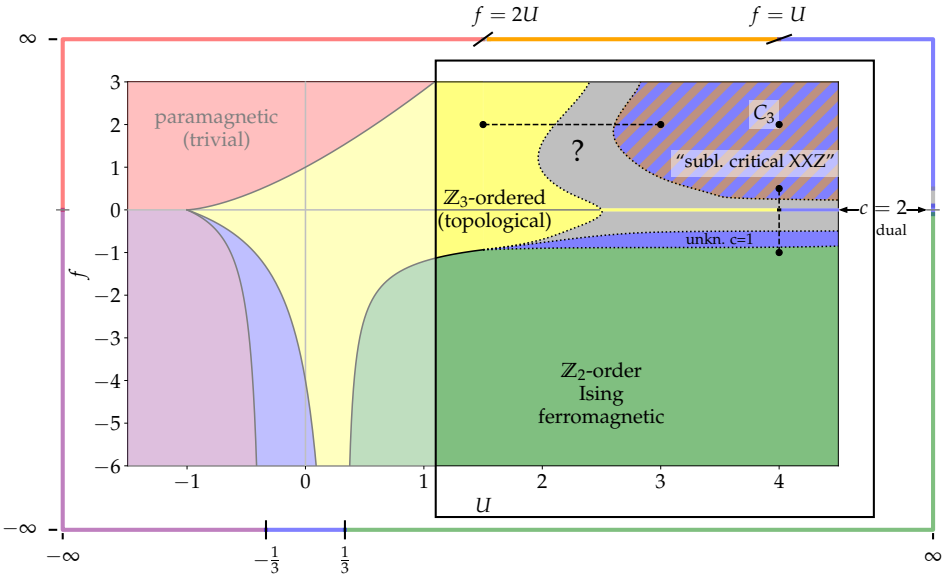

Figure 6.1: An extension of the phase diagram in Figure 5.2, showing $U > 1.5$. Here are some critical region that have been determined in detail. The transitions are still poor understood. The dashed horizontal (Figure 6.6a) and vertical line (Figure 6.6b) correspond to detailed cuts.

6.2 Duality transformation $f = 0$

The duality transformations of Appendix 5.A illustrate that the physics along the $f = 0$ line corresponds to two decoupled copies of the quantum Potts model ($U = 0$) line, where $-U$ takes the role of f. With this in mind we deduce from Section 5.7 that there exists a topological phase for $U \lesssim 4$ and a critical XXZ-like phase for $U \gtrsim 4$ [221]. Since the duality transformations dictate two decoupled Potts copies, the critical line is described by a CFT with $c = 2$, shown in Figure 6.1 as the blue line along the $U = 0$ axis. The topological phase is depicted by the yellow line. In Figure 6.2a the finite size scaled central charge is shown for $f = 0$ and $U \in [2, 5]$. This confirms the $c \approx 2$ for $U \gtrsim 4$. For $U \in [2, 4]$ the central charge data is inconclusive. The gap close to this Pokrovsky–Talapov transition (PTT) opens very slowly, making it seemingly critical. Here we lean on the more detailed results from Ref. [221] and the duality transformation to locate the transition at $U \approx 4$. Moreover, to illustrate the challenge around a PTT we compare it to the $U = 0$, $f = -4$ transition directly related to the results from Ref. [221]. The central charge around this point, shown in Figure 6.2b, displays similar ambiguous behaviour when approaching the soft PTT. Finally, we note that this duality argument does not offer any insight for $f \neq 0$, since the perturbation coupled to f is non-local in the dual representation. Where the numerical results showed conclusive evidence for $f \neq 0$ the phase diagram is coloured accordingly in Figure 6.1. Otherwise, the unknown phase is shown in grey.

6.3 Classical limit $f \gg 1$

In the previous chapter we encountered the paramagnetic phase for $f \gg 1$, see Equation (5.15). The simple product state $|0\rangle_\tau^{\otimes L}$ is the ground state for $f > 2U$. This limit is classical in the sense that all terms of the Hamiltonian commute. Because of the dominating U, f, the σ terms are negligible, the remaining τ terms commute.

In this chapter we focus on large $U > 1.5$, as indicated in Figure 6.1. We will observe that this region connects to the classical limit for $f < 2U$. Contrary to the paramagnetic phase, the ground state for this region is a highly degenerate product state. The low energy states show a two-site pattern in the following way

$$|\ldots, i, 0, j, 0, k, 0, l, \ldots\rangle\,, \quad \text{with } i, j, k, l = 1, 2, \tag{6.1}$$

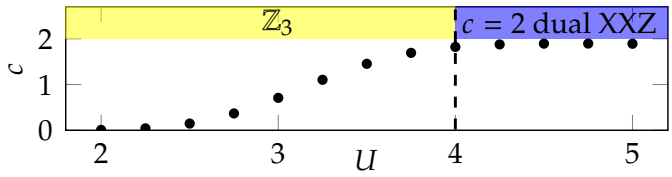

(a) $f = 0$

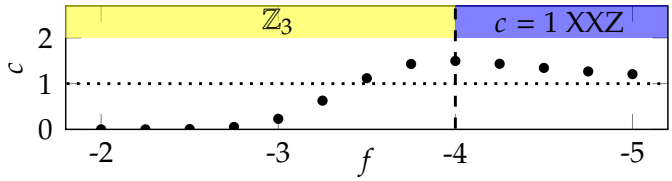

(b) $U = 0$

Figure 6.2: Central charge for $U \in [2,5], f = 0$ in (a) and $U = 0, f \in [-5,-2]$ in (b). Data obtained from fitting Equation 5.20 to the finite size central-cut entanglement from DMRG for $L = 64, 76, \ldots, 100$.

an alternating order of 0's and 1,2's. This is only the local behaviour, the precise form of the ground state will be discussed in Sections 6.4 and 6.5, depending on the parity of the length of the chain. The alternating degree of freedom on the chain presents us with an exponential ($\approx 2^{L/2}$) degeneracy, at first order. In the next sections we will discuss the higher order perturbative terms that paint a clearer picture of low energy behaviour.

We note that the structure of Equation (6.1) resembles the charge density/Mott behaviour ($k = \pi$) encountered in ANNNI, with the addition of the large degeneracy.

6.4 Odd system length

We start the detailed discussion with the simplest case, L is odd. The ground state subspace $G^o(L)$ (the L is usually omitted) in the classical limit ($U, f \gg 1$ and $0 < f < 2U$) is spanned by

$$|\Psi^o_{\vec{i}}\rangle = |0, i_1, 0, i_2, 0, \ldots, i_{(L-1)/2}, 0\rangle\,. \tag{6.2}$$

for $i_1, i_2, \ldots, i_{(L-1)/2} = 1, 2$, with a gap of $\Delta = 3\min(f, 2U - f)$.

Analogous to Section 5.7.2, we recognize an effective spin-1/2 chain, in this case of length $\frac{L-1}{2}$. Every odd site is fixed to 0, while the even sites can be represented by a spin-1/2, matching the local degrees of freedom.

We can reinstate the $\sigma_j\sigma_{j+1}^\dagger$ terms perturbatively for the effective spin 1/2 chain.

$$V^\sigma = -\sum_j \left[\sigma_j^\dagger \sigma_{j+1} + \text{h.c.}\right] \tag{6.3}$$

The first non-vanishing perturbative contributions are second order and as shown in Appendix 6.B yield an effective XXZ-Hamiltonian.

$$H_{\text{eff}}^{(2)} = -\sum_k \left[\frac{2}{3f}(\sigma_k^+\sigma_{k+1}^- + \text{h.c}) + \left(\frac{1}{3f+3U} + \frac{1}{6U} - \frac{1}{3f}\right)\sigma_k^z\sigma_{k+1}^z\right], \tag{6.4}$$

where $k = 1, \ldots, \frac{L-3}{2}$ corresponds to the effective sites of the spin-1/2 chain. The XXZ chain $\left[\sum_k J_{xy}(\sigma_k^+\sigma_{k+1}^- + \text{h.c}) + \frac{J_z}{2}\sigma_k^z\sigma_{k+1}^z\right]$ is critical ($c = 1$) for $\Delta = J_z/J_{xy} \in [-1, 1]$. From Equation (6.4) we observe that Δ takes values from 1 through $-2/3$ for $f \in [0, 2U]$, with $\Delta = 0$ for $f = U$ reducing to the non-interacting XX chain. For odd L and large U, f the system represented by a critical XXZ chain on every odd site. This is represented by the blue and orange outline, depicting the classical limit. We denote this phase as the sublattice critical XXZ phase.

6.4.1 Finite U, f

At finite U, f we recover this sublattice critical XXZ phase. The blue-orange phase in Figure 6.1 is accurately described by the effective spin-1/2 picture for odd L.

Let us look at an exemplary point C_3 ($U = 4$, $f = 2$). In Figure 6.3a, finite size scaled DMRG results confirm that this point is indeed gapless. The system size dependency, resembles the finite size XXZ behave, as discussed in Appendix 5.B.2 (although for a different periodicity, due to the sublattice structure).

The central charge is obtained from the modified Calabrese-Cardy formula [209, 210, 216]:

$$S_{\text{mod}}^{\text{odd}}(L, l) = S(L, l) + \frac{a\cos\left(\pi\frac{l-\frac{1}{2}}{2}\right)}{\frac{L}{\pi}\sin\left(\frac{\pi l}{L}\right)}, \tag{6.5}$$

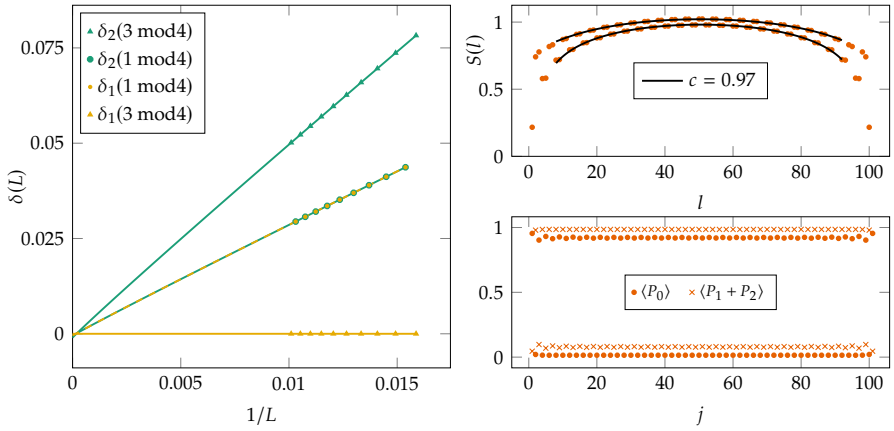

Figure 6.3: DMRG results for $U = 4$ and $f = 2$ for odd system lengths. Finite size scaling for $L = 63, 65, \ldots, 99$ in (a), with the first an second excitation gap $\delta_i(L)$ and the distinction of $L = 1$ and 3 mod 4 branches. Entanglement entropy and eigenstate occupation in (b) for $L = 101$.

where $S(L, l)$ is defined in Equation (5.20), taking into account that the spin-1/2 degrees of freedom live on every second site. Using Equation (6.5) the top panel of Figure 6.3b confirms that the critical XXZ central charge ($c \approx 1$).

The numerical results allow us to directly test the claim that this region has a $|0\rangle$ on every second site, alternating with a $|i\rangle$ with $i = 1, 2$. For this we define the projector on these three eigenstates of τ:

$$P_j^i = (1 + \omega^{-i}\tau_j + \omega^i \tau_j^\dagger)/3 \tag{6.6}$$

for $i = 0, 1, 2$. The spatial expectation values are shown in the bottom panel of Figure 6.3b. The oscillating behaviour $\langle P_j^0 \rangle$ and $\langle P_j^1 + P_j^2 \rangle$ confirms that the ground state subspace shows the signatures of the large U, f limit. Due to the conjugation invariance ($|1\rangle \rightleftarrows |2\rangle$) numerical data shows $\langle P_j^1 \rangle \approx \langle P_j^2 \rangle$.

6.5 Even system length

For even L the story is more complicated. In the classical limit $U, f \gg 1$ there are three low energy subspaces $\mathcal{G}^+$, $\mathcal{G}^-$ and $\mathcal{G}^d$. The first two are spanned respectively by

$$|\Psi^+_{\vec{i}}\rangle = |i_1, 0, i_2, 0, \ldots, i_{L/2}, 0\rangle \tag{6.7}$$

$$|\Psi^-_{\vec{i}}\rangle = |0, i_1, 0, i_2, \ldots, 0, i_{L/2}\rangle\,, . \tag{6.8}$$

for $i_1, i_2, \ldots, i_{L/2} = 1, 2$. The classical energy of these states is

$$E_0^{\pm} = -L\left[\frac{f}{2} + U\right]. \tag{6.9}$$

The third is a family of subspaces $\mathcal{G}^d$ for $d = 1, \ldots, \frac{L}{2}$ spanned by

$$|\Psi^d_{\vec{i}}\rangle = |0, i_1, 0, i_2, \ldots, 0, i_{d-1}, \underbrace{0, 0}_{d}, i_d, 0, \ldots, 0, i_{L/2-1}, 0\rangle] \tag{6.10}$$

There is domain wall $|00\rangle$, left from the dth spin 1/2 degree of freedom. The states left $|0, i_1, 0, i_2, \ldots, 0, i_{d-1}, 0\rangle$ and right $|0, i_d, 0, i_{d+1}, \ldots, 0, i_{L/2-1}, 0\rangle$ of the domain wall are both ground states of odd length systems. The energy of this state is

$$E_0^{\mathrm{dw}} = -L\left[\frac{f}{2} + U\right] - 3(f - U), \tag{6.11}$$

Next we consider the two cases $f < U$ and $f > U$.

$f < U$

In the thermodynamic limit for $f < U$ the first ground state is represented by the first two subspaces $\mathcal{G}^+ \oplus \mathcal{G}^-$, as (6.9) < (6.11).

These two subspaces are decoupled by the perturbative Hamiltonian (6.3), because they only hybridize at Lth order. Like in the odd case, the effective Hamiltonian we obtain from (second order) perturbation is for both subspaces the XXZ model given by (6.4), with a careful repositioning of the spin-1/2 sites. This gives direct sum of the sublattice XXZ model, completely decoupled, with a central charge $c = 1$. This phase is denoted by the blue outline in Figure 6.1.

If we write the XXZ ground state for each respective sector as $|\Psi^{\pm}\rangle$ we can write

$$\frac{1}{\sqrt{|\alpha|^2+|\beta|^2}}\left[\alpha\,|\Psi^{-}\rangle+\beta\,|\Psi^{+}\rangle\right] \tag{6.12}$$

as the generic ground state. The oscillating nature of the $|0\rangle$ states appears as follows (see Equation (6.6))

$$\langle P_j^0\rangle = \frac{1}{\sqrt{|\alpha|^2+|\beta|^2}}\cdot\begin{cases}|\alpha|^2 & \text{for } j \text{ odd}\\ |\beta|^2 & \text{for } j \text{ even}\end{cases} \tag{6.13}$$

Regardless of α,β is shows this observable a two site periodicity. We will use this knowledge in the finite U, f exploration.

$f > U$

For $f > U$ the domain wall subspaces $\mathcal{G}^d$ have the first order lowest energy. For odd system lengths this feature does not appear, domain wall states are always excited. In the outline of Figure 6.1 this phase is coloured orange.

We recognize that every individual $\mathcal{G}^d$ can be written as the direct product of two odd-L subspaces $\mathcal{G}^0(2d-1)\otimes\mathcal{G}^0(L-2d+1)$. Following Section 6.4 second order perturbation theory gives the direct product of two XXZ chains. However, this is not the leading order correction.

Contrary to the previous cases, there is a relevant first order contribution for the $\mathcal{G}^d$'s:

$$V^{\sigma}\,|\Psi^d_{\vec{i}}\rangle = -\left[|\Psi^{d-1}_{\vec{i}}\rangle+|\Psi^{d+1}_{\vec{i}}\rangle\right], \tag{6.14}$$

with V^{σ} defined by Equation 6.3 In other words, the first perturbative term shifts the domain wall back and forth: $V^{\sigma}\mathcal{G}^d = -\left[\mathcal{G}^{d-1}+\mathcal{G}^{d+1}\right]$. If we define $\mathcal{G}=\mathcal{G}^1\oplus\cdots\oplus\mathcal{G}^{\frac{L}{2}}$, the first order contributions on the subspaces can be written as

$$V^{\sigma}\mathcal{G} = -\begin{pmatrix}0 & I & & & \\ I & 0 & I & & \\ & I & 0 & \ddots & \\ & & \ddots & \ddots & I\\ & & & I & 0\end{pmatrix}\begin{pmatrix}\mathcal{G}^1\\ \mathcal{G}^2\\ \mathcal{G}^3\\ \vdots\\ \mathcal{G}^{\frac{L}{2}-1}\\ \mathcal{G}^{\frac{L}{2}}\end{pmatrix}. \tag{6.15}$$

where I acts trivially, if we order $\mathcal{G}^j$ appropriately,. This is the most relevant

perturbation, which we have to consider first. The coupling between the subspaces will lift the degeneracy and dictate the spectrum up to first order. For this simple block tridiagonal matrix, the eigenvalues and vectors are known exactly [244, p.67]. The gapless spectrum is given by

$$E_k = -2\cos\left(\frac{k\pi}{L/2+1}\right), \tag{6.16}$$

for $k = 1, \ldots, \frac{L}{2}$. For $k = 1$ we get the ground state given by corresponding eigenvector $(v_1, \ldots, v_{L/2})^\top$ with

$$v_d = \frac{1}{\sqrt{(L/2+1)/2}} \sin\left(\frac{\pi d}{L/2+1}\right), \tag{6.17}$$

normalized to 1. These v_d weigh the different domain wall subspaces. However, the degeneracy for each subspace still remains. Consequently, first order perturbation theory gives the ground states:

$$|\Psi_{\vec{i}^1,\ldots,\vec{i}^{L/2}}\rangle = \sum_{d=1}^{L/2} v_d \, |\Psi^d_{\vec{i}^d}\rangle \,. \tag{6.18}$$

This is still a large subspace and higher order corrections are required to understand the physics. Adding the second order perturbations (XXZ), is quite non-trivial and beyond the scope of this chapter. Fortunately, we can already obtain some insights from this first order perturbative result. Regardless of the second order contributions, the occupation number $\langle P^0_j \rangle$ (6.6) follows from Equation (6.17)

$$\langle P^0_j \rangle = \begin{cases} 1 - \left[j - \frac{\sin(\pi j/(L/2+1))}{\sin(\pi/(L/2+1))} \right] /(L+2), & \text{for } j \text{ odd}, \\ \left[j + 1 - \frac{\sin(\pi (j+1)/(L/2+1))}{\sin(\pi/(L/2+1))} \right] /(L+2), & \text{for } j \text{ even}. \end{cases} \tag{6.19}$$

6.5.1 Finite U, f

At finite U, f it is a priori not clear whether the $\mathcal{G}^\pm$ or $\mathcal{G}^d$ persists. Fortunately, the 0-occupation number of the respective descriptions, defined in Equations (6.13) and (6.19) is good indicator, since both show very different behaviour. The $\mathcal{G}^\pm$ is simply oscillating, while the 0-occupation number for $\mathcal{G}^d$ shows a cross-over.

Using C_3 ($U = 4, f = 2$) as an example, we see in the top pane of Figure 6.4a the occupation numbers. Note that $\langle P^1 + P^2 \rangle = 1 - \langle P^0 \rangle$. The exact results for the domain wall picture is depicted by the solid lines. Even though the correspondence is not perfect, the nature of the system is clearly the domain wall states. This picture was confirmed for multiple points, both for larger U and large f. One of these point is shown in the top pane of Figure 6.4b. Because of the larger f, the numerical results follow the domain wall prediction.

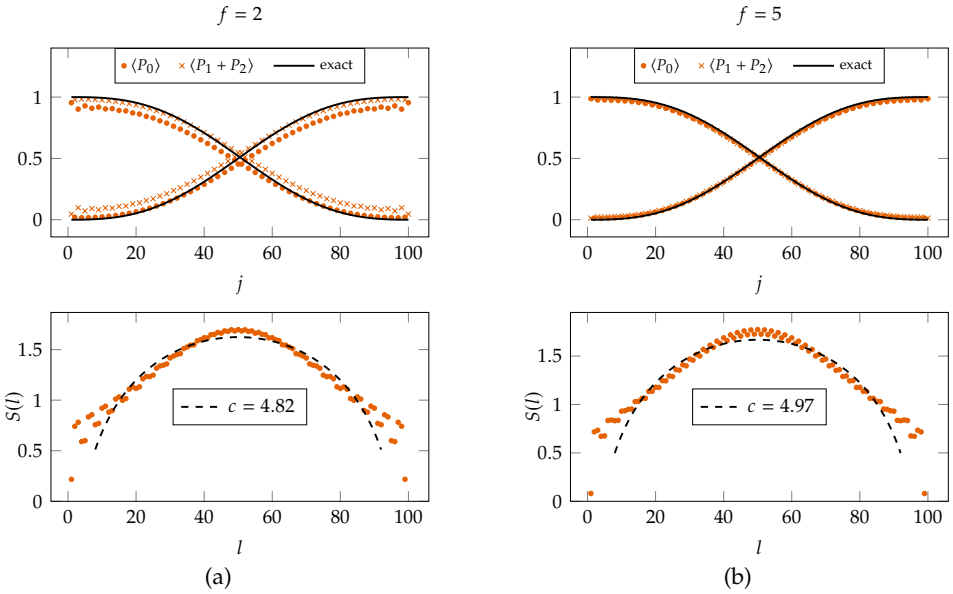

Figure 6.4: Occupation number (top) and entanglement entropy (bottom) for $U = 4$ and even system length ($L = 100$) at C_3 ($f = 2$) in (a) and a point deeper in the critical phase ($f = 5$) in (b). The Calabrese–Cardy fit to the entanglement entropy is very poor, suggesting the absence of a CFT.

In this domain wall picture, proceeding with perturbation theory beyond first order is very non-trivial. The difficulty lies in the mixing of the domain wall mobility and the XXZ-like interactions. The bottom panels of Figure 6.4, showing the entanglement entropy, confirms this obscure behaviour. The Calabrese-Cardy formula 5.20 cannot be fitted to the entanglement. This can mean one of two things. Contrary to the odd L, the system is not described by a conformal field theory, which is very likely because of the intricate nature of the states.

Or the numerical calculations were not sufficient to observe the true critical behaviour. On this, we would like to mention that going to $L = 400$ with sufficient bond dimension did not reveal a clearer picture.

It has to be said that the entanglement entropy presented here does suggest that the system is gapless. In the gapped case, the entanglement entropy usually saturates to a fixed value. Direct calculation of the finite size gap confirms this suspicion for the point C_3, as can be seen in Figure 6.5. Again, the scaling of the gap shows a XXZ-like even-odd effect, as we encountered in Appendix 5.B.2 and 6.4. However, the precise reasoning is not so clear here.

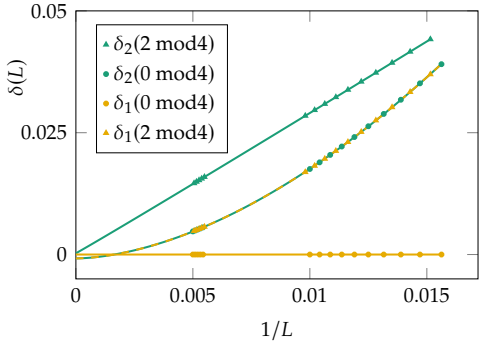

Figure 6.5: DMRG results for $U = 4$ and $f = 2$ for even system lengths. Finite size scaling for $L = 64, 66, \ldots, 102, 182, \ldots, 200$ in with the first an second excitation gap $\delta_i(L)$ and the distinction of $L = 0$ and 2 mod 4 branches.

More importantly, the scaling of $\delta_1(L = 2 \mod)) = \delta_2(L = 0 \mod))$ suggests that there is indeed no underlying CFT at C_3. For a CFT the scaling of all excitations should be proportional to $1/L$. The scaling of $1/L^{1.74\ldots}$ contradicts this requirement.

Nevertheless, in order to understand the precise nature of this phase for L even, more extensive calculations are required.

6.6 Transitions for odd L

The phase diagram presented in Figure 6.1 also shows several grey areas, where we would expect the transition lie. Our numerical methods and computation resources could not fully resolve these regions. Because the critical phase around C_3 for even L is poorly understood we restrict this discussion to odd L.

We will look at two cuts, depicted by the dashed lines in Figure 6.1, crossing the transitions to understand the difficulties. Besides the critical phases described in previous sections, these cuts cover the two gapped phases, the topological (Section 5.6) and the Ising ferromagnetic (Section 5.7).

We use the numerically obtained central charge, the scaling of the correlation function and relevant order parameters to distinguish the phases. The central charge follows from a fit to the (modified) Calabrese-Cardy formula (5.20),(6.5). The relevant correlator $G(l)$ is defined in Equation (5.36) and shows power law behaviour in gapless system, scaling as l^{-b} (l the distance of the two point function). The $\mathbb{Z}_3$ ordered phase can be distinguished with the long range $\mathbb{Z}_3$ order $\left|\langle\sigma_j^\dagger\sigma_{j+L/2}\rangle\right|$. The ferromagnetic phase is characterized by $\left\langle\sum_j \tilde{\sigma}_j^z\right\rangle$, with $\tilde{\sigma}_j^z = \mathrm{diag}(0,1,-1)_\tau$. An extensive explanation of both parameters is in Section 5.7.3. Finally, we introduce an order parameter for the oscillating nature of the sublattice XXZ states. With Equation (6.2) and Figure 6.3b in mind we define the sublattice order as

$$\mathcal{D} = \left|\sum_j (-1)^j P_j^0\right|/L. \tag{6.20}$$

Cut along $f = 2$

The first cut follows $f = 2$ and runs over $U \in [1.5, 3]$, covering the $\mathbb{Z}_3$ to sublattice critical XXZ transition.

In Figure 6.6a we clearly distinguish the $\mathbb{Z}_3$ phase, $c = 0$ (top panel) and $\mathbb{Z}_3$ order (bottom panel) is finite, for $U < 2.3$.

For $U > 2.6$ the central charge and sublattice order ($\mathcal{D}$, bottom panel) confirm the sublattice XXZ phase. The dotted line in the bottom panel denotes the sublattice order in the classical limit $\mathcal{D} = 1/2$.

The grey region in between shows long range $\mathbb{Z}_3$-order ($b = 0$, but $\langle\sigma_j^\dagger\sigma_{j+L/2}\rangle$ finite), however it also shows criticality $c > 0$, with reduced sublattice order. This classifies neither as gapped $\mathbb{Z}_3$-ordered, nor gapless sublattice critical XXZ. Like in incommensurate phase the ANNNI model there could be an additional phase separating the ordered from the density wave phase.

Cut along $U = 4$

The second cut for $U = 4$ and $f \in [-1, 0.5]$ is shown in Figure 6.6b.

Clearly, the gapped Ising ferromagnetic phase is confirmed for $f < 0.875$ by the central charge (top panel) and ferromagnetic order (bottom panel).

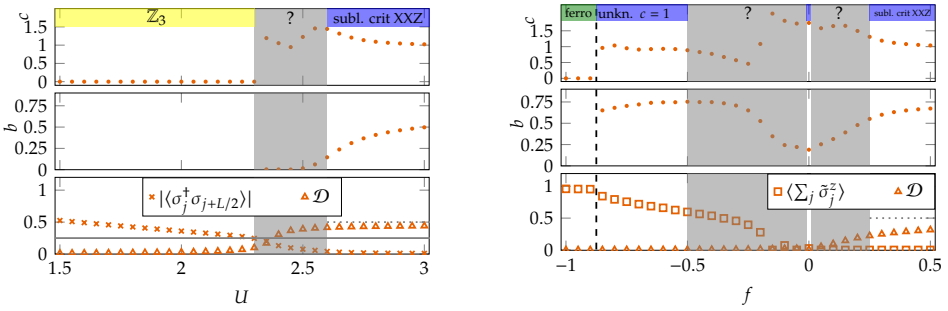

(a) $f = 2$ (b) $U = 4$

Figure 6.6: Numerical results for the $\mathbb{Z}_3$-ANNNP for $L = 201$. The top panes show the central charge from fitting to the CC (5.20). The middle panes show the power law scaling for the $G(l)$. The third panes show the relevant order parameters. The dotted horizontal lines (at $\frac{1}{2}$) in the lower panes indicate the dimerization for the classical limit ($U, f \gg 1$) ground state given by Equation (6.2). The dashed lines show the transitions, with the colours naming the phases. The regions where the results were inconclusive are depicted by the grey areas.

For $f > 0.25$ the sublattice order and central charge confirm the $c = 1$ sublattice XXZ behaviour.

Also, we see evidence of the dual $c = 2$ critical point at $f = 0$. As discussed in Section 6.2, this can be described by two decoupled $c = 1$ Potts chains related. The central charge not exactly 2, this could either be a due to the system size being to short to capture the $c = 2$ entanglement, or there is some hidden coupling (at the boundaries) that gaps out part of the low energy degrees of freedom.

Moreover, there is a $c = 1$ phase for $f \in [-0.875, 0.45]$, which we do not know the origin for. It show ferromagnetic order in seems to be connected to the transition between the ferromagnetic and $\mathbb{Z}_3$-ordered phase, see Figure 6.1.

Finally there are two grey transition regions, that show varying central charge and no definitive order. Together with the unknown $c = 1$ phase, these grey regions require additional investigation.

6.7 Discussion

In this chapter we continued the investigation from Chapter 5 taking the interaction U to a larger regime. With the phase diagram for the large-U ANNNI in mind, we expected this regime to be quite different from the small-U case.

A combination of perturbation theory and numerical DMRG calculations led to the discovery of several critical phases. Duality transformations yielded a $c = 2$ XXZ phase for $f = 0$, and a $c = 1$ phase with unknown origin appeared for $f < 0$. Finally, there is an elusive critical phase covering the top right of the phase diagram, showing a complicated even-odd effect concerning the system size. For odd system sizes this phase is very well described by a $c = 1$ critical XXZ phase, occupying every second site.

For even L the system is still critical, however, not related to a CFT. At first order perturbation theory the ground states show some domain wall behaviour. The exact root of the criticality is unclear, because the second order perturbative contributions had not been resolved. This intricate phase desires further investigation. Unifying the first and second order perturbative term might shed a light on the nature of the even L phase. Also, more advanced computational efforts can help to understand the critical behaviour in this particular regime.

Among the critical phases and the gapped phases (topological and Ising ferromagnetic) lie transition regions, which could not be classified as one of the existing phase, our current methods. Attention in future studies would be required to understand the physical nature of these regions. Moreover, the influence of chirality in this particular corner of the phase diagram is likely to reveal an even more diverse set of phases. The results in Ref. [232] show several novel critical and gapped phase for one particular chirality $\theta = \pi/3$ (defined in Equation 5.7). Finally, also for $\mathbb{Z}_{n>3}$ interesting phases can appear as was shown in Ref. [186] for $\mathbb{Z}_6$.

6.A Rough topography of the phase diagram

Following the same method described in Appendix 5.B.1 we obtain the rough phase diagram for large interactions.

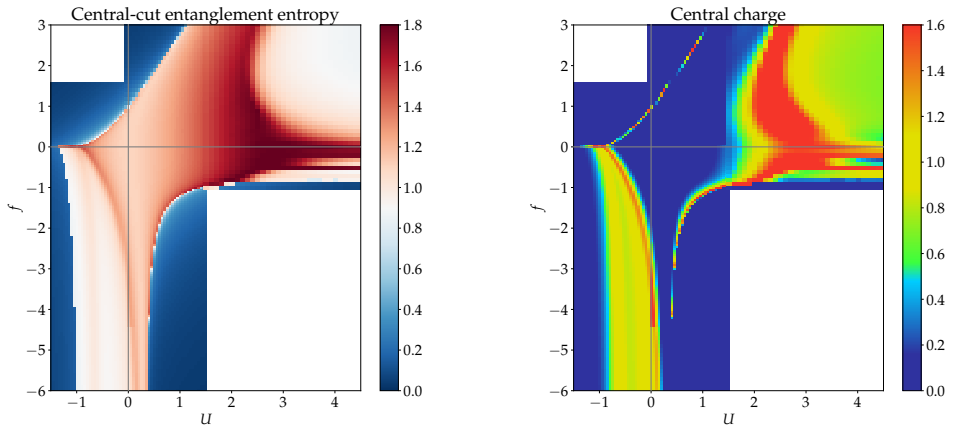

Figure 6.7: Rough topography of the phase diagram for the $\mathbb{Z}_3$-ANNNP model, with large U. The central-cut entanglement entropy and central charge results were obtained for small system sizes L =50–100 and low bond dimension in the parity sector 0. Even though the nature of the phases and transitions cannot be conclusively derived from these plots, it gives a good visual guide for the features to be studied in more detail.

6.B Effective XXZ chain

The different ground state manifolds, defined in (6.2),(6.7),(6.8),(6.10) all share the sublattice spin-1/2 degree of freedom. Therefore, the relevant part for the states is the alternating bulk part

$$|\Psi^{\text{bulk}}_{\vec{i}}\rangle = |\ldots, i_j, 0, i_{j+1}, 0, \ldots\rangle\,, \quad \text{with } \ldots, i_j, \ldots = 1, 2. \tag{6.21}$$

Recall, that the perturbation is given by

$$V^\sigma = \sum_j v^\sigma_j = -\sum_j \left[\sigma^\dagger_j \sigma_{j+1} + \text{h.c.}\right] \tag{6.22}$$

There is no first order contribution, since $\langle \Psi^{\text{bulk}}_{\vec{i}} | V^\sigma | \Psi^{\text{bulk}}_{\vec{i}} \rangle = 0$.

The second-order terms originate from perturbations of the form

$$\sum_k \frac{\langle \Psi_i | V^\sigma | \Phi_k \rangle \langle \Phi_k | V^\sigma | \Psi_l \rangle}{E_\Psi - E_{\Phi_k}}, \tag{6.23}$$

where $E_\Psi = E_{\Psi_i} = E_{\Psi_l}$ the unperturbed energies of the ground states.

On the spin-$\frac{1}{2}$ degree of freedom on every second site we define operators $\sigma^{\pm,z}_j$ acting on $|1\rangle\,, |2\rangle$, such that $\sigma^z\,|1\rangle = |1\rangle$ and $\sigma^z\,|2\rangle = -\,|2\rangle$.

There are hopping terms contributing to the effective Hamiltonian:

$$\frac{\langle 102|v^\sigma_{2j}|222\rangle \langle 222|v^\sigma_{2j+1}|201\rangle}{E_\Psi - E_{\Phi_k}} + \frac{\langle 102|v^\sigma_{2j+1}|111\rangle \langle 111|v^\sigma_{2j}|201\rangle}{E_\Psi - E_{\Phi_k}} = -\frac{2}{3f} \tag{6.24}$$

In operator language this matrix becomes $-\frac{2}{3f}(\sigma^+_j \sigma^-_{j+1} + \sigma^-_j \sigma^+_{j+1})$.

The second contribution comes from the following overlaps

$$\begin{aligned}
&\frac{\langle 01010|v^\sigma_{2j+1}|01220\rangle \langle 01220|v^\sigma_{2j+1}|01010\rangle}{E_\Psi - E_{\Phi_k}} + \frac{\langle 01010|v^\sigma_{2j+1}|01100\rangle \langle 01100|v^\sigma_{2j+1}|01010\rangle}{E_\Psi - E_{\Phi_k}} \\
&+ \frac{\langle 01010|v^\sigma_{2j}|02210\rangle \langle 02210|v^\sigma_{j}|01010\rangle}{E_\Psi - E_{\Phi_k}} + \frac{\langle 01010|v^\sigma_{2j}|00110\rangle \langle 00110|v^\sigma_{2j}|01010\rangle}{E_\Psi - E_{\Phi_k}} \\
&= -\frac{2}{3f + 3U} - \frac{2}{3U}
\end{aligned} \tag{6.25}$$

and

$$\frac{\langle 01020|v^{\sigma}_{2j+1}|01110\rangle\langle 01110|v^{\sigma}_{2j+1}|01020\rangle}{E_\Psi - E_{\Phi_k}} + \frac{\langle 01020|v^{\sigma}_{2j+1}|01200\rangle\langle 01200|v^{\sigma}_{2j+1}|01020\rangle}{E_\Psi - E_{\Phi_k}}$$
$$+ \frac{\langle 01020|v^{\sigma}_{2j}|02220\rangle\langle 02220|v^{\sigma}_{2j}|01020\rangle}{E_\Psi - E_{\Phi_k}} + \frac{\langle 01020|v^{\sigma}_{2j}|00120\rangle\langle 00120|v^{\sigma}_{2j}|01020\rangle}{E_\Psi - E_{\Phi_k}}$$
$$= -\frac{2}{3f} - \frac{2}{6U} \tag{6.26}$$

These terms can be summarized $-\left(\frac{1}{3f+3U} + \frac{1}{6U} - \frac{1}{3f}\right)\sigma^z_j\sigma^z_{j+1}$ modulo an overall energy shift.

The effective Hamiltonian is an XXZ model

$$H^{(2)}_{\text{eff}} = -\sum_j \left[\frac{2}{3f}(\sigma^+_j\sigma^-_{j+1} + \text{h.c}) + \left(\frac{1}{3f+3U} + \frac{1}{6U} - \frac{1}{3f}\right)\sigma^z_j\sigma^z_{j+1}\right] \tag{6.27}$$

The anisotropy is given by $\Delta = -\frac{f}{f+U} - \frac{f}{2U} + 1$. For $f \ll U$ the anisotropy approaches -1, for $f = U$ there is only spin-flip (i.e. $\Delta = 0$) and for $f \to 2U$ we have $\Delta = \frac{2}{3}$. Recall that this discussion is valid for $U, f \gg 1$ and $2U - f \ll 1$. For large U, we can approach $f = 2U$ arbitrarily close, without violating the latter requirement, contrary to the limit $f \downarrow 0$, which cannot be approached perturbatively.

7 Summary and Outlook

The work in this thesis mostly revolved around parafermions, either in the simplest $\mathbb{Z}_2$-Majorana- or the the general $\mathbb{Z}_n$-form. Typically, the systems were examined in their condensed matter lattice representation, with the occasional excursion to the accompanying field theory description. In particular, the work focussed on the low energy behaviour of these one dimensional systems, with several exotic phases, topology, criticality and quantum phase transitions.

In the introduction (Chapter 1) parafermions were presented in the context of condensed matter, strongly correlated systems and quantum computers.

Thereafter, the first part, Chapters 2 and 3 focussed on frustration free systems. These are models with fine tuned parameters, that possess an exact ground state degeneracy. In Chapter 2 the Kitaev chain was met with a combination of an alternating chemical potential and interactions. For a specific set of coupling constants this system was shown to have a two-fold degenerate ground state, with a finite gap, displaying topological order.

Chapter 3 presented a general framework for obtaining frustration free models, mainly topological models. Based on Witten's conjugation argument, the ground state and Hamiltonian were simultaneously deformed, keeping their relation intact. This deformation connected these deformed Hamiltonians to well understood undeformed systems. For instance, we recovered the Peschel–Emery frustration free line for the ANNNI model in Section 3.3.2, deformed from the topological/ferromagnetic classical Ising model. Also recently discovered $\mathbb{Z}_3$ frustration free models were rederived in this framework, as well as the q-deformations for the XXZ and AKLT model. Moreover, two novel classes of $\mathbb{Z}_n$ parafermion models were obtained, showing the straightforward application of the framework. The most important contribution of this chapter was the overarching description for all these, so far disconnected, models, making interpolations and extension more easily accessible. Due to the topological nature of many of the models in question, the presence of these frustration free lines is important, as they give a handle on the ground state degeneracy.

In the second part, two parafermion systems were taken away from analytical safe haven, employing the use of a numerical method called Density Matrix

Renormalization Group. The phase diagrams of the tight binding $\mathbb{Z}_3$ Fock parafermion chain and an extended $\mathbb{Z}_3$ parafermion chain were obtained with a combination of numerical and analytical tools.

Chapter 4 was dedicated to the first of these two models. It was concluded that the phase diagram involves with three distinct critical phases (two $c = 1$ and one $c = 2$) and a gapped line. Perturbatively, some of these phases were linked to effective Luttinger liquids, supported by numerical correlation functions.

Finally, Chapters 5 and 6 discussed a four site interaction added to the parafermion chain. Beside the topological and trivial phase, three phases related to the XXZ model were identified in Chapter 5. Two gapped phases, antiferromagnetic and ferromagnetic Ising phases, were numerically confirmed to show their relevant order. In between lie a critical XXZ phase, or Luttinger liquid phase. Numerical evidence clearly confirmed the central charge ($c = 1$) and Luttinger parameter (K from the correlation functions). Second order perturbation theory uncovered an U(1) breaking term for the effective spin-1/2 theory, only opening a $\mathbb{Z}_3$ ordered gap at the Heisenberg ferromagnetic point.

The discussion of this model was continued in Chapter 6, where focus lie on the large interaction limit. This part of the phase diagram was not fully understood. However, it was clear that some interesting even-odd effect dominated for large interactions. The phase showed clear signs of criticality, related to an effective spin-1/2 description on every second site. The true nature was well understood for odd systems lengths, where even system sizes showed critical non CFT behaviour, with interesting domain wall ground states.

The work of the final two chapters gives a lot of interesting leads for future research. One straightforward continuation for either chapter is a $\mathbb{Z}_n$-symmetric model for $n \geq 4$. Moreover, the extension chosen in Chapters 5 and 6 is by no means the most general, supporting the $\mathbb{Z}_3$ symmetry. Furthermore, if the reality conditional on the coupling constants is lifted, an even larger parameter space appears. Careful deliberation of possible experimental setups can distil the next most relevant interactions, avoiding dealing with an intangibly large set of parameters.

Also, the Fock parafermion model from Chapter 4 can easily be extended, including for instance superconductor-like terms, analogous to the Kitaev chain.

Finally, the conjugation approach for frustration free models from Chapter 3 can naturally be applied to more systems that meet the criteria, involving chiral classical $\mathbb{Z}_n$ models and quantum many-body scar states.

I hope this thesis conveys the fascinating world of parafermions and inspires others to continue fill in the blanks of this still largely unexplored terrain.

Bibliography

[1] R. P. Feynman, International Journal of Theoretical Physics **21** (1982).

[2] F. Arute, K. Arya, and R. Babbush et al., Nature **574**, 505 (2019).

[3] "IBM Quantum Update: Q System One Launch, New Collaborators, and QC Center Plans," (2019).

[4] M. W. Johnson, M. H. S. Amin, S. Gildert, T. Lanting, F. Hamze, N. Dickson, R. Harris, A. J. Berkley, J. Johansson, P. Bunyk, E. M. Chapple, C. Enderud, J. P. Hilton, K. Karimi, E. Ladizinsky, N. Ladizinsky, T. Oh, I. Perminov, C. Rich, M. C. Thom, E. Tolkacheva, C. J. S. Truncik, S. Uchaikin, J. Wang, B. Wilson, and G. Rose, Nature **473**, 194 (2011).

[5] M. H. Devoret, J. M. Martinis, and J. Clarke, Physical Review Letters **55**, 1908 (1985).

[6] T. F. Rønnow, Z. Wang, J. Job, S. Boixo, S. V. Isakov, D. Wecker, J. M. Martinis, D. A. Lidar, and M. Troyer, Science **345** (2014).

[7] J. Preskill, Quantum **2**, 79 (2018).

[8] M. Kjaergaard, M. E. Schwartz, J. Braumüller, P. Krantz, J. I.-J. Wang, S. Gustavsson, and W. D. Oliver, Annual Review of Condensed Matter Physics **11**, 369 (2020).

[9] D. P. DiVincenzo, Fortschritte der Physik **48**, 771 (2000).

[10] T. D. Ladd, F. Jelezko, R. Laflamme, Y. Nakamura, C. Monroe, and J. L. O'Brien, Nature **464**, 45 (2010).

[11] A. Kitaev, Physics-Uspekhi **44**, 131 (2001).

[12] A. Y. Kitaev, Annals of Physics **303**, 2 (2003).

[13] S. Bravyi, Physical Review A **73**, 042313 (2006).

[14] C. Nayak, S. H. Simon, A. Stern, M. Freedman, and S. D. Sarma, Reviews of Modern Physics **80**, 1083 (2008).

[15] A. Kitaev and C. Laumann, Exact Methods in Low-dimensional Statistical Physics and Quantum Computing: Lecture Notes of the Les Houches Summer School: Volume 89, July 2008 **89**, 101 (2010).

[16] R. S. Mong, D. J. Clarke, J. Alicea, N. H. Lindner, P. Fendley, C. Nayak, Y. Oreg, A. Stern, E. Berg, K. Shtengel, and M. P. Fisher, Physical Review X **4**, 011036 (2014).

[17] R. Lutchyn, J. Sau, and S. Sarma, Physical Review Letters **105**, 077001 (2010).

[18] Y. Oreg, G. Refael, and F. von Oppen, Physical Review Letters **105**, 177002 (2010).

[19] J. D. Sau, S. Tewari, R. M. Lutchyn, T. D. Stanescu, and S. Das Sarma, Physical Review B **82**, 214509 (2010).

[20] V. Mourik, K. Zuo, S. M. Frolov, S. Plissard, E. Bakkers, and L. P. Kouwenhoven, Science **336**, 1003 (2012).

[21] H. Zhang, C.-X. Liu, S. Gazibegovic, D. Xu, J. A. Logan, G. Wang, N. van Loo, J. D. S. Bommer, M. W. A. de Moor, D. Car, R. L. M. Op het Veld, P. J. van Veldhoven, S. Koelling, M. A. Verheijen, M. Pendharkar, D. J. Pennachio, B. Shojaei, J. S. Lee, C. J. Palmstrøm, E. P. A. M. Bakkers, S. D. Sarma, and L. P. Kouwenhoven, Nature **556**, 74 (2018).

[22] H. Zhang, C.-X. Liu, S. Gazibegovic, D. Xu, J. A. Logan, G. Wang, N. van Loo, J. D. S. Bommer, M. W. A. de Moor, D. Car, R. L. M. Op het Veld, P. J. van Veldhoven, S. Koelling, M. A. Verheijen, M. Pendharkar, D. J. Pennachio, B. Shojaei, J. S. Lee, C. J. Palmstrøm, E. P. A. M. Bakkers, S. Das Sarma, and L. P. Kouwenhoven, Nature **591**, E30 (2021).

[23] L. D. Landau, Zh. Eksp. Teor. Fiz. **7**, 19 (1937).

[24] K. v. Klitzing, G. Dorda, and M. Pepper, Physical Review Letters **45**, 494 (1980).

[25] R. B. Laughlin, Physical Review B **23**, 5632 (1981).

[26] B. I. Halperin, Physical Review B **25**, 2185 (1982).

[27] D. C. Tsui, H. L. Stormer, and A. C. Gossard, Physical Review Letters **48**, 1559 (1982).

[28] V. Kalmeyer and R. B. Laughlin, Physical Review Letters **59**, 2095 (1987).

[29] X. G. Wen, F. Wilczek, and A. Zee, Physical Review B **39**, 11413 (1989).

[30] X. G. Wen, International Journal of Modern Physics B **04**, 239 (1990).

[31] A. Altland and M. R. Zirnbauer, Physical Review B **55**, 1142 (1997).

[32] X. G. Wen, Physical Review B **41**, 12838 (1990).

[33] E. Majorana, Il Nuovo Cimento (1924-1942) **14**, 171 (1932).

[34] P. W. Brouwer, M. Duckheim, A. Romito, and F. von Oppen, Physical Review Letters **107**, 196804 (2011).

[35] A. M. Lobos, R. M. Lutchyn, and S. D. Sarma, Physical Review Letters **109**, 146403 (2012).

[36] W. DeGottardi, D. Sen, and S. Vishveshwara, Physical Review Letters **110**, 146404 (2013).

[37] A. Altland, D. Bagrets, L. Fritz, A. Kamenev, and H. Schmiedt, Physical Review Letters **112**, 206602 (2014).

[38] F. Crépin, G. Zaránd, and P. Simon, Physical Review B **90**, 121407 (2014).

[39] N. M. Gergs, L. Fritz, and D. Schuricht, Physical Review B **93**, 075129 (2016).

[40] M. McGinley, J. Knolle, and A. Nunnenkamp, Physical Review B **96**, 241113 (2017).

[41] G. Kells, N. Moran, and D. Meidan, Physical Review B **97**, 085425 (2018).

[42] S. Gangadharaiah, B. Braunecker, P. Simon, and D. Loss, Physical Review Letters **107**, 036801 (2011).

[43] E. Stoudenmire, J. Alicea, O. A. Starykh, and M. P. Fisher, Physical Review B **84**, 014503 (2011).

[44] E. Sela, A. Altland, and A. Rosch, Physical Review B **84**, 085114 (2011).

[45] F. Hassler and D. Schuricht, New Journal of Physics **14**, 125018 (2012).

[46] R. Thomale, S. Rachel, and P. Schmitteckert, Physical Review B **88**, 161103 (2013).

[47] A. Milsted, L. Seabra, I. Fulga, C. Beenakker, and E. Cobanera, Physical Review B **92**, 085139 (2015).

[48] A. Rahmani, X. Zhu, M. Franz, and I. Affleck, Physical Review B **92**, 235123 (2015).

[49] H. Katsura, D. Schuricht, and M. Takahashi, Physical Review B **92**, 115137 (2015).

[50] Y.-H. Chan, C.-K. Chiu, and K. Sun, Physical Review B **92**, 104514 (2015).

[51] S. Sarkar, Scientific reports **6**, 30569 (2016).

[52] M. Ezawa, Physical Review B **96**, 121105 (2017).

[53] Y. Wang, J.-J. Miao, H.-K. Jin, and S. Chen, Physical Review B **96**, 205428 (2017).

[54] J.-J. Miao, H.-K. Jin, F.-C. Zhang, and Y. Zhou, Physical Review Letters **118**, 267701 (2017).

[55] M. B. Hastings, C. Nayak, and Z. Wang, Physical Review B **87**, 165421 (2013).

[56] D. J. Clarke, J. Alicea, and K. Shtengel, Nature Communications **4** (2013).

[57] F. Wilczek, Physical Review Letters **49**, 957 (1982).

[58] J. M. Leinaas and J. Myrheim, Il Nuovo Cimento B (1971-1996) **37**, 1 (1977).

[59] H. Bartolomei, M. Kumar, R. Bisognin, A. Marguerite, J.-M. Berroir, E. Bocquillon, B. Plaçais, A. Cavanna, Q. Dong, U. Gennser, Y. Jin, and G. Fève, Science **368** (2020).

[60] E. Fradkin and L. P. Kadanoff, Nuclear Physics B **170**, 1 (1980).

[61] P. Fendley, Journal of Statistical Mechanics: Theory and Experiment **2012**, P11020 (2012).

[62] E. M. Stoudenmire, D. J. Clarke, R. S. K. Mong, and J. Alicea, Physical Review B **91**, 235112 (2015).

[63] J. Slingerland and F. Bais, Nuclear Physics B **612**, 229 (2001).

[64] N. H. Lindner, E. Berg, G. Refael, and A. Stern, Physical Review X **2**, 041002 (2012).

[65] T. Wu, Z. Wan, A. Kazakov, Y. Wang, G. Simion, J. Liang, K. W. West, K. Baldwin, L. N. Pfeiffer, Y. Lyanda-Geller, and L. P. Rokhinson, Physical Review B **97**, 245304 (2018).

[66] Y. Wang, V. Ponomarenko, Z. Wan, K. W. West, K. W. Baldwin, L. N. Pfeiffer, Y. Lyanda-Geller, and L. P. Rokhinson, Nature Communications **12** (2021).

[67] O. Gül, Y. Ronen, S. Y. Lee, H. Shapourian, J. Zauberman, Y. H. Lee, K. Watanabe, T. Taniguchi, A. Vishwanath, A. Yacoby, and P. Kim, arXiv:2009.07836 [cond-mat] (2021).

[68] P. Fendley, Journal of Physics A: Mathematical and Theoretical **47**, 075001 (2014).

[69] F. C. Alcaraz, M. T. Batchelor, and Z.-Z. Liu, Journal of Physics A: Mathematical and Theoretical **50**, 16LT03 (2017).

[70] F. C. Alcaraz and M. T. Batchelor, Physical Review E **97**, 062118 (2018).

[71] M. Suzuki, Progress of Theoretical Physics **46**, 1337 (1971).

[72] R. J. Baxter, Journal of Physics C: Solid State Physics **6**, L445 (1973).

[73] R. J. Baxter, Proceedings of the Royal Society of London. Series A, Mathematical and Physical Sciences **383**, 43 (1982).

[74] R. Baxter, *Exactly Solved Models in Statistical Mechanics*, 3rd ed. (Academic Press, London, 1982).

[75] F. Y. Wu, Reviews of Modern Physics **54**, 235 (1982).

[76] G. Mussardo, *Statistical field theory: an introduction to exactly solved models in statistical physics* (Oxford University Press, 2010).

[77] I. Affleck, M. Oshikawa, and H. Saleur, Journal of Physics A: Mathematical and General **31**, 5827 (1998).

[78] P. Francesco, P. Mathieu, and D. Sénéchal, *Conformal Field Theory*, Graduate Texts in Contemporary Physics (Springer-Verlag, New York, 1997).

[79] R. S. Mong, D. J. Clarke, J. Alicea, N. H. Lindner, and P. Fendley, Journal of Physics A: Mathematical and Theoretical **47**, 452001 (2014).

[80] S. R. White, Physical Review B **48**, 10345 (1993).

[81] U. Schollwöck, Annals of Physics **326**, 96 (2011).

[82] E. Witten, Nuclear Physics B **202**, 253 (1982).

[83] S. B. Bravyi and A. Y. Kitaev, Annals of Physics **298**, 210 (2002).

[84] J. Alicea, Y. Oreg, G. Refael, F. Von Oppen, and M. P. Fisher, Nature Physics **7**, 412 (2011).

[85] M. Deng, C. Yu, G. Huang, M. Larsson, P. Caroff, and H. Xu, Nano Letters **12**, 6414 (2012).

[86] A. Das, Y. Ronen, Y. Most, Y. Oreg, M. Heiblum, and H. Shtrikman, Nature Physics **8**, 887 (2012).

[87] H. Churchill, V. Fatemi, K. Grove-Rasmussen, M. Deng, P. Caroff, H. Xu, and C. M. Marcus, Physical Review B **87**, 241401 (2013).

[88] S. Nadj-Perge, I. K. Drozdov, J. Li, H. Chen, S. Jeon, J. Seo, A. H. MacDonald, B. A. Bernevig, and A. Yazdani, Science , 1259327 (2014).

[89] M.-T. Deng, S. Vaitiekėnas, E. Prada, P. San-Jose, J. Nygård, P. Krogstrup, R. Aguado, and C. M. Marcus, Physical Review B **98**, 085125 (2018).

[90] R. Lutchyn, E. Bakkers, L. Kouwenhoven, P. Krogstrup, C. Marcus, and Y. Oreg, Nature Reviews Materials , 1 (2018).

[91] R. Wakatsuki, M. Ezawa, Y. Tanaka, and N. Nagaosa, Physical Review B **90**, 014505 (2014).

[92] T. Sugimoto, M. Ohtsu, and T. Tohyama, Physical Review B **96**, 245118 (2017).

[93] I. Affleck, T. Kennedy, E. H. Lieb, and H. Tasaki, Physical Review Letters **59**, 799 (1987).

[94] I. Affleck, T. Kennedy, E. H. Lieb, and H. Tasaki, Communications in Mathematical Physics **115**, 477 (1988).

[95] M. Asoudeh, V. Karimipour, and A. Sadrolashrafi, Physical Review A **76**, 012320 (2007).

[96] S. Jevtic and R. Barnett, New Journal of Physics **19**, 103034 (2017).

[97] G. Müller and R. E. Shrock, Physical Review B **32**, 5845 (1985).

[98] J. Kurmann, H. Thomas, and G. Müller, Physica A: Statistical Mechanics and its Applications **112**, 235 (1982).

[99] J. Alicea, Reports on Progress in Physics **75**, 076501 (2012).

[100] R. W. Cherng and L. S. Levitov, Physical Review A **73**, 043614 (2006).

[101] G. Dzhaparidze and A. Nersesyan, JETP Lett **27**, 334 (1978).

[102] V. Pokrovsky and A. Talapov, Physical Review Letters **42**, 65 (1979).

[103] F. Alcaraz and A. Malvezzi, Journal of Physics A: Mathematical and General **28**, 1521 (1995).

[104] J. C. Budich and E. Ardonne, Physical Review B **88**, 075419 (2013).

[105] M. Greiter, V. Schnells, and R. Thomale, Annals of Physics **351**, 1026 (2014).

[106] K. Kawabata, R. Kobayashi, N. Wu, and H. Katsura, Physical Review B **95**, 195140 (2017).

[107] S. Tewari and J. D. Sau, Physical Review Letters **109**, 150408 (2012).

[108] H. Hinrichsen and V. Rittenberg, Physics Letters B **275**, 350 (1992).

[109] H. Hinrichsen and V. Rittenberg, arXiv:9202082 [hep-th] (1992).

[110] H. Hinrichsen and V. Rittenberg, Physics Letters B **304**, 115 (1993).

[111] H. Saleur, in *Recent Developments in Conformal Field Theories (Trieste, 1989)*, edited by S. Randjbar-Daemi, E. Sezgin, and J. B. Zuber (WORLD SCIENTIFIC, Singapore, 1990) pp. 160–164.

[112] J. Alicea and P. Fendley, Annual Review of Condensed Matter Physics **7**, 119 (2016).

[113] I. Peschel and V. J. Emery, Zeitschrift für Physik B Condensed Matter **43**, 241 (1981).

[114] G. Kells, Physical Review B **92**, 155434 (2015).

[115] A. Alexandradinata, N. Regnault, C. Fang, M. J. Gilbert, and B. A. Bernevig, Physical Review B **94**, 125103 (2016).

[116] P. Fendley, J. Phys. A: Math. Theor. **49**, 30LT01 (2016).

[117] R. A. Horn and C. R. Johnson, *Matrix analysis* (Cambridge university press, 1990).

[118] S. R. White, Physical Review Letters **69**, 2863 (1992).

[119] V. Pasquier and H. Saleur, Nuclear Physics B **330**, 523 (1990).

[120] F. Iemini, C. Mora, and L. Mazza, Physical Review Letters **118**, 170402 (2017).

[121] W.-T. Xu and G.-M. Zhang, Physical Review B **95**, 195122 (2017).

[122] L. Mazza, M. Rizzi, M. Lukin, and J. Cirac, Physical Review B **88**, 205142 (2013).

[123] L. Mazza, F. Iemini, M. Dalmonte, and C. Mora, Physical Review B **98**, 201109 (2018).

[124] I. Mahyaeh and E. Ardonne, Physical Review B **98**, 245104 (2018).

[125] K. Kawabata, Y. Ashida, H. Katsura, and M. Ueda, Physical Review B **98**, 085116 (2018).

[126] A. Tanaka, Journal of Physics A: Mathematical and Theoretical **49**, 415001 (2016).

[127] G. Schaller, *Open quantum systems far from equilibrium* (Springer, 2014).

[128] S. Diehl, E. Rico, M. A. Baranov, and P. Zoller, Nature Physics **7** (2011).

[129] B. Kraus, H. P. Büchler, S. Diehl, A. Kantian, A. Micheli, and P. Zoller, Physical Review A **78**, 042307 (2008).

[130] P. D. Johnson, F. Ticozzi, and L. Viola, Quantum Info. Comput. **16**, 657 (2016).

[131] C. Hagendorf, Journal of Statistical Physics **150**, 609 (2013).

[132] M. Cerezo, R. Rossignoli, and N. Canosa, Physical Review A **94**, 042335 (2016).

[133] M. Cerezo, R. Rossignoli, N. Canosa, and E. Ríos, Physical Review Letters **119**, 220605 (2017).

[134] A. Berman and R. J. Plemmons, *Nonnegative matrices in the mathematical sciences*, Vol. 9 (Siam, 1994).

[135] E. Lieb, T. Schultz, and D. Mattis, Annals of Physics **16**, 407 (1961).

[136] H. Bethe, Zeitschrift für Physik **71**, 205 (1931).

[137] V. E. Korepin, N. M. Bogoliubov, and A. G. Izergin, *Quantum Inverse Scattering Method and Correlation Functions*, Cambridge Monographs on Mathematical Physics (Cambridge University Press, Cambridge, 1993).

[138] L. Šamaj and Z. Bajnok, *Introduction to the Statistical Physics of Integrable Many-body Systems* (Cambridge University Press, Cambridge, 2013).

[139] H. Tasaki, *Physics and mathematics of quantum many-body systems* (Springer, 2020).

[140] W. Selke, Physics Reports **170**, 213 (1988).

[141] P. Rujan, Journal of Statistical Physics **29**, 231 (1982).

[142] P. Ruján, Journal of Statistical Physics **29**, 247 (1982).

[143] P. Rujan, Journal of statistical physics **34**, 615 (1984).

[144] I. Peschel and T. Truong, Journal of statistical physics **45**, 233 (1986).

[145] J. Wouters, H. Katsura, and D. Schuricht, SciPost Physics Core **4**, 027 (2021).

[146] F. D. M. Haldane, Physics Letters A **93**, 464 (1983).

[147] F. D. M. Haldane, Physical Review Letters **50**, 1153 (1983).

[148] I. Affleck, Journal of Physics: Condensed Matter **1**, 3047 (1989).

[149] M. T. Batchelor, L. Mezincescu, R. I. Nepomechie, and V. Rittenberg, Journal of Physics A: Mathematical and General **23**, L141 (1990).

[150] A. Klumper, A. Schadschneider, and J. Zittartz, Journal of Physics A: Mathematical and General **24**, L955 (1991).

[151] M. Greiter, S. Rachel, and D. Schuricht, Physical Review B **75**, 060401 (2007).

[152] D. Schuricht and S. Rachel, Physical Review B **78**, 014430 (2008).

[153] H.-H. Tu, G.-M. Zhang, and T. Xiang, Physical Review B **78**, 094404 (2008).

[154] R. Orús and H.-H. Tu, Physical Review B **83**, 201101 (2011).

[155] A. Roy and T. Quella, Physical Review B **97**, 155148 (2018).

[156] D. P. Arovas, K. Hasebe, X.-L. Qi, and S.-C. Zhang, Physical Review B **79**, 224404 (2009).

[157] K. Hasebe and K. Totsuka, Physical Review B **87**, 045115 (2013).

[158] M. Fannes, B. Nachtergaele, and R. F. Werner, Communications in Mathematical Physics **144**, 443 (1992).

[159] D. Perez-Garcia, F. Verstraete, M. M. Wolf, and J. I. Cirac, Quantum Information & Computation **7**, 401 (2007).

[160] N. Schuch, I. Cirac, and D. Pérez-García, Annals of Physics **325**, 2153 (2010).

[161] T. Matsui, Infinite Dimensional Analysis, Quantum Probability and Related Topics **01**, 647 (1998).

[162] Y. Ogata, Communications in Mathematical Physics **348**, 847 (2016).

[163] Y. Ogata, Communications in Mathematical Physics **348**, 897 (2016).

[164] R. Orús, Annals of Physics **349**, 117 (2014).

[165] F. Pollmann, A. M. Turner, E. Berg, and M. Oshikawa, Physical Review B **81**, 064439 (2010).

[166] X. Chen, Z.-C. Gu, and X.-G. Wen, Physical Review B **83**, 035107 (2011).

[167] N. Schuch, D. Pérez-García, and I. Cirac, Physical Review B **84**, 165139 (2011).

[168] F. Pollmann, E. Berg, A. M. Turner, and M. Oshikawa, Physical Review B **85**, 075125 (2012).

[169] K. Duivenvoorden and T. Quella, Physical Review B **87**, 125145 (2013).

[170] A. S. Darmawan, G. K. Brennen, and S. D. Bartlett, New Journal of Physics **14**, 013023 (2012).

[171] A. S. Darmawan and S. D. Bartlett, New Journal of Physics **16**, 073013 (2014).

[172] B. Nachtergaele, Communications in mathematical physics **175**, 565 (1996).

[173] D. Gosset and E. Mozgunov, Journal of Mathematical Physics **57**, 091901 (2016).

[174] M. Lemm and E. Mozgunov, Journal of Mathematical Physics **60**, 051901 (2019).

[175] M. Lemm, Analytic Trends in Mathematical Physics **741**, 121 (2020).

[176] S. Knabe, Journal of statistical physics **52**, 627 (1988).

[177] E. Barouch and B. M. McCoy, Physical Review A **3**, 786 (1971).

[178] F. C. Alcaraz, S. R. Salinas, and W. F. Wreszinski, Physical Review Letters **75**, 930 (1995).

[179] C.-T. Gottstein and R. F. Werner, arXiv:cond-mat/9501123 (1995).

[180] S. M. Giampaolo, G. Adesso, and F. Illuminati, Physical Review Letters **100**, 197201 (2008).

[181] S. M. Giampaolo, G. Adesso, and F. Illuminati, Physical Review B **79**, 224434 (2009).

[182] C. Gómez, M. Ruiz-Altaba, and G. Sierra, *Quantum Groups in Two-Dimensional Physics*, Cambridge Monographs on Mathematical Physics (Cambridge University Press, 1996).

[183] A. Klümper, A. Schadschneider, and J. Zittartz, Zeitschrift für Physik B Condensed Matter **87**, 281 (1992).

[184] E. O'Brien, E. Vernier, and P. Fendley, Physical Review B **101**, 235108 (2020).

[185] E. Cobanera and G. Ortiz, Physical Review A **89**, 012328 (2014).

[186] A. Milsted, E. Cobanera, M. Burrello, and G. Ortiz, Physical Review B **90**, 195101 (2014).

[187] J. J. Rotman, *An Introduction to the Theory of Groups* (Springer New York, New York, NY, 1995).

[188] N. Moran, D. Pellegrino, J. K. Slingerland, and G. Kells, Physical Review B **95**, 235127 (2017).

[189] J. Hauschild and F. Pollmann, SciPost Phys. Lect. Notes , 5 (2018).

[190] G. Ortiz, E. Cobanera, and Z. Nussinov, Nuclear Physics B **854**, 780 (2012).

[191] A. Chew, D. F. Mross, and J. Alicea, Physical Review B **98**, 085143 (2018).

[192] S. Ostlund, Physical Review B **24**, 398 (1981).

[193] S. Howes, L. P. Kadanoff, and M. Den Nijs, Nuclear Physics B **215**, 169 (1983).

[194] N. Shiraishi and T. Mori, Physical Review Letters **119**, 030601 (2017).

[195] S. Moudgalya, S. Rachel, B. A. Bernevig, and N. Regnault, Physical Review B **98**, 235155 (2018).

[196] S. Moudgalya, N. Regnault, and B. A. Bernevig, Physical Review B **98**, 235156 (2018).

[197] S. Choi, C. J. Turner, H. Pichler, W. W. Ho, A. A. Michailidis, Z. Papić, M. Serbyn, M. D. Lukin, and D. A. Abanin, Physical Review Letters **122**, 220603 (2019).

[198] N. Shibata, N. Yoshioka, and H. Katsura, Physical Review Letters **124**, 180604 (2020).

[199] S. Moudgalya, E. O'Brien, B. A. Bernevig, P. Fendley, and N. Regnault, Physical Review B **102**, 085120 (2020).

[200] F. Wilczek, Physical Review Letters **48**, 1144 (1982).

[201] Y.-S. Wu, Physical Review Letters **52**, 2103 (1984).

[202] R. B. Laughlin, Physical Review Letters **50**, 1395 (1983).

[203] G. Moore and N. Read, Nuclear Physics B **360**, 362 (1991).

[204] N. Read and E. Rezayi, Physical Review B **54**, 16864 (1996).

[205] A. S. Jermyn, R. S. K. Mong, J. Alicea, and P. Fendley, Physical Review B **90**, 165106 (2014).

[206] D. Rossini, M. Carrega, M. Calvanese Strinati, and L. Mazza, Physical Review B **99**, 085113 (2019).

[207] P. Calabrese and M. Mintchev, Physical Review B **75** (2007).

[208] A. Calzona, T. Meng, M. Sassetti, and T. L. Schmidt, Physical Review B **98**, 201110 (2018).

[209] P. Calabrese and J. Cardy, Journal of Statistical Mechanics: Theory and Experiment **2004**, P06002 (2004).

[210] P. Calabrese and J. Cardy, Journal of Physics A: Mathematical and Theoretical **42**, 504005 (2009).

[211] T. Giamarchi, *Quantum physics in one dimension* (Oxford university press, 2004).

[212] R. Shankar, *Quantum Field Theory and Condensed Matter: An Introduction*, 1st ed. (Cambridge University Press, 2017).

[213] A. F. Albuquerque, F. Alet, P. Corboz, P. Dayal, A. Feiguin, S. Fuchs, L. Gamper, E. Gull, S. Gürtler, A. Honecker, R. Igarashi, M. Körner, A. Kozhevnikov, A. Läuchli, S. R. Manmana, M. Matsumoto, I. P. McCulloch, F. Michel, R. M. Noack, G. Pawłowski, L. Pollet, T. Pruschke, U. Schollwöck, S. Todo, S. Trebst, M. Troyer, P. Werner, and S. Wessel, Journal of Magnetism and Magnetic Materials Proceedings of the 17th International Conference on Magnetism, **310**, 1187 (2007).

[214] B. Bauer, L. D. Carr, H. G. Evertz, A. Feiguin, J. Freire, S. Fuchs, L. Gamper, J. Gukelberger, E. Gull, S. Guertler, A. Hehn, R. Igarashi, S. V. Isakov, D. Koop, P. N. Ma, P. Mates, H. Matsuo, O. Parcollet, G. Paw\lowski, J. D. Picon, L. Pollet, E. Santos, V. W. Scarola, U. Schollwöck, C. Silva, B. Surer, S. Todo, S. Trebst, M. Troyer, M. L. Wall, P. Werner, and S. Wessel, Journal of Statistical Mechanics: Theory and Experiment **2011**, P05001 (2011).

[215] M. Dolfi, B. Bauer, S. Keller, A. Kosenkov, T. Ewart, A. Kantian, T. Giamarchi, and M. Troyer, Computer Physics Communications **185**, 3430 (2014).

[216] N. Laflorencie, E. S. Sørensen, M.-S. Chang, and I. Affleck, Physical Review Letters **96**, 100603 (2006).

[217] P. R. Corboz, *Simulations of strongly correlated fermions and bosons*, Doctoral Thesis, ETH Zurich (2008).

[218] F. H. L. Essler, H. Frahm, F. Göhmann, A. Klümper, and V. E. Korepin, *The One-Dimensional Hubbard Model* (Cambridge University Press, 2005).

[219] E. O'Brien and P. Fendley, SciPost Physics **9**, 088 (2020).

[220] I. Mahyaeh and E. Ardonne, Physical Review B **101**, 085125 (2020).

[221] Y. Zhuang, H. J. Changlani, N. M. Tubman, and T. L. Hughes, Physical Review B **92**, 035154 (2015).

[222] R. Samajdar, S. Choi, H. Pichler, M. D. Lukin, and S. Sachdev, Physical Review A **98**, 023614 (2018).

[223] W. DeGottardi, M. Thakurathi, S. Vishveshwara, and D. Sen, Physical Review B **88**, 165111 (2013).

[224] A. Rahmani, X. Zhu, M. Franz, and I. Affleck, Physical Review Letters **115**, 166401 (2015).

[225] N. M. Gergs, *Transport and topological states instrongly correlated nanostructures*, PhD dissertation, Utrecht University (2017).

[226] J. Wouters, H. Katsura, and D. Schuricht, Physical Review B **98**, 155119 (2018).

[227] D. Allen, P. Azaria, and P. Lecheminant, Journal of Physics A: Mathematical and General **34**, L305 (2001).

[228] M. Beccaria, M. Campostrini, and A. Feo, Physical Review B **73**, 052402 (2006).

[229] M. Beccaria, M. Campostrini, and A. Feo, Physical Review B **76**, 094410 (2007).

[230] G. v. Gehlen and V. Rittenberg, Journal of Physics A: Mathematical and General **19**, L625 (1986).

[231] W. Li, S. Yang, H.-H. Tu, and M. Cheng, Physical Review B **91**, 115133 (2015).

[232] S.-Y. Zhang, H.-Z. Xu, Y.-X. Huang, G.-C. Guo, Z.-W. Zhou, and M. Gong, Physical Review B **100**, 125101 (2019).

[233] V. Kaskela and J. L. Lado, Physical Review Research **3**, 013095 (2021).

[234] E. Cobanera, J. Ulrich, and F. Hassler, Physical Review B **94** (2016).

[235] V. Lahtinen, T. Mansson, and E. Ardonne, SciPost Physics Core **4**, 014 (2021).

[236] M. E. J. Newman and G. T. Barkema, *Monte Carlo methods in statistical physics* (Oxford University Press, Oxford, New York, 1999).

[237] C. J. Hamer, J. B. Kogut, and L. Susskind, Physical Review D **19**, 3091 (1979).

[238] A. B. Zamolodchikov and V. A. Fateev, Sov.Phys.JETP **63**, 913 (1986).

[239] E. O'Brien, *Exotic phases of interacting Majorana fermions and parafermions*, Ph.D. thesis, University of Oxford (2020).

[240] Y. Alavirad, D. Clarke, A. Nag, and J. D. Sau, Physical Review Letters **119**, 217701 (2017).

[241] R. Jafari and A. Langari, Physica A: Statistical Mechanics and its Applications **364**, 213 (2006).

[242] S. Whitsitt, R. Samajdar, and S. Sachdev, Physical Review B **98**, 205118 (2018).

[243] L. Turban, Journal of Physics A: Mathematical and General **18**, 2313 (1985).

[244] R. Kress, *Numerical Analysis*, Graduate Texts in Mathematics (Springer-Verlag, New York, 1998).

Nederlandse samenvatting

De taal van (theoretisch) natuurkundig wetenschappelijk onderzoek is abstract en wiskundig. Het is een taal die je in een jaar of tien meester wordt, maar die niet geschikt is om het werk aan een breed publiek te presenteren. Met deze samenvatting, geformuleerd in meer gangbare taal, wil ik graag mijn familie, vrienden en andere geïnteresseerden zonder achtergrond in natuurkunde een inkijkje geven in het onderzoek dat ik de afgelopen vier jaar heb gedaan. Ik plaats mijn onderzoek in de hedendaagse wetenschappelijke context, geef een motivatie voor de onderzoeksrichting, en leg de belangrijkste resultaten van dit proefschrift aan u voor.

De hoofdstukken in dit proefschrift dragen alle een eigen steentje bij aan het theoretische onderzoek naar parafermionen en topologische systemen. Beide termen komen in deze samenvatting aan de orde en worden in verband gebracht met de bouw van quantumcomputers.

Quantumcomputers

De smartphone in uw broekzak, de laptop waarop ik dit proefschrift samenstel, de supercomputers van IBM, dat zijn allemaal elektronische rekenaars die de uitkomst zijn van 75 jaar innovatie. De computer is niet meer weg te denken uit ons leven, van de deurbel tot de e-bike en het scheerapparaat. Ons dagelijks leven wordt een stuk eenvoudiger dankzij de computer. Het wetenschappelijk leven ook. De computer neemt repetitieve berekeningen uit handen en doet dat sneller dan de mens ooit met pen en papier zou kunnen. Toch zijn er bepaalde problemen die met de snelste computers die nu voorhanden zijn niet op te lossen zijn. Ondanks dat volgens de wet van Moore de rekensnelheid elke paar jaar verdubbelt, blijven deze problemen altijd buiten bereik van het huidige type computers.

Dit wordt duidelijk met behulp van een simpel voorbeeld. Een pakketbezorger moet 3 pakketjes bezorgen naar adressen A, B, C. Om te bepalen wat de snelste route is moet hij alle adresvolgordes afgaan, eerst A, dan B dan C,

maar ook A–C–B en B–A–C.[a] Voor elke volgorde berekent hij de afstand en zo kan hij de snelste route vinden. Het berekenen van 3 adressen is nog wel te behappen voor de bezorger. Bij 5 adressen wordt het al lastiger, dan zijn er namelijk 60 adresvolgordes mogelijk. Heeft de pakketbezorger 28 adressen om langs te gaan, dan moeten er $1{,}6\times10^{29}$ (ofwel ruim honderd miljard miljard miljard) volgordes bekeken worden. Dat is onbegonnen werk. Routeoptimalisatie groeit als de faculteit ($N!/2$) van het aantal adressen (N). Met andere woorden: het aantal mogelijke volgordes groeit sneller dan exponentieel. Ook in de biologie, scheikunde en natuurkunde zijn er tal van optimalisaties en simulaties die (sneller dan) exponentieel groeien. Voor systemen met veel componenten gaan dit soort berekeningen al snel de beste supercomputer boven de pet en moeten er benaderingen worden gedaan om een zo goed mogelijk antwoord te krijgen.

Al in de jaren tachtig opperde de beroemde natuurkundige Richard Feynman om de hulp van quantummechanica in te roepen om dit soort berekeningen te doen, een quantumcomputer. Die belooft dit soort exponentiële problemen wel het hoofd te kunnen bieden. Om dat te begrijpen kijken we naar de kleinste bouwsteentjes van computers. Normale computers maken gebruik van vele miljarden transistoren, kleine elektronische componenten die verschillende spanningen aan kunnen geven. Als die transistor een lage spanning aangeeft is dat in computertaal een 0. Een hoge spanning correspondeert met een 1. Die 0 of 1, een bit, is de kleinste eenheid van de berekeningen in een computer. De combinatie van veel bits levert een binair getal, bijvoorbeeld 11111100110 (2022 in het decimale stelsel).

Een quantumcomputer werkt anders. Voor deze computer zijn de bouwstenen quantumbits, qubits. Deze bevinden zich noch in 0 noch in 1, maar in een combinatie van de twee, $0+1$. Elke qubit is dus twee toestanden tegelijk. Bij de koppeling van vele qubits komt een magische exponentiële groei naar voren. Als we twee van deze qubits combineren, zijn die gezamenlijk $00+01+10+11$, vier toestanden. Met niet meer dan 10 qubits worden $2^{10} = 1024$ toestanden tegelijk aangesproken. De exponentiële groei werkt hier in ons voordeel, want slechts 100 qubits vertegenwoordigen al $2^{100} = 1{,}3 \times 10^{30}$ configuraties, genoeg voor de pakketbezorger om de perfecte route langs 28 adressen uit te stippelen. In een quantumcomputer kunnen berekeningen op al die configuraties tegelijk worden gedaan, terwijl in een klassieke computer elke toestand apart

[a] De oplettende lezer zal opmerken dat er nog 3 routes mogelijk zijn. Zo is er bijvoorbeeld C–B–A. Omdat dat het omgekeerde van A–B–C is, kunnen we die buiten beschouwing laten.

beschouwd moet worden. Zo kan met één enkele berekening een optimale route worden verkregen.

Er zijn al tal van quantumcomputers in gebruik. Grote techbedrijven als Google, IBM en Microsoft stellen apparaten beschikbaar met enkele tientallen qubits. Deze quantumcomputers kunnen inmiddels goed concurreren met klassieke computers, maar halen nog niet de rekenkracht die nodig is om de grote optimalisatieproblemen aan te pakken. Daarvoor is het aantal qubits in één apparaat simpelweg nog niet groot genoeg.

Een van de grote uitdagingen bij het opschalen van het aantal qubits is de stabiliteit van deze bouwstenen. Het koppelen van veel qubits blijkt lastig omdat ze door externe factoren en wisselwerkingen gemakkelijk kunnen vervallen tot een 0 óf een 1. Dan gaat de combinatie van de twee verloren en is de opgeslagen informatie verdwenen.

De quantummechanische aard van de deeltjes gooit hier roet in het eten. Natuurkundig onderscheiden we grofweg twee soorten systemen, zoals weergegeven in de linker helft van Figuur 2. De systemen bestudeerd in dit proefschrift kunnen worden beschreven door elektronen, geladen deeltjes, die over een draad (kralenketting) van atomen kunnen bewegen. Deze elektronen rangschikken zich in de toestand met de laagste energie. In deze grondtoestand zitten deze deeltjes statisch in het systeem. Dit is te vergelijken met de stilhangende kogels in een Newtonpendel in de linker helft van Figuur 1. De rechter helft van Figuur 1 laat de aangeslagen toestand zien: de beweging wordt er heen- en weergekaatst door de kogels. Als de elektronen worden aangeslagen, door een elektrische spanning of een verandering van temperatuur, gaan ze bewegen en transporten ze hun lading door het materiaal. Met andere woorden: er gaat een stroom lopen.

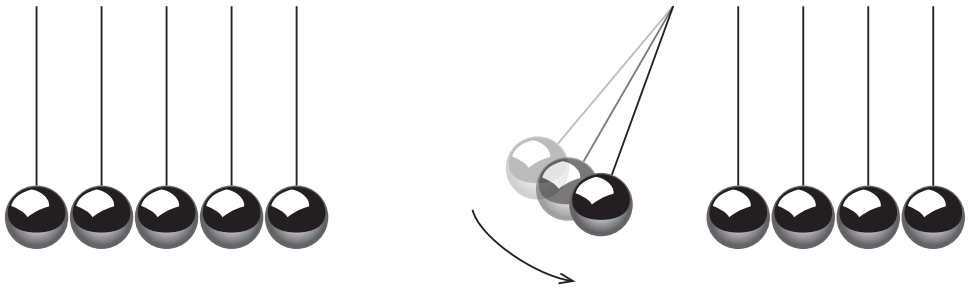

Figuur 1: Newtonpendel, in de grondtoestand (links) en in een aangeslagen toestand (rechts).

Zoals te zien is in Figuur 2 is het aanslaan van zo'n toestand gemakkelijk in een geleider, bijvoorbeeld koper. Daarin is de benodigde energie klein, de lading gaat er gemakkelijk in stromen. Voor isolatoren zoals plastic is dat een stuk lastiger. De hoge energie, benodigd voor het aanslaan, maakt het lastig stroom te laten lopen door dit soort materialen.

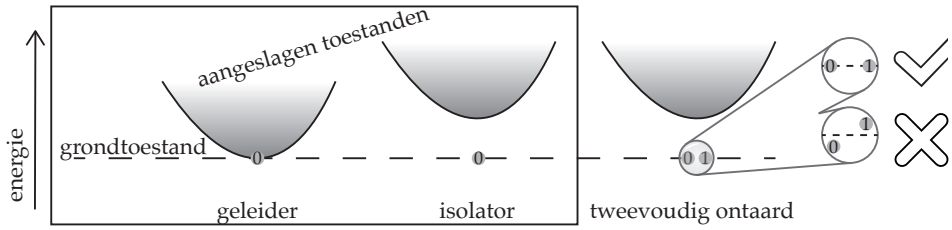

Figuur 2: De aangeslagen toestanden (zwarte lijn) in een geleider (links) liggen qua energie heel dicht bij de energie van de grondtoestand: elektronen kunnen eenvoudig door het systeem stromen. Voor een isolator (midden) is er een energiesprong nodig om het systeem van de grondtoestand in de aangeslagen toestand te brengen: stroom wordt slecht geleid. Sommige isolatoren hebben meerdere toestanden op dezelfde laagste energie. Die zijn tweevoudig ontaard (rechts). Verstoringen kunnen ervoor zorgen dat er een energieverschil ontstaat (cirkels rechts) en de ontaarding verloren gaat.

Er zijn daarnaast verschillende soorten isolatoren. Dat is afhankelijk van hun grondtoestand. In uitzonderlijke gevallen zijn er in die isolatoren twee toestanden met precies dezelfde energie. Dat wordt een tweevoudig ontaarde toestand genoemd. De rechter tekening van Figuur 2 laat deze situatie zien. Deze ontaarding kan gebruikt worden om een quantumbit te creeëren. We wijzen de ene toestand aan als 0 en de andere als 1 en maken een somtoestand $0 + 1$. Deze somtoestand blijft behouden als de twee heel precies op dezelfde energie blijven. Dat laatste is helaas niet gegarandeerd. Kleine verstoringen en onderlinge wisselwerkingen zorgen ervoor dat de twee energieën iets gaan verschuiven. De energie van de 0 wordt bijvoorbeeld lager dan die van 1. Omdat het systeem naar de laagste energie streeft, zal de somtoestand vervallen in 0 en de quantuminformatie is verloren.

In dit proefschrift heb ik naar systemen gekeken die robuust zijn voor dit soort destructieve ontwikkelingen. Deze systemen zijn eendimensionale topologische materialen. Dit zijn draden van atomen, die de bewegingsruimte van driedimensionale elektronen beperken tot één richting. In het kort betekent het "topologische" van deze systemen dat de interessante eigenschappen zich

aan de uiteinden van de draden bevinden, het begin en het eind. Op quantummechanische schaal liggen deze twee uiteinden ver uit elkaar. Omdat de tweevoudige ontaarding van de grondtoestanden zich voordoet aan deze einden, hebben ze geen onderlinge interactie. Dat maakt de ontaarding robuust: de somtoestand kan blijven bestaan, althans, theoretisch. Experimenteel zijn er nog de nodige kinken in de kabel. De natuur is nooit zo perfect als de modellen die we ontwerpen. Daarom is er ook voor theoretici werk aan de winkel. Alle denkbare effecten van experimentele verstoringen en wisselwerkingen dienen in duidelijk in kaart gebracht te worden. Dit proefschrift draagt bij aan het onderzoek naar deze topologische qubits.

Majoranas en parafermionen

In de natuur komen deeltjes voor in twee gedaantes: bosonen en fermionen. Twee bosonen, zoals lichtdeeltjes, kunnen zich op dezelfde plek bevinden. Denk aan twee lichtstralen die elkaar zonder probleem kruisen. Voor fermionen is het expliciet uitgesloten dat twee deeltjes dezelfde plek en snelheid hebben. De elektronen in onze eendimensionale draad behoren tot die categorie. Bovendien gebeurt er iets bijzonders in onze topologische systemen. De natuurkundige beschrijving van dit verschijnsel laat zich mooi vatten in Majoranafermionen. Deze deeltjes, voorgesteld door Ettore Majorana, hebben de eigenaardige eigenschap dat ze hun eigen antideeltjes zijn. Normale fermionen, zoals elektronen, hebben die eigenschap niet. Het antideeltje van een fermion kan zich heel anders gedragen dan het fermion zelf. De qubits vervaardigd uit deze topologische systemen kunnen we daarom ook wel Majoranaqubits noemen.

In Hoofdstuk 2 worden aan zo'n Majoranasysteem verstoringen toegevoegd die zich kunnen voordoen in de experimentele werkelijkheid. Hier laat ik zien dat de topologische eigenschappen, belangrijk voor het qubit, nog steeds behouden blijven.

Recent is gebleken dat het rekenen met de Majoranaqubits in de quantumcomputer veel lastiger is dan voorheen gedacht. De hoop is daarom ook gevestigd op een broertje van de Majoranas, de parafermionen. Dit zijn deeltjes die noch bosonen, noch fermionen zijn, ze bevinden zich er tussenin. Parafermionen zijn natuurkundig niet toegestaan in de drie dimensies waar wij normaal gesproken in leven. Maar als een systeem wordt beperkt tot één of twee dimensies, zoals de draad hierboven, kunnen deze deeltjes onder extreme

omstandigheden de kop op steken. In Hoofdstukken 3, 4, 5 en 6 worden deze parafermionen bestudeerd. Net als Majoranadraden vertonen deze parafermiondraden, onder bepaalde omstandigheden, topologische eigenschappen. Dat maakt ze eveneens geschikt voor het construeren van een quantumbit, een parafermionqubit. In Hoofdstukken 3, 5 en 6 bekijk ik het effect van de verstoring en wisselwerkingen op het topologisch gedrag van de parafermionen. Daarmee draag ik bij aan de theoretische studie vooruitlopend op parafermionqubits. Hoofdstuk 4 is gewijd aan parafermionen in een andere gedaante, Fock parafermionen. Hierin draait de natuurkunde niet om topologie, maar heb ik laten zien onder welke voorwaarden dit exotische systeem zich als geleider of isolator gedraagt.

Het onderzoek dat ten grondslag lag aan dit proefschrift onderscheidt zich in twee categorieën. Ten eerste kan al veel van het gedrag van systemen met pen en papier worden bestudeerd. Formules geven een algemeen beeld van de natuurkunde. Dit heten analytische resultaten. Waar deze methoden tekort schoten, werd de hulp van de computer ingeroepen. Met behulp van algoritmes geven de numerieke resultaten een gedetailleerd beeld van de fysische eigenschappen van de systemen in kwestie. Hiermee heb ik aan den lijve ondervonden hoe lastig een quantummechanisch systeem te simuleren is op een klassieke computer. Deze tak van onderzoek is een goed voorbeeld van een directe toepassing van quantumcomputing en zal in een extreme stroomversnelling komen als snellere quantumcomputers het daglicht zien. Wellicht zijn die binnenkort gebaseerd op de Majorana- of parafermionqubits. In de toekomst gaat zowel de natuurkundige als de pakketbezorger de vruchten plukken van deze opwindende nieuwe technologie.

Geschiedenis van het Instituut voor Theoretische Fysica te Utrecht

This chapter is the odd one out. In the summer of 2020 I investigated the origins of the Institute for Theoretical Physics, spurred by the lack of a founding date. This resulted in a lecture on the history of the institute in October 2020, the publication of a Dutch article in *het Nederlands Tijdschrift voor Natuurkunde* and a shorter English piece in *Fylakra*. Here I present both articles, side by side.

Dit hoofstuk is gebaseerd op: J.J. Wouters, *Ornstein en de ontwikkeling van het Utrechtse Instituut voor Theoretische Fysica*, Nederlands Tijdschrift voor Natuurkunde 87(9), 42-46 (2021).

Tot voor kort was het niet bekend wanneer het Instituut voor Theoretische Fysica was opgericht. Met deze kwestie in gedachten heb ik de geschiedenis van theoretische natuurkunde in Utrecht onder de loep genomen. De rode draad in dat verhaal is de ingewikkelde relatie met de experimentele natuurkunde: onafhankelijk doch onlosmakelijk verbonden.

Ruim een eeuw theoretische natuurkunde in Utrecht heeft tal van wetenschappelijke successen opgeleverd. Denk aan de Nobelprijs voor Gerard 't Hooft en Martinus Veltman of Nico van Kampens bijdragen aan de statistische mechanica, maar ook Hendrik Kramers' werk in de jonge quantumtheorie of Leonard Ornsteins en George Uhlenbecks beschrijving van de Brownse beweging. Ter ere van het 105-jarig bestaan zet het Instituut voor Theoretische Fysica (ITF) in Utrecht komend na-

This chapter is based on: J.J. Wouters, *Celebrating 105 Years Institute for Theoretical Physics*, Fylakra, 65(3), 30 (2021)

We typically associate the Institute for Theoretical Physics (ITP) in Utrecht to the Nobel Prize of Gerard 't Hooft and Martinus Veltman, perhaps to the statistical physics contributions of Nico van Kampen, Hans Kramers' works on quantum theory, and even to the Ornstein-Uhlenbeck effect describing Brownian Motion.[a] However, until quite recently, we did not know when the ITP was founded. Last year, the di-

[a] Last year a mural dedicated to this work was revealed at the Oosterkade in Utrecht, close to the Physical Laboratory.

jaar deze rijke geschiedenis in het zonnetje. Een heuglijk moment met een wat wrange bijsmaak. Het eeuwfeest is namelijk gemist en de huidige pandemie maakt planning van festiviteiten lastig.

De wringende relatie tussen de theoretische en experimentele natuurkunde in Utrecht kwam bijvoorbeeld naar voren toen in 1958 de eerste plannen werden gemaakt voor de verhuizing vanuit de Utrechtse binnenstad naar de Uithof. Het ITF had zes jaar eerder een eigen pand betrokken en zich daarmee ruimtelijk definitief losgemaakt van de experimentele natuurkunde. In de nieuwe huisvesting dreigden de theoretici wederom als een van de onderafdelingen van het Fysisch Laboratorium te worden beschouwd. De verzamelde docenten van de afdeling natuurkunde schreven het bestuur van de universiteit:[a]

> "De vergadering wenst nog eens nadrukkelijk als haar unaniem oordeel te kennen te geven dat het feit dat het Instituut voor Theoretische Fysica organisatorisch een op zichzelf staand instituut is, ook bij de bouw tot uiting moet komen."

Dit bekroonde een periode van zestig jaar waarin theoretische fysica als zelfstandige discipline volwassen werd en zich losmaakte van de experimentele natuurkunde.

De basis voor het ITF werd eind negentiende eeuw gelegd. Toegenomen aandacht en financiering voor natuurkunde leidde tot professionalisering. De experimenten werden duur,

[a] Brief van afdeling natuurkunde aan College van Curatoren d.d. 17 november 1958, in: Archief Bestuursgebouw Universiteit Utrecht, in: Fysisch Laboratorium.

rector of the institute, René van Roij, prompted by the 30th anniversary celebrations of the Debye Institute for Nanomaterials Science[b], asked around for clues concerning the early days of ITP. I took up the baton and spent some time delving into the history of the theoretical physics at Utrecht, focusing on the first half of the twentieth century.

The story of the foundation of the institute, turned out to be as much about the emergence of theoretical physics as it is about theoretical physics' complicated relationship with experimental physics.

Deep into the ninetieth century, there was just physics. The one professor surveyed both the experiments and theory, even though the latter assumed a supporting role. By the end of the ninetieth century, professionalization accelerated the physics research. As a result, specializations, like theoretical physics emerged. Nonetheless the theorists were mere assistants to the experimentalists; even Hendrik Lorentz was the theoretical left hand of Kamerlingh Onnes in Leiden.

[b] See FYLAKRA issue 4 of 2019.

Fig. 1:
Physisch Laboratorium aan Bijlhouwerstraat omstreeks 1920 - Utrechts Archief

Physical Laboratory at Bijlhouwerstraat around 1920 - Utrechts Archief

te tijdrovend en te complex om te combineren met theoretisch werk.

Waar voorheen slechts één leerstoel gereserveerd was voor natuurkunde, werd in 1896 in Utrecht een nieuw professoraat gecreëerd om aan de theoretische wensen te voldoen. Victor August Julius werd de eerste hoogleraar theoretische natuurkunde. Gelijktijdig werd zijn neef Willem Henri Julius benoemd tot hoogleraar experimentele natuurkunde en directeur van het Physisch Laboratorium.

Dat laboratorium, gevestigd aan de Bijlhouwerstraat in Utrecht, was een kwart eeuw eerder in opdracht van Christophorus Buys Ballot neergezet. Om de uitbreiding van zowel de personeelsgeleding, studentenaantallen als experimenten het hoofd te bieden, werden eind negentiende eeuw al meerdere vleu-

In Utrecht, theoretical physics 'started' with the appointment of the first theory professor, Victor Julius[c], on the 12th of August 1896 (around 125 years ago). Alongside him was his nephew, director of the Physical Laboratory and professor experimental physics Willem Julius. Both worked in the lab, commissioned by Buys Ballot in 1875 at the Bijlhouwerstraat. Supporting classes for medicine and pharmacy students were also held at this location,

[c]The one from the Julius institute

gels aangebouwd. Ondanks de verbouwingen bleef er structureel ruimtegebrek: voor een volwaardige werkruimte voor puur theoretisch onderzoek was geen plaats. Dit gaf treffend de positie van theorie binnen de natuurkunde weer. Zij stond slechts ten dienste van de proefondervindelijke oudere broer.

Toen Victor Julius in 1902 kwam te overlijden, werd zijn leerstoel kortstondig bekleed door Henri du Bois (1902-1904) en Cornelis Wind (1904-1911). Het komen en gaan van hoogleraren versterkte de positie van de theoretische natuurkunde allerminst: Du Bois richtte zich voornamelijk op experimenten en Wind deed meer aan meteorologie dan natuurkunde. Door Peter Debye aan te stellen hoopte men in 1912 de theoretische leerstoel nieuw leven in te blazen. Met onder andere Johannes van der Waals in Amsterdam en Hendrik Lorentz en Paul Ehrenfest in Leiden liep Utrecht hopeloos achter in dit snelgroeiende vakgebied. Helaas zat Debye hier niet op zijn plek: hij vertelde later dat theoretici nog altijd niet welkom waren in het lab.[b] In 1914 besloot Debye een aanbod in Göttingen te accepteren. Ondanks de moeizame relatie met het Physisch Lab was Debye een geliefd hoogleraar. Terwijl hij op het punt stond op de trein naar Duitsland te stappen, ondernamen zowel zijn studenten als het bestuur van de universiteit een laatste poging hem te behouden. In april 1914 lobbyden ze bij de Minister van Binnenlandsche Zaken voor uitbreiding van het laboratorium en het aanstellen van een assistent

[b] Interview met Peter Debye door Thomas S. Kuhn en George Uhlenbeck, 3 mei 1962, Niels Bohr Library & Archives, American Institute of Physics.

besides physics research and education. Despite several reconstructions the lab suffered from a continuous shortage on space. Around 1900, there was no longer room for theoretical physics, with teaching and experiments consuming the whole lab. After Julius passed away in 1902, also his successors, Henri du Bois (1902-1904) and Cornelis Wind (1904-1911) did not carry theory in Utrecht into the twentieth century. Du Bois was at heart an experimentalist and Wind fancied meteorology.

In 1912, the physics department hoped to spur on theoretical physics by appointing Peter Debye as Wind's successor. However, the lack of space in the lab was one of the reasons for Debye to leave for Göttingen already in 1914.[d] Both the students as well as the university regretted his decision and requested the minister to allocate additional funding for both extensions of the lab as well as an assistant to facili-

[d] Interview with Peter Debye by Thomas S. Kuhn and George Uhlenbeck, 3 May 1962, Niels Bohr Library & Archives, American Institute of Physics.

om de theoriehoogleraar te faciliteren.[c]

Deze uiterste poging overtuigde Debye niet in Utrecht te blijven, maar het bleek wel een belangrijke aanzet voor de verbetering van de status van de theoretische natuurkunde. Kort daarna gingen het Rijk en de universiteit haast maken met uitbreiding van het lab. In januari 1915 werden de ontwerpen voor de uitbreiding goedgekeurd en kon de bouw beginnen.[d] Gelijktijdig werd Leonard Salomon Ornstein benaderd om Debye op te volgen. Ornstein was een student van de Leidse hoogleraar theoretische natuurkunde Lorentz en promoveerde in 1908 op *Toepassing der statistische mechanica van Gibbs op moleculair-theoretische vraagstukken.*

Na de onvrede van Debye was de bereidheid theorie te faciliteren aanzienlijk vergroot. Dit voelde Ornstein haarfijn aan en hij eiste onmiddellijk een assistent en een leeszaal.[e] De eerste assistent theoretische natuurkunde, A. Koerts, werd een jaar later aangesteld.[f] En toen de verbouwing begin 1916 voltooid was, nam Ornstein met zijn assistent zijn intrek in het lab.[g] Waarschijnlijk kreeg hij twee kamers toebedeeld in de nieuwbouw op de westvleugel. Om de positie van zijn onderzoeksgroep

[c] Brief van J.H.W.Q ter Spill aan Minister van Binnenlandsche Zaken, d.d. 9 april 1914, in: Nationaal Archief, 2.04.13, 475; Brief van Curatoren aan Minister van Binnenlandsche Zaken, d.d. 22 april 1914, in: Nationaal Archief, 2.04.13, 475;

[d] Brief van Rijksbouwkundige voor gebouwen van Onderwijs enz. aan Minister van Binnenlandsche Zaken, d.d. 22 december 1914, in: Nationaal Archief, 2.04.13, 475;

[e] Notulen van de Faculteitsraadvergadering 20 april 1915, in: Archief Bestuursgebouw Universiteit Utrecht, in: Faculteit der Wis- en Natuurkunde, 137.

[f] Nederlandsche Staatscourant 12 februari 1916, p. 2.

[g] Brief van W.H. Julius aan College van Curatoren d.d. 28 september 1916, in: Het Utrechts Archief 59, 2019.

tate the theory professor.[e] It would not persuade Debye to stay. Nonetheless, it would lay the foundation for acceptance of theoretical physics in Utrecht.

Within a year, plans for an extension were approved and the work started. In the meantime Leonard Ornstein was approached by Julius for the vacant theory seat. Ornstein was a lecturer in Groningen at the time, after doing his PhD in Leiden with Lorentz on statistical mechanics. He entered Utrecht in 1915 as a young, but determined theorist, immediately demanding both an assistant and several rooms for theoretical physics. The assistant was appointed less than a year later, concurrent with the completion of the lab renovation. Several rooms on the second floor of the new west wing were reserved for his newly formed research group. He named this group the Institute for Theoretical Physics.

[e] Letter from J.H.W.Q ter Spill to Minister van Binnenlandsche Zaken, d.d. 9 April 1914, in: Nationaal Archief, 2.04.13, 475; Letter from Curatoren to Minister van Binnenlandsche Zaken, d.d. 22 April 1914, in: Nationaal Archief, 2.04.13, 475;

te versterken, gaf Ornstein haar de naam *Instituut voor Theoretische Natuurkunde*.

De eerste aanwijzing daarvoor weerklonk in de openingsrede van rector magnificus prof. Ernst Cohen op 18 september 1916:[h]

> "In het Physisch Laboratorium waren kort na het begin van den afgeloopen kursus de nieuwe bijgebouwde vertrekken zoover gereed, dat zij in gebruik konden worden genomen; hierdoor werd het mogelijk, aldaar een Instituut voor theoretische Natuurkunde onder leiding van onzen ambtgenoot Ornstein te stichten, . . . "

Daarmee kunnen we stellen dat het Instituut voor Theoretische Natuurkunde te Utrecht zijn oorsprong kent in het academisch jaar 1915-1916. Bij gebrek aan vroegere datering, beschouwen wij, bij het ITF, vanaf nu 18 september 1916 als oprichtingsdatum. Ondanks dat dit het startpunt van het ITF is, zullen we zien dat de autonomie van de groep theoretici nog lang beperkt zou blijven.

Al snel verzamelde Ornstein een grote groep onderzoekers om zich heen. Naast een handjevol theoretici waren dit voornamelijk experimentatoren. Toen Ornstein in Utrecht aankwam was hij een verstokt theoreticus, neerkijkend op de experimentele natuurkunde. Maar de geavanceerde instrumenten van Julius en diens assistent Willem Moll wekten zijn belangstelling voor het experiment. De artikelen die in de eerste jaren van Ornsteins hand kwamen waren niet enkel theoretisch, met behulp van de nieuwe

[h] E.J. Cohen, *Dingen en Menschen*, Utrecht, 18 september 1916

Fig. 2: Ornstein, rond 1917 - Universiteitsmuseum

The first notion thereof dates to the 18th of September 1916, when the rector of the university acknowledges that Ornstein "founded the Institute for Theoretical Physics in the newly build rooms".[f] Hence, we can establish this as the founding date of the ITP, almost 105 years ago at the time of writing.

In the remainder of our story, we will discuss that

[f] E.J. Cohen, *Dingen en Menschen*, Utrecht, 18 september 1916

instrumenten verschenen ook al snel experimentele bijdrages uit zijn groep. Samen met Moll deed hij onderzoek naar vloeibare kristallen[i] en met Herman Burger startte het Utrechtse onderzoek naar Brownse beweging. [j] Daarnaast legde hij met zijn oud-collega Frits Zernike de laatste hand aan het, in Groningen gestarte, theoretisch onderzoek naar dichtheidsverdelingen in vloeistoffen, waaruit de Ornstein-Zernike-vergelijkingen voortkwamen.[k] Al deze werken werden door Ornstein en zijn assistenten ondertekend met *Instituut voor Theoretische Natuurkunde Utrecht*.

Hiermee zien we dat er een omslag had plaatsgevonden. Waar het voorheen de theoretici waren die de experimentatoren van dienst waren, zette Ornstein experimentatoren aan het werk om zijn theoriën te onderzoeken en te ondersteunen.

Toen Julius in 1920 door ziekte moest aftreden als directeur van het Physisch Laboratorium, was Ornstein een vanzelfsprekende opvolger. Onderwijl had Ornsteins groep een aanzienlijk deel van het lab tot haar beschikking. Wederom zien we de relatie tussen theorie en experiment veranderen, want Ornstein was de experimentele natuurkunde gaan waarderen. Hij vond het van essentieel belang dat er nauw werd samengewerkt tussen the-

[i] Zie bijv. W.J.H. Moll en L.S. Ornstein, *Bijdrage tot de studie der vloeibare kristallen.*, Versl K Akad Wet Amst 1916, 25, p. 682, 1916.

[j] Zie bijv. H.C. Burger, *Over de theorie der Brown'sche beweging*, Versl K Akad Wet Amst 1916-1917, 25–2, p. 1482, 1917.; Vijftien jaar later volgt hieruit het werk met Uhlenbeck, samengevat in de Ornstein-Uhlenbeck vergelijking. Recent is hierover een muurschildering opgeleverd aan de Oosterkade in Utrecht, nabij het Physisch Laboratorium.

[k] Zie bijv. L. Ornstein en F. Zernike, *Die linearen Dimensionen der Dichteschwankungen*, Phys. Z., vol. 19, p. 134, 1918.

the recognition of an independent group theorist was by no means guaranteed in the century that followed.

The first few years were fruitful for the ITP. Ornstein gathered a group of assistants, both theorists and experimentalists around him and promptly they started writing papers on liquid crystals, Brownian motion, fluid density theory etc.[g] All of these were signed with Institute for Theoretical Physics, but most were based (partly) on experimental results. The pecking order had changed. Ornstein put experimentalists at work to support his theories, instead of the inverse relation of half a decade earlier. Ornstein had also changed. He came in as a pure theorist, looking down at experiments. Yet, the advanced instruments, designed by Julius and his assistant Moll, made him appreciate the value of experimental physics.

When Julius fell ill in 1920, Ornstein's group had practically taken over the lab, and it was more than reasonable that

[g] See for instance: W.J.H. Moll en L.S. Ornstein, *Contributions to the research of liquid crystals* , KNAW, Proc 1916, 19, p. 1315, 1916.

orie en experiment: "Een innige samenwerking van theorie en experiment is de eerste eisch. . . "[l] Vanaf de jaren twintig trad het Physisch Laboratorium weer als een eenheid naar buiten. Hiermee verdween de naam *Instituut Theoretische Natuurkunde* naar de achtergrond.

In deze periode centreerde het onderzoek zich rond de nieuwe fotometer van Moll. Dit apparaat stelde hen in staat met ongekend hoge nauwkeurigheid atomaire emissiespectra te meten. De Utrechtse resultaten waren cruciaal voor validatie en verfijning van de quantummechanische beschrijving van het atoom. Bovendien droegen Burger en Ornstein ook theoretisch bij, met hun som- en intensiteitsregels. De filosofie achter deze theoriën sloot aan bij de quantummechanische ideën van Sommerfeld en Einstein. Hun wiskundige benadering was gestoeld op een deterministisch wereldbeeld. Daartegenover stond de benadering van Bohr en Heisenberg, bekend als de Kopenhaagse interpretatie, die later gangbaar zou worden. Ornstein zou zich nooit kunnen vereenzelvigen met die laatste kijk op de natuurkunde. Hij was van mening dat "physica . . . geen physica meer zou zijn", als Bohr en Heisenberg gelijk hadden.[m]

Het is daarom opvallend dat Ornstein vanaf 1926 een leerling van Bohr, Hans Kramers, aan zijn zijde kreeg als hoogleraar theoretische natuurkunde.

he took over as director. This again signaled a significant change for the ITP, as Ornstein altered course. He started to view theory and experiment as inseparable, all the work from the lab was to be published under *Physical Laboratory*. Moreover, Ornstein reserved the title (Physical) Institute for the entire lab. Nonetheless, there were always several dedicated theory assistants present and Ornstein remained the theory professor.

This would change just a few years later when Julius passed away in 1925. Ornstein took over his experimental seat (as was common for the director) and was looking to fill the theoretical physics vacancy with Herman Burger, a long-time assistant. The faculty preferred a more theoretically inclined candidate and selected Hans Kramers in 1926. As a student of both Niels Bohr and Paul Ehrenfest, Kramers was a representative of modern quantum theory, a supporter of the Copenhagen-interpretation. This stood in stark contrast with Ornstein's quantum philosophy, which was more in line with Arnold Sommerfeld and Alfred Einstein, built upon mathematical

[l] A. M. van Dyck-Huffnagel en L. Ornstein, *Het natuurkundig laboratorium der Rijks-universiteit te Utrecht*. (Utrecht, 1926), p. 52

[m] H. A. Kramers, *Levensbericht van L.S. Ornstein (12 Nov. 1880 - 20 Mei 1941)*, in: Jaarboek der Nederlandsche Akademie van Wetenschappen 1940-1941 (Amsterdam, 1941), p. 227

Fig. 3:
Zittend derde van links: Kramers, vervolgens: onbekend, Ornstein, Moll, Burger. Portret Julius aan muur, 1928 - Universiteitsmuseum Utrecht

Seated third from left: Kramers, therafter: unknown, Ornstein, Moll, Burger. Wall: portrait of Julius, 1928 - UMU

Toen Julius in 1925 overleed, nam Ornstein ook zijn leerstoel over. Van oudsher opereerde de hoogleraar experimentele natuurkunde namelijk als directeur van het Physisch Laboratorium. Voor Ornstein was het niet vanzelfsprekend dat de vrijgekomen theoretische leerstoel naar een theoreticus zou gaan. Zijn voorkeur ging naar zijn vertrouweling Burger om de eenheid te behouden binnen het lab, ook wel aangeduid als 'firma Ornstein-Burger'. De faculteit nam daar echter geen genoegen mee en ging op zoek naar een theoretisch beter onderlegde kandidaat. Professor Ehrenfest in Leiden schoof zijn oud-leerling Kramers naar voren en verzocht Albert Einstein, Max Planck, Niels Bohr en Lorentz hem aan te bevelen bij de faculteit in Utrecht. Met succes.[n]

[n] M. Dresden, *H.A. Kramers Between Tradition and Revolution* (Springer New York, 1987), p. 312

rigor on a deterministic worldview.

There was very little collaboration between Ornstein's and Kramers' groups, which gave Kramers a lot of freedom to choose the direction of his theoretical research.[h] After Kramers left for Leiden in 1934 another modern quantum mechanist, George Uhlenbeck (1936-1939) was appointed. Like his predecessor he experienced a great deal of independence, while working in the experiment-dominated lab.

[h] M. Dresden, *H.A. Kramers Between Tradition and Revolution* (Springer New York, 1987), p. 71

Met Kramers deed de moderne theoretische natuurkunde zijn intrede in Utrecht. Door de verschillen in filosofie tussen Ornstein en Kramers bleef de samenwerking tussen theorie en experiment beperkt.[o] Dit gaf Kramers veel vrijheid zijn eigen richting te kiezen en met enkele assistenten vormde hij weer een onafhankelijk theoretische vakgroep.

Vanwege de geringe uitwisseling had Kramers geen warme banden met het Physisch Laboratorium. Toen Ehrenfest in 1933 overleed, nam Kramers maar al te graag zijn positie in Leiden over, waar de theorie op een hoger voetstuk stond. Kramers' opvolger Uhlenbeck (1936-1939) was eveneens een leerling van Ehrenfest en een vertegenwoordiger van de moderne quantummechanica. Ook hij genoot relatieve vrijheid in het onderzoek, en kon niet op intensieve samenwerking rekenen met zijn experimentele collega's.

Naast het verdwijnen van de etiket Instituut voor Theoretische Natuurkunde, gebruikte Ornstein vanaf 1925 de naam *Instituut* om het gehele natuurkundig lab aan te duiden. Eind 1940 werd Ornstein vanwege zijn Joodse achtergrond ontslagen. De onervaren kernfysicus Pim Milatz volgde hem op. Een half jaar later overleed Ornstein. Kort daarna trad Léon Rosenfeld, eveneens een student van Bohr, aan als hoogleraar theoretische natuurkunde. Samen met promovendus Bram Pais stortten zij zich op de veldenbeschrijving van mesonen.[p] Op 30 april 1943 stuurde Pais een artikel naar een Deens tijdschrift dat hij ondertekende met

This carries us over to WWII. At the end of 1940, Ornstein was fired from the university, for being Jewish. The young professor Pim Milatz took over as director. Meanwhile, Léon Rosenfeld succeeded Uhlenbeck as professor theoretical physics. Together with assistant Abraham Pais he worked on the field theoretical description of mesons. When Pais sent a paper of their newest work to a Danish journal in 1943, he signed it with *Institute for Theoretical Physics*.[i] This is the first time in twenty years that this name surfaced, and it was meant to stay. After the war all scientific contributions from the theory group bore the signature ITP, showing that Rosenfeld felt the urge and freedom to reinvigorate the institute from the 1910s.

Until 1952 the ITP took refuge in the Physical Laboratory, when the expansion of the group, led by Sybren de Groot, urged them to seek better housing. At first a temporary solution was found in the form of a single floor in a residential home at the Maliebaan.

[o] Ibid. p.71

[p] L. Rosenfeld, '*Meson theories in five dimensions*, Proc. KNAW, vol. 45, nr. 2, pp. 155–158, 1942.

[i] A. Pais, *On the photo-disintegration of the deuterion*, Dan Mat Fys Medd, vol. 20, nr. 17, p. 30, 1943.

Instituut voor theoretische Natuurkunde.[q] Het was voor het eerst in twintig jaar dat deze benaming opdook en het betekende het startsein voor de heropleving van het instituut.

Waarom Rosenfeld deze naam weer ging voeren, blijft enigszins gissen. Na Ornsteins ontslag ontstond er een machtsvacuüm bij natuurkunde. Mogelijk gaf dat Rosenfeld, anders dan zijn voorgangers, de ruimte het Instituut voor Theoretische Natuurkunde te herintroduceren.[r]

Tot begin jaren vijftig woonde het instituut in bij het Physisch Laboratorium. Onder Sybren de Groot verhuisden de theoretici in 1952 naar een eigen gebouw aan de Maliebaan, waar ze een verdieping in een woonhuis betrokken. Dat was een noodoplossing, maar in alle opzichten een verbetering ten opzichte van de krappe vertrekken aan de Bijlhouwerstraat. Vanaf dat moment stond het instituut op eigen benen, het was niet meer onderhevig aan de grillen van het Physisch Lab en werd definitief onafhankelijk. Nadat het in 1955 verhuisde naar een volwaardig pand aan de Maliesingel, groeide het uit tot een solide onderzoeksgroep met meerdere professoraten en een vaste bezetting van enkele tientallen promovendi en postdocs.

Fig. 4: Maliesingel 23, 1974 - Gemeentearchief Utrecht, 63356 / collectie Het Utrechts Archief

Fortunately, in 1955 a more permanent solution was realized at the Maliesingel.

The ITP has survived several university reorganizations and in 1973 moved to the Uithof, nowadays occupying the top floor of the Buys Ballot Building. The discontent of Debye and the changing perspective on physics in the 1910s paved the way for a solid theoretical physics group. With the foundation of the ITP, Ornstein acknowledged this newly gained status. In the 1940s and 1950s, the institute matured under Rosenfeld and De

[q] A. Pais, *On the photo-disintegration of the deuterion*, Dan Mat Fys Medd, vol. 20, nr. 17, p. 30, 1943.

[r] Rosenfeld lijkt bekend met Ornsteins instituut voor theoretische natuurkunde, zie: Verslag Rosenfeld, in: Niels Bohr Archives, Léon Rosenfeld Papers, 1911-1974 - Box 6.7.1: Utrecht (1940-47) - Folder 1, Copenhagen

Fig. 5:
Buys Ballotlaboratoriun 1971 - P. van der Linden, 831240 / collectie Het Utrechts Archief.
Buys Ballot Laboratory 1971 - P. van der Linden, 831240 / collectie HUA.

Nu, bijna zeventig jaar later, bepalen de onderzoekers van het ITF nog altijd grotendeels zelf de richting van het onderzoek en onderwijs. Samenwerking met experimentele natuurkunde is aan de orde van de dag, maar gebeurt op voet van gelijkheid. Het belang van toegewijde theoreten werd voor het eerst duidelijk halverwege de jaren 1910, wat Ornstein onderkende door het instituut theoretische natuurkunde te beginnen in 1916. Onder Rosenfeld, De Groot en Léon van Hove ontwikkelde het ITF zich tot een onafhankelijk organisatie, een volwassen onderzoeksgroep. Deze roerige geschiedenis vieren we in september, ter ere van het 105-jarig bestaan van het Instituut voor Theoretische Fysica.

Groot into an independent research group.

This year we celebrate the 105th anniversary. It is of course a shame that we are a few years late celebrating the centenary.

Acknowledgments

First of all, I would like to thank Dirk, for offering me the great opportunity to do a PhD under his supervision. I really enjoyed working together on many different projects. Your patient, thoughtful and open-minded approach to any idea and proposal, but also our endless chats about javelin throwing, chess, solving the pandemic and everyday live made the last four years fly by.

I would like to thank Rembert for being my official promotor. Moreover, I want to thank Lars for all the great discussions, both about physics, but also about sports and Dutch and German habits and quirks.

I am grateful to my collaborators, both in the Netherlands and abroad, Hosho, Iman, Fabian, Dion and Akash. Especially, I want to express my gratitude towards Hosho and his group in Tokyo for their hospitality, offering me a great time in their beautiful city in 2018. Likewise, I want to thank Iman and Eddy for my delightful stay in Stockholm in 2019. I will remember the lovely daily fika and lunch with Theory of Quantum Matter group.

Also, I would like to thank my colleagues at the institute for making the Buys Ballot Building a great place to work.

Graag wil ik mijn familie en vrienden in het zonnetje zetten. Bovenal wil ik mijn ouders, Bernard en Annemieke, bedanken. Dankzij jullie onuitputtelijke en onvoorwaardelijke zorg en aandacht ben ik gekomen waar ik nu sta. Broers en aanhang, Marius en Ilse, Hilbrand en Kalid, bedankt voor de gezelligheid en steun. Ik ben dankbaar dat oma Hannie er nog bij is, opa was vast heel trots geweest als hij mij in de senaatszaal had kunnen zien staan. Bedankt Paul, Marie-José, Anouk en Teun voor alle steun afgelopen jaren.

Matthijs, bedankt voor meer dan 16 jaar vriendschap. Na de middelbare school zijn er periodes geweest dat we elkaar maanden of zelfs jaren niet zagen. Met sommige vrienden is dat geen probleem en is het in een mum van tijd weer als vanouds.

Laurens, het lijkt al een eeuwigheid geleden dat we door ons door de master heen werkten. Bedankt voor alle goede gesprekken over wetenschap en vooral ook over het leven buiten de wetenschap. Dank dat je bij mijn promotie als

paranimf aanwezig wilt zijn.

Ik ben mijn atletiekfamilie heel dankbaar voor het plezier en de sportieve successen. In het bijzonder wil ik mijn coaches Kees en Elliott bedanken. Jullie staan bijna dagelijks belangeloos met mij op de atletiekbaan, en reizen stad en land af om alle diepte-, maar zeker ook alle hoogtepunten mee te maken. Dank Javelin Team Whazzaa! voor alle gezellige trainingen. Erik bedankt voor de hulp bij het ontwerpen van de voorkant van mijn proefschrift. Dank Thijs voor het aanvaarden van de zware taak als paranimf, de afgelopen jaren hebben we veel lief en leed gedeeld.

Tot slot wil ik Tessa bedanken voor alle steun en liefde. Dat ik dit samen met jou mag delen is een voorrecht en ik kijk met veel plezier uit naar alle avonturen die ons nog te wachten staan. Ik prijs mij gelukkig jou aan mijn zijde te hebben.

About the author

Jurriaan Wouters was born on 18 April 1993 in Amersfoort, The Netherlands. In 2011, he obtained his VWO (high school) diploma cum laude at 't Atrium in Amersfoort with a major in Science and Health and extra subject in Geography. Later that year he enrolled in a combined Bachelor degree Physics and Mathematics at the Utrecht University from which he graduated cum laude in 2014. His Bachelor thesis, under supervision of Prof. Dr. René van Roij focussed on blue energy. In 2014, he continued his academic career in Utrecht with a Master in Theoretical Physics. He graduated cum laude in 2017, having written his Master Thesis on the Kondo model and the Kitaev chain, supervised by Dr. Lars Fritz. Later in 2017, he became a PhD candidate in Utrecht under supervision of Dr. Dirk Schuricht. The resulting research is presented in this thesis. In the four years, he collaborated with researchers from Utrecht and elsewhere and he was a teaching assistant to several Bachelor and Master courses. Also he organized several series of talks for the institute. He was a visiting scientist at the Tokyo University, with Prof. Dr. Hosho Katsura in 2018 and at Stockholm University, with Prof. Eddy Ardonne and Dr. Iman Mahyaeh in 2019. In 2020 he conducted historic research involving the origins of the Institute for Theoretical Physics.

FBK Games 2021 © Johan Manders

Concurrent with his academic career he pursued a career as an elite javelin thrower. In 2012 he became 18th in the World Junior Championships in Barcelona (Spain) and in 2015 he reached the Final in the European under 23 Championships in Tallinn (Estonia), taking 11th place. In 2014 and 2020 he became Dutch Champion, winning another bronze medal in 2018. His current personal best is 77.16m, 9th on the Dutch all time ranking.